



**HAL**  
open science

## Polarimetric radar images

Elise Colin Koeniguer

► **To cite this version:**

Elise Colin Koeniguer. Polarimetric radar images. Signal and Image processing. Université Paris Sud, 2014. tel-01090950

**HAL Id: tel-01090950**

**<https://theses.hal.science/tel-01090950>**

Submitted on 5 Dec 2014

**HAL** is a multi-disciplinary open access archive for the deposit and dissemination of scientific research documents, whether they are published or not. The documents may come from teaching and research institutions in France or abroad, or from public or private research centers.

L'archive ouverte pluridisciplinaire **HAL**, est destinée au dépôt et à la diffusion de documents scientifiques de niveau recherche, publiés ou non, émanant des établissements d'enseignement et de recherche français ou étrangers, des laboratoires publics ou privés.



Distributed under a Creative Commons Attribution - NonCommercial 4.0 International License

# MANUSCRIT

Présenté pour obtenir

L'HABILITATION A DIRIGER DES  
RECHERCHES DE L'UNIVERSITÉ  
PARIS-SUD XI

Spécialité: Imagerie Physique

par

Elise COLIN KOENIGUER

## Images polarimétriques radar: de l'acquisition à l'inversion

Soutenue le 26 Novembre 2014 devant la Commission d'examen:

M.	Emmanuel TROUVÉ	(Rapporteur)
M.	François GOUDAIL	(Rapporteur)
M.	Mihai DATCU	(Rapporteur)
M.	Razvigor OSSIKOVSKI	(Examineur)
M.	Thuy LE TOAN	(Examineur)



**Onera**  
Chemin de la Hunière et des Joncherettes  
91 123 Palaiseau CEDEX

# Table des matières

Introduction	4
I Curriculum Vitae	6
II Synthèse Scientifique. L'image polarimétrique radar : de sa formation à son inversion.	25
III Sélection de publications	170

# Introduction

Ce document s'articule en trois parties. La première est un Curriculum vitae qui détaille mes activités de recherche. Il fournit, entre autres, la liste de mes encadrements de thèse, de mes publications et de mes activités d'enseignement.

La seconde partie est une synthèse scientifique de mes travaux portant sur l'imagerie polarimétrique radar. Cette partie est rédigée en anglais, de manière à pouvoir être éventuellement diffusée de manière indépendante pour un public international.

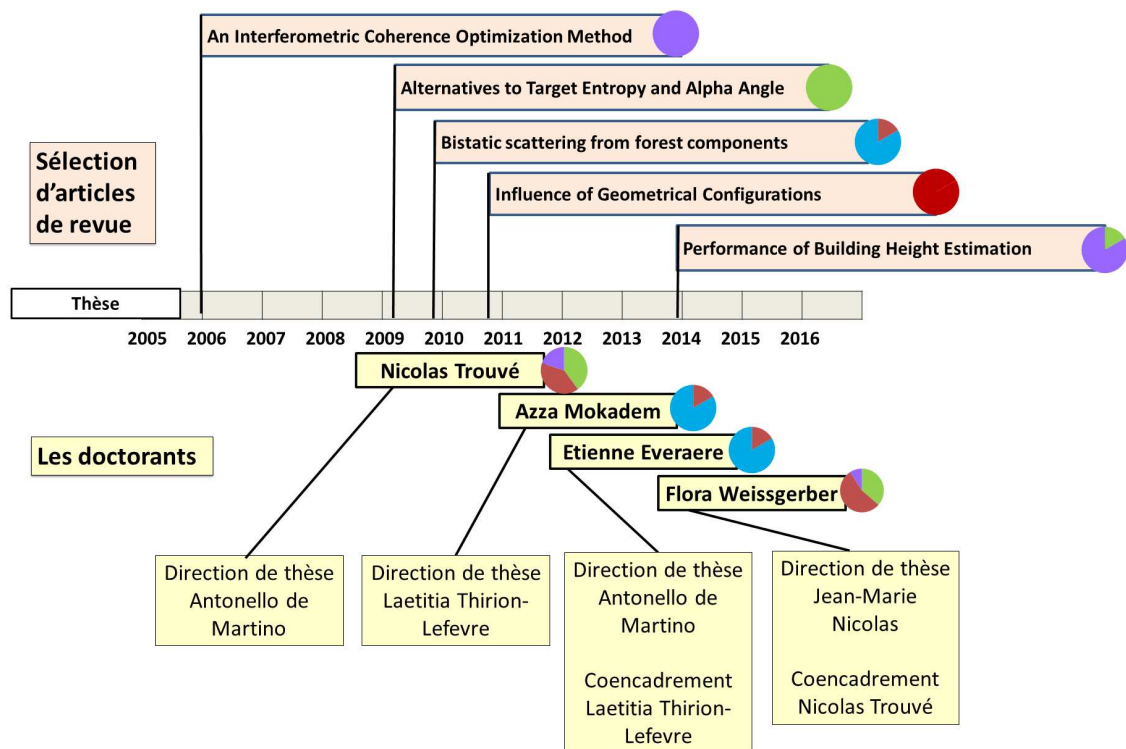
Volontairement, ce dossier ne suit par un ordre chronologique dans mes travaux mais regroupe un ensemble de techniques abordées, en partant du capteur, en abordant les prétraitements, pour aller progressivement aux traitements avancés nécessitant une compréhension fine de l'environnement.

Au fil de ces parties apparaîtront les contributions des quatre doctorants que j'ai pu co-encadrer :

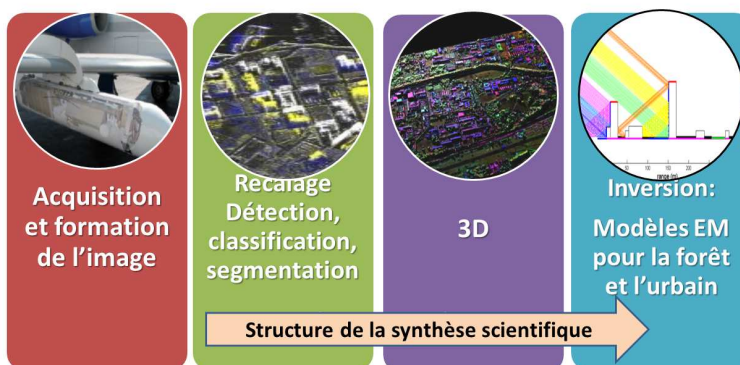
- **Nicolas Trouvé** a effectué sa thèse entre novembre 2008 et novembre 2011 à l'Onera avec comme directeur de thèse Antonello de Martino au LPICM, sur la convergence des outils polarimétriques radar et optique.
- **Azza Mokadem** a effectué sa thèse sous la direction de thèse de Laetitia Thirion-Lefevre au laboratoire SONDRRA, entre janvier 2011 et janvier 2014. Son sujet portait sur la compréhension fine des images SAR de milieux urbains, avec notamment des perspectives de détection de cibles par les multitrajets au sein des canyons urbains.
- **Etienne Everaere** a commencé sa thèse en octobre 2011, qui est en cours de finalisation. Son sujet porte sur la mesure radar de forêts en configuration bistatique polarimétrique, à l'aide d'un instrument optique. La thèse s'est effectuée sous la direction de thèse d'Antonello De Martino, et depuis septembre 2014 de Razvigor Ossikovski au LPICM, ainsi que le coencadrement de Laetitia Thirion-Lefevre.
- **Flora Weissgerber** a commencé sa thèse en novembre 2013 sur l'utilisation combinée d'images SAR haute résolution mono-mode, avec une image polarimétrique de résolution dégradée. Elle travaille sous la direction de thèse de Jean-Marie Nicolas à Telecom Paris-Tech, et le coencadrement de Nicolas Trouvé à l'Onera.

La troisième partie de ce document est une compilation de cinq articles de revue auxquels j'ai contribué. Ce sont des articles représentatifs de mes différentes activités en imagerie radar polarimétrique, exposées dans la synthèse scientifique.

L'apparition chronologique des doctorants encadrés et des articles de revue sélectionnés est donnée sur le schéma de la page suivante. Leurs contributions relatives aux différentes parties de la synthèse scientifique sont représentées par des diagrammes circulaires colorés.



**La structure du dossier scientifique**



Première partie

# Curriculum Vitae

## 1 - Etat Civil

Elise Colin-Koeniguer  
Née le 15 novembre 1979 à Chatenay-Malabry (92)  
Mariée, 2 enfants

Onera  
Chemin de la Hunière et des Joncherettes  
BP 80100  
FR-91123 Palaiseau Cedex Tel. +33 (0)1 80 38 65 70  
Email : elise.koeniguer@onera.fr

## 2 - Titres Universitaires

- 2002-2005 **Doctorat**, *Université Pierre et Marie Curie, Paris 6, Mention Très Honorable.*  
Apport de la Polarimétrie à l'interférométrie radar ; application à l'estimation de hauteurs de cibles et de paramètres de forêts.  
Soutenue le 22 septembre 2005, en spécialité Electronique, devant le jury composé de :  
 Mr Michel Glass, Président du Jury (Université de Paris 6)  
 Mr Andreas Reigber, Rapporteur (Université de Berlin)  
 Mr Eric Pottier, Rapporteur (Université de Rennes 1)  
 Mr Kostas Papathanassiou, Examineur (DLR-Allemagne)  
 Mr Walid Tabbara, Directeur de thèse (Université de Paris 6)  
 Mrs Cécile Titin-Schnaider, Encadrante (Onera)
- 1999-2002 **Diplôme d'Ingénieur SUPELEC**, *1er décile de promotion.*
- 2001-2002 **Master de Recherche**, *CPM Champ Particules Matière, (aujourd'hui NPAC), Université Paris Sud, mention Bien.*
- 1996-1999 **Classes Préparatoires**, *Lycée Saint-Louis, Paris.*
- 1998 **DEUG MIAS**, *Université Pierre et Marie Curie, Paris 6, Mathématiques et Informatique.*  
En parallèle des Classes Préparatoires
- 1996 **Baccalauréat Scientifique**, *Lycée Louis Le grand, Paris, mention Bien.*

## 3 - Parcours

- Octobre 2013 Ingénieur de Recherche à l'Onera, Département de Traitement de l'Information et Modélisation (DTIM)
- 2005-2013 Ingénieur de Recherche à l'Onera, Département ElectroMagnétisme et Radar (DEMR)
- 2002-2005 Thèse menée à l'Onera, Département ElectroMagnétisme et Radar (DEMR)

L'Office National d'Etude et de Recherches en Aérospatial (ONERA), est le centre français de la recherche aéronautique, spatiale et de défense. C'est un Etablissement Public à caractère Industriel et Commercial (EPIC), au service des agences de programmes, des institutionnels et des industriels. J'exerce aujourd'hui la fonction d'Ingénieur de Recherche, menant des activités contractuelles et des activités de recherche, au sein du **Département de Traitement de l'Information et Modélisation** depuis 2013. J'ai acquis auparavant une expertise en imagerie radar, ainsi qu'en polarimétrie radar

et optique, au sein du Département ElectroMagnétisme et Radar. Ces compétences trouvent naturellement leur place dans mon nouveau département, et me permettent d'approfondir les aspects de traitements d'image appliqués à des images dans un plus large spectre.

#### 4 - Activités d'enseignements

- 2010-2014 **Cours Imagerie Radar en dernière année d'Ecole d'ingénieur**, *SUPELEC*, Réalisation d'un cours magistral sur la formation et l'analyse des images SAR, photocopié, et mini-projets matlab sur la formation d'une image à partir de données brutes. 24h00 par an depuis 4 ans, 24 étudiants environ.  
Niveau Bac+5
- 2013 **2nd Advanced Course on Radar Polarimetry**, *Agence Spatiale Européenne*, Cours de Tutorial organisé par l'Agence Spatiale Européenne, Public : Doctorants, Postdoctorants et Personnels de recherche, européen et canadien, représentant une soixantaine de personnes.  
Intervention d'une heure sur le sujet *Urban: Classification and 3D rendering*
- 2009-2010 **Examinatrice T.I.P.E**, *Oraux des Grandes Ecoles d'Ingénieur*, Examinatrice de physique, filière Maths-Physique.
- 2009-2010 **Oraux Concours Ingénieurs Classes Préparatoires ATS**, *Examinatrice oraux des concours aux Ecoles d'ingénieur*, *Examinatrice de physique, filière ATS 2006-2007 : 16h00, 2005-2006 : 32h00, 2004-2005 : 32h00.*
- 2004-2005 **TD probabilités**, *IFIPS - Formation d'ingénieur de l'Université de Paris Sud - 4h30.*
- 2004 **TD Signal Aléatoire**, *Maîtrise EEA, Université Paris 6 - 20h00.*
- 2004 **TP Signal Aléatoire**, *Maîtrise EEA, Université Paris 6 - 20h00.*
- 2003 **TP Electronique**, *License EEA, Université Paris 6 40h00.*

#### 5 - Activités liées à l'administration

L'activité Scientifique de l'Onera s'articule en cinq Branches, chacune d'entre elle regroupant quatre à cinq départements. Mon premier département d'appartenance, le DEMR, fait partie de la branche Physique, tandis que mon département actuel, le DTIM, fait partie de la branche Traitement de l'Information et des Systèmes. Un département contient une centaine de personnes scientifiques et techniques.

##### Membre du Conseil Scientifique de la Branche Physique : 2006-2013

La Branche Physique de l'Onera regroupe quatre départements, dont les coeurs de compétence couvrent entre autres les domaines de l'électromagnétisme, de l'électronique et de l'optique. Le Conseil Scientifique de Branche, constitué d'une vingtaine de membres, est amené à assister le Directeur de la Branche dans ses missions de sélection des sujets de thèse, et d'évaluation des doctorants lors de Journées Annuelles de présentation de leurs travaux.

##### Membre du Conseil Scientifique de Département : 2006-2013

Le rôle du Conseil Scientifique du Département DEMR est d'assister le directeur de département pour l'organisation de Séminaires Internes, de journées de présentation thématiques, du choix des congrès sur lesquels le département doit se positionner, des orientations scientifiques à moyen terme du département.

### Correspondante Communication pour le Département : 2006-2013

La Direction de la Communication s'appuie au sein de chaque département sur un Correspondant Communication dont j'ai assuré le rôle de 2008 à 2013. Ce rôle consiste à diffuser et faire remonter l'information pour en améliorer la diffusion.

### Animateur Qualité pour l'unité : 2007-2013

Au sein de mon unité Traitement du Signal, le rôle de l'animateur qualité est d'aider le Département Qualité et Organisation à déployer les procédures qualités mises en place à l'Onera, un des premiers organismes de recherche à avoir obtenu la certification ISO 9001 en janvier 2009.

### Enseignements

Le statut d'ingénieur de Recherche de l'Onera permet de faire un nombre d'heures d'enseignement limité à une trentaine d'heures par an, que j'ai mis à profit pour assurer chaque année un certain nombre d'heures dédiées aux cours magistraux ou à la participation à des jurys de concours. Le détail de ces enseignements est donné dans la suite.

## 6 - Activités liées à la recherche

### 6-1 Prix

**Interactive Session Prize Award**, IEEE IGARSS 2003, pour le papier *A new parameter for IFPOL coherence optimization methods*, Colin, E ; Titin-Schnaider, C. ; Tabbara, W.

### 6-2 Participation à des comités, Editorial Boards, organisation de colloque, séminaire, etc.

#### Chair Congrès

- Congrès IEEE IGARSS 2006, Denver
- Congrès IEEE IGARSS 2007, Barcelone
- Workshop ESA POLINSAR 2011, Frascati
- Workshop ESA POLINSAR 2013, Frascati

#### Membre de comité de relecture de revues internationales

- IEEE Transactions on Geoscience and Remote Sensing (TGRS)
- IEEE Geoscience and Remote Sensing Letters (GRSL)
- IEEE Journal of Selected Topics in Applied Earth Observations and Remote Sensing (JSTARS)
- Canadian Journal of Remote Sensing, (Can J Rem Sens.)
- Journal of Electromagnetic Waves and Applications (JEMWA)

#### Membre de comité de relecture pour des congrès, workshop

- IEEE International Geoscience and Remote Sensing Symposium (IGARSS)
- International Workshop on Science and Applications of SAR Polarimetry and Polarimetric Interferometry (POLINSAR, Workshop ESA)
- GRETSI, Groupe d'Études du Traitement du Signal et des Images

#### Autres

- Participation à des journées du GDR ISIS (Information, Signal, Image et ViSion)
- Membre du Comité scientifique du workshop POLINSAR 2013, POLINSAR 2015

- Membre du jury de thèse de M. Neumann, Université de Rennes 1, 2010

### 6-3 Collaborations

Liste des laboratoires de recherche avec lesquels j'ai pu collaborer à travers des contrats ou des publications communes:

#### Internationales

- Université d'Helsinki (Finlande)
- Agence de Défense Suédoise, FOI (Suède)
- Université polytechnique de Catalogne, UPC (Espagne)
- Université de Parthenope, Naples (Italie)
- Université d'Alicante, UA (Espagne)
- SONDRRA, Alliance de Laboratoires de Recherche entre Supélec, ONERA, NUS (National University of Singapore) et DSO National Laboratories (Singapour)
- DLR, Centre de Recherche en Aérospatial (Allemagne)

#### Nationales

- LPICM, Laboratoire de Physique des Interfaces et des Couches Minces, Ecole Polytechnique/CNRS
- Telecom Paris Tech, Département Traitement du Signal et des Images
- IETR, Institut d'Électronique et de Télécommunications de Rennes, Université de Rennes 1
- GIPSA-lab, Grenoble Images Parole Signal Automatique, unité mixte CNRS/Université de Grenoble
- CEA, Commissariat à l'énergie atomique et aux énergies alternatives
- CNES, Centre National d'Etudes Spatiales

### 6-4 Valorisations, brevets, logiciels

#### **Brevet : Calibration d'un émetteur ou récepteur de radar polarimétrique - Cas 2437**

Inventeurs : Nicolas Trouvé, Elise Colin-Koeniguer, Antonello de Martino

Brevet pour une invention relative à un système d'étalonnage polarimétrique pour les radars. Les formalités pour déposer la demande de brevet ci-dessus référencée auprès de l'INPI ont été accomplies le 19 décembre 2013. Le numéro d'enregistrement attribué à cette demande est le 13.63047.

#### **Logiciel déposé PAPIRUS : Polarimetric And Polarimetric Interferometric Rendering by Urban Segmentation**

Concepteurs : Nicolas Trouvé, Elise Colin-Koeniguer.

Logiciel déposé pour la reconstruction 3D à partir de données POLINSAR, appuyé par un algorithme de Segmentation Hiérarchique.

Compte tenu de mes activités en tant que Correspondante Communication pour le département DEMR, j'ai pu mener plusieurs activités de Médiation Scientifique parallèlement à mes activités de recherche :

**Court Métrage "Une journée au radar", 2011** Depuis 2007, l'association des doctorants de l'UMPC organise le festival "Les chercheurs font leur cinéma", un festival de très courts métrages de vulgarisation scientifique. Ce festival a pour but de lever le voile sur la recherche scientifique et le quotidien des chercheurs. Je suis à l'initiative d'une participation à l'édition 2011 de ce concours

avec la réalisation du court-métrage "Une journée au radar" (Scénario, Réalisation, Montage).

**Concours Art et Sciences 2010-2012** L'association des docteurs de l'Université Pierre et Marie Curie et l'association des doctorants de Sorbonne Université propose un concours "Arts et Sciences". A l'issue de l'appel à candidatures, une vingtaine de créations sont sélectionnées pour être publiées ou exposées à l'UPMC. Une oeuvre a été proposée en 2010, une autre en 2012. Toutes deux ont été sélectionnées puis exposées.

**Exposition au Musée du radar, Été 2012** Durant l'été 2012, le musée du radar de Douvres-la-Délivrande (Calvados) a accueilli plus de 5000 visiteurs pour l'exposition temporaire "Recherches sur l'avion invisible", conçue par Sylvain Gaultier de la direction de la communication, et moi-même.

**Fête de la Sciences à Palaiseau, Octobre 2012** J'ai participé en 2012 à l'organisation d'un stand animé autour de la thématique "urbain", avec l'élaboration et la présentation d'un court film "Les villes observées par des radars".

**Projet "Ondes" de Scube, 2012-2013** De fin 2012 à 2013, j'ai été membre du Comité Scientifique du projet "Ondes" de l'association S-Cube (Scientipôle, Savoir et Société) de la CAPS, qui est intervenue notamment dans l'organisation de la fête de la Sciences 2013 pour le plateau de Saclay. Réalisations pratiques : Ateliers expérimentaux pour les scolaires, projet " marque-page ", visite des laboratoires de l'Onera.

**Séminaire "Traitement du Signal", 2013** Ce séminaire d'une heure a été conçu et présenté avec l'aide d'Olivier Rabaste, collègue au sein de mon unité. Le séminaire s'adressait au Lycée et Classes préparatoires des Ulis, afin de vulgariser et donner une définition du traitement du signal et de donner des exemples d'applications sur nos domaines de recherche actuels.

**Portes ouvertes Onera fête de la Science - Octobre 2013** J'ai animé la visite de la chambre anéchoïque bistatique de l'Onera, lors de la journée porte ouverte organisée dans le cadre de la fête de la Science.

#### 6-5 Administration liée à la recherche: activités contractuelles

Les recherches menées à l'Onera ont toujours une visée applicative à court, moyen ou long terme. L'Onera a en effet pour mission de favoriser les transferts pour l'industrie, fournir à l'industrie des expertises de haut niveau. Avec près de 60% d'activités contractuelles, il est l'un des centres de recherche les moins subventionnés d'Europe. Les chercheurs de l'Onera ont d'ailleurs cinq fois plus d'activités contractuelles par chercheur que la moyenne nationale.

Dans ce contexte, j'ai été amenée à valoriser mes travaux de recherche en partie à travers la conduite d'un certain nombre d'études contractuelles et par la rédaction de divers rapports techniques.

- R1 **Objet du Contrat** : Etude polarimétrique de cibles leurrées non résolues  
**Client et dates** : DGA-SPNuM, 2005-2006  
**Description** : Cette étude s'inscrit parmi des travaux d'expertise dans les domaines de la pénétration balistique, des senseurs infrarouges, électromagnétiques et de la discrimination de cibles.  
**Ma contribution** : Responsable Technique du poste d'expertise sur l'efficacité des leurres vis-à-vis d'une mesure polarimétrique, Rapport Technique.
- R2 **Objet du Contrat** : Compression d'images SAR  
**Client et dates** : UM-ESIO, 2007-2009  
**Description** : Cette étude concerne la proposition d'algorithmes de compression d'images SAR en mode complexe, et leurs effets sur l'efficacité des *techniques SAR avancées* telles qu'interférométrie et radargrammétrie. L'étude a abouti à la livraison d'un démonstrateur logiciel. Cette étude a été effectuée en cotraitance entre Thales et l'Onera.  
**Ma contribution** : Responsable Technique Onera, livraison de codes logiciels, Rapports Techniques.
- R3 **Objet du Contrat** : Détection sous feuillage (FOPEN) en situation bistatique  
**Client et dates** : DGA, 2007-2008  
**Description** : Cette étude financée en partie pour la DGA a pour but la validation du concept d'utilisation en multistatique aéroporté des basses fréquences pour la détection sous le feuillage. L'étude comprend également la préparation d'une campagne d'acquisition d'images SAR bistatiques pour la détection de véhicules cachés sous le couvert végétal.  
**Ma contribution** : Définition de la situation géométrique la plus adaptée à la détection basse fréquence, appuyée par des études de modélisation électromagnétique et sur le dépouillement et l'analyse de mesures conduites à l'Onera en chambre anéchoïque. Rapports techniques.
- R4 **Objet du Contrat** : Validation des outils de filtrage et d'imagerie SAR sur données réelles.  
**Client et dates** : DGA, 2008-2009  
**Description** : Cette étude concerne la faisabilité d'images radar "SAR" (Synthetic Aperture Radar) à partir de situation d'écoute d'un émetteur d'opportunité de type satellite GPS.  
**Ma contribution** : Evaluation de méthodes d'imagerie bistatique (émetteur et récepteur séparés), Analyse de mesures en chambre anéchoïque.

- R5 **Objet du Contrat** : Amélioration de la reconnaissance non coopérative des cibles  
**Client et dates** : DGA - UM AERO, 2009  
**Description** : Cette étude concerne l'amélioration des traitements pour la reconnaissance de cibles aériennes par les radars, notamment via l'utilisation de l'interférométrie.  
**Ma contribution** : dimensionnement d'une expérimentation interférométrique, évaluation de l'apport de ce mode en classification de cibles. Rapports Techniques.
- R6 **Objet du Contrat** : Compression d'images vidéos dans le contexte de la Pénétration Balistique Stratégique.  
**Client et dates** : DGA, UM COE, 2011  
**Description** : Cette étude concerne la transmission rapide d'images vidéos infrarouges dans le contexte de la pénétration balistique.  
**Ma contribution** : Développement et évaluation des performances de différents compresseurs, Rapport Technique.
- R7 **Objet du Contrat** : Navigation Inertielle Hybridée  
**Client et dates** : Onera, Ressources générales, 2012  
**Description** : Cette étude concerne le dimensionnement des formes d'ondes radar radioaltimétrique pour l'aide à la navigation.  
**Ma contribution** : Article Technique de synthèse.
- R8 **Objet du Contrat** : Démonstrateur des apports de l'imagerie Polarimétrique pour les applications de télédétection en environnement urbain.  
**Client et dates** : ESA - ESRIN, 2011-2013  
**Description** : POLSARAp est une étude visant à démontrer le potentiel des applications phares de la polarimétrie en imagerie civile de télédétection. Un consortium européen s'est formé pour répondre à l'appel d'offre, réunissant plusieurs entités, dont le DLR (Deutschen Zentrums für Luft- und Raumfahrt), le centre de Recherche Aérospatial allemand, manager du projet. L'Onera est responsable de la thématique "Applications urbaines".  
**Ma contribution** : Principal Investigator Onera pour le Projet, Responsable Technique de la tâche *Environnement Urbain*, Rapports techniques. Mon rôle consiste également à définir des experts externes avec lesquels mener une collaboration. Le projet doit s'achever par la publication d'un livre sur l'apport de la polarimétrie en télédétection radar et d'un démonstrateur logiciel destiné à l'enseignement supérieur et à la recherche.

- R9 **Objet du Contrat** : Etude théorique sur l'apport de la polarimétrie pour l'imagerie SAR en environnement urbain  
**Client et dates** : Onera, Ressources Générales, 2012  
**Description** : Cette étude concerne le rôle de la polarimétrie sur les images en environnement urbain, et fait le point sur les performances du mode polarimétrique pour les diverses applications : rendu 3D et classification, en utilisant un spectre d'images beaucoup plus larges que dans l'étude ESA, ainsi que des outils de modélisation.  
**Ma contribution** : Etude, Evaluation des performances, Rapport de Synthèse.
- R10 **Objet du Contrat** : Réseau de radars communicants pour zones urbaines (CORAZON)  
**Client et dates** : Onera, 2013  
**Description** : Corazon est un projet interne de Recherche visant à déployer un système de radars pour la surveillance en zones urbaines, en s'appuyant sur la détection de cibles en visée non directe du radar, par les multitrajets. Dans ce cadre, un modèle simple de propagation par multitrajets de l'onde au sein de plusieurs rues a été développé. Ce modèle s'interface avec les entrées d'un algorithme de filtrage particulière dédié au pistage de véhicule. Une expérimentation radar a été mise en place pour prouver la faisabilité du concept.  
**Ma contribution** : Participation à l'élaboration de l'expérimentation, développement du simulateur simplifié, Rapport Technique.
- R11 **Objet du Contrat** : Détection de superstructures sur des images SAR (EFUSION)  
**Client et dates** : DGA UM ESIO, 2013-2014  
**Description** : Au sein du contrat EFUSION, la tâche concernée a pour objet la détection de superstructures types pylônes, éoliennes et câbles électriques, sur des images radar et sur des images optiques, pour des besoins de cartographie et de navigation à basse altitude.  
**Ma contribution** : Analyse physique de la synthèse des cibles d'intérêt, développement d'algorithmes de détection dédiés, évaluation. Rapports Techniques

---

## 7 - Encadrement

### Thèses

#### **Encadrement de la thèse de Nicolas Trouvé (70%),**

*Comparaison des outils optique et radar en polarimétrie bistatique*

Thèse ONERA-X novembre 2008- novembre 2011

Directeur de thèse : Antonello de Martino (CNRS, X-LPICM)

Thèse soutenue le 22 novembre 2011 devant le jury constitué de :

- Mr Eric Pottier, Université de Rennes 1 (Rapporteur)
- Mr François Goudail, Institut d'optique Graduate School (Rapporteur)
- Mr Antonello de Martino (Directeur de thèse, LPICM - X)
- Me Elise Colin-Koeniguer (Encadrante de thèse, Onera)

- Mr Xavier Orlik (Onera)
- Mr Shane Cloude (AEL Consultant)
- Mr Jihad Zallat (LSIIT)

*Situation Professionnelle Actuelle:* CDI d'Ingénieur de Recherche à l'Onera obtenu à l'issue de la thèse, en traitement du signal radar.

#### **Encadrement de la thèse d'Azza Mokadem (40%),**

*Modélisation électromagnétique de la diffusion en bande X dédiée à l'analyse des techniques SAR avancées pour la détection en milieu urbain*

Thèse ONERA-SONDRA janvier 2011- janvier 2014

Directrice de thèse : Laetitia Thirion (SONDRA, Supélec)

Thèse soutenue le 4 février 2014 devant le jury constitué de :

- Mr Bernard Uguen, Université de Rennes 1 (Rapporteur)
- Mr Yves Lostanlen, Université de Toronto/SIRADEL (Rapporteur)
- Mr Laetitia Thirion, Sondra, Supelec (Directrice de thèse),
- Me Elise Colin-Koeniguer , Onera (Encadrante de thèse)
- Mr Jean-Marie Nicolas, Telecom Paris-Tech
- Mr Juan Carlos Lopez-Martinez, UPC, Université de Barcelone
- Mr Lionel Pichon, LGEP, Supelec
- Mr Regis Guinvarch', Sondra, Supelec

*Situation Professionnelle Actuelle:* Après un CDD de 6 mois pour un projet de Recherche à Supelec, obtenu à l'issue de la thèse, Azza Mokadem est actuellement en poste d'ATER à l'Université Paris 6 en traitement du signal.

#### **Encadrement de la thèse d'Etienne Everaere (35%)**

*Étude polarimétrique de la forêt en configuration bistatique*

Thèse ONERA-X-SONDRA.

Débutée en octobre 2011

Directeur de thèse : Antonello de Martino (CNRS, X-LPICM), thèse co-supervisée par Laetitia Thirion-Lefevre (SONDRA)

#### **Encadrement de la thèse de Flora Weissgerber (35%)**

*Enrichissement monomode de données haute résolution en milieu urbain.*

Thèse Telecom Paris Tech-ONERA, bourse DGA/Club des partenaires défense,

Débutée en octobre 2013.

Directeur de thèse : Jean-Marie Nicolas (Telecom Paris-Tech), thèse co-supervisée par Nicolas Trouvé (Onera)

### Stages

- 2009 **Nicolas Sar** : Faisabilité de la détection d'une cible cachée dans un canyon urbain : analyse des profils distances radar. Stage de MR1
- 2010 **Stanislas Bouchet** : Etude des forêts en imagerie SAR bistatique à l'aide d'un simulateur. Stage de MR1
- 2012 **Arthur Vilhelm** : Développement de fonctions de traitement d'image SAR dédiées à l'analyse polarimétrique de zones urbaines. Stage de MR1

### Projet de Fin d'Etude

- 2011 **IPSA, Ecole d'Ingénieur de l'Air et de L'espace**. Encadrement d'un projet de fin d'étude de trois étudiants niveau MR2. Sujet : Etude des milieux naturels en configuration radar bistatique

## 8 - Synthèse des travaux, Description des principaux résultats, Projets, Perspectives

Mes années de recherche au sein d'un Département ElectroMagnétisme et Radar m'ont conduite à développer une thématique nouvelle ayant pour objet la convergence des théories polarimétriques en imagerie radar et en imagerie optique. Cette thématique a été initiée à travers des publications comme [A 6], [C1,8], puis développée pendant la thèse de N. Trouvé. L'idée initiale était de s'inspirer de l'imagerie optique polarimétrique, afin d'en déduire les bénéfiques potentiels pour les applications radars. Cette voie de recherche a été fructueuse sur plusieurs points :

- Elle a conduit à approfondir la compréhension des relations entre la géométrie de la cible et les émissions de polarisation des antennes. Cette compréhension est indispensable à l'interprétation correcte des données et au transfert des analyses entre le radar et l'optique. Ce point fait l'objet de la publication [A,3].
- Elle a permis d'envisager une utilisation des moyens de mesures optiques pour le radar, en développant des cibles à l'échelle optique. Ces mesures ont permis d'avancer sur la compréhension en imagerie radar des phénomènes de dépolarisation des milieux naturels comme par exemple la forêt, en utilisant des forêts de nanotubes [C2,3]. Ces mesures sont exploitées dans la thèse en cours d'E. Everaere, ayant pour objectif la détermination des configurations d'intérêt pour la détection et l'inversion des paramètres forestiers.
- Elle a ouvert la voie vers l'utilisation des décompositions polarimétriques multiplicatives pour l'inversion des images polarimétriques radar [C1,3].
- Elle a permis de mettre au point une nouvelle technique d'étalonnage bistatique polarimétrique novatrice en radar, qui répond à certains contextes difficiles. Cette technique a fait l'objet d'un dépôt de demande de brevet.

Un autre aspect de mes travaux récents concerne l'étude du milieu urbain en imagerie radar. Cet aspect a été abordé dans plusieurs cadres d'application :

- Pour la détection de cibles (piétons, véhicules) et de la surveillance de zones urbaines à partir de signaux radar. Pour répondre à cette application, la thèse d'Azza Mokadem étudie plus précisément la phénoménologie électromagnétique d'un environnement urbain complexe, en vue de prédire les probabilités de détection d'une cible dans une image radar [C2 9], [C2 10], [C2 12]. Parallèlement à cette thèse, le projet de recherche [R10] aborde le pistage d'une cible au sol à partir du déploiement d'un réseau de capteurs radar déployés dans le tissu urbain [S1].
- Pour le monitoring de la croissance urbaine à partir d'images radar.

La problématique de l'imagerie en zone urbaine a été développée dans le cadre d'un projet de recherche interne [R9] et mise à profit au sein d'une collaboration internationale pour un projet de l'ESA (Agence Spatiale Européenne) [R8]. Cette collaboration vise à mettre en avant les apports de la polarimétrie pour les applications de télédétection urbaine. Cette thématique se poursuit à travers la thèse de Flora Weissgerber en collaboration avec Telecom Paris Tech, portant sur la fusion d'images Haute résolution et d'images polarimétriques acquises en résolution dégradée.

Mon changement de département et d'activités au sein de l'onera résulte d'une volonté de poursuivre des travaux de recherche en imagerie, tout en élargissant le spectre des images traitées, et le type de traitements investigués. Le Département du Traitement de l'Information et Modélisation a ainsi vocation à intervenir sur les traitements appliqués à des images issus de différents capteurs : optiques, radar, lidar, etc. Ceci me permet également de m'investir sur les traitements dans des domaines d'applications plus larges, aussi bien utilisant des ondes radar que des ondes lumineuses et/ou infrarouges. Dans cet esprit, plusieurs pistes sont envisagées :

- La recherche et le développement de traitements d'images polarimétriques, pour des applications biomédicales en imagerie optique.
- La co-conception de systèmes d'imagerie, c'est à dire le développement de capteurs et traitements associés, pour répondre à une fonctionnalité précise.

Mes perspectives de recherche s'orientent suivant les deux axes définis précédemment.

### Traitements polarimétriques d'images optiques

Si la polarimétrie se développe sur les capteurs satellites radar dédiés à la télédétection, on assiste parallèlement à l'essor des systèmes polarimétriques optiques. Une application clé concerne notamment l'imagerie biomédicale. Ce type d'imagerie exploite les propriétés dépolarisantes des tissus biologiques.

Comme en radar, les différentes images acquises en polarimétrie de Mueller optique mettent en relief des éléments aux propriétés polarimétriques différentes. Cette pluralité d'images relatives à une même cible permet d'envisager deux pistes de recherche relatives aux traitements d'images :

#### □ **Représentation optimale d'une image polarimétrique**

Lorsque une image est acquise dans un mode polarimétrique, ce n'est pas une seule valeur d'intensité qui est fournie par pixel, mais seize valeurs différentes. On peut donc voir l'acquisition polarimétrique comme l'acquisition de seize images différentes du même objet. De manière générale, certaines de ces images vont offrir un contraste intéressant pour des zones bien ciblées, que d'autres images ne permettront pas de rendre, et vice-versa. Si l'on veut parvenir à ne représenter au final qu'une seule image dite "optimale", c'est à dire offrant une bonne qualité de contraste et permettant de visualiser des détails sur toutes les zones de l'image, se pose la question de la valeur d'intensité la plus pertinente à retenir. C'est une problématique qui n'est pas sans rappeler celle des algorithmes employés en imagerie HDRi (High Dynamic Range imaging). Dans ce mode d'imagerie, l'idée est de pouvoir représenter ou de mémoriser de nombreux niveaux d'intensités lumineuses dans l'image. Cette technique s'effectue en permettant d'attribuer plusieurs valeurs à un même pixel. En pratique, l'imagerie HDRi utilisée dans le domaine de la photographie enregistre plusieurs images de la même scène, correspondant à des temps d'exposition différents. Des algorithmes sont alors employés afin de profiter de toute la dynamique acquise de l'image en maximisant des contrastes locaux. Ce type d'algorithmes pourra alors être testé sur des images de Mueller optiques, acquises et déjà disponibles à l'Onera pour des applications médicales (détection de cancer, de mélanomes, etc.).

- **Détection polarimétrique de zones d'intérêt et/ou segmentation** L'application majeure de l'imagerie polarimétrique des tissus biologiques est la détection des zones cancéreuses ou la segmentation d'images pour assister le diagnostic médical ou une intervention chirurgicale. Ce type de traitement pourra donc être investigué sur des images acquises dans des polarisations qui maximisent le contraste entre ces zones à détecter et les zones saines. Cette démarche fera l'objet d'une collaboration avec le département optique de l'Onera qui possède un imageur optique de Mueller.

### Co-conception : traitements adaptés à la conception

La co-conception se réfère à l'élaboration de nouveaux systèmes d'acquisition pour lesquels le dispositif d'imagerie, de détection ou de mesure, est fortement associé aux traitements numériques. Le principe est d'utiliser un dispositif d'acquisition, autrement dit un instrument, qui favorise l'efficacité des traitements, quitte à dégrader la qualité du signal brut en sortie du détecteur. Ceci donne lieu au développement de nouveaux systèmes "non conventionnels" ou "hybrides", pour lesquels l'instrument et les traitements sont indissociables. J'envisage aujourd'hui de participer à

deux études pouvant se rattacher à la co-conception et mes connaissances dans les domaines de l'imagerie cohérente :

#### **Détection en imagerie radar : zones urbaines et superstructures**

Les résolutions des premiers capteurs satellites radar, de l'ordre de la vingtaine de mètres dans les années 80, étaient insuffisantes pour envisager certaines applications de la télédétection au milieu urbain. Aujourd'hui, la diversification des porteurs satellites et de leurs bandes de fréquence, l'amélioration constante des résolutions, et le développement des modes dits "avancés" (interférométrie, polarimétrie) les rendent à nouveau possible. Mais il n'en demeure pas moins que le milieu urbain possède une phénoménologie particulièrement complexe, qu'il est nécessaire d'investiguer afin d'adapter au mieux les traitements. Je poursuis ainsi mes travaux en imagerie SAR, en couplant traitement et analyse physique, pour plusieurs sous-thèmes :

- **Fusion Haute Résolution et Polarimétrie Basse Résolution**

Dans le cadre de la thèse de Flora Weissgerber, nous nous intéressons à l'apport d'un mode polarimétrique non plus isolé, mais associé à des données Haute Résolution, presque systématiquement disponibles sur une même zone à une date différente. Les applications s'orientent aujourd'hui plus précisément à la classification des zones urbaines et à la détection de changements dans de tels milieux.

- **Détection de Superstructures**

La détection de structures particulières telles que pylônes, câbles, et éoliennes, répond à des besoins opérationnels de renseignements et de navigation basse altitude. La compréhension fine du comportement électromagnétique de ces cibles, ainsi que de la synthèse d'images radar SAR, permet d'adapter au mieux les critères de détection. Cette compréhension permet également de déterminer les modes opératoires les plus favorables (résolutions, bandes de fréquence, mode polarimétrique, interférométrique) ainsi que la robustesse des traitements vis à vis de modifications du mode opératoire. Ce sujet fait notamment l'objet d'un contrat en cours.

#### **Navigation 3D, apport de la polarimétrie**

Le DTIM développe des outils de reconstruction de l'environnement 3D embarqué sur drone, par stéréovision par exemple. Dans ce contexte, il est intéressant d'envisager l'utilisation de la polarimétrie optique, lorsque la stéréovision a des performances moins bonnes, par exemple sur des surfaces transparentes ou au comportement très spéculaire.

#### **Tomographie**

Un projet d'imagerie 3D entre le DEMR et le DTIM concerne la détection d'explosifs ou d'armes par le biais d'une imagerie dite de tomographie utilisant les micro-ondes. Les technologies d'imagerie micro-ondes sont largement étudiées dans le domaine biomédical où elles s'appuient sur les propriétés diélectriques des tissus. Or, les propriétés diélectriques des tissus du corps humain sont généralement différentes de celles des produits type explosifs, ou armes. En conséquence, les techniques d'analyse de signaux micro-ondes peuvent être utilisées à des fins de détection des différents types de matériaux qui pourraient être cachés sur le corps humain. L'enjeu principal aujourd'hui est de pouvoir construire un tel système au meilleur coût, et en un temps d'acquisition "raisonnable" pour être déployé à grande échelle. Cet enjeu nécessite à la fois de maîtriser les différentes techniques de la reconstruction de l'image, ou simplement du type de signal recherché, ainsi que la phénoménologie associée.

## 9- Liste de Publications

### Articles de revue

- [A 1] O. Rabaste, D. Poullin, **E. Colin-Koeniguer**, A. Cheraly, J-F. Pétex, and P. Huykhang. Around-the-Corner Radar: Detection of a Human Being in Non Line of Sight. *IET Radar, Sonar and Navigation*, 2014. submitted on 2014, August, accepted in September, in press.
- [A 2] A. Mokadem, **E. Colin-Koeniguer**, and L. Thirion-Lefevre. A new light on SAR backscattering coefficient and interferometric coherence in layover areas. *IEEE Geoscience and Remote Sensing Letters*, 2014. accepted.
- [A 3] **E. Colin-Koeniguer** and N. Trouvé. Performance of buildings height estimation using High Resolution PolInSAR images. *IEEE Trans. Geosc. Remote Sensing*, 52(9):5870–5879, 2014.
- [A 4] N. Trouvé, **E. Colin-Koeniguer**, P. Fargette, and A. De Martino. Influence of geometrical configurations and polarization basis definitions on the analysis of bistatic polarimetric measurements. *IEEE Trans. Geosc. Remote Sensing*, 49(6):2238–2250, June 2011.
- [A 5] L. Thirion-Lefevre, **E. Colin-Koeniguer**, and C. Dahon. Bistatic scattering from forest components. Part 1: Coherent polarimetric modelling and analysis of simulated results. *Waves in Random and Complex media*, 20(1):36–61, February 2010.
- [A 6] **E. Colin-Koeniguer** and L. Thirion-Lefevre. Bistatic scattering from forest components. part 2: First validation of a bistatic polarimetric forest model at VHF-UHF band [225-475 MHz] using indoor measurements. *Waves in Random and Complex Media*, 20(1):62–85, February 2010.
- [A 7] J. Praks, **E. Colin-Koeniguer**, and M. Hallikainen. Alternatives to Target Entropy and Alpha angle in SAR Polarimetry. *IEEE Trans. Geosc. Remote Sensing*, 47(7):2262–2274, July 2009.
- [A 8] L. Thirion-Lefevre and **E. Colin-Koeniguer**. Investigating attenuation, scattering phase center, and total height using simulated interferometric SAR images of forested areas. *Geoscience and Remote Sensing, IEEE Transactions on*, 45(10):3172–3179, 2007.
- [A 9] L. Thirion, **E. Colin**, and C. Dahon. Capabilities of a forest coherent scattering model applied to radiometry, interferometry, and polarimetry at P- and L-band. *IEEE Trans. Geosc. Remote Sensing*, 44(4):849–862, April 2006.
- [A 10] **E. Colin**, C. Titin-Schnaider, and W. Tabbara. An interferometric coherence optimization method in radar polarimetry for high-resolution imagery. *IEEE Trans. Geosc. Remote Sensing*, 44(1), January 2006.
- [A 11] **E. Colin**, C. Titin-Schnaider, and W. Tabbara. Coherence optimization methods for scattering centers separation in polarimetric interferometry. *JEMWA*, 19(9):1237–1250, 2005.

- [A 12] **E. Colin**, M. Tria, C. Titin-Schnaider, W. Tabbara, and M. Benidir. SAR imaging using multidimensional continuous wavelet transform and applications to polarimetry and interferometry. *Int.J. of Imaging Systems*, 14(5):181–221, 2004.

#### Articles soumis en cours de relectures

- [S 1] E Everaere, **E. Colin-Koeniguer**, L. Thirion-Lefevre, J. Tran, C. Costel-Sorin, A. Demartino, and R. Ossikovski. An optical scale device to characterize the forest in bistatic radar polarimetry. *Selected Topics in Applied Earth Observations and Remote Sensing, IEEE Journal of.* submitted on 2014, September.

#### Articles de congrès en auteur principal - Avec Actes et Comité de Relecture

- [C1 1] **E. Colin-Koeniguer** and N. Trouvé. POLSARap: investigating the benefits of polarimetry for urban applications using X-band SAR images. In *POLINSAR*, 2013.
- [C1 2] **E. Colin-Koeniguer** and N. Trouvé. A review about alternatives to classical polarimetric SAR parameters. In *SONDRA workshop*, 2013.
- [C1 3] **E. Colin-Koeniguer**, N. Trouve, E. Everaere, and A. De Martino. Bistatic polarimetric decompositions applied to depolarizing targets. In *IGARSS*, 2012.
- [C1 4] **E. Colin-Koeniguer** and N. Trouvé. Coherence optimization for estimation of building heights on a segmented high resolution PolInSAR urban area. In *POLINSAR*, 2011.
- [C1 5] **E. Colin-Koeniguer**, N. Sar, L. Thirion-Lefevre, and A. Mokkadem. Preliminary studies on the detection of a NLOS target in a 2D urban canyon using PolInSAR data. In *POLINSAR*, 2011.
- [C1 6] **E. Colin-Koeniguer**, N. Trouvé, and J. Praks. A review about alternatives to classical polarimetric SAR parameters. In *Synthetic Aperture Radar (EUSAR), 2010 8th European Conference on*, pages 1–4. VDE, 2010.
- [C1 7] **E. Colin-Koeniguer** and N. Trouvé. Alternatives to classical polarimetric parameters: optics applied to SAR images. In *SONDRA workshop*, 2010.
- [C1 8] **E. Colin**. Polarimetric optical tools and decompositions applied to SAR images. In *IGARSS*, 2007.
- [C1 9] **E. Colin** and F. Garestier. Polarimetric interferometry applied to high resolution imagery and urban areas. In *IGARSS*, 2006.
- [C1 10] **E. Colin**, H. Cantalloube, and X. Dupuis. FOPEN and change detection using POLINSAR data at P-band. In *EUSAR*, 2006.
- [C1 11] **E. Colin**. A mathematical study about the coherence set in polarimetric interferometry. In *EUSAR*, 2006.
- [C1 12] **E. Colin**, C. Titin-Schnaider, and W. Tabbara. FOPEN with polarimetric interferometry: validations with experimental data at P-band. In *POLINSAR*, 2005.

- [C1 13] **E. Colin**, C. Titin-Schnaider, and W. Tabbara. Polarimetric interferometry and time-frequency analysis applied to an urban area at X-band. In *IGARSS*, 2005. presented by A. Reigber.
- [C1 14] **E. Colin**, L. Thirion, C. Titin-Schnaider, and W. Tabbara. Comparison between simulations and interferometric polarimetric SAR P-band data on a pine-trees forest. In *IGARSS*, 2004.
- [C1 15] **E. Colin**, H. Cantalloube, and W. Tabbara. Validations of IFPOL tools with two flash images of the nezer forest. In *EUSAR*, 2004.
- [C1 16] **E. Colin**, C. Titin-Schnaider, and W. Tabbara. Investigation on different interferometric coherence optimization methods. In *POLINSAR*, 2003.
- [C1 17] **E. Colin**, C. Titin-Schnaider, and W. Tabbara. A new parameter for IFPOL coherence optimization methods. In *IGARSS*, 2003.

#### Articles de congrès en co-auteur - Avec Actes et Comité de Relecture

- [C2 1] F. Weissgerber, **E. Colin-Koeniguer**, N. Trouvé, and J-M. Nicolas. Statistics for complex correlation coefficients applied to advanced SAR modes: Interferometry and Polarimetry. In *International Radar Conference*. SEE, 2014.
- [C2 2] L. Thirion-Lefevre, Guivarc'h R., and **E. Colin-Koeniguer**. Investigating low frequency in urban areas. In *Geoscience and Remote Sensing Symposium (IGARSS), 2014 IEEE International*. IEEE, 2014.
- [C2 3] E. Everaere, **E. Colin-Koeniguer**, L. Thirion Lefevre, and A. De Martino. Understanding and validation of the polarimetric scattering of a forest for bistatic P-band SAR measurements. In *Geoscience and Remote Sensing Symposium (IGARSS), 2014 IEEE International*. IEEE, 2014.
- [C2 4] F. Weissgerber, **E. Colin-Koeniguer**, and F. Janez. Urban change detection by comparing SAR images at different resolutions and polarimetric modes. In *10th European Conference on Synthetic Aperture Radar (EUSAR 2014)*, Berlin, Germany, June 2014.
- [C2 5] L. Thirion-Lefevre, R. Guivarc'h, **E. Colin-Koeniguer**, and A. Mokadem. Propagation mechanisms in urban canyons. distortions and entropy. In *10th European Conference on Synthetic Aperture Radar (EUSAR 2014)*, Berlin, Germany, June 2014.
- [C2 6] F. Janez and **E. Colin-Koeniguer**. Détection de changement sur des images SAR de résolutions et de mode polarimétrique différents. In *GRETSI, Groupe d'Etudes du Traitement du Signal et des Images*, 2013.
- [C2 7] N. Trouvé and **E. Colin-Koeniguer**. Hybrid PolInSAR: high resolution and polarimetry applied to urban. In *POLINSAR*. ESA, 2013.
- [C2 8] O. Rabaste, A. Lepoutre, and **E. Colin-Koeniguer**. Exploitation des multi-trajets en milieu urbain pour le pistage d'une cible en zone d'ombre par filtrage particulière. In *GRETSI, Groupe d'Etudes du Traitement du Signal et des Images*, 2013.

- [C2 9] A. Mokadem, L. Thirion-lefevre, and **E. Colin-Koeniguer**. Analysis of a NLOS canyon in an InSAR image of a urban area at Ka-band. In *POLINSAR*, Frascati, 2013. ESA.
- [C2 10] A. Mokadem, L. Thirion-Lefevre, **E. Colin-Koeniguer**, R. Guinvarc'h, and J.-F. Nouvel. Analysing urban areas in the frame of Non Line Of Sight target detection. electromagnetic modelling, validation and application to real data in Ka-band. In *Electromagnetics in Advanced Applications (ICEAA), 2013 International Conference on*, pages 543–546. IEEE, 2013.
- [C2 11] N. Trouvé, M. Sangnier, and **E. Colin-Koeniguer**. Statistics on high resolution urban polarimetric images: Application to segmentation and classification. In *Synthetic Aperture Radar, 2012. EUSAR. 9th European Conference on*, pages 26–29. VDE, 2012.
- [C2 12] A. Mokadem, L. Thirion-Lefevre, **E. Colin-Koeniguer**, and F. Tupin. Determination of mechanisms that can occur in NLOS urban canyon. In *Synthetic Aperture Radar, 2012. EUSAR. 9th European Conference on*, pages 99–102. VDE, 2012.
- [C2 13] E. Everaere, **E. Colin-Koeniguer**, L. Thirion Lefevre, and A. De Martino. Influence of bistatic angle and forest structure description on classical polarimetric parameters. In *Geoscience and Remote Sensing Symposium (IGARSS), 2012 IEEE International*, pages 6531–6534. IEEE, 2012.
- [C2 14] N. Trouve and **E. Colin-Koeniguer**. Shape Constraint Region Growing process and application to 3D Rendering of High Resolution Urban Images. In *POLINSAR*, 2011.
- [C2 15] P. Formont, N. Trouvé, J-P Ovarlez, F. Pascal, G. Vasile, and **E. Colin-Koeniguer**. PolSAR classification based on the SIRV model with a region growing initialization. In *POLINSAR*, 2011.
- [C2 16] N. Trouve and **E. Colin-Koeniguer**. SIRV based distance for polarimetric SAR images hierarchical segmentation. In *EUSAR*, 2010.
- [C2 17] J. Praks, M. Hallikainen, and **E. Colin-Koeniguer**. Polarimetric SAR image visualization and interpretation with covariance matrix invariants. In *Geoscience and Remote Sensing Symposium (IGARSS), 2010 IEEE International*, pages 2035–2038. IEEE, 2010.
- [C2 18] N. Trouve and **E. Colin-Koeniguer**. Polarimetric study of an anisotropic cloud of cylinders in a bistatic configuration. In *POLINSAR*, 2009.
- [C2 19] L. Thirion-Lefevre and **E. Colin-Koeniguer**. First polarimetric validation and results on the bistatic scattering by a set of cylinders using a forest scattering model. *Synthetic Aperture Radar (EUSAR), 2008 7th European Conference on*, pages 1–4, June 2008.
- [C2 20] H. Cantalloube, H. Oriot, and **E. Colin-Koeniguer**. Physic and experimental issues on high resolution SAR imaging of urban area. In *Geoscience and Remote Sensing*

*Symposium, 2008. IGARSS 2008. IEEE International*, volume 1, pages I-70–I-73. IEEE, 2008.

- [C2 21] H. Cantalloube and **E. Colin-Koeniguer**. Assessment of physical limitations of high resolution on targets at X-band from circular SAR experiments. In *Synthetic Aperture Radar (EUSAR), 2008 7th European Conference on*, pages 1–4. VDE, 2008.
- [C2 22] H. Cantalloube, **E. Colin-Koeniguer**, P. O. Frolind, and L. Ulander. Merging of the stereogrammetry and interferometry techniques as relative bandwidth grows. illustration with VHF carabas SAR images. In *Geoscience and Remote Sensing Symposium, 2007. IGARSS 2007. IEEE International*, pages 141–143. IEEE, 2007.
- [C2 23] H. Cantalloube, **E. Colin**, and H. Oriot. High resolution SAR imaging along circular trajectories. In *IGARSS, 2007*.
- [C2 24] H. Cantalloube and **E. Colin**. POLINSAR for FOPEN using flashlight mode images along circular trajectories. In *IGARSS, 2007*.
- [C2 25] L. Thirion, C. Titin-Schnaider, **E. Colin**, and C. Dahon. Modeling of the polarimetric bistatic scattering of a forested area at P-band. In *EUSAR, 2006*.
- [C2 26] L. Thirion and **E. Colin**. Relation between the attenuation coefficients and interferometric phase center heights behaviors from P-band to L-band. In *IGARSS, 2006*.
- [C2 27] F. Cellier and **E. Colin**. Building height estimation using fine analysis of altimetric mixtures in layover areas on polarimetric interferometric X-band SAR images. In *IGARSS, 2006*.
- [C2 28] L. Thirion and **E. Colin**. FOPEN and change detection using POLINSAR data at P-band. In *POLINSAR, 2005*.

#### Participation à des communications sans acte

- mars 2006 **Journées d'imagerie optique non-conventionnelle, GDR Ondes / ISIS**, *Analyse de cibles et problèmes inverses en imagerie polarimétrique radar*
- mars 2008 **Journées d'imagerie optique non-conventionnelle, GDR Ondes / ISIS**, *Comparaison des outils optique et radar en polarimétrie*
- novembre 2012 **Journée GDR ISIS Analyse de scènes urbaines en image et vision**, *Apport de la polarimétrie à l'imagerie SAR en environnement urbain*
- avril 2013 **Journée GdR-ISIS / CCT-TSI CNES Fusion des données en télédétection**, *Conférence invitée, Détection de changement et Fusion sur des images SAR de résolutions et de modes polarimétrique différents*

Deuxième partie

Synthèse Scientifique.

L'image polarimétrique radar : de sa formation à son inversion.

POLARIMETRIC RADAR IMAGES

ELISE COLIN KOENIGUER

Manuscrit présenté pour l'habilitation à diriger des Recherches  
26 Novembre 2014



Dedicated to the loving memory of Antonello de Martino.

1954–2014

San Francisco itself is art, above all literary art. Every block is a short story,  
every hill a novel. Every home a poem, every dweller within immortal.

— William Saroyan



## CONTENTS

---

<b>I</b>	<b>FROM RAW DATA TO THE IMAGE</b>	<b>5</b>
1	SAR IMAGE PROCESSING	7
1	The monostatic mode	7
1.1	A generalization of classical radar	9
1.2	The geometrical approach	10
1.3	The frequency domain	11
1.4	The mathematical approach	14
2	Different Algorithm Class	15
3	The circular trajectory case	16
4	Bistatic SAR images	20
2	MEASUREMENT DATA	23
1	General information on advanced modes	23
2	Definition of Polarization basis, Polarimetric matrices and conventions	24
2.1	The spatial coordinates system	24
2.2	The state of polarization of a wave	28
2.3	The polarimetric measurement of a target	28
3	Second moments in polarimetry	30
3.1	An alternative parameter to entropy	31
3.2	An alternative measurement device to understand the origin of depolarization	33
4	monostatic vs bistatic: consequences	35
4.1	Where can the reciprocity assumption fail in a monostatic configuration?	36
4.2	Can optical polarimetry be applied to radar polarimetry?	37
3	DESIGN OF A POLARIMETRIC RADAR: TECHNOLOGICAL CONSTRAINTS	39
1	High resolution or polarimetric mode?	39
1.1	The maximum PRF: avoid range ambiguities	39
1.2	The minimum PRF: avoiding azimuth ambiguities.	39
1.3	Polarimetric mode: reducing swath or loss of spatial resolution?	40
2	Calibration	42
3	Data transmission: Compression	47
<b>II</b>	<b>POLARIMETRIC IMAGE PROCESSING</b>	<b>51</b>
4	CO-REGISTRATION	53
1	Proposition of an innovative method for SAR images	53
2	Application to interferometry and change detection	55
5	STATISTICS MODELLING	57
1	Amplitude and intensity Statistics	57

1.1	State of the Art about classical distributions for Intensity and Amplitude	57
1.2	Speckle is not an electronic noise	57
1.3	Multilook and mechanism mixture	58
2	Polarimetric Statistics	59
3	Coherent Signal Statistics	60
6	APPLICATIONS TO SEGMENTATION, DETECTION	65
1	Segmentation	65
2	Detection: building, superstructures	66
3	Change detection	68
4	Spectrum Reconstruction	71
III	FROM 2D TO 3D	75
7	3D FROM PURE POLARIMETRIC INFORMATION	77
1	Reconstitution of a relief by a polarimetric imaging radar	77
2	Prospects for 3D navigation in optical polarimetry	78
8	3D FROM POLARIMETRIC INTERFEROMETRY	81
1	Different generalized coherence	81
2	N bright points without interaction	82
3	Optimization	83
4	Generalized Properties of the coherence shape for N bright point modeling	85
4.1	Two mechanisms	85
4.2	One mechanism, for at least three points, and statistics on amplitudes	86
4.3	for $N < 3$ points using one mechanism and general noise statistics	90
9	TOMOGRAPHY	93
IV	INVERSE PROBLEMS IN POLARIMETRIC IMAGES: FOREST AND URBAN	95
10	THE USE OF ELECTROMAGNETIC TOOLS FOR INVERSION	97
1	Different types of scattering models. How to choose one?	97
2	A way of investigating: cross understanding and validation	98
11	POLARIMETRY FOR FOREST IMAGES	101
1	PolInSAR forest inversion	101
2	Inversion of bistatic polarimetry in forests	102
12	URBAN IMAGES	107
1	Detection of built-up areas	108
2	3D reconstruction	115
3	Urban canyons	119
	BIBLIOGRAPHY	131

## List of Acronyms

RAR	Real Aperture Radar
SAR	Synthetic Aperture Radar
PolSAR	Polarimetric SAR
InSAR	Interferometric SAR
DInSAR	Differential Interferometric SAR
PolInSAR	Polarimetric Interferometric SAR
PolTomSAR	Polarimetric Tomographic SAR
RVoG	Random Volume over Ground
SSIM	Similarity Structural Invariant Measurement
PSF	Point Spread Function
RDA	Range Doppler Algorithm
PFA	Polar Format Algorithm
CSA	Chirp Scaling Algorithm
RMA	Range Migration Algorithm
FOPEN	Foliage Penetration
GAF	Generalized Ambiguity Function
RCS	Radar Cross Section
SIRV	Spherically Invariant Random Vectors
DEM	Digital Elevation Model
HR	High Resolution
SOMA	South of Market, a large neighborhood in San Francisco, California
ROC	Receiver Operating Characteristic
BaBi	An indoor coherent bistatic RCS measurement in Onera
PEC	Perfect Electric Conductor
POA	Polarization Orientation Angle
LOS	Line of Sight
NLOS	Non Line of Sight

SONDRA	Supélec Onera NUS DSO Research Alliance
LPICM	Laboratoire de Physique des Interfaces et Couches Minces, CNRS-Ecole Polytechnique
FOI	Swedish Research Defence Agency
SATIE	Laboratoire des Systèmes et Applications des Technologies de l'Information et de l'Energie
NTU	Nanyang Technological University, Singapore

## INTRODUCTION

---

Remote Sensing is the science of acquiring information about the Earth's surface without actually being in contact with it. This is done by sensing and recording reflected or emitted energy and processing, analyzing and applying that information. The microwave portion or radar portion of the spectrum covers the range from approximately one centimeter to one meter in wavelength. There are two primary advantages of radar: all-weather and day or night imaging. Moreover, radar images are quite different from images acquired in the visible and infrared portions of the spectrum and have special properties. Due to these differences, radar offers different perspectives of the Earth's surface.

One of the main differences from conventional images comes from the processing that enables the final image to be produced. Radar imaging deals with a coherent processing, which means that the image is produced from the transformation of a complex variable: the Electrical Field. This image processing explains the speckle and the particular statistical distributions encountered in radar images.

The difficulty of interpreting radar images is also their greatest asset: the fact that the phase of the wave is controlled offers new possibilities in terms of so-called advanced techniques such as polarimetry and interferometry. For a plane electromagnetic (EM) wave, polarization refers to the locus of the electric field vector in the plane perpendicular to the direction of propagation. Many radars are designed to transmit microwave radiation that is either horizontally polarized (H) or vertically polarized (V). A transmitted wave with a given polarization can generate a backscattered wave with a variety of polarizations. It is the analysis of these transmitted and received polarization combinations that constitutes the science of radar polarimetry.

Although polarimetry has a long history that reaches back to the 18th century, the earliest work related to radar dates back to the 1940s. G.W. Sinclair introduced the concept of the scattering matrix to describe the radar cross section of a coherent scatterer in 1945. In the late 1940s and the early 1950s major pioneering work was carried out by E.M. Kennaugh. Polarimetry continued after Kennaugh, but only a few notable contributions were made until Huynen's studies in 1970s. The beginning of a new age began with the doctoral thesis of Huynen in 1970 which renewed interest in radar polarimetry. However, the full potential of radar polarimetry was never fully realized until the early 1980s, due in no small part to the advanced radar device technology. Technological problems led to a series of negative conclusions in the 1960s and 1970s about the practical use of radar systems with polarimetric capability. Among the major contributions of the 1970s and 1980s are those of W-M Boerner who pointed out the importance of polarization in addressing vector electromagnetic inverse scattering.

Together with these theoretical advances, sensors were developed, both for civilian and military purposes. First, polarimetric sensors were airborne sensors. The first polarimetric image distributed by NASA was acquired by the AIRSAR system, a practical fully polarimetric airborne system implemented by JPL in 1985. The well-known corresponding polarimetric image of Fig.1 was taken over San Francisco.

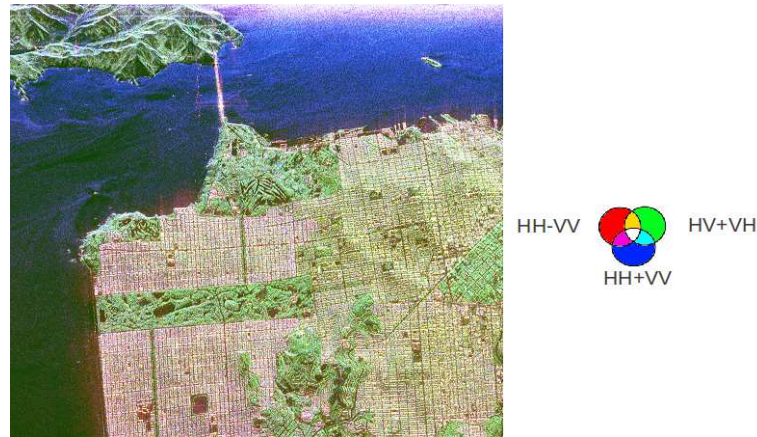


Figure 1: A well-known polarimetric image taken over San Francisco by the airborne system AIRSAR

Why did this image over San Francisco raise enthusiasm? Certainly because in this image we can distinguish different types of land covers that are very well discriminated by polarimetric false colors: ocean, built-up areas, and vegetation.

Then, NASA also launched the first fully polarimetric space-borne SAR in 1994 with the space shuttle SIR-C. This system was flown as a science experiment on the Space Shuttle Endeavor in April (SRL-1) and October 1994 (SRL-2). At the same time, many polarimetric airborne systems flourished in the early 1990s. The interferometric mode was also developing. Interferometry is another key technique of imaging radar, which can be used in differential mode, or for three-dimensional imaging. The POLINSAR mode, which combines polarimetry and interferometry was proposed in a 1997 paper [Cloude and Papathanassiou \(1997\)](#), and in [Cloude and Papathanassiou \(1998\)](#). The first Onera SAR images were acquired in this mode in 1999 on the Beaugency and Brétigny sites. At the beginning of my thesis, this new discipline grew, with the creation of the POLINSAR workshop by ESA, the European Space Agency, in January 2003.

Studies are ongoing, supported by an earlier in-depth knowledge gained from more defense-oriented issues. This knowledge has developed historically in Onera through anechoic chamber measurements, where polarimetry was used for target recognition on military vehicles. As the contribution of polarimetry to remote sensing applications was being demonstrated around the world, it became possible to use this technology for satellites. The first polari-

metric satellite SAR sensor was the ALOS PALSAR satellite, launched in 2006, followed by TerraSAR-X and RADARSAT-2 launched in 2007.

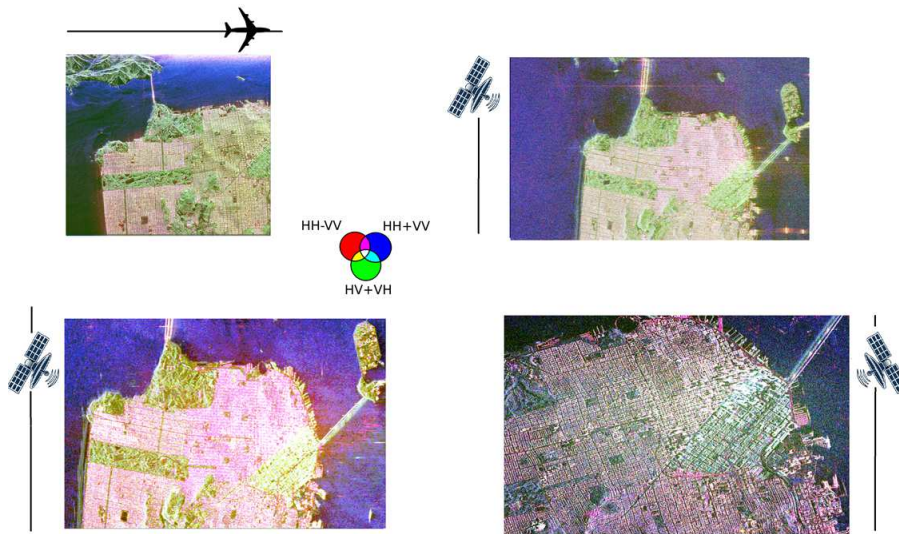


Figure 2: Different polarimetric images over San Francisco: AIRSAR (L-band), ALOS(L-band), RADARSAT-2(C-band), and TerraSAR-X (X-band)

These sensors each operate at different wavelengths, have different resolutions and different Signal-to-Noise ratio. For these reasons, the images in Fig. 2 differ greatly from one sensor to another. Indeed, in order to interpret them, we must take into account the specific sensor, since it soon becomes clear that the images obtained depend on the technological parameters. Thus, there is no optimal treatment for an image, but one treatment can only be considered as optimal according both to the environment considered and sensor dimensioning, such as wavelength, resolution and noise levels.

Due to the complexity of the environments considered and of the diversity of the sensors, in order to be able to propose the most appropriate treatment, it is also necessary to understand the underlying physical signals and the complex phenomenology involved between the wave and the environment. For this purpose, simulation is invaluable. Attempting to link together electromagnetic comprehension and information processing is at the heart of my research. This approach has been mainly applied both for applications concerning the forest and for applications in urban areas.

In order to present this approach in this paper, in the first part I discuss the intricate relationship between measurement and technological constraints. At this stage it is necessary to understand how the image is derived from the raw data acquired by the system, and also to know how measured quantities are defined exactly. This part of my research primarily involves the acquisition of knowledge on SAR imagery. I want to return to this point in a more general overview, especially to illustrate the diversity of possible approaches. I will illustrate how this knowledge was useful, especially for understanding the images acquired in new ways, circular SAR or bistatic SAR. This first part

was also an opportunity to file a patent for the calibration of polarimetric measurements, to suggest a more suitable spatial reference frame for data interpretation of bistatic polarimetric images, and, finally, to propose alternatives to conventional polarimetric parameters derived from statistical estimation.

Once SAR images are computed, we often have to process them, either to perform classification or detection. In order to do this, if several images are used, it is necessary to coregistrate them together. Then, according to the type of data, the statistical nature of the products provided may change. Our knowledge of statistics can be used to adjust the functions commonly encountered in imaging, such as detection and classification. The second chapter presents my contributions to coregistration, to statistical studies and their application to detection and classification functions.

The images thus processed are two-dimensional images. The scenes that contain terrain are projected onto the horizontal plane, unless dedicated techniques are used to restore their relief. Interferometry is one of these techniques, but polarimetry can also help to provide volumetric information. The third chapter will be devoted to the help of polarimetry for the transition from a two-dimensional image to a three-dimensional one.

Finally, the last chapter will cover the finer understanding and inversion methods of specific complex media, in close connection with the use of physical models, for two examples of environments: forest and urban areas.

To conclude, we will see how this general approach for developing processing, starting from the analysis of the raw measurements, improving our understanding of the physical interaction of the scene and the sensor, can be generalized to different imaging systems, both for co-design and processing of the data.

## Part I

### FROM RAW DATA TO THE IMAGE

SAR is an active imaging method based on microwaves that is used on mobile platforms such as airplanes or satellites. SAR is a form of radar that is used to create images of Earth's surface or of an object. The SAR algorithm enables an image of backscattering reflectivity to be obtained from the measurement of raw complex data. In this part, we first present studies that involve SAR image formation. Then we conduct a study about the way the different useful polarimetric parameters are obtained from this image. Finally, technological constraints concerning the polarimetric mode are discussed.



## SAR IMAGE PROCESSING: HOW CAN AN IMAGE BE DERIVED FROM A RAW SAR SIGNAL?

---

Synthetic-aperture radar (SAR) is a form of radar that is used to create images of an object, such as a landscape. In order to create a SAR image, successive radio wave pulses are transmitted to illuminate a target scene and the echo of each pulse is received and recorded. Signal processing of the recorded radar echoes, called raw data, enables the recordings from the multiple antenna locations to be combined to create the image.

The signal processing relating to this image formation is called the SAR algorithm. Different types of algorithms exist, and differ according to approximations that they make. However, in all cases, the SAR algorithm is able to transform the raw data into a reflectivity image, with physical resolutions that depend only on the mean frequency, the frequency bandwidth, the integration length which is the distance between the first pulse and the last pulse, and the geometrical configuration of acquisition.

In order to understand how we are able to achieve an image with these resolutions, several approaches are possible. While many books exist that detail SAR algorithms, there are very few that present different ways of understanding how, from an acquisition that returns a pulse of a certain frequency bandwidth, it is possible to obtain a reflectivity image with resolutions along two spatial axes.

Also, while an approach is generally sufficient to grasp the understanding of a SAR image under standard conditions (far-field, rectilinear path, monostatic configuration when sending and receiving antennas are co-located), it is quite different when this classic setting is left. During my years of research, innovative SAR imaging modalities have emerged: the bistatic SAR and the circular SAR.

Also, in first section we present all of the different approaches that enable the understanding of how a resolved image can be obtained from recording pulses along a trajectory. Then we will see which have been used to tackle more innovative modes, such as the circular mode or bistatic mode. These four approaches act in a complementary way to determine exactly how these new modes can affect the resulting image and have implications for the polarimetric mode.

### 1 THE MONOSTATIC MODE

For all approaches, we will use the same configuration and the same variables, described in Fig. 3. We will deal with the monostatic case, in which the radar receiver is at the same location as the transmitter.

A signal  $s_0(t)$  is transmitted from each antenna position  $u$ , with a bandwidth  $B$  and a central wavelength  $\lambda$ . The signals collected are written  $s(t, u)$  where  $t$  is called the short-time and  $u$  is a position of the antenna or long-time. The SAR image is synthesized from these acquisitions made during the path of the antenna, with a length  $L$ .  $L$  is also called the integration length.

The SAR image corresponds to a mapping of the ground reflectivity along two axes: the azimuth axis  $y$ , which corresponds to the axis of the trajectory, and the transverse axis  $x$ , or range axis.

SAR processing is the way in which we obtain this SAR image from the recording of the pulse echoes. At least four complementary approaches can explain how we are able to obtain a reflectivity image with resolutions according to two spatial axes  $x$  and  $y$  from the recorded pulses.

- An approach based on the generalization of classical radar, able to determine the range and the velocity of objects.
- A purely geometric approach dealing with iso-range lines and iso-Doppler lines. The density and orientation of the contours determine the image resolutions.
- A frequency approach, for which the signal is described in the two dimensional frequency domain, in terms of two variables  $k_x$  and  $k_y$  which are the dual variables of the space coordinates  $x$  and  $y$  of the image.
- A purely mathematical approach, which gives an analytical formulation of the problem of calculating a density reflectivity map  $f(x, y)$  from the received signal  $s(t, u)$  depending on time  $t$  and position  $u$  of the radar.

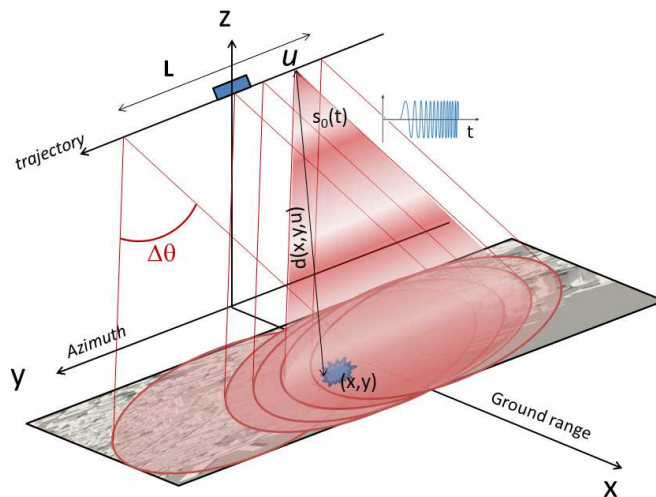


Figure 3: Geometrical parameters for a SAR acquisition

### 1.1 *A generalization of classical radar*

Classical radar is able to discriminate between separate echoes only if the difference between their delays is greater than the pulse width. Then the range resolution with a sinusoidal pulse is  $\delta_x = \frac{\tau c}{2}$  where  $\tau$  is the pulse duration and  $c$  is the celerity of the wave. Consequently, to increase the resolution, the pulse length must be reduced. Since SNR is proportional to the pulse duration, this introduces a trade-off between SNR and resolution. In order to still have a good SNR at the receiver, the pulse compression enables a large enough pulse: a signal is transmitted with frequency modulation, with a long enough length so that the energy budget is correct. This signal is designed in such a way that, after matched filtering, the width of the intercorrelated signals is smaller than the width obtained by the standard sinusoidal pulse. It is often a linear chirp, which is a signal whose instantaneous frequency increases linearly with time.

The range resolution attainable with a linear frequency modulation of a pulse on a bandwidth  $B$  is  $\delta_x = \frac{c}{2B}$ .

Thus, a range profile obtained by a classical radar can be considered as a one dimensional imaging process. In order to obtain a two-dimensional image, a first solution is to acquire several range profiles. This is what is done by Side-Looking Airborne Radar (SLAR) or Real Aperture Radar (RAR). In this case, the radar platform moves in the direction of the  $y$ -axis. The system uses an antenna that sends one pulse at a time and measures what is scattered back. The azimuthal resolution (better known as the cross-range resolution) depends on the beam width of the radar antenna. It is derived from the ratio of the physical size of the antenna (the real aperture) to the wavelength used. Due to the spreading of the beam it is also dependent on the slant range. However, they are limited by the physical size of the antenna: a uniform aperture antenna has a lobe with an aperture angle  $\phi = \frac{\lambda}{L}$  where  $L$  is the dimension of the antenna. One of the first RAR images acquired by an airborne system belonging to NASA is shown in Fig.4.

For satellite systems that are far away from Earth, the size of the footprint of one antenna measuring one meter in size would cover several kilometers. The azimuth resolution of an image improves as the aperture size increases. Unfortunately, increasing the aperture size (antenna length) may simply be impractical (antenna lengths of the order of kilometers). It is apparent that real aperture SLAR antennas could not be built large enough to achieve the desired azimuth resolution. In fact, it was never feasible to use SLAR in space because the antennas would be too large and their launch into space would be too expensive. In order to overcome this issue, Synthetic Aperture Radar refers to a method for improving the azimuth resolution. By using the entire set of recorded pulses for all antenna positions to synthesize the image, resolution depends on the integration length  $L$ . The distance that the SAR device travels over a target creates a large synthetic antenna aperture that plays the role of the size of the antenna. As a rule of thumb one can assume that the larger the aperture is, the higher the image resolution becomes, regardless of whether



Figure 4: A first Real Aperture Radar image acquired by a Side Looking Airborne System developed by Westinghouse, under sponsorship from the United States Air Force in 1954

physical aperture or synthetic aperture is used. This allows SAR to create high resolution images with comparatively small physical antennas.

### 1.2 The geometrical approach

In SAR imaging, the points of the scene to be imaged are separated according to two main physical parameters: their distance from the antenna and their Doppler frequency, due to the fact that the antenna velocity relative to the target changes. For an antenna position and its associated instantaneous velocity:

- The iso-range surfaces are spheres centered on the antenna. The intersections of these spheres with the horizontal ground are called iso-range lines. They are circles, as represented in Fig. 5. Far away from the radar, they can be approximated by segments.
- Physically, if the antenna emits a monochromatic wave, all points on the cone will be seen with the same Doppler frequency. If  $\mathbf{R}$  is a unit vector from the platform to the target, and  $\mathbf{v}$  is the platform velocity, the set of points  $\mathbf{R}$  for which  $\mathbf{R} \cdot \mathbf{v}$  is constant is a cone whose axis is the vector  $\mathbf{v}$ . This cone intersects the horizontal plane in a hyperbola. Such a constant Doppler curve is an iso-Doppler curve. Note that in the general case where  $\mathbf{v}$  is not necessarily horizontal, these intersections with a plane are quadrics: ellipses, parabolas or hyperbolas.

The intersection of a cone and a sphere is a circle. All points on the circle defined by the intersection of the *iso-range* sphere and *iso-Doppler* cone will be seen on the same pixel of the image. This means that if we consider only the points on the ground, there may be a possible ambiguity: the scene to the right

of the aircraft will be superimposed on the symmetrical scene on the left. In our configuration, it is not a problem because the antenna is quite directive and illuminates one side of the earth. The grid thus obtained on a flat surface is represented in Fig 5.

Away from the trajectory, the grid of resolution cells thus obtained can be regarded as rectangular. In this approach, we can summarize the SAR algorithm as follows: **The purpose of the SAR algorithm is to separate the contributions of the scatterers in the signal according to their distance and their Doppler relative to the antenna.**

### 1.3 The frequency domain

This approach considers the description of the signal in the two dimensional dual space plane from the one where we want to form our image plane. In each direction, the process may be viewed as a Fourier transform, as detailed in the following. The image-extraction process that we use can then be seen as another Fourier transform that is a reversal of the original natural one. In other words, acquiring an image involves recovering an amplitude or intensity function  $s(x, y)$ , according to two spatial dimensions  $x$  and  $y$ . Rather than physically acquiring this function directly, we try to obtain its Fourier transform, defined by  $S(k_x, k_y)$ . Once  $S(k_x, k_y)$  is obtained, then the inverse Fourier transform recovers the desired signal.

Physically, the support of the function  $S(k_x, k_y)$  is finite, which determines the resolution of its Fourier Transform  $I(x, y)$ . Thus, the study of the support shape of the registered signal immediately gives the resolutions that we can obtain. In practice, the radar system has limited frequency and angular support. This leads to incomplete filling of the signal support. The inverse Fourier transform of this finite support gives the point spread function (PSF) which describes the response of an imaging system to a point source. For a rectangular support, this PSF is the cardinal sine function. When the resolution increases, when the acquisition geometry changes, this support ceases to be the same and the study of this not perfectly rectangular shape allows the theoretical shape of the PSF to be found.

This approach can be illustrated for imaging in an anechoic chamber where the antenna is mounted on a circular railway. The antenna moves along an arc in the plane  $(x, y)$ , whose center is the center of the scene to be imaged. The position of the antenna is described by a two dimensional vector  $\mathbf{R}_0$  as shown in Fig.6. The position of each elementary target is given by a vector  $\mathbf{r}_i = (x_i, y_i)^t$ . For each antenna position, a wave with wave vector  $\mathbf{k}$  is emitted towards the scene center. Thus, the signal returned by the whole scene considered as a set of elementary targets with reflectivity  $\sigma(x_i, y_i)dx_i dy_i$  will be written as:

$$H(\mathbf{k}) = \int \exp(j2\mathbf{k}\mathbf{r})\sigma(x_i, y_i)dx_i dy_i = \int dx_i dy_i \sigma(x_i, y_i)\exp(j2\mathbf{k}\mathbf{r}_i) \exp(-j2\mathbf{k}\mathbf{R}_0). \quad (1)$$

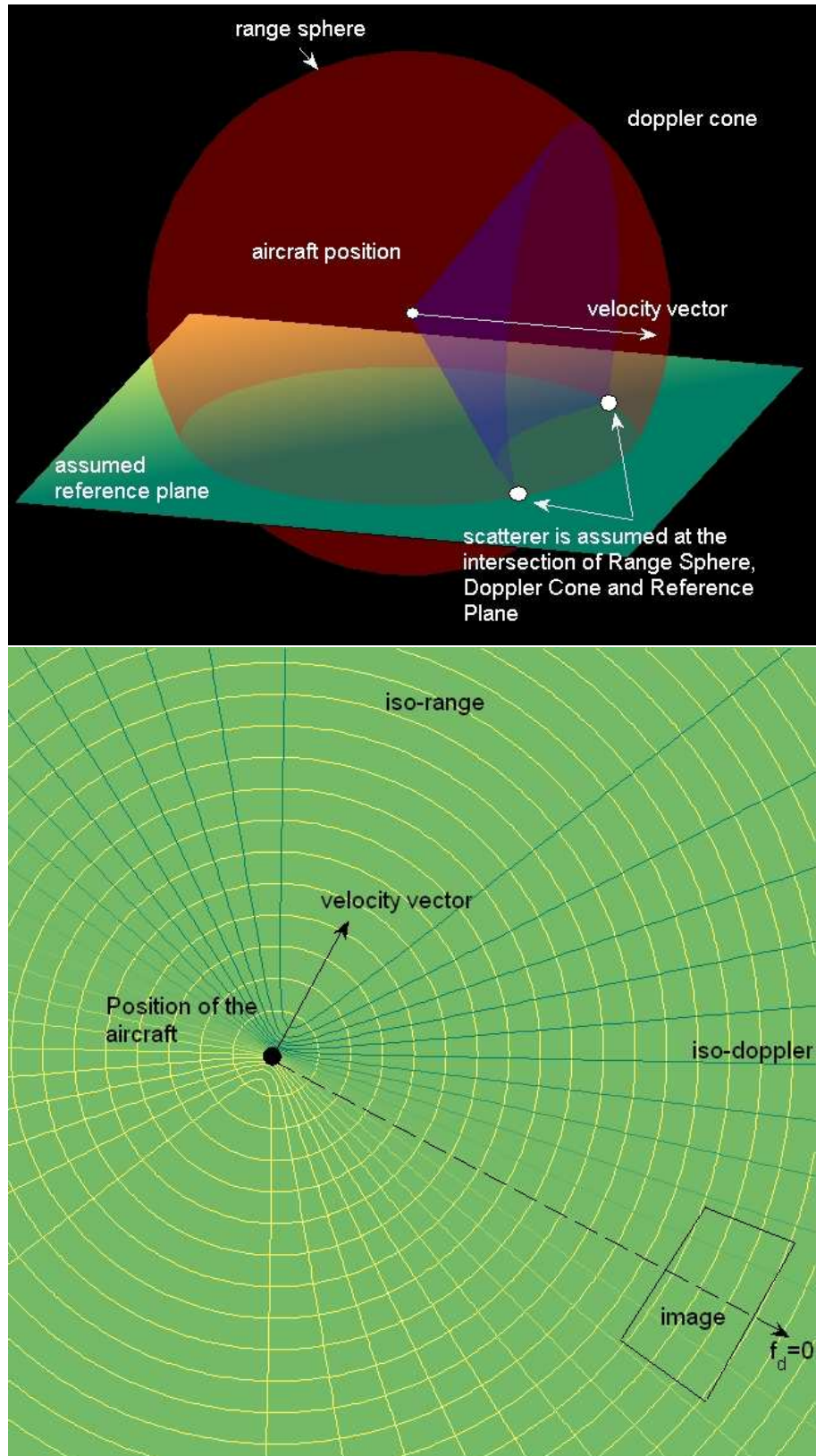


Figure 5: Resolution grid on the ground obtained by the intersection of the iso-range and iso-Doppler surfaces with a flat horizontal surface

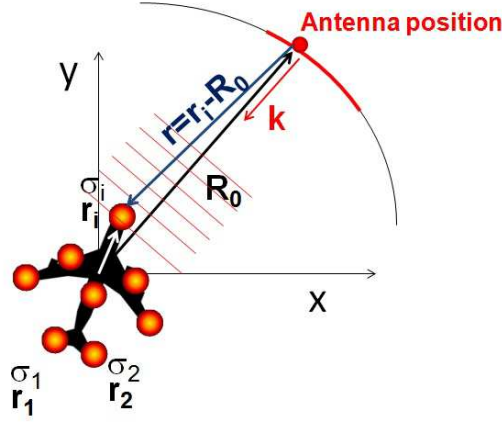


Figure 6: Geometrical parameter definition for illustrating the imaging of a target from an antenna mounted on a circular rail

The factor 2 comes from the consideration of the go-and-return path of the wave. Writing

$$\exp(j2\mathbf{k}\mathbf{R}_0)H(\mathbf{k}) = \int dx_i dy_i \sigma(x_i, y_i) \exp(j2(k_x x_i + k_y y_i)) \quad (2)$$

Let  $K_x = 2k_x = 2k \cos \theta$  and  $K_y = 2k_y = 2k \sin \theta$  one recognizes in the right term the two-dimensional inverse Fourier transform of the reflectivity function  $\sigma(x, y)$ :

$$\sigma(x, y) = \text{TF}_{k_x \rightarrow x, k_y \rightarrow y}^{-1}(\exp(j2\mathbf{k}\mathbf{R}_0)H(\mathbf{k})) \quad (3)$$

However, the signal is not regularly sampled along the  $(x, y)$  coordinates of  $\mathbf{K}_x$  and  $\mathbf{K}_y$ . Let us see how the signal is sampled. The angle of  $\mathbf{k}$  corresponds to angle positions of the antenna on the circular rail. This angle lies between two values and we will choose the axis directed towards the mean value as the  $x$  – axis. The modulus of  $\mathbf{k}$ ,  $k = 2\pi f/c$  is proportional to the frequency. Thus, this modulus is also constrained by the minimum and maximum frequencies. The excursion domain of  $\mathbf{K}_x$  and  $\mathbf{K}_y$  represented on a plane in Fig.7 is the intersection of a circular crown, whose thickness is related to the frequency bandwidth and whose angular sector is linked to the opening excursion angle of the antenna positions:

If this area is approximated by a rectangular area, then the resolution along the  $x$  and  $y$  axis can be deduced as follows:

$$\Delta K_x = 2\Delta k = 4\pi \frac{\Delta f}{c}, \Delta K_y = 2k_0 \Delta \theta \quad (4)$$

$$\delta_x = \frac{2\pi}{\Delta K_x} = \frac{c}{2\Delta f}, \delta_y = \frac{2\pi}{\Delta K_y} = \frac{c}{2f_0} \frac{1}{\Delta \theta} \quad (5)$$

where  $dx$  and  $dy$  are the excursions along  $x$  and  $y$ . This allows us to make the following important observations:

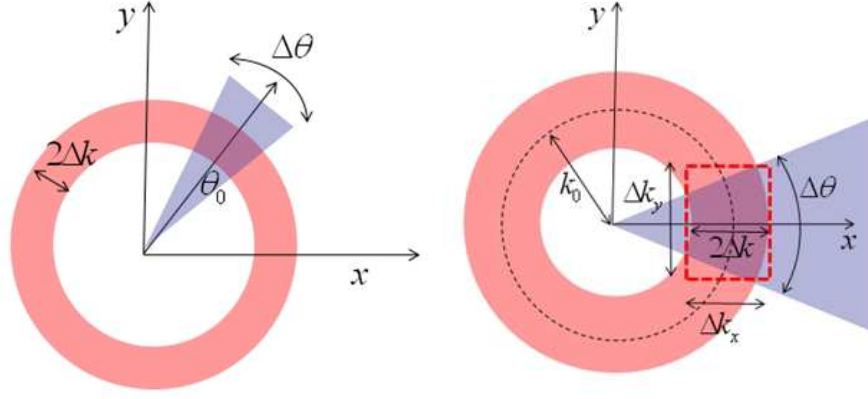


Figure 7: excursion representation of mathematical dual variables  $K_x$  and  $K_y$

- Along an axis of the image, the resolution is inversely proportional to the frequency bandwidth.
- Along the other axis, the resolution is inversely proportional to the angular extent on which the scene is viewed.

Similarly, the maximum image size that can be achieved will be related to the sampling performed in the Fourier plane. For SAR acquisitions, the path is no longer circular; expressions between the conjugate variables, and data acquisition radar such as look angles and frequencies are more complex. However, the reasoning remains the same: the resolutions in  $x$  and  $y$  are related to the dual variables and their excursions; the maximum dimensions of the image will be related to the sampling of these variables.

#### 1.4 The mathematical approach

The approach consists first in modeling the signal received by a radar according to the reflectivity of each pixel  $f(x, y)$  signal. Then from the received signal, the aim is to isolate the reflectivity  $f(x, y)$  which represents the desired image, by a series of treatments that may or may not involve approximations.

Generally, in a simplified two dimensional configuration, we can write the acquired signal  $s(t, u)$  as:

$$s(t, u) = \iint dx dy f(x, y) s_0(t - \frac{2}{c} d(x, y, u)) \quad (6)$$

where  $d(x, y, u)$  is the distance between an elementary target located at a position  $(x, y)$  and the antenna at a position  $u$ , and  $s_0(t)$  is the transmitted signal in each pulse.  $f(x, y)$  is the reflectivity of the elementary targets. The purpose of the SAR algorithm is to deduce the image reflectivity  $f(x, y)$  from the recorded signal  $s(t, u)$ .

For this, we generally assume the scatterers to be white and isotropic, which means that  $f(x, y)$  does not depend on the frequency or look angle used during acquisition. In addition, various algorithms exist according to a certain number of other approximations performed.

## 2 DIFFERENT ALGORITHM CLASS

The general mathematical problem has no simple solution. In practice, there are several algorithms to calculate  $f(x, y)$  from  $s(t, u)$ . These algorithms can be divided into several large classes that vary mainly depending on the domain in which what is called *focusing* or *aperture synthesis* is performed. Depending on the choices made and the mathematical solutions, the algorithms differ in:

- The way in which the topography is taken into account. Since SAR imagery is 2D imaging, the scene is projected onto a flat horizontal surface, unless we want to take a numerical elevation model into account.
- The ability to take into account a large bandwidth or wide swaths. Some algorithms can lead to hypotheses that are not compatible with increasing resolutions.
- The complexity of implementation, with the number of interpolations to be produced, for example.
- The speed of execution.
- The flexibility to compensate for the motion so that it is not perfectly rectilinear. This is particularly an important concern for airborne imaging systems where deviations from a nominal path cannot be neglected. More generally, algorithms differ in terms of the capability to image with non-linear trajectories such as circular path.
- The validity in near field conditions, for example in an anechoic chamber.

The following is a list of the major types of SAR algorithms:

- **Spatio temporal methods: temporal correlation, backprojection.** They are called temporal because the focusing step is performed in the time domain. Unlike other algorithms, spatio-temporal methods easily take into account the exact geometry between the antenna and the imaged scene. The SAR image can be synthesized directly in any reference frame. The so-called temporal correlation method is intuitive but very expensive. The backprojection method is identical to the previous mathematical formulation; it requires an interpolation that significantly improves the computation efficiency. The so-called fast backprojection method is an improved version that divides the synthetic aperture into several sub-apertures. The final image is obtained by coherently summing all sub-aperture images computed with a degraded azimuth resolution.

- **Polar format.** The RDA (Range Doppler Algorithm) algorithm, also called PFA (Polar Format Algorithm), is used on most satellite platforms. It makes use of the polar type of data in the frequency domain. An interpolation is required before the Fourier transform. The curvature of the wavefront is not totally compensated for. The CSA (Chirp Scaling Algorithm) avoids interpolation by making use of chirp structure in the azimuth processing.
- **RMA (Range Migration Algorithm) or  $(\Omega, K)$  algorithm.** Focusing is done in the two dimensional frequency domain. Motion compensation is done with respect to a line. The algorithm is not suitable for a circular path. It fully compensates the curvature of the wavefront, and is therefore suitable for wide bandwidths. I have used it for most new SAR configurations, especially for high resolution, and for simulation purposes. This algorithm is also the one chosen to propose the multidimensional continuous wavelet transform (CWT) in radar imaging, initially developed to highlight the image degradations due to the assumption of anisotropic and white behavior of scatterers. In (Colin, Tria, Titin-Schnaider, Tabbara, and Benidir, 2004b) and (Colin, C.Titin-Schnaider, and Tabbara, 2005a), the wavelet transform method has been extended to the polarimetry and interferometry fields, to improve the results of these techniques.

### 3 THE CIRCULAR TRAJECTORY CASE

As we have seen before, the best azimuthal resolution is achieved when the target is viewed under all aspect angles. This is one of the reasons why circular SAR has been investigated. We see at least three other interests in circular trajectories:

- we will see in Part 3 that it could enable 3D imaging.
- when the directionality of targets has been proven to be crucial for signal response, a circular trajectory ensures the achievement of the best configuration for detection.
- shadow effects can be avoided, as an overlay problem through the rotation of the slant range projecting direction. This has been emphasized in (Cantalloube, Oriot, and Colin-Koeniguer, 2008).

Hence, in 2004 Onera performed airborne circular SAR acquisitions jointly with FOI, the Swedish defense agency, during the LORAM campaign in Sweden. The airborne radar system RAMSES collected data over the Swedish forest to investigate the detection capabilities in the P-band and influences of different SAR parameters like resolution, central frequencies and look angle. In this context, circular trajectories have been used in order to analyze the presence of anisotropic scattering from the targets in the P-band. This campaign was to our knowledge the first one that made it possible to experiment with the processing of such images in the P and L bands, in full polarimetric mode.

These data have also been for me the opportunity to explore the potential of the PolInSAR circular mode to yield a higher detection rate.

In 2006, a new series of circular acquisitions was performed in the RAMSES calibration test area and two industrial and airport areas in France and Germany. The processing of these signals has been described in (Cantalloube, Colin, and Oriot, 2007). At X-band, the tridimensional aspect of the circular SAR imaging has been addressed on man-made targets (buildings, vehicles).

Thus, the airborne radar system RAMSES collected data over the Swedish forest to investigate the detection capabilities in the P-band and circular trajectories were used again in order to analyze the presence of anisotropic scattering from targets in the P-band. A general description of the operating mode of *flashlight SAR images* in the interferometric mode and the use of this for FOPEN purposes has been given in (Cantalloube and Colin, 2007).

Research on this circular mode in which I participated mainly in collaboration with Hubert Cantalloube at Onera, led to progress in all of the following aspects:

- **The choice of the SAR processors to be used in such configurations.** A serious difficulty with real circular data is motion compensation, which requires an accurate trajectory to be recovered, and for this, a point scatterer with an isotropic return to be observed. Focusing is very sensitive to motion compensation, thus it requires the use of the same techniques as in the case of very high resolution images. Moreover, some traditional SAR processors have to be rejected, because in the particular case of the circular trajectory and imaging within the circle, the geometry is stationary and singular at the circle center: the target has a same Doppler whatever the position of the plane. Finally, the wider relative bandwidth also disqualifies simplified range/Doppler types of algorithms. For these reasons, the flashlight mode has been proposed.
- **The limitation in the best achievable physical resolution.** Using this new imaging possibility, we have clearly demonstrated the strong anisotropic behavior of the main scatterers in the X-band. This proves both the limitations of the autofocus techniques based on the tracking of isotropic strong echoes for very high resolution images, and the impossibility of recovering a three-dimensional content by this method in the X-band. This has been the subject of several papers: Cantalloube, Oriot, and Colin-Koeniguer (2008), Cantalloube and Colin-Koeniguer (2008).
- **The useful directions for 3D reconstruction.**

When computing an image on a given horizontal plane, elevated targets with respect with this given plane are not well focused on, and the direction of the focusing error changes with the observer; consequently an elevated point is mapped onto a circle. The radius of this circle is equal to  $\Delta H/i$  where  $\Delta H$  is the elevation error and  $i$  is the incidence angle. This artifact could be used to deduce the elevation  $H$  of the target, from the detection of the arc segments, as shown in Fig. 8. Our studies have revealed

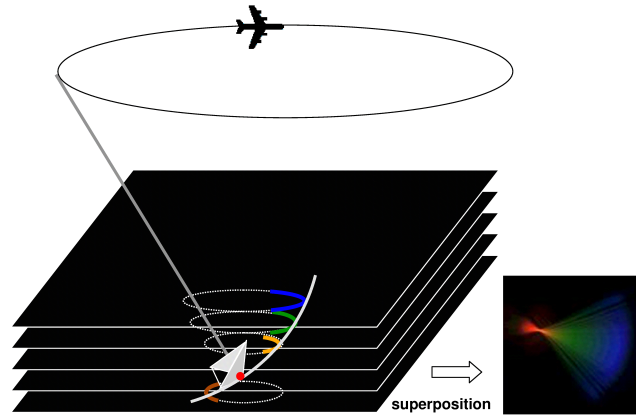


Figure 8: A trihedral corner illuminated by a circular flight: the different images obtained according by focusing on different elevation planes are surimposed on a single image on the right using different colors

that unfortunately, the strong anisotropy of artificial targets illustrated in Fig. 9 at X-band makes this type of reconstruction impossible for vehicles. I have also proposed a new technique for DEM reconstruction from polarimetric circular images, which is presented in Part 3.

- **The link between the polarimetric return and the look angle.** These acquisitions have been an opportunity to demonstrate the importance of the look angle in the polarimetric behavior of artificial targets. The most emblematic example is the canonical trihedral corner. Seen laterally by a radar antenna, it becomes a dihedral effect, as illustrated in Fig. 10. These targets correspond to different canonical polarimetric returns.
- **The benefit of this configuration for FOLIage PENetration (FOPEN) purposes.** A study has used the polarimetric content of the data in this unusual geometry to improve the detection rate of the targets hidden in the forest. During the campaign in Sweden, it was shown that using circular trajectories improves target detection. In this new campaign, detection appeared to be very difficult on classical SAR images because the forest was very dense. Since the targets were very sensitive to the orientation angle, the circular mode improved detection performances. Thus the full-polarimetric and interferometric information have been used in order to explore the potential of the POLINSAR circular mode to yield a higher detection rate. A polarimetric contrast enhancement algorithm has been tested successfully for all look images of the flight. Results have been presented in (Colin, Cantalloube, and Dupuis, 2006a).

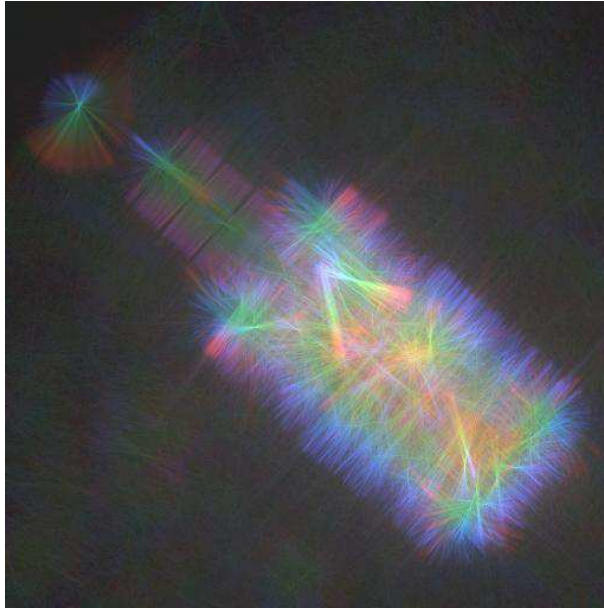


Figure 9: Representation of a military vehicle obtained by a circular trajectory: the different images obtained by focusing on different elevation planes are superimposed using different colors

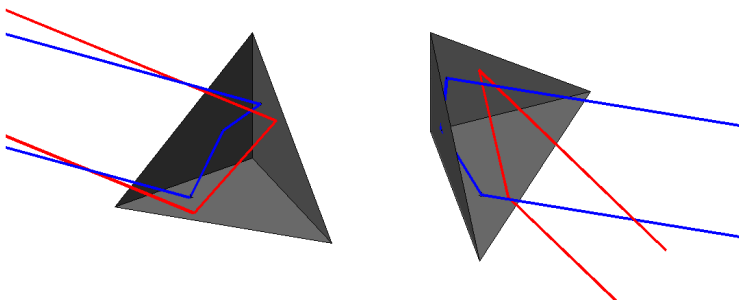


Figure 10: A trihedral corner viewed from a different look angle becomes a dihedral effect

#### 4 BISTATIC SAR IMAGES

Bistatic image processing, with separated emitter and receiver, also opens promising applications. I have investigated algorithms for forming SAR images in a bistatic settings through several studies:

- In a stationary mode, where two aircraft systems acquire an image along parallel paths. This mode has been the one used for Onera bistatic experiments, with DLR, the German national aeronautics and space research centre, and with FOI. I have implemented a SAR simulator in this simplified configuration, coupled with a forest scene simulator, in order to be able to simulate the effects of bistatic imaging forest images.
- In a passive mode, with a receiver on the ground listening to a transmitter of opportunity, satellite or airborne system. This latter method has been investigated especially in the context of GPS transmitters, to see to extent a listening ground radar is able to use the signals of opportunity to form SAR images. It is also an interesting configuration for stealth technology. Anechoic measurements have been used in this context, on four spherical targets to investigate achievable resolutions in space. These measures have been used to highlight the effects of SAR integration on polarimetric bistatic images. In particular, we pointed out the effect of the change of polarimetric bases and polarimetric signatures during integration. This will be detailed in the next chapter.

During this last study, we have shown that an important feature of the radar image is the resolution. In any bistatic configuration, the calculation of the resolution becomes a topic in its own right, which has been treated in different ways:

- Following the frequency approach, the description of the extension of the signal frequency definition. It is an approach that we have developed at Onera.
- By studying the Generalized Ambiguity Function (GAF) of the radar system, obtained by the signal processing approach. This ambiguity function corresponds to the result of the matched filter. The resolution calculation was obtained from the expression of this function. This approach was proposed by the team of Franck Daoult (University of Ville d'Avray, SATIE).

Both approaches were compared at Onera. In both cases, the theoretical formulas for range resolution and azimuth resolutions were established. The calculation of the ellipse resolution was then conducted. This allowed us to calculate the resolution for any direction, as well as for a set of preferred directions:

- The range axis is directed along the bisector of the bistatic angle, and is denoted by  $\beta$ . Along this axis, the distance resolution is equal to that of the monostatic case divided by the term  $(\cos \beta)/2$ . This term vanishes for

$\beta = \pi/2$ . This result has an important consequence: it shows in particular that imaging cannot be performed with a mean bistatic angle of  $\pi/2$

- The axis or Doppler azimuth corresponds to the direction of the derivative of the vector  $\beta$  over time.
- The axis orthogonal to the range axis or transverse axis.
- The minimum and maximum resolutions, respectively corresponding to the minor axis and major axis of the ellipse.

The characterization of this ellipse resolution was calculated. It provides important information on the features of the image that can be obtained. As an example, a bistatic image of four spheres obtained in an anechoic chamber shown in Fig. 13 highlights the elliptic shapes of the point spread function.



## MEASUREMENT DATA

---

Now that I have shown how a radar image is processed, I present the content of the physical information carried by the value associated with each pixel of the image. This content is first analyzed for a typical SAR image, then for polarimetric and interferometric images.

Moreover, in order to understand the link between a polarimetric radar image and polarimetric images in other areas such as optics, we review all types of conventions that fall within the definition of polarimetric data.

Still with the aim of understanding the specifics of radar polarimetry, discussions are conducted on the relationship between the geometry of the acquisition and the polarimetric measurement.

Finally, the influence of the statistical estimation techniques necessary to obtain polarimetric parameters called second order parameters is presented.

### 1 GENERAL INFORMATION ON ADVANCED MODES

A conventional SAR image is a complex image, provided in modulus and phase. Generally, the phase information alone is not made use of. The modulus meanwhile, is relevant information, which is representative of the energy backscattered to the antenna. In this context, a calibration can quantify this modulus to give physical content to its value. Two types of variables can thus be provided:

- Radar Cross Section RCS which summarizes the ability of a target to reflect radar energy and has units of  $m^2$ . The RCS of an object is the cross-sectional area of a perfectly reflecting sphere that would produce the same strength reflection as the object in question would. Quantitatively, RCS is calculated from a ratio of Electric field intensities.
- The backscattering coefficient  $\sigma_0$  or sigma naught, which is the average radar cross-section of a set of objects per unit area.

A polarimetric radar transmits with two orthogonal polarizations, often linear horizontal (H) and linear vertical (V), and receives the backscattered wave on the same two polarizations. This results in four received channels, i.e. HH, HV, VV and VH, where both the amplitude and relative phase are measured. The backscattering properties of the target in one pixel of the image can be completely described by a 2x2 complex scattering matrix  $\mathbf{S}$ . This matrix, called the Sinclair matrix in radars, is a coherent polarimetric representation relating the incident and scattered Jones vectors, describing the states of polarization of incident and scattered waves.

Interferometry processing is a method to analyze differences of phase information by combining two data observed from almost identical positions of a

satellite in orbit. This analysis method is devoted to either producing elevation data or measuring subsidence.

When the interferometric data are acquired in polarimetric mode, we have a PolInSAR mode which is currently an established remote sensing technique that allows the investigation of the 3D structure of natural volume scattering. When superimposing not only 2 but  $N$  images, we can make multibaseline interferometry or tomography. When multibaseline interferometric data are also polarimetric, we are speaking of PolTomSAR.

## 2 DEFINITION OF POLARIZATION BASIS, POLARIMETRIC MATRICES AND CONVENTIONS

Whether to set the polarization state of a wave, or to define the polarimetric behavior of a target, the choice of a base is dominant, and involves convention choice. Depending on the application field of polarimetry, optics or radar, we see that not only the measured quantities differ, but also the conventions used. Yet it is necessary to know these conventional choices precisely if we want to be able to transfer knowledge from one field to another. There are altogether three types of convention choices that it is necessary to bear in mind:

- The choice of a spatial reference, through the definition of three space vectors for each antenna of emission and reception antenna.
- The choice concerning the definition of the polarization state of a wave, usually through the definition of a vector, that can be either the complex 2-component Jones vector, or a real 4-component Stokes vector. Traditional bases use orthogonal linear polarizations, but circular polarizations are sometimes also useful.
- The choice concerning the polarimetric basis definition to define the polarimetric matrix representative of the target.

Since I have proposed new elements to better understand these different points, I will detail them hereafter.

### 2.1 *The spatial coordinates system*

The spatial coordinate system used to describe the polarimetric state of the incident and scattered wave is always perpendicular to the direction of the wave. However, in this perpendicular plane, the coordinate system is entirely arbitrary. This permits a degree of freedom, namely rotation about the propagation direction. This degree of freedom can be fixed by using a reference plane. Traditionally for remote sensing, we use the horizontal plane linked to the plane of Earth's surface, which is assumed to be locally plane. This leads to defining the horizontal axis as parallel to the surface of the Earth and the vertical axis as perpendicular to the latter and the wave vector. For the incident wave, the polarimetric vectors thus defined are denoted as  $\mathbf{h}_i$  and  $\mathbf{v}_i$ , while for

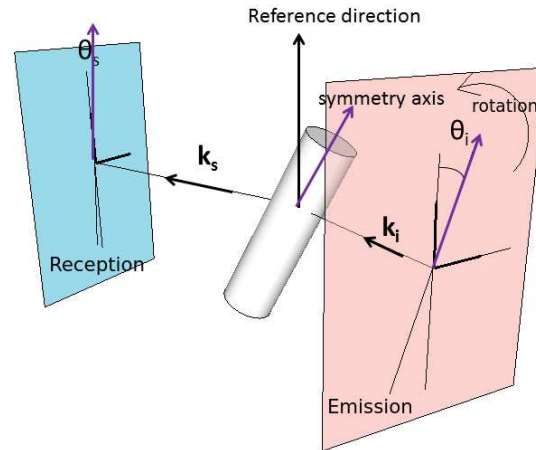


Figure 11: Orientation angles of a uniaxial object, in the incidence and scattered planes

the scattered wave they are denoted as  $\mathbf{h}_s$  and  $\mathbf{v}_s$ . They are represented in Fig.12.

In optics, the reference plane can also be the transmitter-receiver-target plane. We will now explain why we prefer the use of this convention in the case of a bistatic radar acquisition.

Even in monostatic configurations, the exact definition of the geometry of the system has a major impact on the polarimetric information, due to its heavy dependence on the polarimetric basis used in the definition and measurement of the signals. In the bistatic case, we have shown that the geometry is much more difficult to handle.

To illustrate this, we have taken the example of a cylinder viewed in a bistatic setting, to illustrate three different geometrical effects:

1. The target orientation around the lines of sight in emission and reception. It can be described by two orientation angles  $\theta_i$  and  $\theta_s$  in the incident and scattered wave plane, defined with respect to a reference direction, as shown in Fig.11.
2. Emitting and Receiving antenna polarimetric orientations (or linear polarimetric basis). These can be described by two rotation angles in the incident wave plane and the scattered wave plane.
3. Emitting and Receiving antenna relative positions, described by a single angle  $\beta$ , the bistatic angle.

In a monostatic setting, the antenna polarimetric basis and target orientation effects (Points 1 and 2) are usually considered together because a target rotation about the propagation axis is equivalent to an antenna rotation. The basis invariance of one target decomposition makes parameter roll invariant, i.e. the parameters are independent from the rotation of the target about the radar line of sight. It also means that the parameters can be computed regardless of the polarization basis. Thus, polarimetric basis issues are solved either by

roll-invariant parameters or appropriate rotations. In a bistatic setting, the first point and the second one are no longer equivalent:

- Physical target rotations around the line of sight (in the incident or scattered direction) are not only related to rotations in the scattering matrix. A change of the target orientation in the incident wave plane can change the mechanism viewed by the reception antenna, and not only the tilt angles.
- The term **disoriented target** means that the scattering matrix does not contain any more information about its tilt angles, as presented in (Huy-nen, 1970), and more recently in (Titin-Schnaider, 2010). When the tilt angles are estimated and removed or roll-invariant parameters are used, a rotation of the target in the incident wave plane or in the scattered wave plane (Point 1) can still affect the remaining parameters.

In order to perform a classical polarimetric study, eventually involving the usual tilt angle estimation, we have shown in (Trouvé, Colin-Koeniguer, Fargette, and De Martino, 2011) the importance of carefully defining our convention, which allows us to make a polarimetric analysis regardless of the orientation angles defined in Point 2. In this way the knowledge of the remaining tilt angles can improve the understanding of the remaining parameters.

If we want to focus on the influence of Emitting and Receiving Antenna relative positions (Point 3), using a single angle  $\beta$ , we have also shown that it is better to choose a convention linked to the scattering plane (emitter-target-receiver) to define the polarimetric bases, as illustrated in Fig. 12. This convention effectively removes the influence of Point 2 and reduces the analysis to a single variable: the bistatic angle. This point is detailed in (Trouvé and Colin-Koeniguer, 2009).

However, our recommendation is not the classical convention imposed by the classical radar measurement. For this reason, we have expressed, still in the same paper, the transition from the classical convention imposed by measurement, to the convention chosen here. We have proven that it is equivalent to two rotations.

We have also illustrated the importance of this choice for the polarimetric analysis performed, by bistatic measurement for isotropic targets, starting with a single metallic sphere, and gradually increasing the complexity by increasing the number of spheres, then finally considering a cloud of spheres.

As an example, in Fig. 13, two images of four spheres acquired in an anechoic chamber in a bistatic setting are represented using the different conventions: the classical convention in radar imaging on the left, and the one that we recommend for a bistatic analysis. In the image on the right, we see that the three spheres that are away from the center of the image appear in red, as is classically obtained for a canonical sphere in a monostatic setting, whereas the image on the left contains blue colors linked to cross-polarization, which are representative of the geometrical configuration of acquisition but not of the target itself.

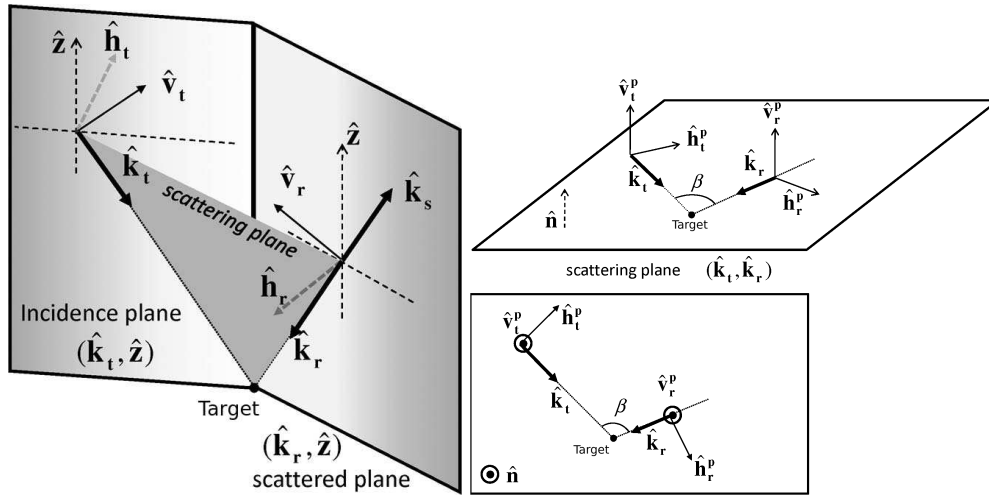


Figure 12: Convention of polarimetric spatial definitions based on the reference plane:  $\mathbf{h}_i^p$  and  $\mathbf{h}_s^p$  are in the scattering plane,  $\mathbf{v}_i^p$  and  $\mathbf{v}_s^p$  are orthogonal to this plane;  $\mathbf{v}_i$  and  $\mathbf{v}_s$  are in the incident and scattered planes,  $\mathbf{h}_i$  and  $\mathbf{h}_p$  are orthogonal to these planes.

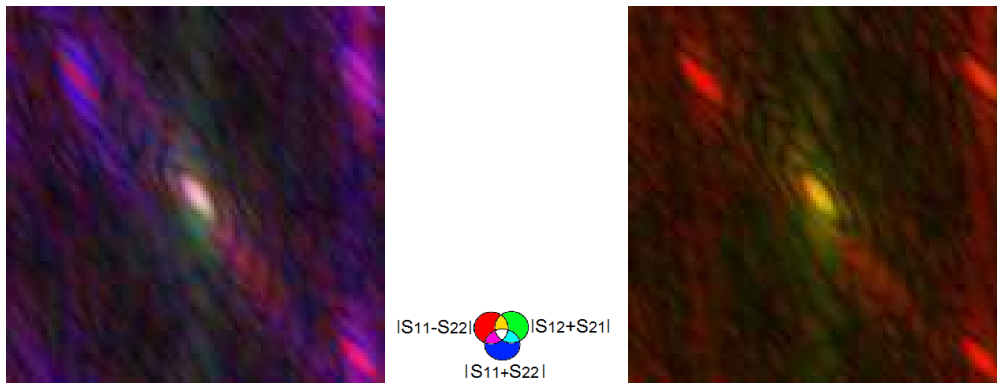


Figure 13: Bistatic polarimetric images of four spheres processed for two different spatial conventions: the radar classical convention on the left and those proposed in our studies on the right. The colors refer to combinations between the four elements of the Sinclair matrix  $S_{ij}$

Moreover, in order to completely describe the coordinate systems, once the orientation of the two polarimetric vectors have been chosen in the wave planes, we also have to choose the convention about the directions of the unit vectors relative to the sense of propagation. This leads to two different conventions: *Forward Scatter Alignment* FSA and *BackScatter Alignment* BSA.

In the FSA convention, the  $z$ -axis is defined by the direction of propagation of the wave. In the BSA convention, the  $z$ -axis is positive when pointing towards the target both before and after the wave is scattered. This BSA convention is less intuitive, but is generally chosen in SAR polarimetric images because in the particular case of backscattering (monostatic case), the coordinate systems are the same for the cases of the EM wave propagating from the antenna to the target and for the wave scattered from the target back towards the antenna.

These conventions are important to express the relationships among polarimetric radar variables and optics variables. These relationships are explained in the following.

### 2.2 The state of polarization of a wave

The definition of the state of polarization of a wave is done either by using the Jones vector, which is a complex two-dimensional vector, or by using the Stokes vector, which is a four-dimensional real vector. The radar is able to perform a coherent measurement of the signals, and then deals with the measurement of a Jones vector, whereas optical devices refer to the definition of a Stokes vector. In both cases, the polarimetric basis used to define the Stokes vector or Jones vector must be composed of two orthogonal polarization states.

### 2.3 The polarimetric measurement of a target

The polarimetric measurement behavior of a target can be described by a polarimetric  $2 \times 2$  scattering matrix that connects two complex Jones vectors. In optics, the scattering matrix is defined using the FSA convention and is called the Jones matrix, whereas in the radar field it is defined using the BSA convention and is called the Sinclair matrix. The Sinclair matrix  $\mathbf{S}$  and the Jones matrix  $\mathbf{J}$  are related by:

$$\mathbf{J} = \begin{pmatrix} 1 & 0 \\ 0 & -1 \end{pmatrix} \mathbf{S}^*. \quad (7)$$

The elements of the Sinclair matrix  $\mathbf{S}$ , often denoted as  $S_{HH}$ ,  $S_{HV}$ ,  $S_{VH}$  and  $S_{VV}$  can be arranged into a measurement vector by projection onto the Pauli matrix. This vector is called the scattering vector:

$$\mathbf{k} = \frac{1}{\sqrt{2}} [S_{HH} + S_{VV}, S_{HH} - S_{VV}, S_{HV} + S_{VH}, j(S_{HV} - S_{VH})]^T \quad (8)$$

The Sinclair matrix  $\mathbf{S}$  and Jones matrix  $\mathbf{J}$ , as well as the scattering vector  $\mathbf{k}$  are said to be *first order polarimetric parameters*. In a radar image, they are

contained in the information linked with a single pixel and do not require a statistical estimation.

In order to study the statistical behavior of polarimetric information in radar images, *second order polarimetric parameters* are considered. The coherence matrix is defined as an expected value of the product of the scattering vector  $\mathbf{k}$  with its complex conjugate  $\mathbf{k}^\dagger$ :

$$\mathbf{T} = \langle \mathbf{k}\mathbf{k}^\dagger \rangle \quad (9)$$

The  $\langle \dots \rangle$  operator denotes the statistical averaging and  $^\dagger$  denotes the complex conjugate transpose. In SAR polarimetry the averaging is usually done spatially. The coherence matrix is always Hermitian matrix, i.e. a matrix that is equal to its conjugate transpose. Hermitian matrix diagonal elements are real and it has real eigenvalues, denoted by  $\lambda_1$ ,  $\lambda_2$  and  $\lambda_3$ . The eigenvectors form a unitary basis. A current set of parameters derived from an eigenvalue decomposition of the coherence matrix are the Cloude-Pottier parameters. Among these, the polarimetric entropy is defined in terms of the logarithmic sum of eigenvalues:

$$H = \sum_{i=1}^3 p_i \log_3 p_i, \quad p_i = \lambda_i / \sum \lambda_i, \quad (10)$$

where the  $p_i$  are the corresponding probabilities recovered from the eigenvalues  $\lambda_i$ . Cloude and Pottier also introduced a parameterization of the eigenvectors of matrix  $\mathbf{T}$ .

Mueller and Kennaugh matrices are alternative second order polarimetric matrices. They both link the Stokes vectors of the emitted and received wave. The Mueller matrix is expressed using the FSA convention whereas the Kennaugh matrix is expressed using the BSA convention.

The link between the classical Mueller matrix and the Kennaugh matrix is:

$$\mathbf{M} = \begin{pmatrix} 1 & 0 & 0 & 0 \\ 0 & 1 & 0 & 0 \\ 0 & 0 & -1 & 0 \\ 0 & 0 & 0 & 1 \end{pmatrix} \mathbf{K}, \quad \mathbf{K} = \begin{pmatrix} 1 & 0 & 0 & 0 \\ 0 & 1 & 0 & 0 \\ 0 & 0 & -1 & 0 \\ 0 & 0 & 0 & 1 \end{pmatrix} \mathbf{M} \quad (11)$$

Mueller polarimetry consists in the measurement of the Mueller matrix. Mueller polarimetry can be integrated into almost any active imaging or spectroscopic system, and can thus provide polarimetric information at any spatial scale, by adding a Polarization State Generator (PSG) in the illumination part, and a Polarization State Analyzer, or PSA, in the detection part.

In summary, optical imaging polarimeters measure second order parameters directly, while the radar imaging systems measure the first order parameters and estimate those of second order, usually from a spatial average.

### 3 SECOND MOMENTS IN POLARIMETRY: THE ORIGIN OF THE *depolarization* PHENOMENON

An essential concept of polarimetry lies in what we call here depolarization. By this term, we understand the ability of a target to transform a wave that is totally polarized, and that can be described in a deterministic way, into a random or partially polarized wave.

A deterministic target has a zero depolarization factor, whereas a so-called ideal depolarizer will have a depolarization factor equal to 1. Radar entropy contains the same kind of information on the randomness of the target.

However, one single measurement of the Sinclair matrix does not allow the randomness of the polarization of the received wave to be assessed. However, if the measurement is repeated many times with the same target, the statistical analysis of the matrices thus measured can tell us about the deterministic or random nature of the wave scattered by the target.

Thus in radar, we could quantify this random or deterministic behavior by considering statistical moments of order 2 of the scattering vector through the coherency matrix  $\mathbf{T}$ .

If all Sinclair matrices measured are identical, then the corresponding coherence matrix  $\mathbf{T}$  is of rank 1, one of its eigenvalues is non-zero, and the polarimetric entropy or depolarization of this target is then zero. Conversely, if all eigenvalues are non-zero, then the corresponding target is non deterministic, and its entropy is strictly greater than zero.

Practically, the ergodic hypothesis states that the statistical estimation which should be made by using several samples of the measurement, can be made using the values of several adjacent pixels belonging to the same area.

The calculation of polarimetric parameters related to statistical properties through spatial estimation in radar suffers from many drawbacks:

- First, it involves spatial averaging, which is performed at the expense of resolution.
- Up to now, radar parameters have been investigated mainly in a monostatic configuration.
- Polarimetric entropy has a high computational cost. This can be a handicap for the use of this parameter, including its use for polarimetric visualization of large images, as developed in (Praks, Hallikainen, and Colin-Koeniguer, 2010).
- The physical interpretation of polarimetric entropy is not obvious.
- Finally, whether or not the statistical estimation is equivalent to that which would be made on several pixels remains to be seen. It is likely that the sampling consequences and spatial resolutions are involved in this estimate, in a manner that is not necessarily controlled. Indeed, a non-trivial problem is to determine the physical phenomena that originate the depolarization.

In order to meet these different points, two parallel approaches were undertaken:

- The first is the proposed new alternative to entropy. This approach is the subject of the publication (Praks, Colin-Koeniguer, and Hallikainen, 2009). It has also led to propose an alternative for another polarimetric parameter: alpha. This approach meets the first four points as follows:
  - The resolution degradation is avoided for the alternative parameter to alpha.
  - The associated computational costs are greatly reduced.
  - New physical interpretations inspired by optics have been proposed for these alternative parameters
  - The extension of these parameters to the bistatic case is better understood.
- The second is to use an optical measurement device, which does not require spatial estimation to make measurements of depolarization or entropy, and conduct studies at the optical scale. This has allowed us to understand the physical origin of the depolarization in the particular case of nanotube forests, related to the integration of a variety of angular responses introduced by multipath. This progress is the result of the PhD thesis by Etienne Everaere, co-supervised by Laetitia Thirion-Lefevre from SONDRRA and Antonello de Martino from the LPICM.

Both of our approaches are detailed below.

### 3.1 *An alternative parameter to entropy*

We describe here the first approach. It comes from the convergence of two completely different visions:

- Jaan Praks, from Aalto University in Finland, proposed alternative polarimetric parameters that can be calculated without eigendecomposition (Praks and Hallikainen, 2000b). He based the construction of these parameters on similarity invariants of Hermitian matrices, which are the determinant, the Frobenius norm and the trace (Praks and Hallikainen, 2000a).
- My own approach, presented first in (Colin, 2007), was to rise to the formulation of entropy, to understand the logarithmic form. As detailed below, by relaxing the additivity property that has little interest for radar, I came precisely to the same expression as that proposed by Jaan Praks. I also drew the link between this new parameter and those used in optics.

Following the conference paper (Colin, 2007), this alternative was studied in depth. The entropy parameter, either for thermodynamics, information theory

or polarimetry, is characterized by a certain number of mathematical properties, which originate from certain physical boundary conditions, each of these having a physical interpretation in the field of application:

- Continuity: entropy is a continuous measure. This means that a small change in the measurement produces a small change in entropy.
- Symmetry: the parameter value remains unchanged if the outcomes  $x_i$  are re-ordered.
- Maximum: if all outcomes are equiprobable, then entropy should be maximal.
- Additivity: the amount of entropy should be the same, even if the process is divided into parts.

Any definition of a parameter  $A$  satisfying these four assumptions has the form:  $A \propto \sum_{i=1}^n p_i \log p_i$ , where  $p_i$  is the probability of the output  $i$ . The necessity of the logarithm form is explained by the additivity property. Additivity property means that the entropy of a system composed by independent sub-systems is the sum of the entropies of its sub-systems. If sub-systems are not independent, the entropy of a system can still be calculated from the entropy of its sub-systems provided that we know how the sub-systems interact with each other. In the context of radar polarimetry, a sub-system would correspond to a partially polarimetric system. This property has a limited physical importance, since polarimetry operates in a space with less than three or four dimensions and moreover dividing the measurement of a fully polarimetric radar into several partially polarimetric radars does not decrease the total number of measurements nor the computation complexity, since it is the Sinclair matrix that is measured before computing the coherence matrix.

The parameter is called scattering diversity. It is similar to classical entropy but it does not have the additivity property. However, all of the other properties are verified. In order to achieve the same extreme points as for entropy, we have defined the following parameter in the monostatic case:

$$\hat{H} = \frac{3}{2} \left( 1 - \|\mathbf{N}\|_F^2 \right) \quad (12)$$

where  $\|\cdot\|_F$  is the Frobenius norm and  $\mathbf{N}$  is the coherence matrix normalized by the SPAN. In order to extend our scattering diversity parameter to the bistatic case, achieving 0 and 1 as extreme points, we define:

$$\hat{H}_{\text{bistatic}} = \frac{4}{3} (1 - \|\mathbf{N}\|_F^2) = \frac{8}{9} \hat{H}_{\text{monostatic}} \quad (13)$$

We have linked this parameter with at least two parameters that are used in optical polarimetry and have a physical interpretation. The first is called **degree of purity** (Gil, 2000) or **depolarization index** (Chipman, 2005). It is defined as the Euclidian distance of the normalized Mueller matrix  $\mathbf{M}/M_{00}$  to the ideal depolarizer of the non-reciprocal case:

Optical polarimetry uses another parameter called the depolarization of the matrix:

$$\text{dep}(\mathbf{M}) = 1 - \frac{\sqrt{\sum_{i,j} M_{ij}^2 - M_{00}^2}}{\sqrt{3}M_{00}} \quad (14)$$

This parameter indicates how far the matrix is from a set of Mueller matrices of non-depolarizing targets. It is connected to the average depolarization of the outgoing light. It is related to  $\hat{H}_{\text{bistatic}}$  by:

$$\text{dep}(\mathbf{M}) = 1 - \sqrt{1 - \hat{H}_{\text{bistatic}}} \quad (15)$$

To conclude with this, the scattering diversity that we propose as an alternative parameter to entropy is strongly related with the physical interpretation of average depolarization of the outgoing wave, and can be viewed as a distance of the target to an ideal depolarizer. Note that the ideal depolarizer has different Kennaugh matrices in the monostatic reciprocal case and in the bistatic case.

The proposed scattering diversity is also directly connected to the depolarization coefficient in optical polarimetry. Thus it quantifies the ability of the target to transform a perfectly polarized wave into a partially polarized one.

Finally during this study, we have also shown that the alpha angle can be replaced by the first element of the  $\mathbf{N}$  matrix, called the **surface scattering fraction**.

Both proposed parameters have been proven to be suitable for image interpretation, classification and visualization in the same way as classical ones. For example, they are shown in a colored representation in Fig. 14 and compared to the classical ones, using the polarimetric AIRSAR image. In this figure, we see that the colored representations are very similar. However, the parameters used for the second one are easier to interpret and to calculate since they do not require calculation of eigenvalues or eigenvectors of the coherence matrix.

### 3.2 An alternative measurement device to understand the origin of depolarization

The physical origin of the depolarization is still poorly controlled in radar images. In all cases, entropy or depolarization comes from a coherent integration, which means a summation over intensities. This can be either:

- a temporal summation,
- a spatial summation,
- an angular summation,
- a frequency summation.

The classical estimation of entropy in radar images involves a spatial average. Indeed, the signal contained in a pixel is the coherent sum of contributions



Figure 14: Polarimetric colored representation using first classical parameters Entropy and alpha, and then new proposed parameters scattering diversity and surface scattering fraction.

from all scatterers. However, it is difficult to predict the result of the interaction of all of these polarimetric phasors. Furthermore, it is unlikely that adjacent pixels contain exactly the same spatial distributions. The coherent sum of the contributions will be different, which can lead to the depolarization phenomenon that we will call spatial depolarization.

The frequency or angular summation is sometimes used to estimate coherence matrices from a radar indoor measurement. Usually, it is assumed that the target will have the same polarimetric behavior under different look angles. However, when an angular integration is done on a too large excursion, this assumption may not be true. Some targets such as dihedral corners have returns that are strongly dependent on the angle of orientation. Similarly, a variation of the frequency behavior can result in a depolarization effect.

The temporal integration, inherent to an optical device, can induce depolarization effects. A temporal incoherent average can also be applied in radar images by using successive acquisitions. In this case, the depolarization could be linked to the notion of temporal correlation. Indeed, it reflects movement or change in the polarimetric behavior of the scene during the integration period.

#### 4 MONOSTATIC CASE AND BISTATIC CASE: CONSEQUENCES IN POLARIMETRY

SAR images have so far been acquired in the monostatic mode. In 2004, ONERA and the DLR conducted a first bistatic airborne campaign, dedicated to the feasibility of this imaging mode, at X-band. It was soon followed by other campaigns organized with FOI in Sweden, at lower frequencies, for the application of target detection under vegetative cover. These bistatic images of forest areas were not acquired in a polarimetric mode, because the technological constraints are numerous. However, we may thus wonder how a bistatic acquisition will affect the polarimetric analysis.

Until then, classical radar polarimetric theory made use from the beginning of the reciprocity property, which fails in a bistatic configuration. The first line of research to develop bistatic radar polarimetry has considered the theoretical development established so far in radar, and tried to extend it without using the simplifying assumption of symmetry. This approach was conducted in the same manner as for radar theory, first distinguishing deterministic targets and the Huynen theory and then addressing natural targets. This is the method that was first proposed in the dissertation of Anne Laure Germond ([Germond, 1999](#)), and later by Cécile Titin-Schnaider at Onera ([Titin-Schnaider, 2008](#)), ([Titin-Schnaider, 2010](#)).

I have proposed an alternative line of investigation to develop the bistatic polarimetry theory. It is to be guided by theories developed for optical polarimetry. First, a study was conducted on the physical origin of the reciprocity assumption, and any monostatic case that may be impaired. Then the available optics tools for analyzing a possible polarimetric bistatic acquisition were investigated. My approach was to see whether the arguments made so far on the optical scale have meaning on the radar scale, and therefore cross both

fields. This work was part of a more general approach that could be called *optical and radar convergence*. It was the subject of the PhD thesis of Nicolas Trouvé whose main results and perspectives have been presented in (Colin-Koeniguer, Trouvé, Everaere, and DeMartino, 2012). It is partly resumed in the dissertation of Etienne Everaere, and is developed in the last part of this book.

#### 4.1 Where can the reciprocity assumption fail in a monostatic configuration?

The reciprocity assumption is a consequence of the Lorentz reciprocity theorem, which applies for targets composed of a linear isotropic, homogeneous material, and of finite dimensions. In this context, the theorem proves from Maxwell's equations, that we can exchange the roles of emission and reception antennas (Tsang and Li, 1985). Thus, it is trivial to show by applying the superposition theorem that the property extends to the superposition of several *Linear Homogeneous Isotropic* (LHI) targets without interactions between these. Let us view the first LHI hypothesis in more detail.

A material can be described by the most general relation  $\mathbf{D} = f(\mathbf{E})$  where  $\mathbf{D}$  is the electric displacement field and  $\mathbf{E}$  is the electric field. When the material is linear, then this relation is linear too and the multiplicative coefficient linking  $\mathbf{E}$  and  $\mathbf{D}$  is a matrix called permittivity, and denoted by  $\epsilon$ :

$$\mathbf{D} = \epsilon(\mathbf{r}, \omega)\mathbf{E}. \quad (16)$$

The imaginary component of this permittivity is related to absorption loss, the rate at which energy is absorbed by the medium during the propagation, whereas the real component is linked to the phase velocity of the wave. The matrix contains the three dimensions of space. According to the different particular case of this tensor, we can then distinguish various material properties.

A medium is referred to as homogeneous when the permittivity does not depend on the spatial coordinates in the material. This concept defines the scale of the wavelength used. Thus, a medium may be regarded as quasi-static homogeneous in regimes where the correlation inhomogeneity length is much smaller than the wavelength of the incident electric field. The case of a target where a discontinuity occurs in the structure at the wavelength scale will therefore be more complex. It is thus necessary to generalize the reciprocity principle, to consider an equivalent effective dielectric permittivity, and consider its properties. Finally, a material will be isotropic if its permittivity does not depend on space coordinates and therefore is scalar.

Many media are not isotropic. However, there are some extensions of the Lorentz reciprocity theorem in the literature. For example, it has been shown that the principle is valid in the following cases:

- The target is anisotropic, but its permittivity matrix is symmetrical complex. This is the case encountered in most radar cases.
- The target consists of two contiguous LHI materials.

- The target is bianisotropic: it is constituted by a stack of horizontal layers of different permittivities (Tai, 1992).

On the contrary, it is possible to produce a number of cases where this property is no longer guaranteed, even in monostatic conditions:

- for the magneto optical media. The most common example is the radio waves passing through the Earth's ionosphere, which are likewise subject to the Faraday effect. The permittivity tensor is then Hermitian, but not symmetrical. Such materials are also known as gyromagnetic. The case of ferromagnetic materials is included.
- for nonlinear media, that is, media in which the dielectric polarization responds nonlinearly to the electric field of the light. This nonlinearity is typically only observed at very high light intensities when the electric field values are comparable to those of interatomic electric fields, such as those provided by lasers.
- for the active media whose permittivity varies over time, for example when permittivity is modulated in time by some external process.

#### 4.2 *Can optical polarimetry be applied to radar polarimetry?*

Whatever the field of application, polarimetry refers to the measurement and interpretation of the polarization of transverse waves, most notably electromagnetic waves, that have traveled through or have been reflected, refracted, or diffracted by some material in order to characterize that object. The main difficulty encountered to provide an exchange between the optical polarimetry and radar polarimetry communities lies mainly in the vocabulary and convention differences. Practically, optical polarimetry and radar will differ by measurement types, and by the types of decompositions traditionally used for the notion of canonical targets, i.e whose behavior is representative of a given mechanism.

Originally for polarimetric radar, data were acquired in an anechoic chamber, by the way, as for optics, through obtaining Stokes matrices. The targets under study were deterministic targets. Also, the new capabilities offered by the coherent acquisition of a Sinclair matrix were a huge progress in reducing the number of measured observables. In the case of natural targets, theoretical developments have been proposed to estimate coherence matrices from several samples. At the optical scale with Mueller imaging systems, Mueller matrices are also measured. It is therefore possible to establish a bijective relationship between the optical measurements of Mueller matrices and the radar measurements of coherence matrices.

Once I highlighted when and how it is possible to draw the link between radar polarimetric acquisitions and optics polarimetric acquisitions, I also investigated the types of decompositions that are used in each field, in (Colin-Koeniguer, Trouvé, and Praks, 2010), and (Colin-Koeniguer and Trouvé, 2013).

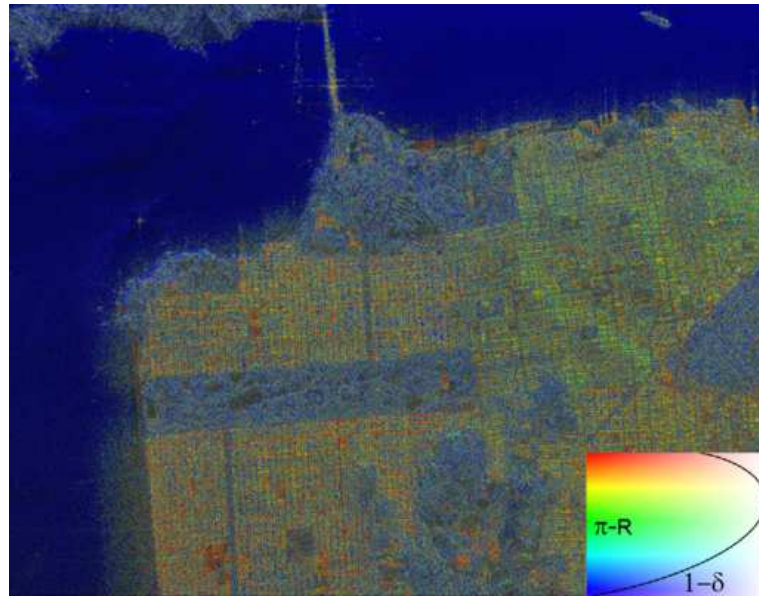


Figure 15: Colored representation of alternative optical parameters depolarization and retardance applied to the AIRSAR image

Traditionally, radar decompositions are additive decompositions, whereas optical decompositions are multiplicative. During my research, I was able to show that it was possible to use multiplicative polarimetric decompositions to SAR data. This work is largely in line with that proposed in (Souyris and Tison, 2007) on deterministic targets and their polar decomposition. This use of multiplicative optical decompositions is promising, especially for environments such as the forest, where a multiplicative description is particularly appropriate for stratified layers.

As an example, a colored representation of the AIRSAR image of San Francisco is proposed in Fig. 15, using the classical parameters of the Lu and Chipman decomposition, retardance and depolarization. Retardance is the difference in phase shift between two characteristic polarizations of light. It has been proven to be strongly related to  $\alpha$ . The resulting image offers a good contrast between the different areas of the image: water and building areas, as for a classical radar colored representation.

## DESIGN OF A POLARIMETRIC RADAR: TECHNOLOGICAL CONSTRAINTS

---

### 1 HIGH RESOLUTION OR POLARIMETRIC MODE?

To date, most polarimetric SAR have predominantly been implemented as experimental add-on modes to existing designs for single-pol or dual-pol systems. As a result, current and planned spaceborne SAR have full-polarimetric modes that are severely limited in swath width, are restricted in the range of look angles, suffer from low SNR and ambiguity problems, and are difficult to calibrate (Freeman, 2009). The consequence of this is that the high potential science return expected from polarimetric SAR data has not been realized.

In order to overcome this limitation, it is important to understand what the constraints that limit the polarimetric mode are.

If we want to alternate the emission of different polarizations, it will of course affect the pulse repetition frequency. The PRF is constrained by both the range ambiguities, and the azimuth ambiguities (McCandless and Jackson, 2004). The first condition imposes a maximum PRF to ensure a sufficient swath. The second imposes a minimum PRF to ensure an antenna small enough, and thus, consequently, a satisfactory azimuthal resolution. Let us express now these two kinds of requirement.

#### 1.1 *The maximum PRF: avoid range ambiguities*

In order to avoid range ambiguity, the pulse repetition frequency must be smaller than the time it takes to collect returns from the entire illuminated swath. This condition can be written as:

$$\text{PRF} < \frac{c}{2W'_x} \quad (17)$$

where  $W'_x$  is the maximum swath along the range axis, as shown in Fig.16 .

#### 1.2 *The minimum PRF: avoiding azimuth ambiguities.*

In order to understand why a sufficiently rapid pulse rate is necessary, we must remember that targets along the azimuth axis are separated according their Doppler frequency, that is the apparent change in frequency between one target and the wave source, because of their relative motion. Then, the difference between the frequency of the transmitted signal and the returned signal must be less than the repetition frequency. The maximum Doppler shift is obtained for a point that is illuminated at a maximum distance ahead of the

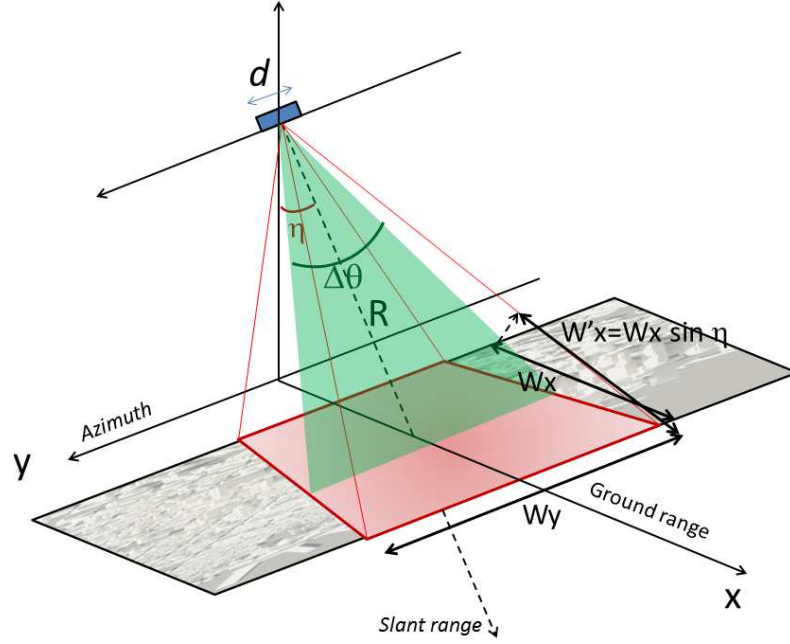


Figure 16: Geometrical representation of the SAR acquisition

radar, then at the farthest points of the illumination lobe. The shift Doppler frequency  $\Delta f_d$  obtained for a point with a relative radial velocity to the radar  $v_r$  is:

$$\Delta f_d = 2 \frac{v_r}{\lambda} \quad (18)$$

where  $\lambda$  is the central wavelength. If  $\Delta\theta$  is the angular aperture of the antenna, then the maximal value is obtained for  $v_r = v \sin \Delta\theta/2$ . With the condition  $\Delta f_d \max < \text{PRF}$  and  $\sin \Delta\theta/2 \approx \Delta\theta/2 = \frac{\lambda}{2d}$ , where  $d$  is the along-track dimension of the antenna aperture, we set the lower bound of the Pulse Repetition Frequency:

$$\text{PRF} > \frac{2v}{d}$$

This requirement necessitates the radar to send a pulse each time that the radar platform translates half of the along-track antenna length  $d$ . In other words, the maximum along-track distance between samples is  $d/2$  (Freeman, 2006).

### 1.3 Polarimetric mode: reducing swath or loss of spatial resolution?

Azimuth resolution is also constrained by the antenna real dimension, and is thus related to the minimum PRF.

A RAR system achieves its resolution through the physical dimensions of its aperture, sometimes referred to as diffraction limited performance. As described previously, a SAR obtains a better azimuth resolution by using all

echoes acquired along an integration path, whose length is called the synthetic aperture length. However, the scene must be illuminated for all of the positions of the integration path. This means that the antenna must have a large angular extent, which is inversely proportional to the aperture dimension.

Let  $L$  be the integration length. Then

$$L < \Delta\theta R \quad (19)$$

where  $\Delta\theta$  is the angular aperture of the antenna, and  $\Delta\theta = \lambda/d$  where  $d$  is the dimension of the real antenna aperture. Let us recall that the azimuth resolution can be written as  $\delta\alpha = \frac{\lambda_0}{\Delta\theta} R$ , obtaining

$$\delta\alpha \geq \frac{d}{2}. \quad (20)$$

Thus, the best achievable for a focused SAR is approximately one half of the along-track real radar-antenna length.

Finally, we can express the conditions on PRF as a condition relation between the azimuth resolution and the range swath  $W'_x$ :

$$\delta\alpha > 2 \frac{v}{c} W'_x. \quad (21)$$

Since this condition depends on the speed of the platform, it is more critical for spaceborne systems. This means that there is a trade-off between swath and azimuth resolution. Note that other parameters involve trade-off such as the transmitted powers. For example, in order to enable shorter pulses to be sent, the transmitted frequency bandwidth is often reduced, which is therefore at the expense of the range resolution.

Up to now, the polarimetric mode has been therefore designed at the expense of azimuth resolution. On all polarimetric satellites already sent, resolutions in the polarimetric mode are worse than those the single polarization modes. Conventional quad-pol SAR operate with interleaved transmission of alternate H-polarized and V-polarized pulses, receiving both H-polarizations and V-polarizations to build up a measurement of the full scattering matrix for each pixel on the ground. The SAR designer typically adopts an overall PRF that is twice as high as for conventional modes of operation. In the dual pol mode of TerraSAR-X for example, the radar toggles the transmit and/or receive polarization on a pulse-to-pulse basis. The effective PRF for each polarimetric channel is half of the total PRF, which means that the azimuth resolution is also reduced (Tomiyasu, 1978).

Therefore, it is very difficult to prove the benefit of polarimetric data, especially in the case of applications where the resolution is an essential criterion, such as in urban areas for the detection of buildings, or the identification of manufactured targets.

For this reason, urban studies were first made by using airborne data offering higher resolutions. Recently I have led polarimetric studies over urban scenes using satellite data, in particular after the launch of TerraSAR-X. TerraSAR-X polarimetric data have resolutions of the order of 2m x 6m, while

the single polarimetric modes have sub-metric resolutions. In addition, rather than abandoning the polarimetric mode when the resolution is insufficient, Nicolas Trouvé proposed in (Trouvé and Colin-Koeniguer, 2013) to combine it with high resolution images. This is the aim of the PhD thesis of Flora Weissgerber which began at the end of 2014. This thesis has led to two key contributions:

- The first concerns the statistical study of complex data used in polarimetry and interferometry, in particular through statistical studies about the coherence parameter. This will be explained in more detail in the next chapter. The underlying idea is to better understand the influence of the signal-to-noise ratio, which is sometimes different for the various polarimetric channels.
- The second relates to the reconstruction of the spectrum of a polarimetric image, using the spectrum of a single polarimetric image acquired at a higher resolution. This reconstruction would allow a polarimetric analysis while maintaining the maximum spatial resolution information.

The latter technique offers opportunities for a variety of applications, including the detection of urban buildings, and for changing detection between a polarimetric image and a High Resolution one. These works are developed in the next chapters.

It is clear that the future spaceborne SAR sensor and system parameters such as resolution, noise level, baseline, cross-talk isolation, revisit time, etc. can be optimized for the data acquisition with polarimetry for each group of applications (forestry, urban, agriculture). There is a need to make a first iteration between the PolInSAR community and the SAR system designers in order to consider the parameter specification in the design of future spaceborne SAR systems, the orbit selection and mission planning. Our recommendation is to promote resolution in polarimetric images for urban applications, and to maintain the swath for forestry

## 2 CALIBRATION

For polarimetric radar images, calibration is an essential step, to be able to rely on the physical values of intensity and phases that are measured.

The elements of the transmitter and receiver can introduce phase shifts and losses in signals. The attenuation and phase shifts are different for the horizontal and vertical antenna, and are the cause of calibration problems. Calibration consists in measuring these losses and phase shifts induced by the system, in order to eliminate them afterwards in the measured data. The relative calibration in phase and intensity between the two antennas is thus essential to consider working on polarimetric data.

Most polarimetric calibration techniques use signals from known sources, such as trihedral or dihedral corners, or active transponders. These targets are called *reference targets* or *canonical targets*. Consider, for example, the wave

backscattered by a trihedral corner. Its polarimetric signature with the BSA convention is the identity matrix. Practically, given that the antennas do not have exactly the same gains, and since no radar system has ideal characteristics, we do not measure this identity matrix. However, measuring these imbalances between polarimetric channels makes it possible to correct them during calibration. Most methods thus involve placing a number of these reference targets on the scene illuminated by the incident wave. Similarly, in an anechoic chamber, preliminary measurements are performed on calibration targets.

The calibration methods involve distortion matrices to characterize disturbances in emission and reception channels. They can be divided into two classes:

- general methods that make no assumptions about the distortion matrices to characterize disturbances and require three standard targets.
- simplified methods seeking to make the implementation easier, which make some assumptions about the distortion matrices.

We consider any bistatic configuration using two different antennas for transmission and reception. We model all disturbances induced in the transmission antenna by the Sinclair matrix  $\mathbf{A}$ , and all of the perturbations induced by the antenna reception by  $\mathbf{W}$ . The response of the target is  $\mathbf{S}$ .

Uncalibrated measured data mix information about the target and the disturbances induced by the system. The measured matrix  $\mathbf{B}_0$  is as follows:

$$\mathbf{B}_0 = \mathbf{A} \cdot \mathbf{S} \cdot \mathbf{W} \quad (22)$$

Calibration is aimed at estimating matrices  $\mathbf{A}$  and  $\mathbf{W}$ , in order to finally obtain the matrix  $\mathbf{S}$ . In anechoic chamber, we can also consider the noise matrix  $\mathbf{N}$ :

$$\mathbf{B}_0 = \mathbf{A} \cdot \mathbf{S} \cdot \mathbf{W} + \mathbf{N} \quad (23)$$

However, this matrix  $\mathbf{N}$  is eliminated by subtracting a measurement of the empty chamber. In a SAR image, this matrix is neglected. Calibration thus consists in finding the eight complex coefficients of matrices  $\mathbf{A}$  and  $\mathbf{W}$ . This principle is illustrated in Fig. 17.

There are several techniques to solve this problem. Limitations arise from the use of the canonical targets for all of the previous existing methods. In addition, all of the disadvantages are related to their installation: size, difficulty of deployment, sensitivity to the positioning angle, signal amplitude especially for bistatic settings, and the *a priori* knowledge of their polarimetric matrices. All related limitations can be avoided using the method proposed in the PhD thesis of Nicolas Trouvé, for which a patent has been filed.

If we consider any target, we know none of the three matrices  $\mathbf{A}$ ,  $\mathbf{W}$  and  $\mathbf{S}$ . Unlike previous conventional methods, the idea is not to use a canonical target and therefore the method does not make *a priori* make the matrix  $\mathbf{S}$  considered.

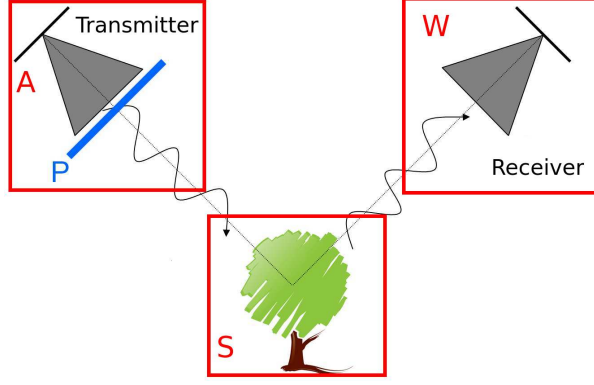


Figure 17: Principle of the new calibration method.

In any case, we will assume that the target matrix  $\mathbf{S}$  is not singular and hence invertible.

We will now add a perturbation to the transmitting antenna. This disturbance  $\mathbf{P}$  will affect the signal, so the final matrix measured is then:

$$\mathbf{B}_1 = \mathbf{A.P.S.W} \quad (24)$$

Assumptions about the disturbance are: two distinct and non-zero eigenvalues, and no eigenpolarization parallel to the polarization axes of the transmitting antenna. We suppose also that it is possible to turn the disturbance, in order to change the orientation of the eigenvectors relative to the polarization. Knowledge of the eigenvectors and eigenvalues is not necessary, all of the parameters will be estimated during calibration. The main property used here is the conservation of eigenvalues for similar matrices. This will allow us to find, first, the parameters of the disturbance and, as a second step, the calibration parameters of the antenna. One example of the simplest disturbance is the matrix  $\mathbf{P}$  as follows:

$$\mathbf{P} = \begin{pmatrix} 1 & 0 \\ 0 & \lambda \end{pmatrix} \quad (25)$$

If we use Eq. 22 and 24 we find:

$$\mathbf{B}_1.\mathbf{B}_0^{-1} = \mathbf{A.P.S.W.W^{-1}.S^{-1}.A^{-1}} = \mathbf{A.P.A^{-1}} \quad (26)$$

Then we let:

$$\mathbf{C}_1 = \mathbf{B}_1.\mathbf{B}_0^{-1} = \mathbf{A.P.A^{-1}} \quad (27)$$

$\mathbf{C}_1$  is known and measured twice;  $\mathbf{A}$  is unknown. However, we know that  $\mathbf{P}$  has two non-zeros eigenvalues, because  $\mathbf{C}_1$  and  $\mathbf{P}$  are similar, as can be seen from Equation 27. Thus, both matrices have the same eigenvalues.

Suppose that we carry out a rotation of our perturbation around the axis (it is desirable to depart from the limit angles 0 and 90 degrees, for example an angle  $\theta = 45$  degrees is the best choice). We measure:

$$\mathbf{C}_n = \mathbf{B}_n \cdot \mathbf{B}_0^{-1} = \mathbf{A} \cdot \mathbf{R}(\theta_n) \cdot \mathbf{P} \cdot \mathbf{R}(\theta_n)^{-1} \cdot \mathbf{A}^{-1} \quad (28)$$

with

$$\mathbf{R}_\theta = \begin{pmatrix} \cos \theta & -\sin \theta \\ \sin \theta & \cos \theta \end{pmatrix} \quad (29)$$

For more simplicity we let:

$$\mathbf{P}_n = \mathbf{R}_{\theta_n} \cdot \mathbf{P} \cdot \mathbf{R}_{\theta_n}^{-1} \quad (30)$$

And we obtain:

$$\mathbf{C}_n = \mathbf{A} \cdot \mathbf{P}_n \cdot \mathbf{A}^{-1} \quad (31)$$

$\mathbf{A}$  is then the solution of the Sylvester equation:

$$\mathbf{C}_n \cdot \mathbf{X} - \mathbf{X} \cdot \mathbf{P}_n = 0 \quad (32)$$

Our knowledge of  $\mathbf{P}_n$  is limited, but we can find the eigenvalues and eigenvectors from equations. Then for each new measurement  $n$  we obtain 4 different equations for each measured term, and 3 new unknown variables ( $\lambda_1$ ,  $\lambda_2$  and  $\theta$ ), and 4 common unknown variables for each measurement: the 4 components of  $\mathbf{A}$ . For each measurement, we add 4 new equations for only three new unknowns and then 4 measurements allow us to find *a priori*  $\mathbf{A}$ . If we ignore the phase and amplitude absolute value, we can consider that one eigenvalue is equal to one. Thus, two different angles are sufficient to find  $\mathbf{A}$ .

To summarize, the protocol is to perform:

- A measurement of any non-singular target. It may therefore be the target of interest, or a target of opportunity on the image.
- A measurement of the same target, adding a linear disturbance.
- A measurement of the same target, adding the same linear disturbance affected by a suitable rotation.

In general, the calibration consists in solving a system of 2 (or 4) Sylvester equations. For this resolution, one approach is to vectorize matrices and use Kronecker products. Thus, the following convention is used:

$$\mathbf{X} = \begin{pmatrix} x_1 & x_2 \\ x_3 & x_4 \end{pmatrix} \quad \text{vec}(\mathbf{X}) = \begin{pmatrix} x_1 \\ x_3 \\ x_2 \\ x_4 \end{pmatrix} \quad (33)$$

and the following properties:

$$\text{vec}(\mathbf{AB}) = (\mathbf{B}^t \otimes \mathbf{I})\text{vec}(\mathbf{A}) = (\mathbf{I} \otimes \mathbf{A})\text{vec}(\mathbf{B}). \quad (34)$$

We then find:

$$\text{vec}(\mathbf{C}_n \mathbf{X} - \mathbf{X} \mathbf{P}_n) = (\mathbf{I} \otimes \mathbf{C}_n - \mathbf{P}_n^t \otimes \mathbf{I})\text{vec}(\mathbf{X}) = 0 \quad (35)$$

We let:

$$\mathbf{H}_n = (\mathbf{I} \otimes \mathbf{C}_n - \mathbf{P}_n^t \otimes \mathbf{I}) \quad (36)$$

Since  $\mathbf{A}$  is a solution of the system, by construction, we know that  $\mathbf{A} \in \text{Ker}(\mathbf{H}_n)$  but we know  $\mathbf{H}_n$  to within a constant  $\theta_n$ . We cannot ascribe a random value  $\theta_n$ . However, we know that the system always has a solution. Thus, if we impose:

$$\dim(\text{Ker}(\mathbf{H}_1(\theta_1)) \cap \text{Ker}(\mathbf{H}_2(\theta_2)) \cap \text{Ker}(\mathbf{H}_3(\theta_3)) \cap \text{Ker}(\mathbf{H}_4(\theta_4))) \geq 1 \quad (37)$$

There is a vector  $(\theta_1, \theta_2, \theta_3, \theta_4)$  that fulfills this, we have shown that this vector is unique to within a constant and we have proposed a method to estimate the vector. Given that the matrices and vectors are complex, it is impossible to use the method of least squares as the optical Mueller imaging systems do on Mueller matrices.

The main advantage of the invention proposed here is that during the entire calibration process the target  $\mathbf{S}$  does not require to be known. Furthermore, no assumption about the position of the antennas has been made and thus this method works in a bistatic configuration.

In order to validate this approach, an experiment was set up. The proposed disturbance is a filter made in Alkard G produced by the Company Dediene Multiplasturgie, whose main interest is to present a dielectric permittivity with non-zeros real and imaginary parts and well controlled throughout a certain range of radar frequencies. For a frequency of 10 GHz for example,  $\epsilon = 11.7 + 2.06i$ .

The filter was designed in collaboration with Tatiana Novikova from LPCIM to accurately model the performance of the network and to select the dimensions of slots, in order to achieve a network with two very different eigenvalues. Indeed, solving the resolution of the equation system assumes a simplification by  $(\lambda_1 - \lambda_2)$ . There will therefore be interest in having two distinct eigenvalues. In addition, the more the eigenvalues are different, the more accurate the numerical solution is. Once the perturbation had been designed, a first experiment was performed using it in the anechoic chamber BABI of ONERA. The filter and the experimental setup are depicted in Fig. 18.

This first experiment has validated the principle of analytical solution of the system proposed for a simple example, i.e., by fixing one of the eigenvalues of the perturbation at one. This is of course acceptable since we are not trying anyway to estimate the absolute phase and intensity anyway. After a measurement was made for the oriented and tilted filter, it was possible to find the angle of rotation, and thus demonstrate the feasibility of the method.

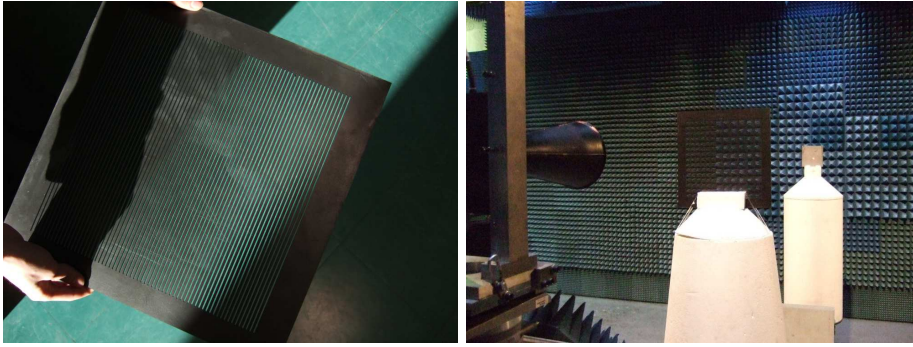


Figure 18: Pictures of the experimental setup to validate the new calibration method principle

### 3 DATA TRANSMISSION: COMPRESSION

All space-based SAR designs have an inherent limitation in regard to the amount of data that can be acquired. As in the case of range and Doppler ambiguities, the conflict between swath width and along-track resolution re-occurs in the data rate relationship. As the along-track resolution becomes smaller and the swath width grows, the swath width time and interpulse time approach one and time expansion buffering is no longer available to reduce data rates.

Again, the polarimetric channel multiplication is a problem, in regard to the transmission rate technologically feasible. Thus, to reduce data rates, compression techniques are often considered. The compression can be done before the image formation and is then called raw data compression. More recently, we have studied compression algorithms directly on the image itself.

One feature of polarimetric image compression is that it contains complex information. Part of my research concerned radar image compression whose phase is relevant: whether for interferometric or polarimetric techniques. The main conclusion of this study conducted with Gilles Vieillard at Onera has shown that it is preferable to perform the compression separately on the modulus and the phase, as on the real part and imaginary part. The solution that we have suggested consists in a vector quantization bloc compression for the modulus, and a linear quantization for the phase. I also performed other studies which showed that the wavelet compression was effective not only for the quality of the compressed image, but also for the speckle filtering.

The problem of image compression is involved in a more general problem called *big data*. Once the image sizes become large, and the number of temporal images increases, classic treatments become intractable. For this reason, it is necessary to consider alternatives, such as data compression, or segmentation, or speckle filtering for coherence estimation. This compression or segmentation can be made parallel to the treatment. In all cases, it is then necessary to keep in mind that the pretreatments such as compression, in essence, amend the statistical nature of the information contained in the image.

In the following, we present the statistical properties of the data, and all of the developments made on the raw images before any operation.

## SUMMARY:

This section has described a number of advances in terms of image formation and associated variable descriptions, as well as technological aspects of the radar design.

- Regarding the formation of SAR images presented in the first chapter, my contribution was mostly conducted in collaboration with researchers at Onera in the DEMR. The related work enabled the understanding of the different approaches to SAR image formation, in order to better address innovative modes, such as circular and bistatic modes.
- The second chapter deals with radar measurable definitions, including polarimetric ones. This section includes the study of polarimetric second parameters. This work quickly led to a spontaneous collaboration with Jaan Praks in University of Helsinki. This collaboration has led to the proposal of alternative parameters to entropy and the alpha parameter. This line of research led me to the proposal of a first thesis on the comparison of polarimetric tools in optics and in radar. This thesis was conducted by Nicolas Trouvé, and directed by Antonello de Martino at LPICM. The optical device was proposed as an alternative to radar bistatic polarimetric measurement. The thesis of Nicolas Trouvé also allowed the theoretical development of bistatic polarimetry, boosting the use of multiplicative polarimetric decompositions. A study was conducted on the influence of the choice of polarimetric bases for bistatic settings and their consequences on the geometry. It led to the recommendation of using a new reference spatial basis for analyzing polarimetric bistatic images.
- The final chapter in this section concerns the radar design. An innovative method of calibration dedicated to polarimetric radars, both for bistatic and monostatic cases was proposed. This method differs from traditional calibration methods in that it does not require the deployment of reference targets on the ground. Also, a study of the technological constraints explains why the polarimetric mode leads to the degradation of the resolution. It is behind the latest proposed thesis, which focuses on the combination of high resolution single polarization images and polarimetric images acquired with degraded resolution. This thesis is being conducted by Flora Weissgerber in partnership with Telecom Paris Tech with the supervision of Nicolas Trouvé and Jean-Marie Nicolas.



## Part II

### POLARIMETRIC IMAGE PROCESSING

Once an image has been computed through a SAR algorithm, we can perform some operations on it, in order to obtain an enhanced image or to extract some useful information from it. These kinds of operations are part of image processing. Image pre-processing is the technique of enhancing data images prior to computational processing. The goal is to enhance the visual appearance of images and/or to improve the manipulation of datasets. It includes coregistration of several images, appropriate radiometric and geometric corrections and filtering. I begin this chapter by presenting an innovative method for the co-registration of images, which has been proven to be effective even in a challenging context. Then, I present my work on the statistical nature of the images, which is particularly important for the implementation of higher level processing. The features of the highest level, such as classification or detection, are finally addressed in this part.



## 1 PROPOSITION OF AN INNOVATIVE METHOD FOR SAR IMAGES

Registration is a fundamental task in image processing used to match two or more images obtained, for example, at different times, from different sensors, or from different viewpoints. The precision required for this registration depends on the application (Li and Bethel, 2008), which may be:

- change detection
- interferometry, either for *Differential Interferometry*, DInSAR with velocity measurements, or for elevation estimations.
- information fusion between images from different sensors.

The methods can be divided into two different categories: spatial methods and frequency domain methods.

- Spatial methods operate in the image domain, matching intensity patterns or features in images. Intensity-based methods compare intensity patterns in images via correlation metrics, while feature-based methods find correspondences between image features such as points, lines, and contours.
- Frequency-domain methods find the transformation parameters while working in the transform domain.

Frequency domain methods work for simple transformations, such as translation, rotation and scaling. Phase correlation is a fast frequency-domain approach to estimate the relative translational offset between two similar images. Applying the phase correlation method to a pair of such images produces a third image which contains a single peak. The location of this peak corresponds to the relative translation between the images. Unlike many spatial domain algorithms, the phase correlation method is robust to noise, occlusions and other defects that are typical of satellite images. Additionally, phase correlation uses the fast Fourier transform to compute the cross-correlation between the two images, generally resulting in large performance gains.

These types of methods are traditionally the ones that are used for radar. Given that the transformation sought is not necessarily a rigid translation all over the image, we compute this method in order to estimate the translation for a grid of points, which is then fitted on a polynomial surface to evaluate the deformation all over the image.

However, these methods remain quite time consuming: it can take several hours for large images. Moreover, the applications encountered become increasingly challenging. This is the case, for example, for:

- close images in non-interferometric conditions, whose deformation between images depends on terrain elevation, and can vary by several pixels over the entire image.
- images with very big temporal decorrelation, for example images at X-band with several years of revisit time. Many geophysical data sets suffer from severe decorrelation problems due to a variety of reasons, making precise coregistration a non trivial task.
- images acquired in different SAR modes (stripmap, spotlight) with different resolutions and speckle patterns.

Part of my research has been devoted to investigating a registration method already developed and used at ONERA-DTIM, but within a different context: an optical flow method applied to stereovision and to real-time video processing applications. This method fits into spatial methods rather than frequency, which means that it takes into account the intensity and not the phase. This operation is also efficient for non-interferometric conditions. EFolki is a special implementation of the initial Folki optical flow ([Champagnat, Plyer, Le Besnerais, Leclaire, Davoust, and Le Sant, 2011](#)) on GPU, developed by Aurélien Plyer during his PhD thesis. This variant leads to performances unchallenged by previous techniques in terms of robustness and acceleration of its computation time ([Plyer, Le Besnerais, and Champagnat, 2014](#)). By adapting the method parameters such as the size of the search window and the scale level for radar images, subject to speckle noise, the result is more than conclusive:

- The robustness makes the registration method efficient under all conditions encountered. It has been, for example, used for change detection of images of Toulouse under non interferometric conditions, without the use of a Digital Elevation Model to correct the misregistration effects due to the relief.
- The execution time of the code was of the order of one minute, on our 4000x4000 pixel image. Comparatively, another available frequency method took several hours on the same image. Moreover, a GPU implementation of the method exists and would make it faster, less than a second.
- The accuracy of the estimated determined offset is of the order of one twentieth of the pixel. It is sufficient for all of the most demanding applications such as interferometry.

This is yet another example of a response to a problem, found by investigating methods for other application areas, i.e, optical video, analyzing the specifics of the radar in this context (here, speckle and the complex nature of the signals), and making the necessary adjustments to this method to fit these characteristics. This initiated work opens the door to many opportunities, including the application for registration algorithms in more complex situations

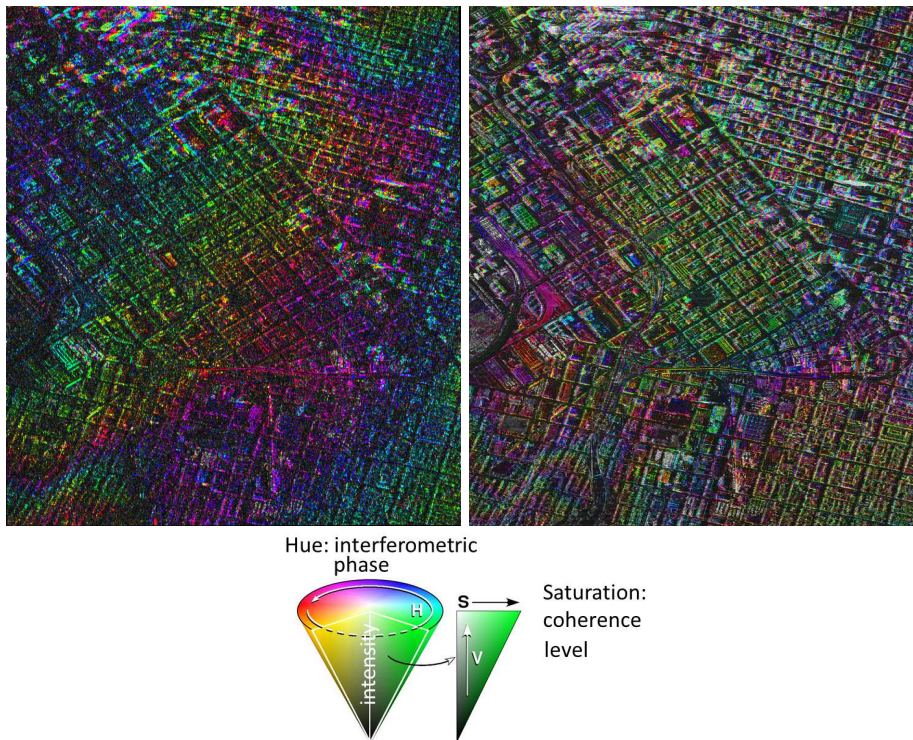


Figure 19: Different interferograms obtained after coregistration by eFolki: on the left, between two polarimetric images with an 11-day temporal baseline, on the right, at a high resolution and with an 11-day temporal baseline

and the feasibility of the joint registration and intended application, for example, change detection.

## 2 APPLICATION TO INTERFEROMETRY AND CHANGE DETECTION

This coregistration technique has been applied to various images under interferometric conditions. For example, the image in Fig. 19 on the left is the resulting interferogram obtained by combining two low resolution polarimetric images with an 11-day revisit time, whereas the figure on the right is the resulting interferogram obtained by combining two spotlight high resolution images with the same revisit time.

Efolki has also been proven to be effective for images with a long temporal baseline at X-band, in a situation of high temporal decorrelation. A special effort has been focused on the co-registration of data with different resolutions. In Fig.20, two images with two different resolutions and a revisit time of 18 months are combined.

eFolki has also been applied under non-interferometric conditions, still combining different resolutions, but with close incidence, in order to aid in change detection, on images of Toulouse (Weissgerber, Colin-Koeniguer, and Janez, 2014).

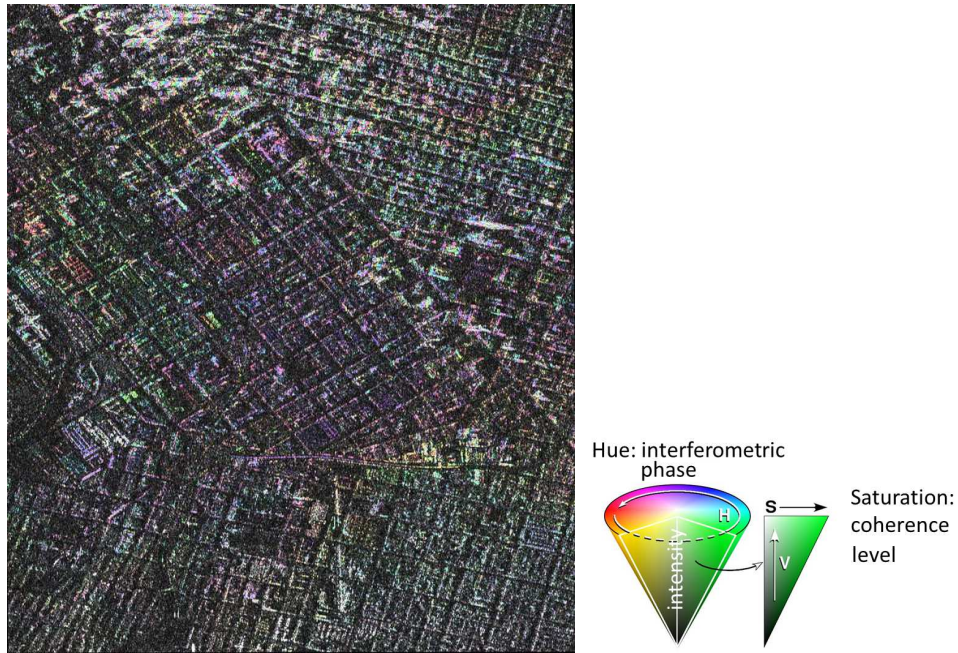


Figure 20: interferograms obtained after coregistration by eFolki, between two different resolutions and radar mode with a 18 month temporal baseline.

More challenging applications include coregistration also between optical and radar images, as is successfully demonstrated in Fig.21, on images of the Deepwater Horizon oil spill, collected in 2010 at an interval of one day. Coregistration is successful using the coast structure. It reveals the displacement of the extent of the spill.

Given these results, the question is: how far can we go in the coregistration of remote sensing images using eFolki?

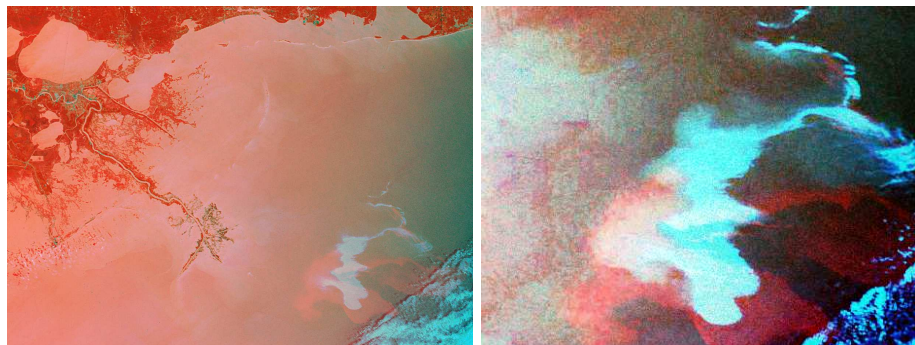


Figure 21: Coregistration between an optical image and a radar image of ENVISAT. Red: radar image, Green and Blue: MERIS optical channels. Zoom on the oil spill is given on the right.

Knowing the statistical laws of the measured quantities is essential for many treatments, involving in particular the concepts of estimation and the notion of distance. This is the case for:

- Speckle filtering
- Detection
- Classification or Segmentation
- Coherence estimation

First, I recall the state of the art knowledge on the statistical variables for SAR images, then for polarimetric SAR and PolInSAR images, and I show what theoretical advances were made during my research about the perspectives raised by statistical tool advances.

## 1 AMPLITUDE AND INTENSITY STATISTICS

### 1.1 *State of the Art about classical distributions for Intensity and Amplitude*

Goodman developed a speckle modeling in 1975 for a resolution cell containing a large number of scatterers, under the following assumptions:

- the amplitude and phase of the signal transmitted by each scatterer are independent,
- the phase of a scatterer is uniformly distributed between  $[-\pi, \pi]$ ,
- scatterers are independent.

Under these assumptions, it is possible to show that the complex signal received  $Z$ , which is the sum of contributions from all scatterers, follows a circular complex Gaussian centered distribution. The real and imaginary parts  $Z_R$  and  $Z_I$  of this signal follow a standard normal distribution with variance  $\sigma^2$ .

The amplitude follows a Rayleigh-phase Nakagami distribution and a uniform distribution between  $[0, 2\pi]$ . Finally, the intensity  $I = A^2$  signal follows an exponential law.

### 1.2 *Speckle is not an electronic noise*

Here, care must be taken with regard to the meaning of the word *speckle* for radar, and the definition of what we call noise. Speckle is often considered or

treated as a granular *noise* because it degrades the quality of SAR images and causes difficulties for image interpretation. In that sense, speckle is often regarded as a multiplicative noise. However, speckle is explained by the physics of the measurement. It inherently exists due to the coherent image process, and must not be considered the same as the classic thermal additive noise that affects the measurement.

Thermal noise is the background energy that the radar receiver channel generates and is another additive noise.

In order to obtain the statistical representation of the signal including both speckle and noise influence, a scattering vector  $\mathbf{k}$  of an image measured on a multichannel SAR system can be modeled by the following equation:

$$\mathbf{k} = \mathbf{s} + \mathbf{b} = \boldsymbol{\tau} \circ \mathbf{x} + \mathbf{b} \quad (38)$$

where  $\circ$  is the Hadamard term-to-term product. The signal  $\mathbf{x}$  is the signal backscattered by the target and the vector  $\boldsymbol{\tau}$  is called the texture, whereas  $\mathbf{b}$  is the thermal noise.

In agreement with the speckle theory modeled by Goodman,  $\mathbf{x}$  follows a zero-mean Gaussian circular statistics of covariance matrix  $\boldsymbol{\Upsilon}$ . Contrariwise,  $\boldsymbol{\tau}$  is deterministic and due to the material from which various parts of the scene are made.

The thermal noise  $\mathbf{b}$  also follows a zero-mean Gaussian circular statistics of covariance matrix  $\boldsymbol{\Gamma}$ .

In statistics studies, we must differentiate the statistical influence of the speckle from studies that deal with thermal noise and finally from those that consider clutter as a signal that comes from the scene (for example vegetation, ground) but is not the target of interest.

### 1.3 Multilook and mechanism mixture

Let  $I_1 I_2 \dots I_L$  be  $L$  independent and identically distributed intensity measures. Then, it is already known that the average of these measures follows a gamma law of order  $L$ . This result is useful when dealing with multilook data, when intensities are averaged together, to reduce the speckle for example.

However, there is another case where we must consider the summation of different intensity samples: this is the case of layover. The previous Goodman signal model is that of a resolution cell containing a single type of scatterer or electromagnetic mechanism. However, sometimes in resolution cells, there can be an overlap of several different mechanisms. For example, this is the case for roofs of buildings that are projected in the same range resolution cell. During the PhD thesis of Azza Mokadem, the problem of the superposition of several mechanisms of different types within the same resolution cell was discussed. Within this framework, an apparently simple result whose proof is counter-intuitive has been raised: it has been shown that the intensity distribution of an overlap always follows an exponential law, and not a gamma of order 2, which one expects to find in the case of the sum of two exponential laws.

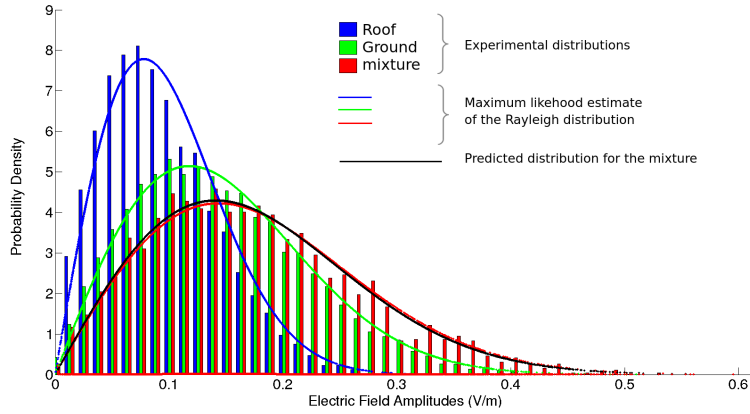


Figure 22: Example of validations of statistical behavior of a layover area.

An experimental validation of this result has been conducted and is represented in Fig.22. This validation also concerns the interferometric coherence modeling.

## 2 POLARIMETRIC STATISTICS

When dealing with polarimetry, we must describe the law of multivariate data. Taking again the expression of the signal:

$$\mathbf{k} = \mathbf{s} + \mathbf{b} = \boldsymbol{\tau} \circ \mathbf{x} + \mathbf{b} \quad (39)$$

Polarimetric Synthetic Aperture Radar (PolSAR) data are usually modeled by a multivariate circular Gaussian probability density function for  $\mathbf{s} = \boldsymbol{\tau}\mathbf{x}$ , which is completely determined by the multilook polarimetric covariance matrix that follows a complex Wishart distribution. In this case, texture  $\boldsymbol{\tau}$  can be considered as a deterministic scalar and  $\mathbf{x}$  describes the polarimetric information.

For high resolution textured areas, the Gaussian clutter model may no longer be valid and is commonly replaced by the compound Gaussian model: In this case the clutter is modeled as a product between the square root of a scalar random variable  $t$  that corresponds to the texture and an independent complex circular Gaussian random vector.

$$\mathbf{k} = \sqrt{t} \circ \mathbf{x} + \mathbf{b} \quad (40)$$

Many texture models have been studied and applied to classification and segmentation. The Gamma texture distribution leads to the classical K distributed covariance matrix and more recently the Fisher distribution has been studied in [Bombrun et al. \(2011\)](#) and leads to the KummerU distribution. Good results have been demonstrated using a more accurate texture distribution but require a prior knowledge. These distribution parameters also need a large

amount of samples to be estimated, which is not possible at the early stage of a segmentation process, when each segment contains very few pixels.

The SIRV model (*Spherically Invariant Random Vectors*) is based on the same traditional product where  $\mathbf{x}$  is an independent complex circular Gaussian random  $m$ -vector. The SIRV model includes most texture distributions and does not require estimation of the texture parameters. This model is very convenient for PolSAR segmentation when we need a more accurate result than the Gaussian model, and allows us to use the full resolution available while maintaining reduced computing times (Trouvé, Sangnier, and Colin-Koeniguer, 2012).

### 3 COHERENT SIGNAL STATISTICS

For most advanced applications that use coherent signals whose relative phase is meaningful, we use the complex correlation. Practically, this correlation  $C(s_1, s_2) = \gamma e^{i\Phi_{1,2}}$  is defined for two signals  $s_1$  et  $s_2$  by:

$$\tilde{C}(s_1, s_2) = \frac{\sum_{k=1}^L s_{1,k} s_{2,k}^*}{\sqrt{[\sum_{k=1}^L s_{1,k} s_{1,k}^*][\sum_{k=1}^L s_{2,k} s_{2,k}^*]}} = \tilde{\gamma} e^{i\tilde{\phi}_{1,2}} \quad (41)$$

If averaging is not needed, i.e. with  $L = 1$ , the modulus of this correlation is 1 and the resulting interferometric phase is very noisy.

Without taking into consideration the noise for such signals, and still under the Goodman hypothesis, it is possible to derive the PDF of the estimated coherence modulus  $\tilde{\gamma}$  and the estimated phase  $\tilde{\phi}_{1,2}$ , in terms of  $L$ , the number of samples used in the estimation. These expressions reveal that the higher  $\gamma$  is, the more precise the estimation of the phase is. However, the number of samples  $L$  has a more important effect than  $\gamma$  on the shape of the phase distribution. The higher  $L$  is, the more precise the phase estimation is, even with a low coherence level.

To go further in the statistical analysis of the coherence behavior, including the link between the coherence level and the accuracy of its phase, we need statistical tools that are able to describe complex quantities. Generally, this problem is reduced to the joint statistical study of its real and imaginary parts. These last two terms can be written as the complex variable of its complex conjugate.

In her thesis, Flora Weissgerber addressed the problem in an original way by considering the statistics of coherence in amplitude and phase. For phase statistics, she used the directional statistics.

The signal phase  $\phi$  is an angular variable defined as modulo  $2\pi$ . Hence linear statistics cannot be used because any angular  $\phi$  and  $\phi + 2\pi$  correspond to the same phase. For directional random variables such as the phase, the probability density  $P(\phi)$  is defined in (Mardia, 1999) as follows:

- $P(\phi) \geq 0$  on  $(-\infty .. +\infty)$
- $P(\phi + 2\pi) = P(\phi)$  on  $(-\infty .. +\infty)$

- $\int_0^{2\pi} P(\phi) d\phi = 1$

We can define the moment of order  $p$  of the probability density by the following formula:

$$\Phi_p = E[e^{jp\phi}] = \int_0^{2\pi} e^{jp\phi} P(\phi) d\phi \quad (42)$$

We can show that  $\Phi_0 = 1$ . The first moment  $\Phi_1 = Re^{i\theta}$  is particularly useful since  $\theta$  gives the preferred direction of the distribution  $P(\phi)$  and the mean resultant length  $R$  gives information about the concentration of the distribution  $P(\phi)$ . If the distribution is really narrow and centered around its preferred direction,  $R$  will be close to 1. In the case of a less concentrated distribution  $P(\phi)$  or a multimodal distribution,  $R$  will decrease. It will be really close to 0 when the distribution is uniform around the circle or bimodal with the two modes separated by  $\pi$ .

By leading different simulations, it has been shown that in the presence of thermal noise, the distribution of the estimated phase is a better way of gathering the information of similarity between the two images as compared to the degree of coherence or the mean resultant length.

Flora Weissgerber investigated  $R$  and  $\gamma$ , which yield information regarding the level of cross information of images. They evolve as with the covariance of speckle or the SNR. Both are overestimated when only few samples are used in their empirical estimator. They differ substantially when the SAR images have a strong texture. Indeed,  $\Phi_1$  does not take into account the amplitude of the scatterer, whereas the texture has an influence on  $C$  computation. It can artificially increase the  $C$  value. The estimated phase depends on the relative amplitude of the scatterer. A strong scatterer will impose its phases in the correlation computation to any window that it is part of. Thus the choice between the use of the correlation or first moment will depend on the importance of the texture. If only strong scatterers must be taken into account, the correlation should be used. This can be the case in polarimetry if only the behavior of some target is needed. However, when the response of all scatterers is important, the first moment should be used. This is the case in interferometry when the height of both streets and buildings must be retrieved.

When using these estimators, one must keep in mind that both  $\gamma$  and  $R$  qualify the phase distribution that they use for estimation and not the estimated phase distribution. The coherence  $\gamma$  or the mean resultant length  $R$  will be high when the pixel-to-pixel phase difference distribution is really narrow. Even for distributions with low  $\gamma$  or  $R$ , the distribution of the estimated phase can be narrow. This averaging reduces the phase noise.

In order to estimate the interferometric phase, Flora Weissgerber has proposed a double averaging as a good alternative to obtain a good estimation of the phase difference in the presence of thermal noise. This promising estimation method is illustrated in Fig. 23 and 24 on a simulated image highlighting the effects of resolution. For the double estimation, first a classical spatial estimation is computed and then the circular moments are estimated.

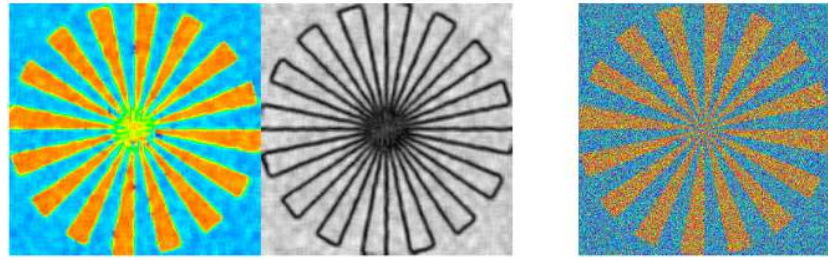


Figure 23: A classical estimation of interferometric coherence in phase and modulus, with an  $18 \times 18$  window on the left, interferometric coherence without averaging on the right.

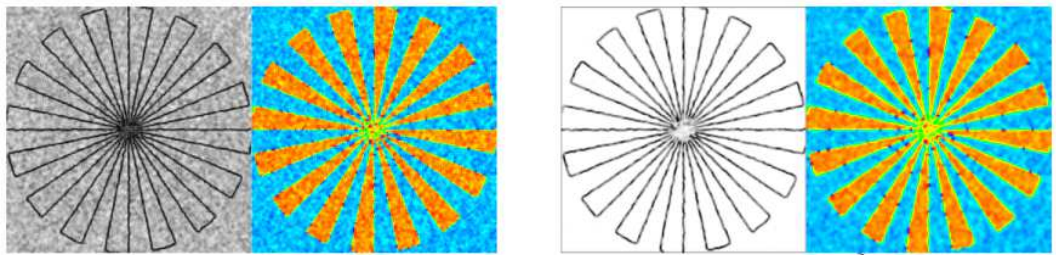


Figure 24: A classical estimation of interferometric coherence in modulus and phase, with a  $9 \times 9$  window on the left, followed by a circular moment estimation on the right

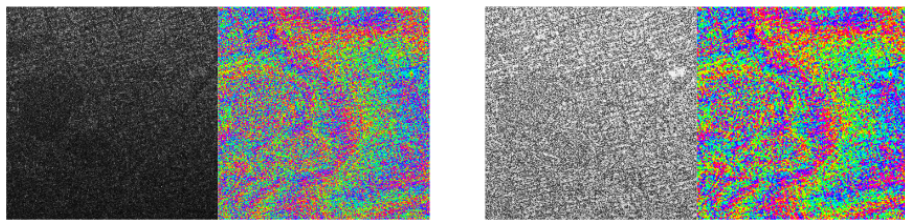


Figure 25: Different kinds of averaging to estimate interferometric coherence, with a  $9 \times 9$  window on the left, followed by a circular moment estimation on the right

These simulated results prove the efficiency of this averaging: the quality of the phase seems to have improved, the coherence level is better contrasted. Coherence is higher in homogeneous in large areas, and lower in the transitions. The interferometric phase is homogeneous in large areas but takes on median values in the transitions. These simulations are assessed by coherence estimation on real data in Fig. 25. The figure on the right, corresponding to the double estimation, clearly shows an estimation of the phase with lower noise. The corresponding coherence level offers a better contrast and a higher coherence level.

This is on-going work and several parametric studies are still under investigation. In addition, in this thesis several questions are raised about the relationship between some polarimetric parameters and the noise, including:

- How the entropy of depolarization estimation is affected by the noise level.
- What the exact relationship between the quality of a polarimetric phase and the quality of the correlation module is.



The previous sections cover preliminary steps that are essential to be able to then propose processing algorithms, such as segmentation, detection and classification. I present here some of the processing that I have investigated in SAR images, and the potential benefits of polarimetry.

## 1 SEGMENTATION

Image segmentation is aimed at gathering pixels into regions. Segmentation can have several goals. It may for example separate objects from the background. The segmentation can also be a method of compressing the information: by keeping a value for the segment found. Finally, the segmentation allows a better estimation of the coherence matrices by using pixels belonging to a homogeneous region. In this context it can therefore be seen as a speckle filter.

During his PhD thesis, Nicolas Trouvé proposed a segmentation method for POLSAR images over urban areas (Trouvé and Colin-Koeniguer, 2011). For this segmentation, he investigated:

- The definition of a POLSAR statistical distance, adapted to different metrics. For example, using a SIRV based distance, adapted to any kind of texture (Trouvé and Colin-Koeniguer, 2010).
- The sensibility of Polarimetric information vs Intensity (SPAN) in these different methods.

While it is the regular choice for most classification and segmentation algorithms, the Wishart distance has multiple issues regarding the impact of the SPAN. If this distance is applied to the non-normalized matrix (dividing by the span) then the polarimetric information becomes negligible compared to the SPAN information. However, on the other hand the SPAN remains a very reliable information, that must be used in the segmentation process.

The main interest of SIRV is that we do not need to know the modeling of the said texture, which can be particularly interesting for very high resolution data. The SIRV coherency estimator is also much better at estimating the boundaries between two areas since there is no "mixed" zone between both. The Fixed Point estimator has been shown to be very robust in the presence of strong singular targets that may have been included in the averaging windows. The SIRV distance is power invariant since the covariance matrices are normalized. SPAN information remains useful to improve segmentation but the Wishart distance used on non-normalized covariance matrices had the major issue of drastically favoring the power information over the polarimetric information.

In order to provide segmentation mostly focused on the polarimetric information, Nicolas Trouvé included the SPAN information but pondered to a level comparable to the polarimetric information.

- Sample Covariance Matrix, even though it is optimal in the Gaussian case is very sensitive to noise pixels (hence the "box" effects even in uniform areas). Spatial variations such as the transition from the top to the bottom area are very noise sensitive: a virtual area is even created by mixed effects from the two areas and is located at the boundary. Singular small targets are blurred, their size is overestimated and their real location is lost.
- SIRV Fixed Point Covariance Matrix is much more accurate for each area, the edges, and the singular target.
- Wishart Segmentation based on the Sample Covariance Matrix suffers from the same side effects, which is not the case for the SIRV distance Segmentation.
- Colors, and hence the covariance matrix, for each segment are much brighter in the SIRV Segmentation, since the Fixed Point Covariance Matrix is unaffected by noise pixels that are included as the segments grow.

Shape parameters are also used to:

- encourage the segmentation of very small pixels once the number of segments have been reduced to 20% of the initial segmentation.
- encourage linear edges according to the maps that highlight them as shown in Fig. 26.

This type of algorithm can be useful:

- Coupled with a classification algorithm, as proposed in (Formont, Trouvé, Ovarlez, Pascal, Vasile, and Colin-Koeniguer, 2011).
- For 3D rendering, as presented in (Trouvé and Colin-Koeniguer, 2011) and (Colin-Koeniguer and Trouvé, 2011). A 3D reconstruction has been obtained over Toulouse (France), using only the PolInSAR data in single pass mode, required for this types of algorithm, and with an adequate ambiguity height. The result will be detailed in the following part.
- For data compression.

## 2 DETECTION: BUILDING, SUPERSTRUCTURES

Localization of lines and pylons is part of the important information for mapping the territory:

- For communities that need to develop their urban plan or agricultural development.

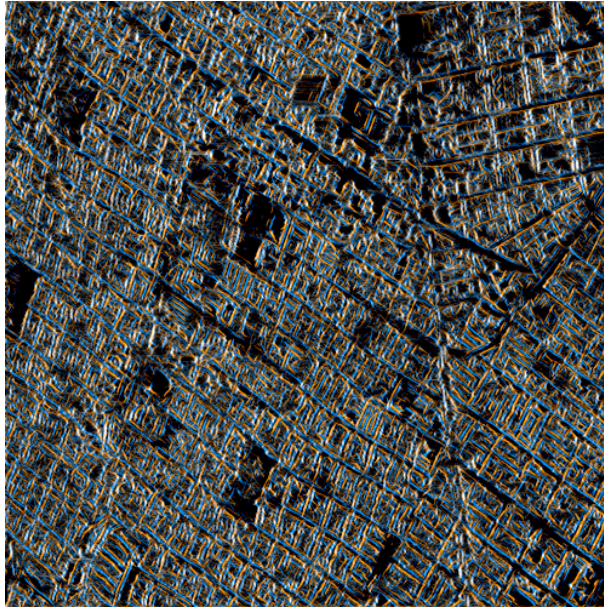


Figure 26: Map used for shape criteria in the segmentation software, emphasizing linear elements of positive contrast in orange, and negative contrast in blue, over a UAVSAR image of San Francisco

- For tourist organizations. A pylon tower is an excellent marker on the map and in the landscape to locate.
- The aeronautical Information Services: identifying obstacles at great heights (including pylons and lines) to regulate air navigation.

Regarding this last point regarding low altitude navigation, electrical cables are in fact a very common source of accidents. Many collision accidents with pylons or cables by helicopters have been identified, making it the highest risk of fatal accident. The most recognized causes are poor pilot vision and poor appreciation of the environment, taking off, landing or during phases of flight at low altitude [Goy \(2012\)](#).

In order to define tools for the automatic detection of superstructures such as pylons, power cables, wind turbines, etc., a phenomenological study was first conducted. It was shown that among the advanced modes, the most reliable to detect such superstructures were interferometric methods, which make it possible both to detect a bright object, and to provide an interesting contrast level with the interferometric coherence.

Polarimetry also allows a more reliable signature of objects such as pylons or wind turbines, in which we invariably find a strong double-bounce mechanism at the structure bottom.

Finally, the intensity spatial signature for such a structure has been shown to be relatively stable for a given structure and given image parameters. For this reason we have developed a method of correlation between pixels of the most significant intensity, with the pixels obtained on a reference image intensity. This method gave the most successful results, analyzed in terms of ROC

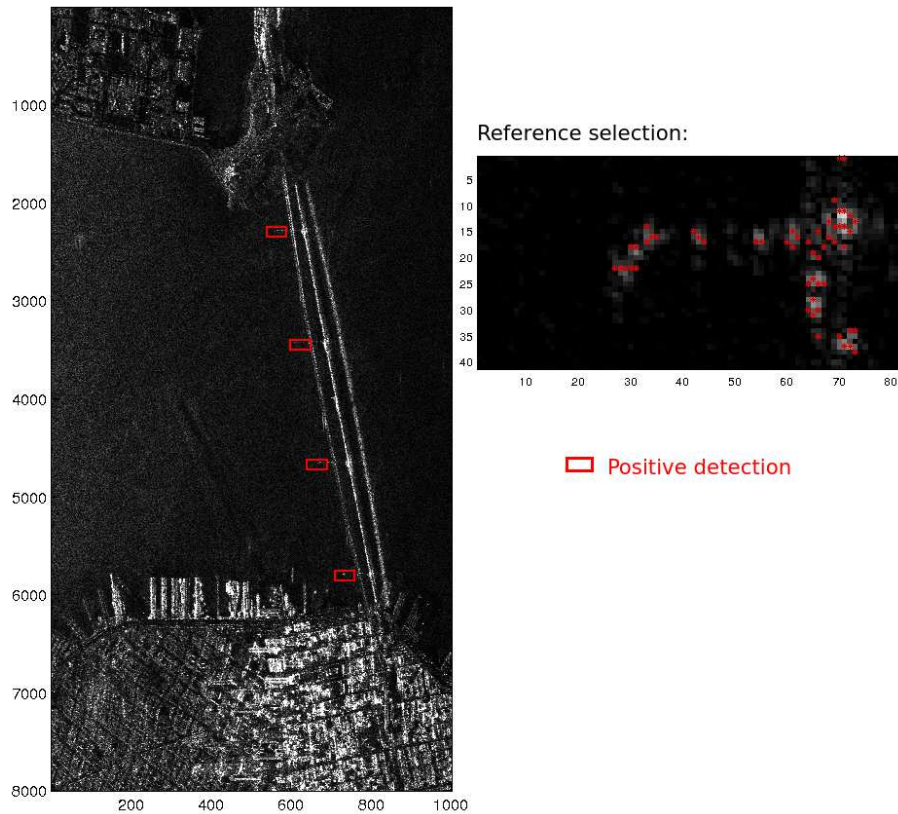


Figure 27: SAR total image on the left, selection of one suspender of the Oakland Bay bridge, and results of the corresponding detection

curves. One example of its efficiency is given by the SAR image of the Oakland Bay Bridge in San Francisco in Fig. 27. We have selected one of the vertical suspenders on the right and determined the spatial distribution of the brightest pixels. The result of a hysteresis threshold on the correlation map is given by the red rectangles in Fig. 27. It gives the good detections of the four vertical suspenders of the bridge exactly.

### 3 CHANGE DETECTION

In satellite remote sensing, change detection is a functionality of interest for many applications, such as monitoring of urban growth. The objective is to identify and analyze changes in a scene from images acquired on different dates. In this context, radar imaging is emerging as one of the most relevant sensors. In fact, thanks to its ability to observe at any time (day and night), it is an indispensable means of observation in emergency situations when weather conditions are unfavorable for an optical acquisition.

In addition, under some acquisition configurations, it provides very good detection performance, including in complex environments such as in urban areas [White \(1991\)](#).

The most relevant configuration is when the available data is of the same type from the same sensor with the same parameters (incidence, resolution, and frequency).

However, obtaining such data is not always possible in the short term if the revisit time of a single sensor is too large, or if the characteristics (incidence) during its passage are not close enough. In particular, the current situation tends to favor the use of images from different sources (TerrarSAR-X, CSK, RADARSAT, etc.).

Recent works [Kempf and Anglberger \(2013\)](#) showed that change detection can remain effective for different sensors where the resolutions and frequencies differ. It is worth noticing that it concerns the case of low resolution images which means a negligible impact from the differences in the other parameters. However, the resolution of current sensors continues to improve and in this case, the effects of the difference in the other characteristics such as the incidence can greatly complicate the comparison of data, especially in the presence of 3D objects. Therefore, it is necessary to focus on configurations with few or no differences in these features to ensure the detection function. Then, another difficulty always lies in the interpretation of changes detected.

Given that polarimetric modes that enhance analysis capabilities are nowadays deployed on several satellites, the use of polarimetric analysis to improve the characterization of the change can be considered. However, we have already seen that up to now, polarimetric acquisitions are always done at the expense of a loss in spatial resolution.

Thus, I have been interested in the comparison of images where only the resolution strongly differs, as is the case when the SAR sensors switch in polarimetric mode.

I have investigated several types of data and presented results in ([Weissgerber, Colin-Koeniguer, and Janez, 2014](#)):

- Satellite images under interferometric conditions: a high resolution SAR image (spotlight mode with a resolution of 1m x 1m and a HH polarization) acquired in October 2011, and a polarimetric SAR image (StripMap mode with a resolution of 2m x 6m) acquired in April 2010, over San Francisco
- Airborne images under non-interferometric conditions: A high resolution SAR image (Stripmap mode with a resolution of 10 cm x 20 cm with a HH polarization) acquired in 2004, and a polarimetric SAR image (StripMap mode with a resolution of 60 cm x 60 cm) acquired in 2005, over Toulouse.

As highlighted in previous works by [Kempf and Anglberger \(2013\)](#), the main difficulty for change detection is to have comparable images. This requires several pre-processing steps. The main difficulty lies in the difference in radiometry. This difference in appearance is due to:

- Differences in radiometric calibration.

- Differences in texture, linked to the difference in resolution.
- Differences in signal-to-noise ratio.

The pre-processing thus consists in bringing the images to a similar geometry and in matching their radiometric levels. This involves the following operations:

- Calculating the images in a common grid and coregistration. We choose to compute the image in the worst resolution of the polarimetric image by selecting the common spectrum portion.
- Making amplitudes and spectra shapes comparable A first step is to adjust the histogram of the high-resolution image on the polarimetric one. At a higher resolution over Toulouse, the differences in radiometry still exist but are less important. Moreover, different spectrum windows have also been applied to the processed data, which must be corrected before their use for a change detection operation: the spotlight HR image is filtered by a Hamming window whereas the polarimetric stripmap mode is not.

Once the pre-processing steps were done, I investigated a new change criteria for detection. Despite pretreatments, it turns out that the comparison of both images is not always perfect. The challenge is to find a criterion that is independent from the changes in texture, and highlights changes in the structure content of the image itself. This is precisely the idea of the Structural Similarity Index: SSIM. This index has been proposed to quantify the quality of an image after a processing operation such as a compression. It may nevertheless be used for change detection [Thomas et al. \(2012\)](#), although this is rarely presented in SAR.

The preprocessing steps previously proposed are essential to improve the efficiency of the change detection process as seen in [Fig. 28](#) about an area with only one change that can be seen in the lower left area.

The last step consists in a hysteresis threshold on the SSIM map. For results that are presented below, the low and high thresholds have been automatically set to  $m + \sigma$  and  $m + 5\sigma$  respectively where  $m$  is the mean of the parameter that is considered, and  $\sigma$  is the standard deviation.

The biggest change that is detected corresponds to a building construction, the City College of San Francisco, constructed between 2009 and 2012. Analysis is possible using the content of the polarimetric information available here before the change. The parameter double-bounce from the Yamaguchi decomposition ([Yamaguchi et al., 2006](#)), adapted to the case of urban areas, shows that the observed appearance is an area of bare soil without vegetation or building.

This study has been demonstrated also on airborne images acquired under non-interferometric conditions, over the Toulouse site. Here, the co-registration algorithm previously presented, eFolki, was particularly useful, since it allowed the images to be superimposed with a subpixellic precision, adapting

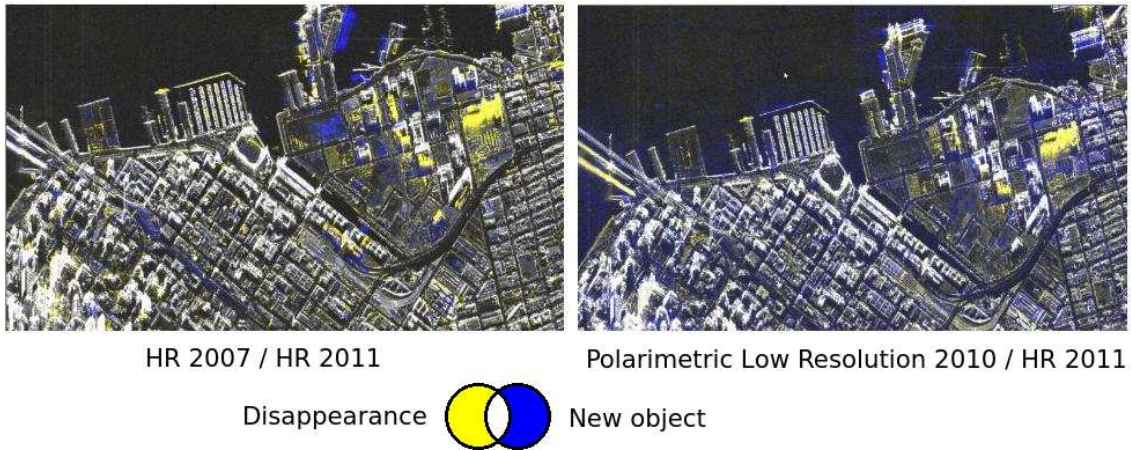


Figure 28: Change detection maps on San Francisco after preprocessing

to terrain elevation. Registration accuracy has allowed the detection of change of car positions. The main changes that have been detected are of three types: one new building, car parks and growth of the trees that are along a canal.

Comparisons between the SSIM and a classical intensity ratio parameter roughly show that:

- SSIM is less sensible to vegetation changes, or homogeneous change in intensity, because SSIM overcomes homogeneous changes of mean intensity or standard deviation. Similarly, the SSIM emphasizes less changes resulting from the presence of the shadow behind the building.
- Both are well able to detect the new presence of the cars on the parking lot.
- Generally, false alarms that appear for both parameters are small. The elastic intensity ratio most often generates false alarms in the low intensity areas, for example, bare soil, while SSIM false alarms appear most often in high intensity pixels, for example some strong echoes of buildings that have not been modified.

The proposed benefit of polarimetry is twofold: polarimetry can help to analyze and characterize detections, and can also be a way of reducing the number of false alarms. For example, false alarms belonging to strong echoes located on the double bounce line can be immediately identified as such: a real change that would be linked to the construction of a building could not give isolated detections. It therefore appears possible to improve the detection performance by eliminating some false alarms through their polarimetric analysis.

#### 4 SPECTRUM RECONSTRUCTION

As we have already seen, the polarimetric mode is often acquired with a degraded resolution. The PhD thesis of Flora Weissgerber concerns the enrichment of a high-resolution image by a polarimetric image with a degraded

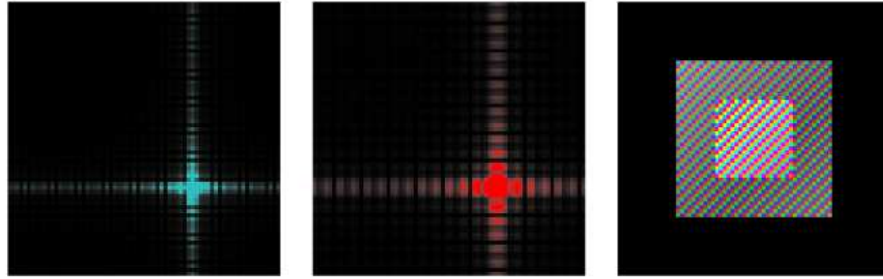


Figure 29: The bright point estimation and complementarity of spectra

spatial resolution. At the beginning of her PhD, Flora Weissgerber designed an algorithm for spectrum reconstruction or resolution enhancement.

She designed a sliding window algorithm that works in two steps:

- In the first step, each sliding window containing  $N$  pixels is supposed to contain only one bright point. The ratio of the energy between both windows of the same polarization but different resolutions is estimated using the amplitude ratio of common portions of spectra.

This estimation is followed by the estimation of the entire polarimetric vector. By inverse Fourier transform, we obtain an estimation of the polarimetric vector for the window, enriched by the high resolution one.

- These estimations are stored until the window has covered the whole image. The mean amplitude and phase values, computed using the circular first moment, are then derived for each pixel.

This algorithm has been tested on an ONERA data set acquired over Toulouse in a full-polarimetric acquisition. In order to obtain a low resolution image and a ground truth, she created a lower resolution image of the given one, using half of the initial resolution spectrum, in range and in azimuth.

The efficiency of the method has been illustrated on an example of two bright scatters that are separated in the HR image but not in the low resolution one. These scatters are separated again in the resulting enriched polarimetric image, as illustrated in Fig.30.

Moreover, the stability of the polarimetric answers has also been checked.

The actual drawback of the algorithm is the polarimetric correlation that appears in clutter. This artifact is due to the initial hypothesis of the algorithm, which considers a one bright point model for each window. The algorithm is being improved by the inclusion of cases where the window contains only clutter, or possibly a segment. This improvement would include the sequential extraction of bright scatters of the image.

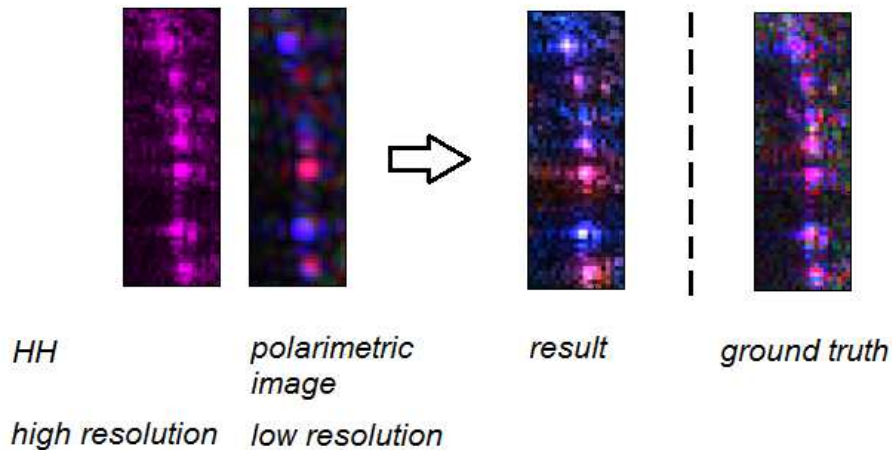


Figure 30: Reconstruction of a polarimetric image using HR image

#### SUMMARY

This second part concerned all studies relating to the processing of a radar image. Here is a summary of the points that we discussed:

- The first section of this part was about the co-registration of images. The algorithm called eFolki proposed by Aurelien Plyer has been diverted from its original field of work. It was particularly useful for the registration of data under interferometric or non-interferometric conditions and for images in the presence of a very strong temporal decorrelation. Given that it seems very promising when adapted for the radar, this should be the result of future developments for remote sensing imagery and in particular to respond to the issues of big data.
- The following section is focused on the advances made in regard to the statistics of radar signals. It led to three important aspects, developed over three different thesis; respectively those of Nicolas Trouvé, Azza Mokadem and Flora Weissgerber, including:
  - A decline in the use and effectiveness of SIRV to process polarimetric signals, and a study on the matrix distances suitable for polarimetric detection or segmentation.
  - A result concerning coherent addition of radar speckle patterns, different from the addition of speckle patterns in optics: the coherent addition of two speckle patterns following exponential laws always follows an exponential law, instead of a gamma law with shape parameter 2 in optics. New results regarding the statistical behavior of the interferometric coherence are also given.
  - The proposal of circular statistics to address the polarimetric or interferometric phase signals and a study on the relationship between amplitude and phase of a complex statistical correlation.
- Finally, the last section in this part was constituted by works on the detection of targets of interest and change detection. A final application for the enrichment of the spectrum of a polarimetric image using a High Resolution spectrum is being developed by Flora Weissgerber and showed very encouraging results.



## Part III

### FROM 2D TO 3D

The classic SAR image is projected onto an image plane. However, advanced techniques can provide three-dimensional information: either by the reconstruction of three-dimensional surfaces, or by 3D SAR imaging, i.e a reflectivity map along three spatial axes. In order to obtain a 3D image of the terrain surface, interferometric SAR is typically used. We first try to obtain the same kind of results using only the polarimetric information. Then, polarimetry is considered as a means to improve the result of interferometry. Finally, we discuss how polarimetry can help tomographic SAR, the imaging technique that produces slices of the target at various heights to form a 3D data cube.



## 3D FROM PURE POLARIMETRIC INFORMATION

---

### 1 RECONSTITUTION OF A RELIEF BY A POLARIMETRIC IMAGING RADAR

Traditionally, interferometry or formerly radargrammetry techniques have been dedicated to the production of three-dimensional maps. Polarimetry can act as an aid to these techniques. However, as we have already seen, polarimetry is highly dependent on the geometry of the scene, and it can also be investigated alone for the purposes of 3D reconstruction.

In fact, part of my studies have attempted to answer this question: how can we use purely polarimetric information for the volumetric reconstruction of the target?

In the polarimetric vision systems existing for some animals, two main criteria are investigated:

- The depolarization effect, whose orientation can be linked to the polarizing effects in the presence of an oriented flat surface.
- The polarimetric orientation angle.

The orientation angle is well known in polarimetric radar images. Several studies have shown that this angle is related to the azimuth slope of a surface. If the ground is modeled as a set of oriented facets, the polarimetric orientation angle  $\Psi$  is related to the azimuthal slope and range slopes according to:

$$\tan\Psi = \frac{-\tan\zeta}{-\sin\theta + \tan\eta\cos\theta} \quad (43)$$

where  $\zeta$  refers to the azimuthal slope,  $\eta$  to the range slope and  $\theta$  is the orientation angle, as schematized in Fig.31. However, this data is insufficient to recover both orientations, since there is one relation for two unknowns.

It is possible to compensate for this missing data in several ways:

- Statistically by an iterative method which ensures the continuity of the particular area.
- or with the aid of a flight with a different azimuth, and a clever combination of data from these two flight orientations.

The first solution was successfully performed during my PhD, but for a particular case: it was applied to a P-band image of the dune of Pyla in France, where the slope was considered to not be significant along the azimuth axis, and where the initialization method was particularly facilitated from the horizontal surface of the sea.

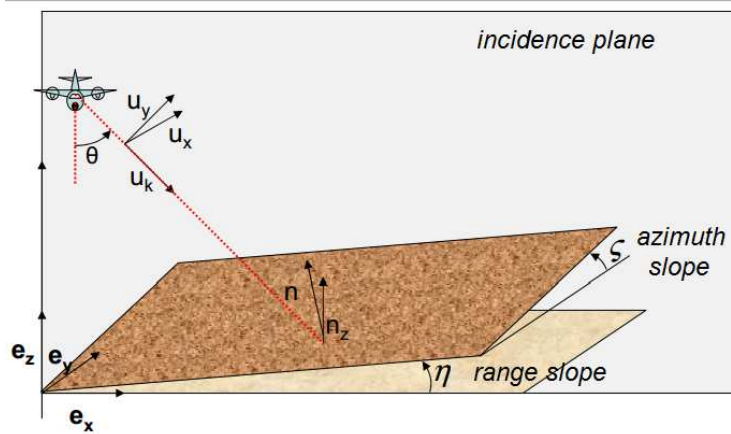


Figure 31: Definition of the orientation of a surface with the radar

Computed on several satellite San Francisco images, the estimate of the orientation angle  $\Psi$  was too noisy to be used for direct 3D reconstruction, including at lower frequencies (L-band) where this method is supposed to work best.

In order to study this subject more in depth, I also proposed a method that combines the polarimetric information with that provided by a circular imaging. We saw earlier that the circular imaging alone could theoretically provide a volumetric imaging of the scene. Unfortunately, at X-band in particular, 3D imaging is very difficult if not impossible, due to the fact that scatterers are very anisotropic. The solution that I have proposed to reconstruct the slopes of the terrain from a circular polarimetric image consists in two steps:

- the range directed slopes could be estimated by the look angle which maximizes the response of the ground. The resulting look angle is represented in 32 for a P-band circle SAR image in Sweden. The effectiveness of this estimation has been shown by comparison to ground truth elements.
- Thus, the azimuthal slope could be estimated classically by the polarimetric orientation angles for the trajectory segment whose line of sight is perpendicular to the precedent one. This orientation angle represents a rotation of the antenna about the line-of-sight for which the Sinclair matrix becomes diagonal. Hence this angle is measured in a plane perpendicular to the look-direction.

This solution has unfortunately not had the opportunity to be tested on real data, but could be investigated in a simulation.

## 2 PROSPECTS FOR 3D NAVIGATION IN OPTICAL POLARIMETRY

In general, issues of 3D space information reminiscent of those that could be used in navigation, for robotics for example.

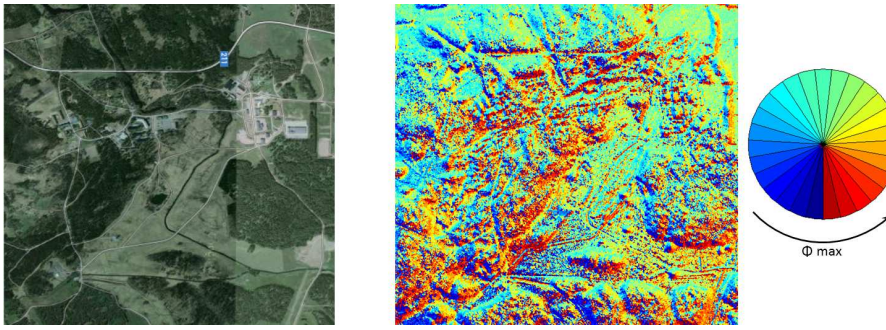


Figure 32: on the right, look angle maximizing the answer on a P-band circle SAR image in Sweden, and on the left the corresponding site

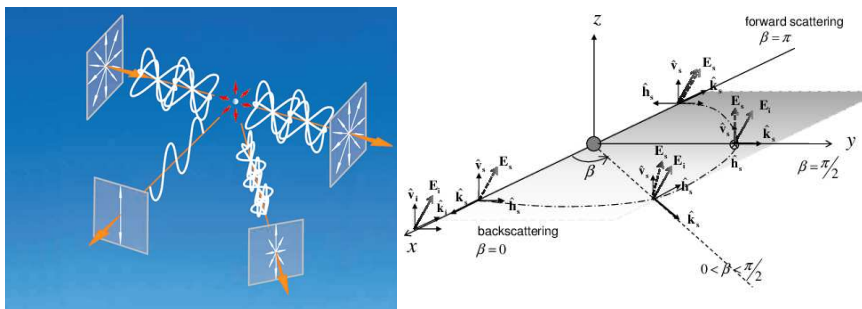


Figure 33: The degree of polarization of light changes with the look angle of the receiver, after diffusion on molecules

Searches can then be guided by the navigation systems that some animals develop using to their polarimetric vision. Polarized light is widely used by some animals, for defense, communications and navigation.

When unpolarized sunlight enters the atmosphere, the air particles cause Rayleigh scattering and the light becomes partially linearly polarized, as is illustrated in Fig.33. The zenith angle of the sun can be estimated from patterns of incident polarization. This analysis of the sky polarization is the navigation technique that honeybees use for orientation.

This change in the polarization degree with the angle of the receiver is the same as in bistatic radar images, as we highlighted in (Trouvé, Colin-Koeniguer, Fargette, and De Martino, 2011).

Similarly, the orientation of smooth surfaces such as water surfaces can be detected from the reflection-polarization patterns. Similarly in robotics, these polarimetric techniques could be used to detect surfaces and estimate their positions, whereas other sensors such as stereo-vision cameras fail in the presence of specular returns in particular.



One of the key ideas of PolInSAR data is that it is possible to obtain interferometric coherence from all possible linear combinations of polarization states.

#### 1 DIFFERENT GENERALIZED COHERENCE

Several definitions for this generalized coherence have been successively proposed. In the first one, these linear combinations are described by two vectors called the two generic mechanisms: one for each image of the pair. Using different vectors makes it possible to take into account polarimetric decorrelation between the two scattering mechanisms. The definition of this coherence for the two mechanisms  $\omega_1$  and  $\omega_2$  is (Cloude and Papathanassiou, 1998):

$$\gamma(\omega_1, \omega_2) = \frac{\omega_1^\dagger \mathbf{T}_{12} \omega_2}{\sqrt{\omega_1^\dagger \mathbf{T}_{11} \omega_1} \sqrt{\omega_2^\dagger \mathbf{T}_{22} \omega_2}} \quad (44)$$

If the same projection vector  $\omega$  is chosen for both images, the generalized coherence can be written as follows:

$$\gamma = \frac{\omega^\dagger \mathbf{T}_{12} \omega}{\sqrt{\omega^\dagger \mathbf{T}_{11} \omega} \sqrt{\omega^\dagger \mathbf{T}_{22} \omega}}. \quad (45)$$

This generalized coherence is defined using the same polarimetric projection vector for the first and the second antenna. This definition of the coherence set constrained to a unique mechanism is well suited in the case of an interferometric configuration where both antennas as well as the incidence angles are very close. It is even more suitable in a single-pass acquisition since signals are not affected by temporal decorrelation effects.

In practice, matrices  $\mathbf{T}_{11}$  and  $\mathbf{T}_{22}$  are very similar because they are both coherence matrices of the target viewed under very close incidence angles. Provided that this assumption is valid, the mean average on the denominator is very close to the geometric average. It is then possible to replace the definition of  $\gamma$  by the following:

$$\tilde{\gamma} = \frac{\omega^\dagger \mathbf{T}_{12} \omega}{\omega^\dagger \mathbf{T} \omega}, \quad (46)$$

where matrix  $\mathbf{T}$  is defined as  $\mathbf{T} = (\mathbf{T}_{11} + \mathbf{T}_{22})/2$ . Since the arithmetic mean of non-negative real numbers is greater than or equal to their geometric mean, the modified coherence  $|\tilde{\gamma}|$  is lower than the generalized coherence  $|\gamma|$ , and

thus always lies between 0 and 1. Moreover, the argument is not modified by this definition change:

$$|\tilde{\gamma}| \leq |\gamma|, \arg \gamma = \arg \tilde{\gamma}. \quad (47)$$

The set of all complex coherences can be plotted in the complex plane. It will be called the *coherence set* and written as  $\Gamma(\mathbf{T}_{12}, \mathbf{T})$ .

It is mathematically proved in (Flynn et al., 2002) that:

$$\Gamma(\mathbf{T}_{12}, \mathbf{T}) = \Omega(\mathbf{T}^{-\frac{1}{2}} \mathbf{T}_{12} \mathbf{T}^{-\frac{1}{2}}). \quad (48)$$

The set  $\Omega(\mathbf{A})$ , is also called the *field of values of matrix A*, or *numerical range* of matrix  $\mathbf{A}$ , and is defined by

$$\Omega(\mathbf{A}) = \{\mathbf{x}^\dagger \mathbf{A} \mathbf{x} : \mathbf{x} \in \mathbb{C}^n, \|\mathbf{x}\| = 1\} \quad (49)$$

In an attempt to propose a physical interpretation of the linear combination of the generalized coherence, a possibility is to define it as an elliptic state. It is the so-called *polarization subspace method* (PSM) based on finding local maxima of the copolar or crosspolar coherence functions (Pascual et al., 2002). Physically, the mechanisms must be represented as an elliptic polarization transformation. The *polarization state conformation* (PSC) algorithm is very similar: it is based on the knowledge of the polarimetric basis transformation along with the polarization signatures of both interferometric images (Qong, 2005). Finally, we will see in next section that these different definitions can be extended to the multibaseline case, using  $3 \times N$  complex vectors.

Once the generalized coherence set has been defined, it is possible to model it for different objects of interest: a forest scene, building, bare soil, etc. In the next section I present my contributions to one particular modeling case: the  $N$  point scatterer modeling, which is especially useful for deterministic targets.

## 2 N BRIGHT POINTS WITHOUT INTERACTION

We use the same data model as in the ESPRIT algorithm, but without the thermal noise. This model can be applied for resolution cells containing several point scatterers without taking into account the interactions between scatterers or the volume effects. The signal  $\mathbf{k}_i$  acquired by the antenna  $i$  in polarization  $xy$  consists of a sum of  $N$  different elementary scattering contributions or bright points:

$$\mathbf{k}_i^{xy} = c_A s_A^{xy} e^{-j4\pi \frac{\rho_{iA}}{\lambda}} + c_B s_B^{xy} e^{-j4\pi \frac{\rho_{iB}}{\lambda}} + \dots \quad (50)$$

$c_A$  is the total power or *span* of point  $A$ ,  $\rho_{iA}$  is the distance between point  $A$  and the antenna  $i$ , and  $s_A^{xy}$  is the complex reflectivity coefficient for polarization  $xy$ . Since the span is described by  $c_A$ , we can assume that the complex

diffusion vector  $\mathbf{s}_A = (s_A^{xx}, s_A^{xy}, s_A^{yy})$  is normalized. All bright points  $A, B, \dots, N$  are in the same resolution cell defined by the first antenna, so that one may assume that  $\rho_{1A} = \rho_{1B} = \dots = \rho_{1N} = \rho$ .

Equation 1 can be rewritten in the matrix form:

$$\mathbf{k}_1 = \mathbf{S}\mathbf{c}, \quad \mathbf{k}_2 = \mathbf{S}\mathbf{D}\mathbf{c} \quad (51)$$

where  $\mathbf{S}$  is a complex  $3 \times N$  matrix whose columns contain the normalized polarimetric diffusion vectors for each point,  $\mathbf{c}$  is the real column vector of length  $N$  containing the span of each point, and  $\mathbf{D}$  is the  $N$ -diagonal matrix containing the interferometric phases  $\Phi_i = 4\pi \frac{\Delta \rho_i}{\lambda}$ :

$$\mathbf{D} = \text{diag}(e^{-j\Phi_A} \dots e^{-j\Phi_M}) \quad (52)$$

The coherence matrices can be computed by means of the matrices  $\mathbf{S}$ ,  $\mathbf{D}$  and  $\mathbf{c}$  by:

$$\begin{aligned} \mathbf{T}_{12} &= \langle \mathbf{k}_1 \mathbf{k}_2^\dagger \rangle = \langle \mathbf{S}\mathbf{c}\mathbf{c}^\dagger \mathbf{D}^* \mathbf{S}^\dagger \rangle, \\ \mathbf{T}_{11} &= \langle \mathbf{k}_1 \mathbf{k}_1^\dagger \rangle = \langle \mathbf{S}\mathbf{c}\mathbf{c}^\dagger \mathbf{S}^\dagger \rangle, \\ \mathbf{T}_{22} &= \langle \mathbf{k}_2 \mathbf{k}_2^\dagger \rangle = \langle \mathbf{S}\mathbf{D}\mathbf{c}\mathbf{c}^\dagger \mathbf{D}^* \mathbf{S}^\dagger \rangle \end{aligned} \quad (53)$$

As shown by (Colin, Titin-Schnaider, and Tabbara, 2006b), points having different polarimetric responses represented by a matrix  $\mathbf{S}$ , will be represented by the mechanisms in the space orthogonal to the space spanned by  $\mathbf{S}$ , described by the columns of the matrix  $\mathbf{M} = \mathbf{S}^\dagger^{-1}$ .

### 3 OPTIMIZATION

Maximizing coherence means finding polarimetric combinations that maximize the interferometric coherence module. Interferometric coherence optimization can have several goals, as we will develop in the future. More importantly, the optimization methods obviously differ depending on the definition of generalized coherence that we seek to optimize.

During my PhD, I proposed an algorithm to provide a numerical solution for the optimization of coherence defined using a single mechanism, bringing this problem to calculate the numerical radius of a matrix.

Thereafter, I investigated several applications where this optimization could be useful. Coherence optimization is first connected to the following conclusion: in the absence of thermal noise, and under the assumption of Goodman speckle for one type of scatterer, the estimate of the phase coherence is more accurate when the modulus of the coherence is high. Also, the coherence optimization can be envisaged to improve the quality of the phase:

- Either to improve the phase unwrapping algorithms.
- or to improve the estimation of DEM.

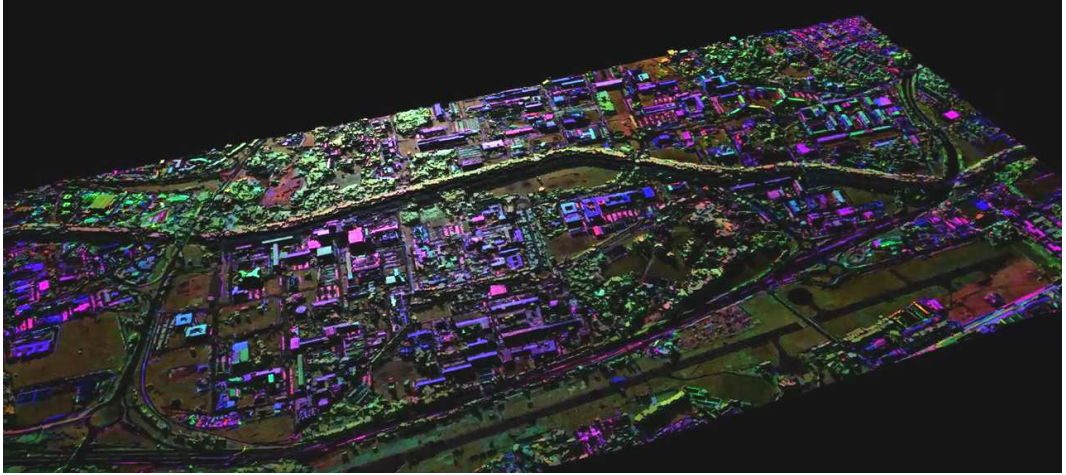


Figure 34: 3D rendering obtained over Toulouse (France), using single pass PolInSAR data acquired by RAMSES (Onera)

As regards the improvement of 3D estimation, the coherence optimization has been interfaced with the segmentation method discussed in Part 2. Results obtained on PolInSAR data acquired by RAMSES (Onera) over Toulouse are shown in Fig. 63. An animation of this reconstruction is given on the web site <http://www.onera.fr/fr/imagetudumois/la-ville-en-3d-avec-le-radar>. The precision of estimates was investigated in (Colin-Koeniguer and Trouvé, 2014).

However, I have also shown that the coherence optimization can be viewed in various contexts: for example, when using optimized coherence for classification. Several classification algorithms use coherence modules defined in the polarimetric base found by optimization, since they generally offer better contrast than those calculated in the Pauli basis. One parameter has been proposed to see how the coherences of the optimal basis differ (Colin, Titin-Schnaider, and Tabbara, 2003). An example of such an application will be shown in the following part.

Finally, in general, the optimization can be used in inversion algorithms based on the modeling of the generalized coherence. This may be the case in the inversion of the Random Volume over Ground model. In particular, I demonstrated in my PhD thesis that under certain assumptions, the extremities of the coherence set determined by proper optimization allowed the separation of different phase scattering centers present in the same resolution cell.

Also, much of my work has involved the study of the geometrical properties of the coherence shape in a particular modeling of the resolution cell, containing a superposition of  $N$  mechanisms without interaction. It is the summary of these studies that I present in the next section.

## 4 GENERALIZED PROPERTIES OF THE COHERENCE SHAPE FOR N BRIGHT POINT MODELING

## 4.1 Two mechanisms

Let us recall the definition of the generalized coherence set for two mechanisms:

$$\gamma(\boldsymbol{\omega}_1, \boldsymbol{\omega}_2) = \frac{\boldsymbol{\omega}_1^\dagger \mathbf{T}_{12} \boldsymbol{\omega}_2}{\sqrt{\boldsymbol{\omega}_1^\dagger \mathbf{T}_{11} \boldsymbol{\omega}_1} \sqrt{\boldsymbol{\omega}_2^\dagger \mathbf{T}_{22} \boldsymbol{\omega}_2}} \quad (54)$$

The results that follow have been proposed in (Colin, 2006) Without any mathematical constraint, the coherence set is a disk centered on zero in the complex plane. Indeed, it is invariant by rotation around zero because  $\gamma(e^{j\theta} \boldsymbol{\omega}_1, \boldsymbol{\omega}_2) = e^{j\theta} \gamma(\boldsymbol{\omega}_1, \boldsymbol{\omega}_2)$ . This means that all interferometric angles can be obtained using a well selected couple of mechanisms.

Let  $\mathbf{v}_1 = \mathbf{T}_{11}^{\frac{1}{2}} \boldsymbol{\omega}_1$  and  $\mathbf{v}_2 = \mathbf{T}_{22}^{\frac{1}{2}} \boldsymbol{\omega}_2$ .  $\gamma$  is now written as:

$$\gamma(\mathbf{v}_1, \mathbf{v}_2) = \frac{\mathbf{v}_1^\dagger \mathbf{T}_{11}^{-\frac{1}{2}} \mathbf{T}_{12} \mathbf{T}_{22}^{-\frac{1}{2}} \mathbf{v}_2}{\|\mathbf{v}_1\| \|\mathbf{v}_2\|} \quad (55)$$

In the case of  $\arg(\mathbf{v}_1^\dagger \mathbf{v}_2) = 0$ , let  $\mathbf{u}_1 = \frac{1}{\|\mathbf{v}_1\|} \mathbf{v}_1$  and  $\mathbf{u}_2 = \frac{1}{\|\mathbf{v}_2\|} \mathbf{v}_2$ . We still have  $\arg(\mathbf{u}_1^\dagger \mathbf{u}_2) = 0$ , and  $q = \mathbf{u}_1^\dagger \mathbf{u}_2$  is a real number between 0 and 1. Thus, the 2MC coherence set with the constraint  $\arg(\mathbf{v}_1^\dagger \mathbf{v}_2) = 0$  is the union of all  $q$ -numerical ranges of matrix  $\mathbf{A} = \mathbf{T}_{11}^{-\frac{1}{2}} \mathbf{T}_{12} \mathbf{T}_{22}^{-\frac{1}{2}}$

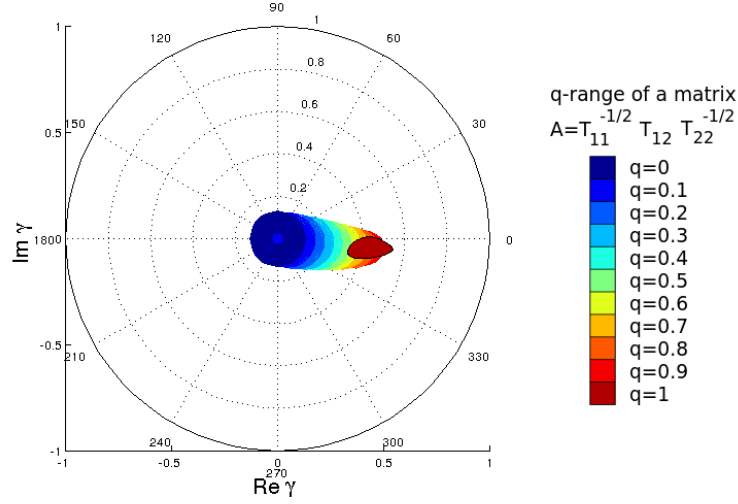
$$\Gamma = \bigcup_q F_q(\mathbf{A}) \quad q \in [0, 1[$$

$$F_q(\mathbf{A}) = \left\{ \mathbf{u}_1^\dagger \mathbf{A} \mathbf{u}_2, \|\mathbf{u}_1\| = \|\mathbf{u}_2\| = 1, \mathbf{u}_1^\dagger \mathbf{u}_2 = q \right\} \quad (56)$$

The  $q$ -numerical range of a matrix is a mathematical object whose following properties are already known Li et al. (1994): it is still a compact and convex subset of the complex plane ; the spectrum of  $\mathbf{A}$   $\sigma(\mathbf{A})$  satisfies  $q\sigma(\mathbf{A}) \subseteq F_q(\mathbf{A})$  ;  $F_q$  is invariant under unitary similarities, and  $F_0(\mathbf{A})$  is a disk whose center is at the origin and whose radius is  $R_{\mathbf{A}} = \min\{\|\mathbf{A} - \lambda \mathbf{I}\|\}$  where  $\|\cdot\|$  denotes the spectral norm. Examples of a  $q$ -numerical range for a given matrix are given in Fig. 35.

Once again, and despite the constraint, all interferometric angles can be obtained because  $F_0(\mathbf{A})$  lies in  $\Gamma$ . Moreover the boundary  $\partial F_q(\mathbf{A})$  is  $C^1$  smooth, which means that the boundary cannot have corners. Thus, the theoretical shape of this set will probably not add useful information regarding the numerical range.

Most generally, the constraint that is most commonly proposed in the literature Cloude and Papathanassiou (1998) to defined the 2 MC coherence is

Figure 35: q-numerical ranges of a matrix  $\mathbf{A}$ 

$\arg(\omega_1^\dagger \omega_2) = 0$ . This constraint is different from the preceding one. However, it should be noted that the set of  $\arg(\gamma(\omega_1, \omega_2))$  under the constraint  $\arg(\omega_1^\dagger \omega_2) = 0$  is equal to the set of all arguments of  $(F_q(\mathbf{T}_{12}))$ . Considering  $F_0(\mathbf{T}_{12})$ , we see that the conclusion about all interferometric angles that can be obtained is still valid.

These conclusions are independent from the type of targets under study or modeling considerations. To our knowledge, they have been drawn for the first time in literature in (Colin, 2006).

#### 4.2 One mechanism, for at least three points, and statistics on amplitudes

Given that the study of the geometrical properties of generalized coherence seems to not be useful for interferometric height inversion, we now restrict the study to the case of one mechanism.

The first modeling that has been proposed is the case in which statistical variations concern only amplitudes. The following hypotheses are chosen: statistical variables  $\mathbf{S}$ ,  $\mathbf{D}$ , and  $\mathbf{c}$  are independent, and  $\mathbf{C} = \langle \mathbf{c} \mathbf{c}^\dagger \rangle$  describes the coherence matrices of the polarimetric powers.

##### *Monostatic configuration: the case of three independent points*

The previous mathematical study in (Colin, Titin-Schnaider, and Tabbara, 2006b) focuses on the case of a modeling of 3 bright points. It allows the following assertion to be deduced introducing the matrix  $\mathbf{A} = \mathbf{T}^{-\frac{1}{2}} \mathbf{T}_{12} \mathbf{T}^{-\frac{1}{2}}$  the local maxima of the numerical range of  $\mathbf{A}$  are located on the unit circle and their phases match the interferometric angles of the bright points.

Moreover it is possible to introduce another matrix  $\mathbf{B} = \mathbf{T}_{11}^{-\frac{1}{2}} \mathbf{T}_{12} \mathbf{T}_{22}^{-\frac{1}{2}}$ . If  $\mathbf{C}$  is diagonal, then the numerical range is exactly a triangle whose vertices have phases corresponding to the interferometric angles, as represented in Fig. 36.

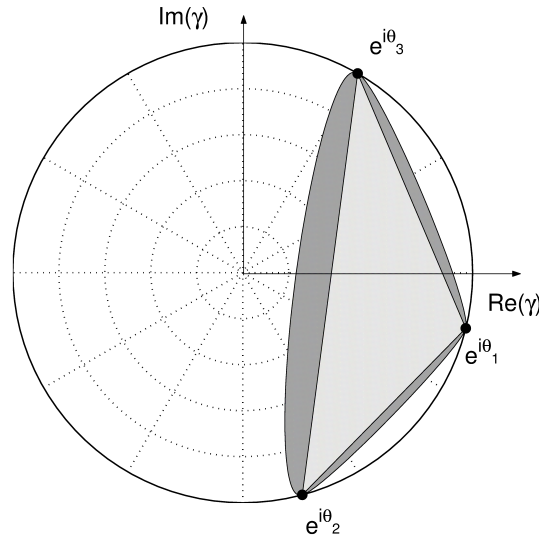


Figure 36: Coherence shape for a model of three types of scatterers

A bias is introduced if non-diagonal elements of  $\mathbf{C}$  are not equal to zero and  $\mathbf{S}$  is not a unitary matrix.

The representation of the coherence set makes it possible to have a mathematical representation of the adequacy of our model. For example, it provides a graphical way to study the consequences of polarimetric changes in the statistical population that is used, or the consequences of additive noise, as shown in Fig. 37.

Moreover, it shows that an optimization procedure is able to separate the different interferometric angles and to retrieve the matrices  $\mathbf{S}$  and  $\mathbf{C}$ . For the thorough treatment of the optimization we refer the reader to (Colin, Titin-Schnaider, and Tabbara, 2005b).

*Monostatic configuration: the case of four independent points*

Here  $\mathbf{S}$  is considered as a  $3 \times 4$  matrix. We distinguish three sub-cases by the number of points that are orthogonal to the subspace formed by the others. These points will be located on the unit circle.

- No point is orthogonal to the others. It is thus possible in this case to use another property of the numerical field of values, called the *Poncelet property*:

*For any point  $\lambda$  on the unit circle, there is a unique  $n$ -gon (polygon with  $n$  sides) which circumscribes  $\partial W(\mathbf{A})$ , is inscribed within the unit circle and has  $\lambda$  as a vertex.*

If  $\mathbf{A} \in S_n$  then its numerical range has the  $n$ -Poncelet property Gau and Wu (2003).  $\mathbf{A} \in S_n$  if and only if  $\mathbf{A}$  is a contraction, it has no eigenvalue of

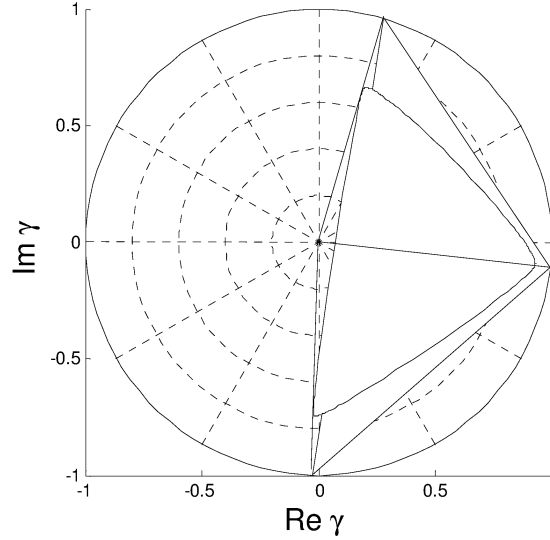


Figure 37: Coherence shape with and without statistical variations on  $\mathbf{S}$ , the polarimetric returns

modulus 1, and  $\text{rank}(\mathbf{I} - \mathbf{A}\mathbf{A}^\dagger)^{\frac{1}{2}} = 1$ . We can prove that this last property is true if  $\mathbf{C}$  is diagonal (no correlation between polarimetric channels). As a consequence of this property, the numerical range of  $\mathbf{A}$  is inscribed in a quadrilateral whose vertices are exactly on the unit circle, as in the example given in Fig.38.

- one bright point is on the unit circle. Let  $\mathbf{s}_1$  be the polarimetric diffusion vector that is orthogonal to the space spanned by the others. We can express all matrices in the basis  $(\text{vect}(\mathbf{s}_1), \text{vect}(\mathbf{s}_1)^\perp)$ . Matrix  $\mathbf{A}$  will be

$$\mathbf{A} = \begin{bmatrix} \lambda_1^* & 0 & 0 \\ 0 & \mathbf{A}' \\ 0 & \end{bmatrix}, \lambda_1 = e^{-j\Phi_1} \quad (57)$$

The numerical range of this matrix is the convex hull of an ellipse and the point  $\lambda_1$ . Moreover, the submatrix  $\mathbf{A}'$  has the same properties as the matrix  $\mathbf{A}$ ; this means that if  $\mathbf{C}$  is a diagonal matrix, the ellipse will be inscribed in a triangle whose vertices are on the unit circle, as in the representation given in Fig.39.

- If two bright points are on the unit circle, this means that the two last points cannot be independent. It is thus equivalent to the case of three independent points, whose last one has a modulus lower than 1.

In the case of bistatic measurements, we can transfer the above analysis back to  $4 \times 4$  matrices. The optimization procedure will be able to separate up to

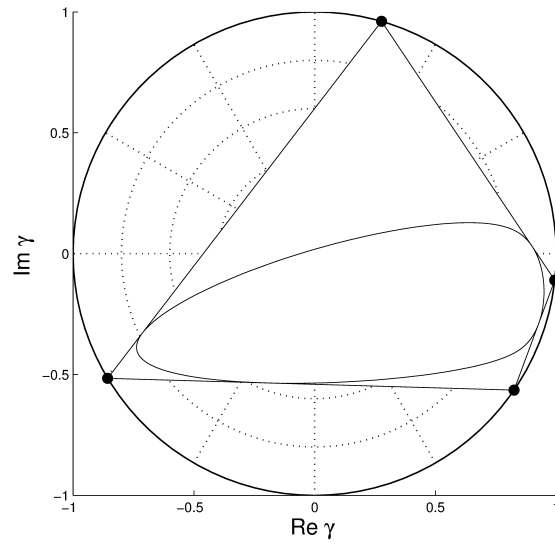


Figure 38: Coherence shapes for a 4 point scatterer mixing model

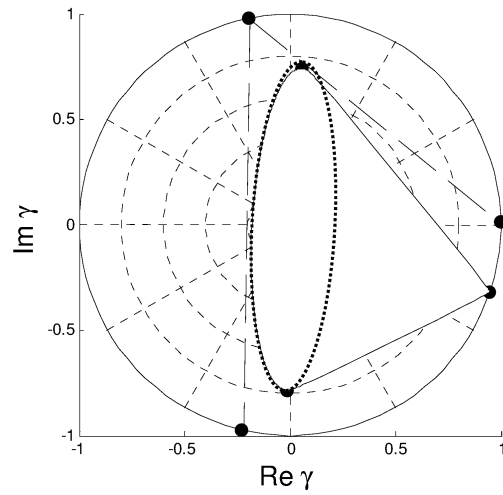


Figure 39: Coherence shapes for a 4 point scatterer mixing model

four independent points, and the Poncelet property can be extended to the case of five independent points.

#### 4.3 for $N < 3$ points using one mechanism and general noise statistics

The previous modeling is not satisfactory to simulate resolution cells containing 1 to 2 types of scatterers, or to study the impact of polarimetric decorrelations regardless of power fluctuations. For this reason, we have also considered alternatives to be able to simulate the important cases of the one and two scatterer type.

*for one single point*

Let us first consider that the statistical population observed concerns only one physical type of targets, denoted by A. This is the case for bare soil. When only one type of bright point exists in the resolution cell, then the polarimetric scattering vector samples are simply written as:

$$\mathbf{k}_1^i = c_A^i \mathbf{s}_A^i = \mathbf{x}_A^i, \quad \mathbf{k}_2^j = e^{-j\Phi_A^j} c_A^j \mathbf{s}_A^j = e^{-j\Phi_A^j} \mathbf{x}_A^j, \quad (58)$$

where  $\mathbf{k}_1^i$  is one sample of scattering vector of the first image population, and  $\mathbf{k}_2^j$  is the corresponding sample of the scattering vector of the same population in the second image. In order to account for statistical fluctuation, we can simply assume that:

- vectors  $\mathbf{x}_A^i = c_A^i \mathbf{s}_A^i$  and  $\mathbf{x}_A^j = c_A^j \mathbf{s}_A^j$  are two samples of the same population of vector  $\mathbf{x}_A$ , classically described by the probability density function of a circular Gaussian vector with a zero mean [Lee et al. \(1994a\)](#), [Lee et al. \(1994b\)](#).
- the statistical distribution of the interferometric angle follows a normal distribution. In reality the theoretical distribution for the interferometric phase deduced from a Gaussian speckle pattern is more complicated but it has already been shown that the Gaussian distribution is a good approximation.

Once these variables have been generated, we are able to reconstruct sets of polarimetric scattering vectors  $\mathbf{k}_1$  and  $\mathbf{k}_2$  and create associated coherence matrices. As an example, three different coherence sets are represented in [Fig. 40](#). They have been generated using different coherence Wishart matrices  $\mathbf{M}_A = \langle \mathbf{x}_A \mathbf{x}_A^\dagger \rangle$ . This shows that this simple model allows us to describe coherence sets representing various cases that we encounter in practice on an image.

*for  $N=2$  points*

Due to the presence of overlays, we can find several cells on urban images that can contain two different types of bright scatterers, with different polarimetric

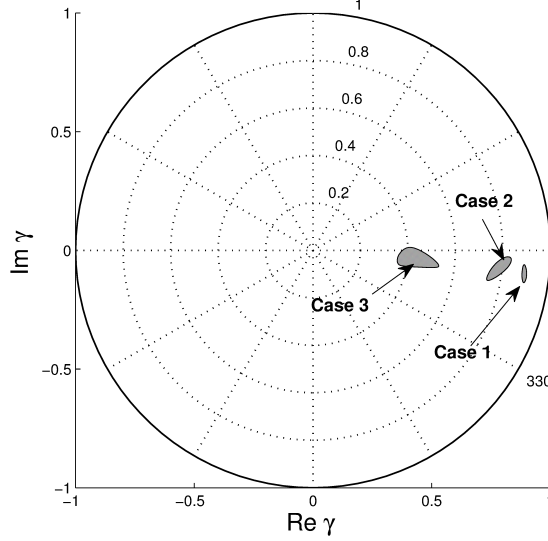


Figure 40: Coherence shapes for a 1 point scatterer model

behaviors and different elevations. The most frequent cases are superposition of the ground and diffraction by the roof, the ground and the scattering by the roof, or the strong double bounce echo and the scattering by the roof.

Now the mathematical modeling of the statistical population becomes:

$$\mathbf{k}_1^i = \begin{bmatrix} \mathbf{s}_A^i & \mathbf{s}_B^i \end{bmatrix} \cdot \begin{bmatrix} c_A^i \\ c_B^i \end{bmatrix}, \quad (59)$$

$$\mathbf{k}_2^j = \begin{bmatrix} \mathbf{s}_A^j & \mathbf{s}_B^j \end{bmatrix} \cdot \begin{bmatrix} e^{-j\phi_A^j} & 0 \\ 0 & e^{-j\phi_B^j} \end{bmatrix} \cdot \begin{bmatrix} c_A^j \\ c_B^j \end{bmatrix}. \quad (60)$$

Given that it seems difficult to envisage the polarimetric statistical fluctuation independently from the total power fluctuation, we can consider here that  $c_A$  and  $c_B$  are just deterministic parameters quantifying the mixture of two types of scatterers A and B. Thus, they can be viewed as a proportion rather than amplitude, and replaced by  $p$  and  $1-p$ , where  $0 < p < 1$ , and the model becomes:

$$\mathbf{k}_1^i = p\mathbf{s}_A^i + (1-p)\mathbf{s}_B^i \quad (61)$$

$$\mathbf{k}_2^j = p\mathbf{s}_A^j e^{-j\phi_A^j} + (1-p)\mathbf{s}_B^j e^{-j\phi_B^j} \quad (62)$$

We can still also assume the same distribution for the interferometric phase as in the previous section. Now we just need to define two statistical laws for the distribution of  $\mathbf{s}_A$  and  $\mathbf{s}_B$  vectors, using two covariance matrices

$$\mathbf{M}_A = \langle \mathbf{s}_A \mathbf{s}_A^\dagger \rangle \quad \text{and} \quad \mathbf{M}_B = \langle \mathbf{s}_B \mathbf{s}_B^\dagger \rangle. \quad (63)$$

Once this modeling has been assumed, it is possible to see that the corresponding coherence shape looks like an ellipse.

Different cases of similarity between  $\mathbf{M}_A$  and  $\mathbf{M}_B$  can be considered. It is possible to see that the more similar  $\mathbf{M}_A$  is to  $\mathbf{M}_B$ , the less we describe the angular diversity.

To conclude with this section, we have shown empirically that:

- A good way to model coherence shapes is to separately model the statistical laws of the various matrices or vectors used to parameterize our model: interferometric phase, polarimetric coherence matrices and deterministic relative powers.
- Statistical fluctuations on the power only allow the interest of maximizing coherence to be understood, but cannot account for the actual shapes nor model cell resolution containing one or two mechanisms only.
- The coherence shape corresponding to a two-mechanism resolution cell looks like an ellipse whose major axis is parallel to the segment joining the two interferometric phases of the mixture. This result has been used in (Cellier and Colin, 2006). In the case where fluctuations in phase are not too large, then the major axis of the ellipse intersects the unit circle on the two interferometric phases involved in the mixture.

Recent studies Cui et al. (2015) make use of this knowledge on coherence shapes. They show that research in this field for POLINSAR applications is still active. These theoretical results are also put to use in an inversion algorithm for building heights, presented in the last part.

The basic idea of three dimensional imaging algorithms is to form a second synthetic aperture in the direction of the translational movement. This direction, denoted as the normal direction, is perpendicular to the range and azimuth directions. This situation is achieved in the dual domain, by obtaining several slices of the reflectivity spectrum. For the case of airborne SAR, there are especially two kinds of acquisition that make it possible to obtain three dimensional images: the first one is the circular flight path, and the second one is the multibaseline flight path. The second one corresponds to the "tomographic SAR" and is the subject of this section.

The generalization of multibaseline interferometry is the tomography approach, which allows a resolution in the third direction. The resolution in the elevation direction depends on the elevation aperture size, i.e., on the spread of orbit tracks. Tomography or multibaseline Interferometry can be used for layover scatterer elevation separation, to locate different scatterers interfering in the same pixel.

3-D SAR focusing using tomographic processing of multibaseline interferometric data sets, may be considered as a spectral estimation problem. A wide variety of spectral analysis techniques can be used to perform tomography, ranging from classical Fourier-based methods to High-Resolution (HR) approaches.

At the stage of the technique, polarimetry has been investigated only as information *a posteriori* to compare the tomography obtained in the various polarization cases, or to analyze the data after 3D mapping. In this case, a fully polarimetric dual-baseline configuration improves the tomographic accuracy significantly, compared with single-polarization ones, in cases where the estimation in one single polarization is not the most adapted one. Polarimetry also provides additional information, related to scattering mechanisms, which helps building features, such as geometrical shapes, as well as dielectric properties, etc. to be better characterized.

However, polarimetry can also be used in a multibaseline optimization procedure [Neumann et al. \(2008\)](#). Comparisons between the various optimization algorithms are treated as an extension of the studies proposed in the single baseline case.

I followed these developments. Although today tomography is a line research that I have not had time to get involved in, I think that it is a topic of interest that should be considered. Today, the contribution of polarimetry to tomography usually comes after tomographic treatment itself, mainly for analysis purposes. I would advocate a tomography study in urban areas, in relation to any multipath that changes the associated interferometric phases, and which could be detected at the early stage of treatment, using polarimetry.

## SUMMARY

This third part has presented the main benefits of polarimetry for tridimensional aspects. It is based on the more in depth knowledge of PolInSAR acquired during my PhD thesis. This work has reinforced my expertise in this field.

- The first section contains more research ideas for the future than actual results. In particular, it offers perspectives on the use of polarimetry for navigation, and more generally on the orientation of surfaces.
- The second part deals with the modeling and mathematical properties of coherence shapes in PolInSAR, particularly for urban areas. From these properties, height inversion algorithms can be proposed.
- The last section opens up opportunities for subsidence and tomography studies.

## Part IV

### INVERSE PROBLEMS IN POLARIMETRIC IMAGES: FOREST AND URBAN

An inverse problem in remote sensing is aimed at converting observed measurements into information about the physical scene. Inverse problems deal with governing equations that relate the model parameters to the observed data. For radar images, it is related to inverse scattering and involves scattering simulation tools. This last part presents my contribution to research in this field, applied to forest scenes and urban areas.



## THE USE OF ELECTROMAGNETIC TOOLS FOR INVERSION

---

SAR data are potentially helpful for a wide variety of human activities, ranging from agriculture to rural and urban planning, disaster monitoring and assessment. However, practical use of these data is often limited by the lack of efficient, possibly unsupervised, tools for the retrieving of effective information. Then, analyzing, interpreting and anticipating SAR images requires support of appropriate electromagnetic modeling.

### 1 DIFFERENT TYPES OF SCATTERING MODELS. HOW TO CHOOSE ONE?

Modeling takes into consideration the radar geometry and the scene description. The choice of the types of algorithms to solve Maxwell equations and the way of describing the scene are the two important steps to define a simulation tool.

Let us detail the choices concerning the description of the scene. For example, concerning the way of describing forests, trees can be described as cylinders for the trunks and branches. However, it raises the question of how to distribute these cylinders. It can be either fractal, using realistic models of biological growth, or more randomly with statistical distributions. In reality, a model that seems realistic for a given application, for example biological growth, will not necessarily be the most appropriate for another application: the scattering of the electromagnetic wave. In other cases, some simplifying choices for scene description can be justified under certain assumptions that must be assessed. For example, a square base cylinder observed by a radar gives a mesh that can improve efficiency significantly for exact modeling computation in respect to the circular one, and is still representative for trunks when they are observed at very low frequency, as demonstrated in (Colin-Koeniguer and Thirion-Lefevre, 2010). A fractal distribution is not more effective than a uniform distribution, as has been pointed out by several studies in monostatic configurations, and as has been confirmed in (Thirion, Colin, and Dahon, 2006). We have extended this conclusion to the bistatic case in (Everaere, Colin-Koeniguer, Thirion Lefevre, and De Martino, 2012). In all cases, it is necessary to control the domain of validity of the approximations that are made in regard to the description of the scene, and to find the best compromise between the simplicity of the calculations and the validity for the application and configuration studied.

Let us now discuss the choices of algorithms to solve Maxwell equations. Simulation models must be sufficiently detailed to ensure high accuracy, but not so detailed as to preclude a numerical solution on real-world computers. Of course, the exact models take into account all scattering mechanisms, but

their computational complexity restricts their application to simple and small scenes.

Furthermore, it is important to determine the type of model outputs: should it be a description of the complex electric fields, a description of their temporal or frequency variation, or the synthesized SAR image?

## 2 A WAY OF INVESTIGATING: CROSS UNDERSTANDING AND VALIDATION

Generally, models are supposed to respond to a lack of real data in order to anticipate and predict the performance of post-processing algorithms. Meanwhile, models help to understand the underlying phenomenology in the signal. For example, they allow the different mechanisms present in resolution cells containing vegetation to be distinguished. However, the models themselves involve choices of different types:

- The way to describe the scene (a 3D triangular mesh model, or canonical elements such as cylinders).
- The way to describe materials.
- The way to describe how the sensor and the scene interact: raytrace, or rasterization.
- The type of physical approximations made, neglecting certain mechanisms when beyond the scope of exact modeling, since we want to improve the computation time.

Therefore, how justified are these approximations *a priori*? It is often a vicious circle, because simulators can help us to understand what phenomena are important to take into account. In order to answer to this apparent contradiction, Laetitia Thirion Lefevre from SONDRRA and myself have developed a research line using a modeling approach that simultaneously leads to the physical understanding and the validation of the model. This approach appears in several applications such as forest (Colin, Thirion, Titin-Schnaider, and Tabbara, 2004a), (Thirion-Lefevre and Colin-Koeniguer, 2008) and urban areas.

For the forest for example, we know that the exact models are constrained by the extent of the scene that they are able to simulate. Also, we used a coherent scattering modeling (COSMO) of vegetation developed by Laetitia Thirion Lefevre during her PhD thesis. This simulation tool describes the forest by means of a set of dielectric cylinders organized in several layers above a rough dielectric ground, representative of trunks and branches. For each cylinder it computes the direct scattering, the double-bounces implying the ground, and the triple bounce. It also takes into account the attenuation effects. However, this is an approximate tool that neglects the direct contribution of the ground, and neglects the multiple interactions between cylinders. This type of model has allowed us to go further in our understanding of the scattering by a forest than the more simplified models, such as that called Random Volume over Ground. In particular, it makes it possible to understand that:

- Most false alarms in forests are due to strong double bounce echoes between the trunks and the ground (Thirion and Colin, 2005).
- At P-band, the Random Volume over Ground model is insufficient to represent the influence of the layer of trunks. Also, the RVoG model was extended to an additional layer of trunks and associated FOPEN detection methods were developed (Colin, Cantalloube, and Dupuis, 2006a).
- The COSMO model allowed us to deduce the relationship between the height of the phase center of a forest measured by an interferometric radar, the attenuation coefficient, and the total height (Thirion-Lefevre and Colin-Koeniguer, 2007).
- In bistatic polarimetry, it has been shown that the contribution of trunks was predominant in the backscattering configuration, while the branches contributed mostly via simple diffusion in the specular direction.
- This type of model has also allowed us to understand that horizontal polarization is favored in the double bounce mechanism, because of the asymmetry of the Fresnel coefficients on the ground. Meanwhile, successive validations of the code were made from measurements in an anechoic chamber, first on an isolated cylinder, then on a group of up to six cylinders. As often as possible, comparisons were made between simulation results and actual SAR measurements.

Concerning urban areas, the collaboration continued between electromagnetic modeling and intended application, including target detection from multipath. This collaboration has been extended by the joint supervision of the PhD thesis of Azza Mokadem. In this thesis, the idea was to achieve the state of the art on all of the types of simulators that can be used, in order to choose the best one able to give us a way of:

- better understanding the mechanisms in this type of environment,
- anticipating configurations suitable for detection,
- both justifying or denying the approximations made by the considered model.

This thesis led to the following research approach: we chose to make scaled controlled measurements in an anechoic chamber. The first difficulty that we faced in the experimental part was that we cannot conduct an experiment with both a valid scale factor and far-field condition. Also, we conducted experiments without respecting the scale ratio to validate experimentally the exact codes, representative of all of the phenomena encountered. The frequency of application of these codes has been taken to the maximum computational capacity. Thus, at this limit scale, approximate codes such as MOCEM or Fermat could also be compared, and their ability to account for predominant full-scale phenomena could be proved.

In both application cases, forest and urban areas, the research approach was the same:

- Use exact modeling to understand the phenomenology of essential representative blocks for the representation of the scene (cylinder over ground for the forest, urban canyons for urban areas).
- Transition to higher frequencies.
- Propose faster simulators making approximations to the real frequencies for inversion purposes: a *Trunk and Volume over ground* for a forest, our own geometrical code *Urban Canyon* for the urban areas, or an extension of MOCEM to canyons.

In the following sections, the results for these two application frameworks, forest and urban, are detailed, with both experimental the approach and simulation studies.

Understanding the terrestrial carbon cycle and predicting future climate changes are important topics in climate research. One of the major uncertainties in the current carbon cycle models lies in terrestrial ecosystems, mainly forests. Rather than estimating forest carbon directly, biomass can be used instead since about half of biomass is carbon.

The forest being a dense object, the radar is an ideal tool for analysis, because of its penetration capabilities. Polarimetry has immediately been shown to be of interest for this type of environment, due to the presence of several orientation and geometric effects. Later the forest was the first medium studied with PolInSAR data.

## 1 POLINSAR FOREST INVERSION

The canopy height is a key parameter for describing forests since many studies have tried to link it to biomass. Also, interferometry allows the height of the scattering phase center of a forest to be calculated. However, this height is not directly the total height of the vegetation, because the wave penetrates the medium. Moreover, the elevation of this scattering phase center depends on the height found by polarimetry, and this is the key idea of PolInSAR.

In an attempt to model this dependence between the height of the vegetation, and the interferometric height found for the different polarizations, the model most used in the literature is the Random Volume over Ground model. During my PhD thesis, using the traditional methods of inversion for this model of forests at P-band, it turned out that the penetration at this frequency made the presence of trunks prevailing. Thus, I proposed to take into account a layer of trunks in the model in (Colin, Titin-Schnaider, and Tabbara, 2005c).

This kind of modeling is also used for FOPEN. Foliage Penetration Radar is a technical approach to find and characterize man-made targets under dense foliage, as well as characterizing the foliage itself. The algorithm proposed by S. Cloude for the detection of targets behind the forest, using a filtering of the RvoG model, has been adapted to our model of random volume and trunks successfully.

However, some questions have remained open. In particular, new measurement campaigns led in Sweden have shown that the detection of vehicles hidden in the forest was much more complex in this new area, particularly because of the density of the forest, and perhaps also the wet conditions. Moreover, it appears that the attenuation of the forest is the most difficult parameter to obtain by inverting a model. For this reason, we continued to explore the possibilities of these attenuation values with Laetitia Thirion Lefevre. We proposed a study on the link between extinction and height of the phase centers.



Figure 41: Scale equivalence principle illustrated to study forest scattering

We also have led a study about the statistical behavior of attenuation by simulation in (Thirion, Colin, and Dahon, 2006).

## 2 INVERSION OF BISTATIC POLARIMETRY IN FORESTS

The bistatic configuration has recently renewed the studies concerning forests, both for civilian and military aspects. For civilian aspects, the bistatic configuration leads to an additional degree of freedom by breaking the assumption of reciprocity. Also, the additional measured cross-polarization coefficient allows to a more promising inversion to be considered. For military applications, the idea is to choose a better acquisition geometry for detection, finding the one for which the ratio between forest and target signals is maximized.

The lack of real data is the main difficulty to conduct these studies. Concerning bistatic SAR data, there are only a few stationary measurements with parallel trajectories, which therefore offer a limited potential in terms of geometry cases. Bistatic acquisition performed at X-band is not the band of interest for penetration capabilities. Finally, bistatic SAR data conducted over a forest between ONERA and FOI are not polarimetric.

Also, my studies have mainly relied on two types of data:

- data at the scale of anechoic chambers,
- data at the optical scale.

This last point, initiated during the PhD thesis of Nicolas Trouvé, is the subject of the PhD thesis of Etienne Everaere. This original principle of scale equivalence between nanotube forests and real forests is illustrated in Fig. 41.

Meanwhile, the simulation tool COBISMO, an extension of COSMO suitable for a bistatic situation continues to be used in the process discussed previously:

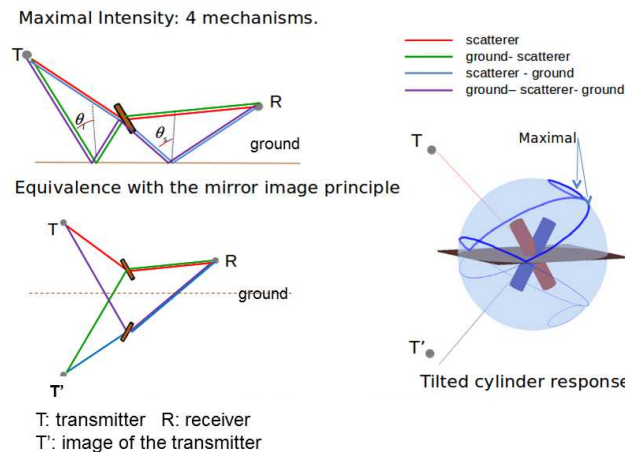


Figure 42: The maxima of intensities in the forest are explained by the cylinder return and the mirror principle

it is a tool both to develop our understanding of the forest, and to deepen the validation of the tool.

A first validation phase was conducted in parallel to the LORAMBIS campaign on simple and controlled elements measured in an anechoic chamber. Groups of metallic cylinders have been measured, as military vehicles scaled from their CAD.

During this contract, I was able to show that when we consider only the trunks over ground without interaction between them, the optimal geometric configuration for detection is a configuration with a bistatic angle lying in the incidence plane. The value of the optimal angle depends both on the wavelength, and on the ratio of the heights of the target and the height of trunks. For the low frequency at 250 MHz, and a classical trunk height of 10 meters, this optimal bistatic angle is around twenty degrees. At 400 MHz, the optimal angle decreases to about ten degrees. These configurations are found using simulations of forests with the COBISMO tool, and bistatic indoor measurements for the military vehicles.

Meanwhile, these simulations have helped us to understand the bistatic scattering of the main components of forest, and cylinders, and the type of mechanisms involved: simple scattering, and bounces involving the ground. In the bistatic configuration, double bounces mechanisms differ according to the order of the impact of the element itself and the impact on the ground. Using simulations on cylinders, we are able to predict the receiver positions where the returned energy will be maximum. For a single cylinder, the maximum energy is located on a cone whose aperture angle is the angular difference between the incidence direction and the cylinder axis. The mirror principle enables us to understand the maximum return as a superposition of single mechanisms. The maximum power for one cylinder above the ground is repre-

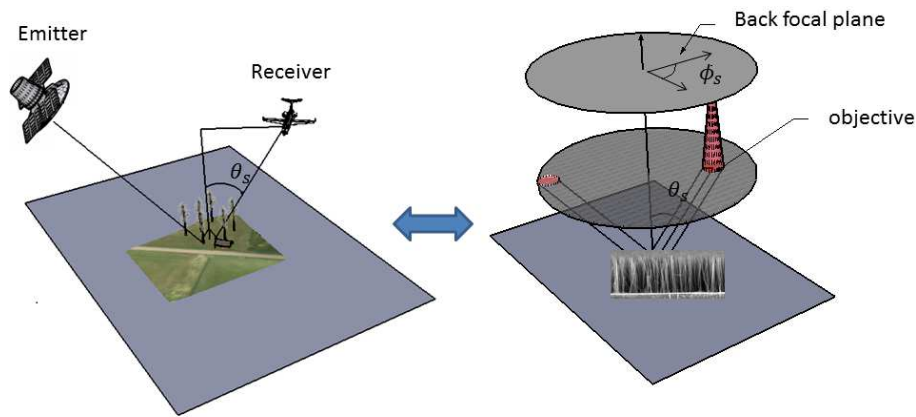


Figure 43: Convergence between a bistatic radar measurement and an optical device to study forest scattering

sented on the half reception sphere, in Fig. 42. The pattern comprises a set of circular rings, each corresponding to a particular mechanism.

In order to improve the search for an optimal configuration, we have also taken into consideration the effects of attenuation according to the bistatic angle. In this context, the COBISMO tool may be insufficient because it neglects the interaction between branches. While this approximation was shown to be realistic enough to reproduce many cases of monostatic measurement, we cannot be sure that it remains valid in the bistatic configuration. Also, realizing sufficiently dense scaled targets in an anechoic chamber is tricky. Nicolas Trouvé initiated an attempt to do so, with a forest of nails measured in an anechoic chamber, as presented in (Trouvé and Colin-Koeniguer, 2009). However, to go further, the complexity related to the increase in the number of elements is binding.

In order to answer this issue, the use of an optical device has led to significant advances. The measurement tool used and developed in collaboration in the LPCIM has the following advantages:

- it enables rapid use and lower cost, compared to radar measurements
- it offers a variety of bistatic geometries: for a given position of the emitter, the signal is collected for all receiver positions, as represented in Fig. 43.
- Various scenes, performed using nanotube forests, can be varied in their descriptive parameters. For example, several nanotubes forests used for our study are pictured in Fig. 44.

These measurements have led to a better understanding of a number of points:

- Deterministic polarimetric parameters are well reproduced by simulation by COBISMO, for sparse forests, corresponding to standard forests of trunks, as presented in (Thirion, Colin, and Dahon, 2006).

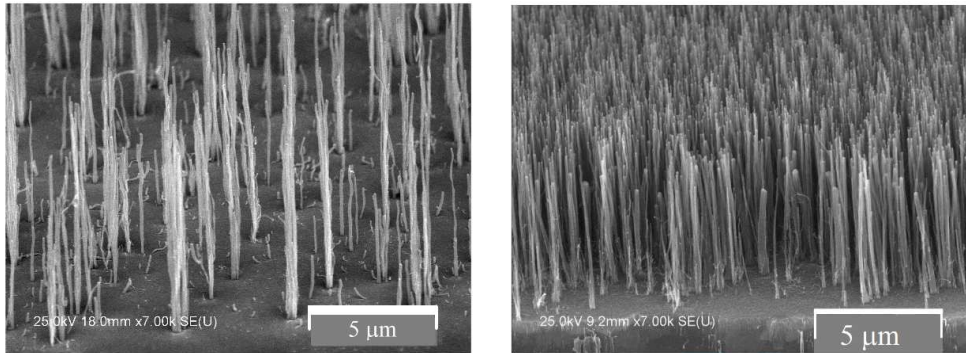


Figure 44: Pictures of two Carbon Nanotube samples measured for analysis. On the left, the so called sparse forest and on the right the so called dense forest. The length of the CNT is around  $l = 7.5 \mu\text{m}$  and the ratio is  $l/\lambda = 12$

- Some behaviors that we had already predicted by the simulation of the forest are well reproduced:
  - The intensity has a local maximum for the monostatic configuration, and an overall maximum for the specular configuration, as already predicted in (Thirion-Lefevre, Colin-Koeniguer, and Dahon, 2010).
  - The double bounce effect predominates in the monostatic configuration and the simple scattering effect is dominant in the specular direction.
- For very dense forests, corresponding to densities of branches, the comparison becomes more difficult. We have recently understood with the help of Antonello de Martino (LPICM) that non-deterministic effects are due to the angular integration of the various multipaths between elements of the scene. If we consider the angular variation of the receiver only for the simple scattering of a set of vertical cylinders on a horizontal surface, it is thus not sufficient to cause depolarization. This is why CO-BISMO is not able to find the level of measured depolarization. On the contrary, it appears that while the angular diversity and multipath are now included, in this case we would obtain a significant depolarization. Multiple interactions have the effect of creating disorder in the directions of the resulting mechanisms.

This leads to probably one of the important findings of this research: the consideration of interaction effects between cylinder scatterers is probably a key step to be able to predict levels of depolarization in bistatic geometries.

Moreover, this line of research still offers many opportunities for the future:

- The actual determination of the appropriate geometry for FOPEN or inversion purposes.
- The measurement of scenes of nanotubes that are more representative of whole trees, with branches. Recent developments for the growth of

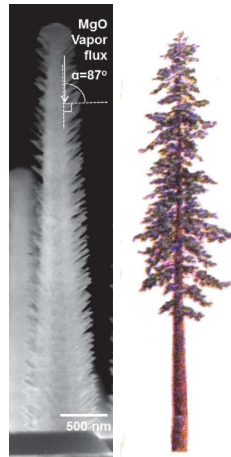


Figure 45: nanotube forest for sequoia

vertically arrays of nanotubes could be used for more complex targets, as proposed by Costel Sorin Cojocaru in LPICM, and as pictured in Fig.

45

- The encoding of multiple interactions in order to be able to predict depolarization effects. This depolarization parameter seems a very promising one for the inversion of parameters such as density of the forest.

In the context of rapid global urbanization, urban environments represent one of the most dynamic regions on earth. Even in developed countries the yearly conversion of natural or agricultural space into residential, industrial or transport areas frequently exceeds 100 ha. The current increase in population has resulted in widespread spatial changes, particularly rapid development of built-up areas, in the city and the surrounding area. Due to these rapid changes, up-to-date spatial information is requisite for the effective management and mitigation of the effects of built-up dynamics. Various studies have shown the potential of high resolution optical satellite data for the detection and classification of urban area. Nevertheless optical satellite imagery is characterized by a high dependency on weather conditions and daytime. Thus, particularly in case of regional and national surveys within a short period of time, disaster management, or when data must be acquired on specific dates, radar systems are more valuable.

Thus, the new generation of civil space borne Synthetic Aperture Radar (SAR)-Systems with short revisit times can serve as a valuable instrument. Promising approaches towards the classification of urban areas include the analysis of multipolarized image analysis.

Unfortunately, we have already seen that SAR sensors using the polarimetric mode often have degraded resolution. However, to ensure detailed mapping of urban structures, we need high ground resolution. Therefore, the emergence and recognition of urban remote sensing appears to be linked to the continuous improvement of the spatial resolution offered by generation sensors. This is why, in order to evaluate the benefits of polarimetry in the urban areas, we have tried to use the satellite data with the best achievable resolution for urban environment, which is often achieved today by X-band systems.

The polarimetric analysis of urban images in this band is still almost unexplored. Over the past years of research, the first data analysis showed that at this small wavelength, polarimetric analysis of urban environment starts to be particularly complicated. Indeed, urban areas are a spatially complex mixture of many scatterers whose electromagnetic and geometric properties are varied, and have to be understood at the wavelength scale.

During my research, and more specifically since 2011, I have studied polarimetric SAR images of urban scenes for at least three different applications: the first one concerns the detection of built-up areas, the second one concerns building elevation, and the final one concerns the study of urban canyons and the potential of multipath for detecting targets not in the line of sight of the radar.

## 1 DETECTION OF BUILT-UP AREAS

The contribution of urban polarimetry can be justified by the diversity and complexity of the interpretation of the different mechanisms involved. Briefly, the recorded observations are summed up by the scatterings from the targets on the same wave front. For example, the layover areas contain the scatterings from the roof, wall and ground. A mixture of volume scattering by vegetation and double-bounce scattering from buildings can also be observed in low density areas. The total scattering is strongly influenced by the looking directions and the alignment of structures: man-made structures that are arranged perpendicularly to the illumination direction increase the oriented double bounce contribution. In order to use polarimetric parameters within the framework of built-up area detection, four main features of polarimetric analysis in the context of urban areas can be used:

- The first one is that polarimetry is able to distinguish between deterministic or man-made targets and non-deterministic or natural targets.
- The second one is that built-up areas contain a lot of orientation effects that induce a non-zero polarization orientation angle. This polarization orientation angle is defined by the angle of rotation about the line of sight. It has been shown that the polarization orientation angle shifts are induced either by dihedral effects between the ground and a vertical wall not aligned in the along-track direction, or by tilted roofs.
- The third one is that double bounce effects between vertical walls and the ground often produce very strong echoes in the SAR image. On the UAVSAR polarimetric image in Fig. 46, these double-bounce echoes are visible. Due to the worse resolution on TerraSAR-X, they cannot be distinguished. However, we can hope to separate these double bounce effects from the others, by using physical decompositions, such as Freeman-Durden or Yamaguchi decompositions.
- The last one is the lack of azimuthal symmetry. This implies that correlation coefficients between cross-polarization and co-polarization are not equal to zero, contrary to flat surfaces or vegetated areas.

Tested over the TerraSAR-X images of San Francisco, all of these features have failed to correctly detect built-up areas, for several reasons.

- At X-band, the conventional polarimetric parameters of second order (entropy, depolarization) do not behave in the same way as in the previous images acquired at lower frequencies: AIRSAR at L-band, RADARSAT-2 at C-band. More precisely, it appears that entropy remains very high on all of the pixels considered.
- All physical decompositions such as Yamaguchi and Freeman-Durden, fail as soon as the disorientation effects increase, as in the SOMA district,



Figure 46: Double bounce echoes visible on UAVSAR polarimetric images

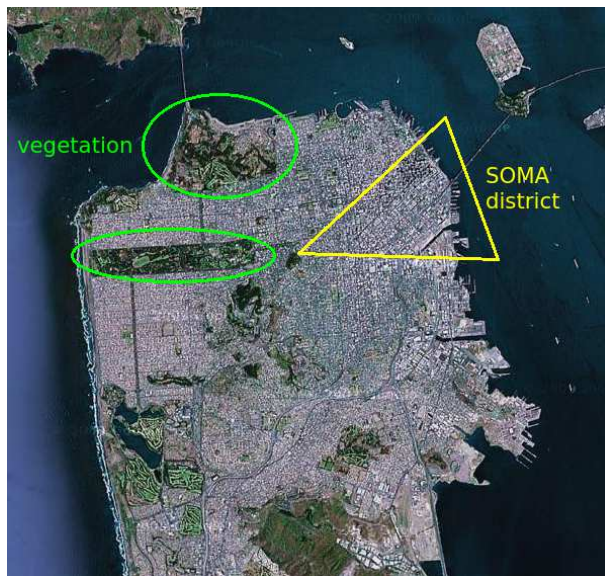


Figure 47: Optical image of the San Francisco test site. The SOMA district is indicated in the yellow triangle.



Figure 48: Entropy in the first polarimetric image of San Francisco: AIRSAR

indicated in Fig. 47. In this case, the medium becomes random and decompositions are not able to separate the different effects. In the same way, polarization orientation angle shifts induced by surfaces with buildings that are not aligned in the along-track direction are very noisy and their estimation becomes irrelevant.

Conventional polarimetric parameters, such as double bounce powers, have all failed to provide a correct classification in a specific area, for all of the images viewed from different sensors. This area is called the SOMA district in San Francisco, and contains many sky scrapers. Moreover, entropy of the image is very high over the whole image.

Looking more carefully at the classification results previously published on San Francisco with other sensors ALOS, AIRSAR and RADARDAT, it turned out that all polarimetric classifications in this area fail. For example, in Fig. 48 we see that the triangle corresponding to the SOMA district has the same entropy as the vegetated areas.

Orientation effects related to this area on the polarimetric response have been identified. Given that this area has an orientation far from the axis of the sensor, it was subsequently shown that the level of HV return is high. It is thus necessary to perform a disorientation in an attempt to reassess these canonical mechanisms in a way that removes the orientation effect. However, this operation is rendered ineffective, mainly because this area has very high entropy, therefore it becomes impossible to make a reliable assessment of the orientation angle and an effective correction.

Also, we summarize our approach to confirm our answers to two different questions:

- Why is the level of entropy high over our entire TerraSAR-X image?
- Why is the level of entropy high in this particular SOMA district?

Several assumptions can be made to answer these questions. For the first one: high entropy in TerraSAR-X images is due to the relative noise of the sensor, or it is due to the degree of complexity of the scene, compared to resolutions, to pixel sizes, and/or to wavelengths.

For the second one: the high entropy of SOMA relates to the complexity of the area which contains many buildings and possibly multipaths, or the high entropy of SOMA mainly relates to the orientation of the streets.

We managed to invalidate the initial assumptions and to confirm the second ones, by using:

- electromagnetic simulations on urban canyons and the influence of multipath, within the framework of the PhD thesis of Azza Mokadem,
- statistics simulations on resolutions and pixel size, within the framework of the PhD thesis of Flora Weissgerber,
- analysis of available images and search for new ones (UAVSAR).

A comparison of all entropy maps thus obtained is given in Fig.49.

This comprehensive study allows us to reach the following conclusions:

- Entropy is obviously affected by the thermal noise of the sensor. However, this influence is less compared to the following two other influences: building orientation and cell size resolution.
- Disorientation in urban areas is not only accompanied by an increase in the cross pol signal, but also an increase in entropy. This means that disorientation leads to mixing the mechanisms randomly, and it is impossible or at least very difficult to correct the effect of disorientation in order to isolate the double bounce component: even if we are able to highlight the presence of this effect, other mechanisms involved remain mixed in the resolution cell. This leads to common misclassification results, even with disorientation algorithms.
- High entropy in urban areas is strongly linked to cell resolution size. For a given wavelength, at L-band, entropy remains low when resolution is poor. Entropy increases with improved resolutions, probably because the spatial variability of polarimetric behavior is more important. For large resolution cells on the contrary, the behavior is more stable from one cell to another.

Once the difficulty linked to the TerraSAR-X polarimetric parameters is better understood, we turn to the initial problem of the best approach to detect built-up areas in this image. Special care has been given to the quantitative performances of the various parameters used for detection. In order to quantify the contribution of polarimetry for building detection, we plotted ROC

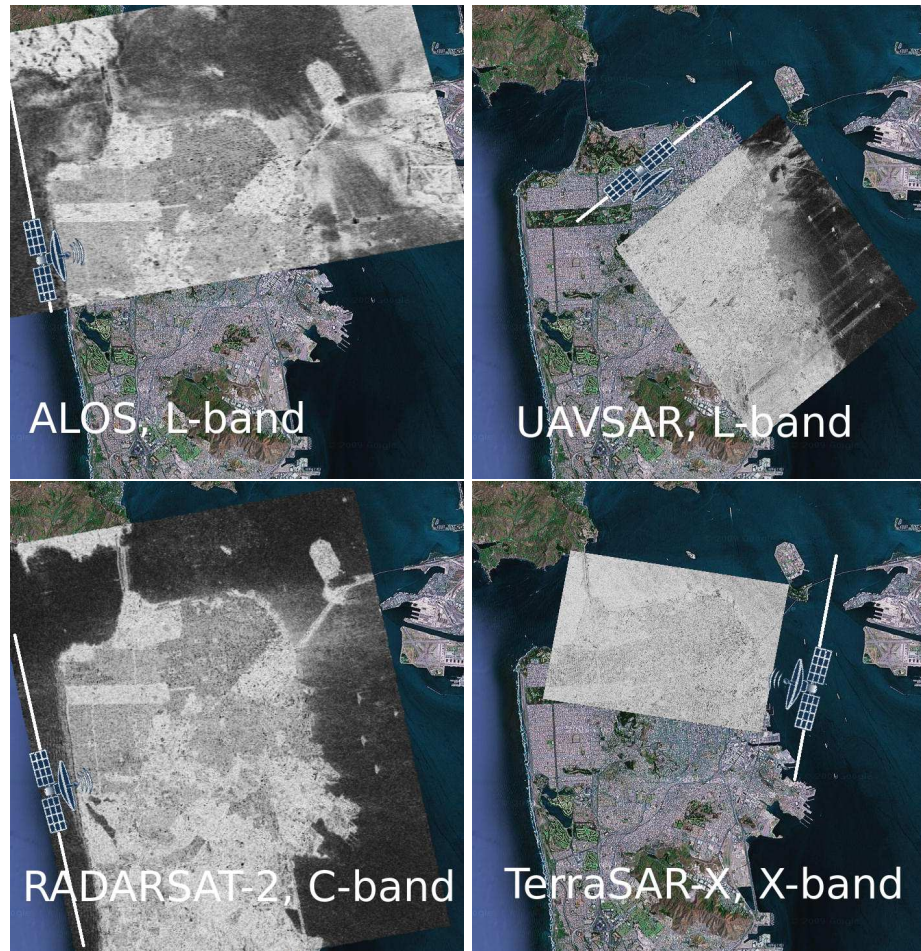
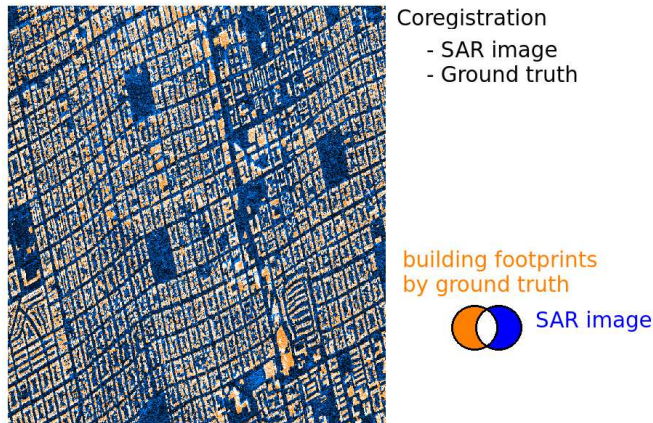


Figure 49: Comparison between the Entropy of various polarimetric images



Resulting map for evaluation of detection algorithms:

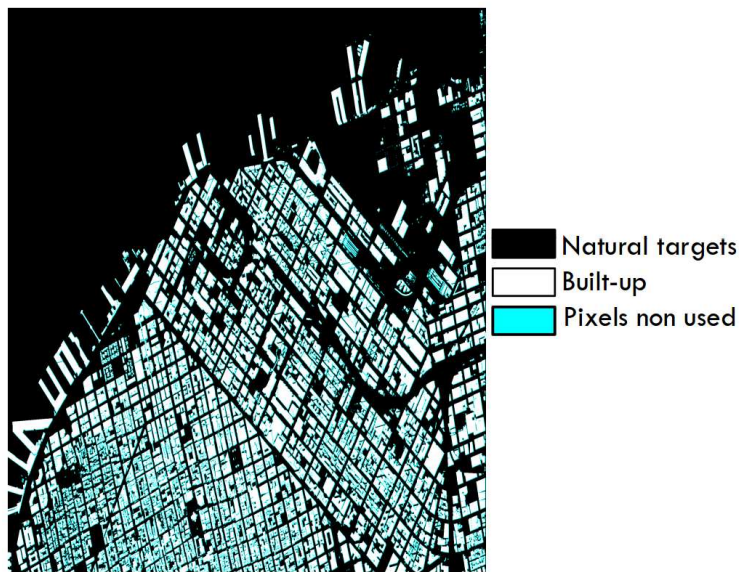


Figure 50: Constitution of a ground truth for classification performance evaluation

(Receiver Operating Characteristic curve) curves that are a plot of the true positive rate against the false positive rate for the different possible cut points of a diagnostic test.

These curves analyze the efficiency of using various input parameters and various distances between the two classes defined by the ground truth, built-up and natural areas. The closer the curve follows the left-hand border and then the top border of the ROC space, the more accurate the test is. Distances between the two classes have been calculated using different parameters: entropy, Yamaguchi double bounce components and the various polarimetric correlations existing in case of non-symmetry. Concerning the ground truth required for this evaluation, a dedicated one has been produced, using a shapefile describing building footprints and their elevation. In order to use this file ground truth to evaluate the performance of different classifications, the coordinates of the buildings were converted into TerraSAR-X longitude-latitude, the height of buildings was taken into account, and each of the masks was recalculated in

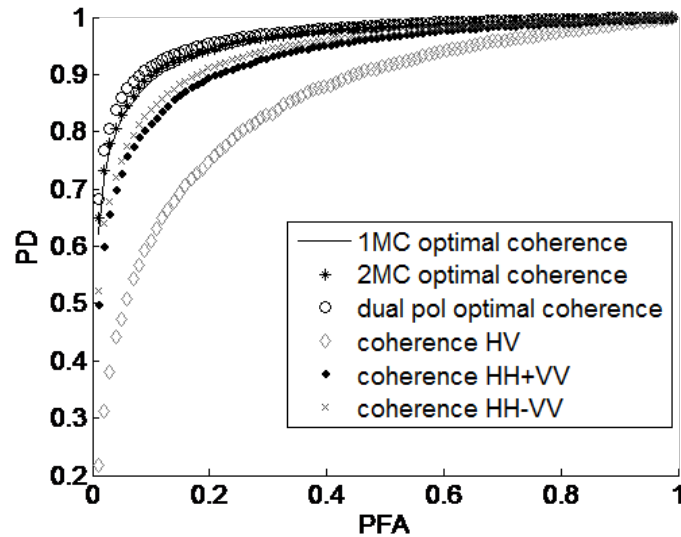


Figure 51: ROC curves for the performance of various interferometric coherences for detection.

the repository sampling of the image. As a precaution, the pixels on the edges of the buildings were not taken into account. Others allow us to define two classes: buildings and outdoor environment. An extract of the Ground Truth thus generated is given in Fig. 50.

These curves clearly show that the best discriminating parameter among those tested is the Yamaguchi double bounce component. However, we must keep in mind that the Yamaguchi parameter does not only depend on the polarimetric content, but also on the powers. When we compare this parameter to the polarimetric intensity channels, we see that it is always less efficient than the polarimetric amplitudes. This proves that polarimetric parameters that are independent from the span (entropy, correlation) do not improve the results found by intensity alone to identify built-up areas.

Since at X-band, the traditional polarimetric parameter fails to identify man-made targets, we propose to use polarimetry contribution to a repeat pass interferometric mode. Indeed, the temporal decorrelation will be very high in this frequency band, because it will be sensitive to displacements of the order of a few centimeters. Thus, the interferometric correlation image exhibits a much better contrast than the intensity image between natural and artificial targets. Again, ROC curves clearly show the benefit of using interferometric coherence for discriminating buildings, at least with HH and VV polarization. Thus, the benefit of polarimetry has been considered through the use of a coherence optimization. The ROC curves shown in Fig. 51 also show that the contribution of polarimetry to optimization allows the detection performance to be improved regardless of the type of coherence optimization.

The solution proposed is therefore to use optimized repeat-pass coherent polarimetry as an essential criterion for an unsupervised 2-class classification that will eventually be improved by shape criteria extracted from the span

image. Detection results of this parameter are represented as a binary map in Fig.52.

## 2 3D RECONSTRUCTION

3D rendering is a logical extension to the classification of buildings proposed in the previous section, to enrich the data necessary to monitor the growth of the urban extension. However, it can also be considered as part of the diagnosis of urban areas after natural disasters such as tsunamis or earthquakes. Natural disaster monitoring and the evaluation of their effects is a complex problem in urban areas, because a lot of parameters can be investigated. Areas of significant changes can be detected making use of high-resolution satellite data, areas where a 3D model can be established on a large scale by interferometry. In this context, the contribution of radar is its immediate use regardless of weather or smoking out due to fires.

The interferometric phase is related to the elevation of the scatters. The quality of its estimation depends mainly on the conditions of acquisition:

- The ambiguity height, corresponding to a phase variation equal to  $2\pi$ . Phase is defined only for modulo  $2\pi$  radians, so the resulting elevation map is wrapped with respect to some modulus or ambiguity. If the ambiguity height is too high, as for UAVSAR images over San Francisco, then the precision on height is not sufficient to estimate building elevation. If the ambiguity height is on the order of 50m, as for TerraSAR-X images, then the precision in regard to the height becomes sufficient. For example, in 53 we can see that the double-bounce echo has a different elevation than the roof. However, it is necessary to perform phase unwrapping: for high variations of the relief, or for high buildings, several wrappings of the phase are clearly visible, as shown on the right.
- Temporal decorrelation: the loss of coherence depends strongly on the wavelength and becomes critical at X-band. Thus, still on repeat-pass TerraSAR-X images, coherence is too low on the ground to be able to estimate the ground elevation.

We have already seen that polarimetry combined with interferometry, can improve the product of the latter, either by separation of scattering phase centers, or by improving the interferometric correlation map, by enhancing its value and reducing the noise level of the interferometric phase. I have investigated these two aspects.

For the separation of phase centers, the goal in urban areas can be to obtain the ground height jointly with the elevation of the roof. Within this framework, the benefits of polarimetry are often compared with the benefits of pure technical image processing. The results of techniques for phase separation will obviously depend on three factors:

- The resolution of the images. This is even the essential criterion. Indeed, if the resolution is low, a vertical wall will be found synthesized into

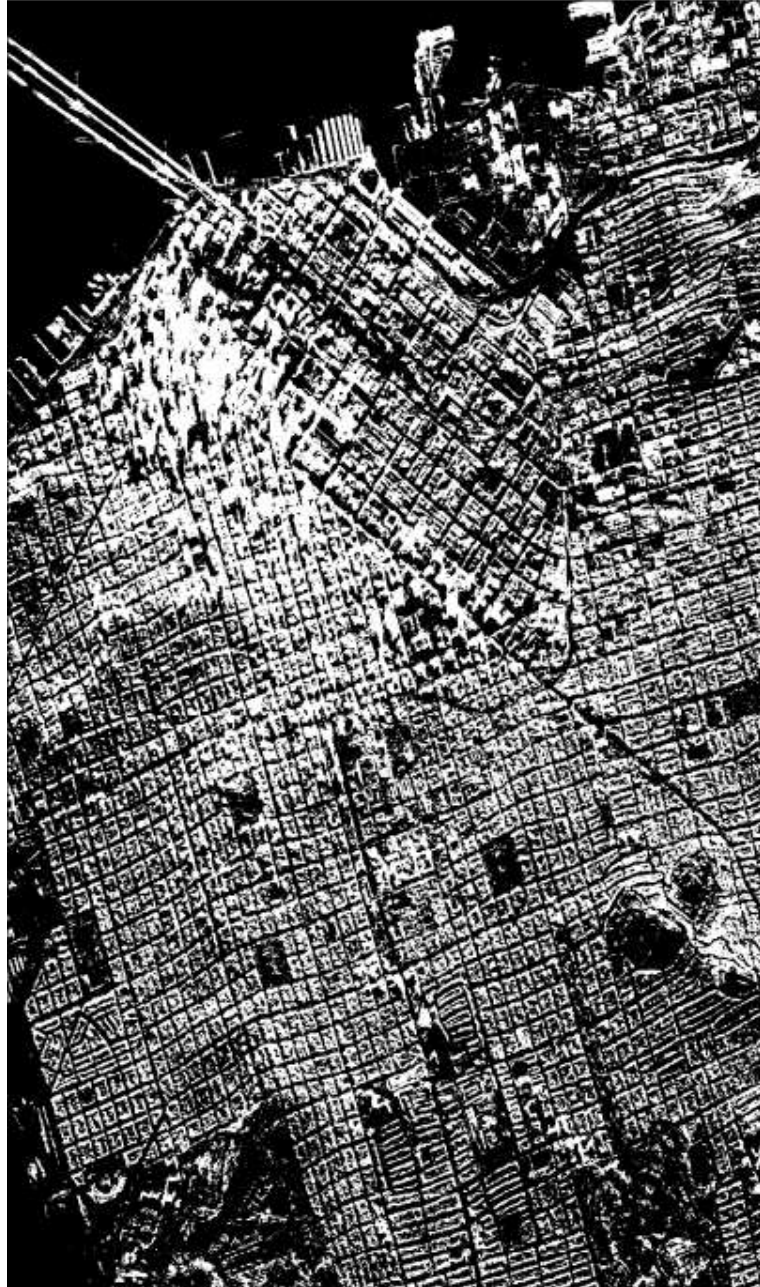


Figure 52: Built up area detection

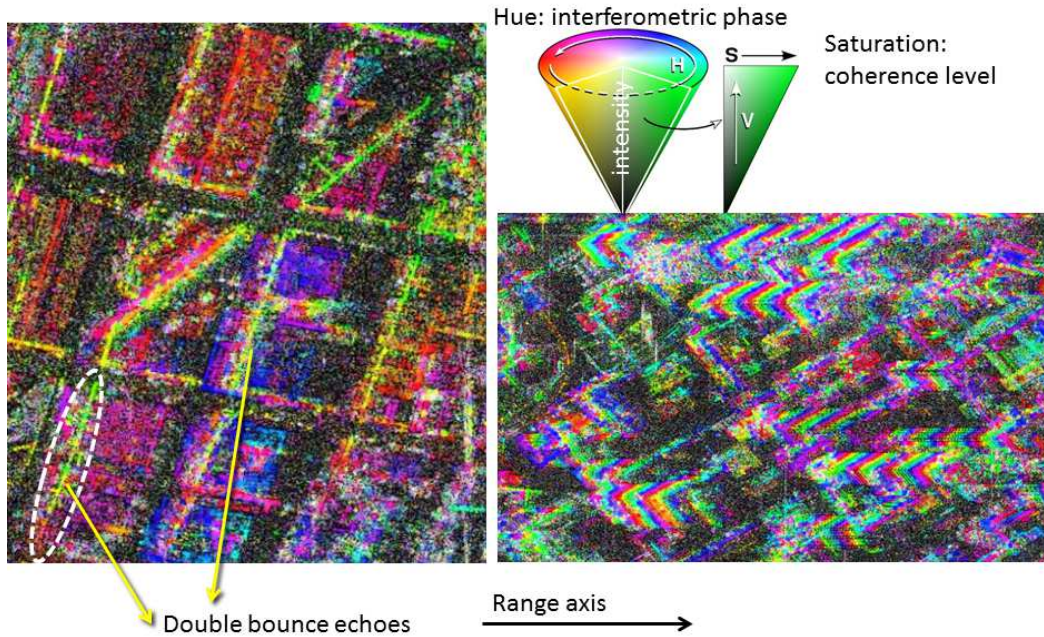


Figure 53: Two extracts of a repeat-pass HR interferogram of TerraSAR-X

a single resolution cell. This wall will include several scattering centers, and potentially different polarimetric returns with different heights will therefore be mixed.

- The frequency. At low frequencies, the wave will not necessarily be sensitive to details. Thus, even a large resolution cell will see a limited number of mechanisms.
- The ambiguity height for the interferometric process, as already pointed before. The distribution of heights observed depends on this parameter: if the ambiguity height is small, then the angular diversity of the generalized coherence will be very important.
- The temporal decorrelation. We have seen that at X-band, the temporal decorrelation of the images is very fast. Particularly in the resolution cells of the San Francisco images containing layover phenomenon, it is clear that the phase of the roof is mixed with the ground phase. However the ground seems to induce a high decorrelation in the mixture and therefore its elevation cannot be estimated satisfactorily.

Thus, concerning the TerraSAR-X images of San Francisco, if the estimate of the height of the roof is possible, at present we have no satisfactory estimate of the height of the associated ground. Our conclusion is that at X-band, it is necessary to have single pass data or very small temporal baselines to be able to provide a 3D rendering over the entire image.

Still at X-band but using single pass POLINSAR images, we have proposed an algorithm to recover the respective heights of the roof and ground from

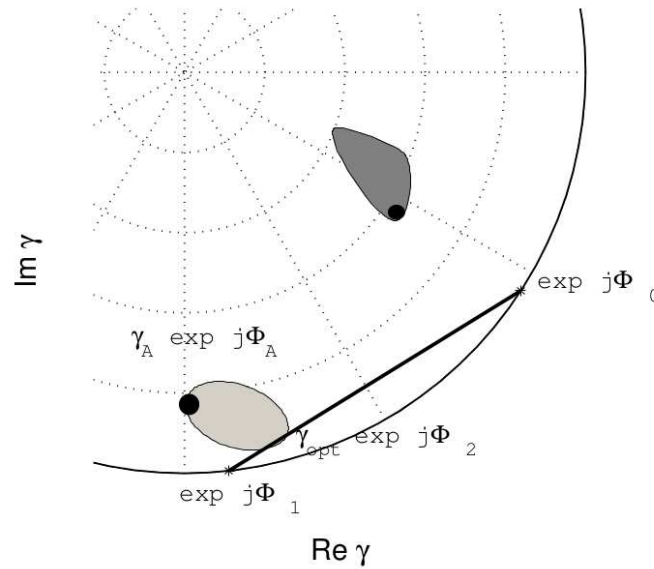


Figure 54: Algorithm to inverse building heights through the coherence shape

their coherence shapes. We have seen in Chapter 3 that in layover areas, the coherence set corresponding to the top of the roof mixed with the ground is a narrow ellipse. If the noise of the interferometric phase is low, then the major axis of this ellipse will intersect the unit circle in the interferometric phase of the roof and the interferometric phase of the ground. However, most of the time, the ground alone is not necessarily visible, or its interferometric phase can be noisy. Thus, the extension of major axis of the ellipse is not always sufficient to ensure a robust regression. Another issue is that it is not uncommon, even in layover areas, for the polarization diversity in the roof pixels to be insufficient to estimate the relevant information on the ground. Moreover, we were also interested in solutions that remain robust even when the pixels selected are not located in the layover area. This is why it seems more appropriate to use the information of both coherence shapes: that associated with the bare ground pixels, and that associated with the roof pixels. In order to estimate the interferometric phase of the ground, the solution of the optimized coherence seems relevant, since it has already been demonstrated that it is a good way to estimate the elevation of one resolution cell containing only one type of scatterer by reducing the noise level. This optimization enables us to find the point  $\exp(j\phi_0)$  where  $\phi_0$  corresponds to the interferometric phase of the ground. This point is represented in Fig. 54.

The optimal coherence linked to the ground alone is also used to make a more robust linear regression of the ellipse in the layover area, especially in the case where the angular range observed is rather limited. Practically, we superimpose the two representations: the first coherence set related to the ground, and the second one related to the roof of the building. Then a line is drawn between two points. The first point is on the unit circle and its phase is the phase of the optimal coherence of the ground. The second point is the

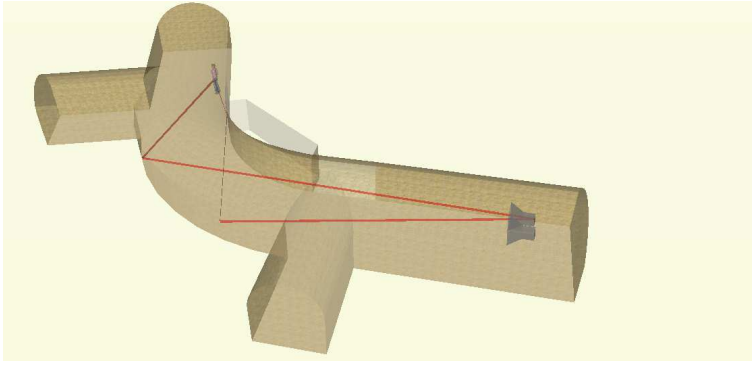


Figure 55: Caponier corridor

optimal coherence of the roof. The intersection of the line joining these points with the unit circle corresponds to  $\exp(j\phi_1)$ . The total height is deduced from  $\phi_1 - \phi_0$ .

This solution has been shown to be effective in many cases encountered. It has been tested on 140 buildings of a Toulouse POLINSAR image. It is the subject of the paper ([Colin-Koeniguer and Trouvé, 2014](#)).

### 3 URBAN CANYONS

In our analysis of entropy effects, probably related to the presence of complex multipaths in urban areas, we discussed the modeling of urban canyons. It was the central point of the PhD thesis of Azza Mokadem, the aim of which was to know whether vehicles or other types of targets placed in the shadow of buildings could be detected by multipath. Note that this detection problem in urban canyons, is not unconnected with the general problem of detecting a vehicle by means of a radar behind a crossroads. I have been able to address this issue by participating in an experiment set up in an underground corridor, for detecting a pedestrian by multipath returns induced by the vertical walls, as shown in Fig. 55.

In order to address the problem of detecting a target in urban areas in a SAR image, we had recourse to experiments, but also simulation tools. Many tools relating to electromagnetic propagation through an urban area exist already. Thus, the aim of the thesis was not to develop one of these simulators, but to determine which could help us to answer the question regarding detection.

Meanwhile, the same approach as for the forest was implemented: cross validation of the codes, and parallel understanding of the urban environment.

Various codes have been considered:

- A code dedicated to the propagation for Telecommunications: Wireless Insite, developed by Remcom.
- A modeling code of SAR images, dedicated to vehicles: MOCEM developed by Alyotech and led by the DGA.

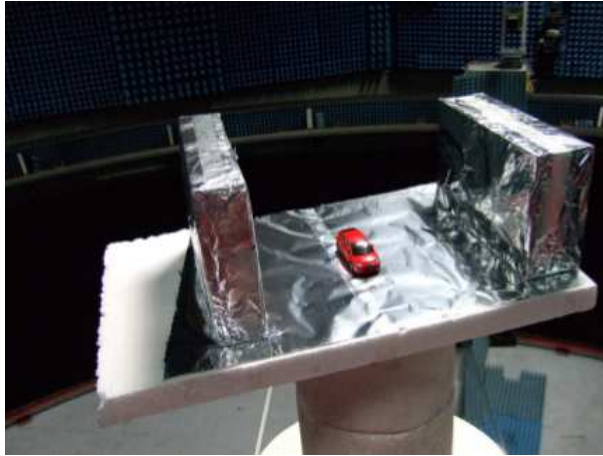


Figure 56: Picture of the scaled measurement performed in the anechoic chamber BABI at Onera

- Exact modeling EM codes: ELSEM 3D at Onera and FEKO, a commercial code.
- An asymptotic model: Fermat, an Onera-Oktale code.

Conducted in collaboration with SONDRRA, this PhD thesis has resulted in several measures of PEC urban canyons in an anechoic chamber. The first measurement was carried out full-scale but under near-field conditions, at the NTU (Singapore). A second measurement, pictured in Fig. 56 was performed under far-field conditions, but without complying with the scale ratio in the BABI anechoic chamber at Onera.

This measurement confrontation places us directly before the first validation problem: it is impossible, given the dimensions of existing chambers, to ensure both the scale ratio and the far-field condition.

Near-field range profiles of a canyon were theoretically analyzed, especially during the internship of Nicolas Sar. This complex range profile consists of several equally spaced peaks, associated with different responses, all explained by specular multipath involving the vertical plates or the ground, and arising for different numbers of bounces permitted by all incidence angles covering the opening of the canyon. One example of such a range profile measured in an anechoic chamber is given in Fig. 57. The presence of target results, according to geometrical conditions, in additional peaks.

A first set of simulations with FEKO conducted by Sophie Langlet at the DEMR showed that, even under far-field conditions, although the angle of incidence can be considered unique, a large number of peaks can always be found in the range profiles for certain scale ratios of the canyon. This fact has been confirmed by measurements in the BABI anechoic chamber. Once again, the different peaks present in range profiles are explained by the different paths involving different numbers of bounces, but these different numbers of bounces are achieved by considering the scattering of the plates outside the specular direction. In this case it is not the diversity of incidence angles that

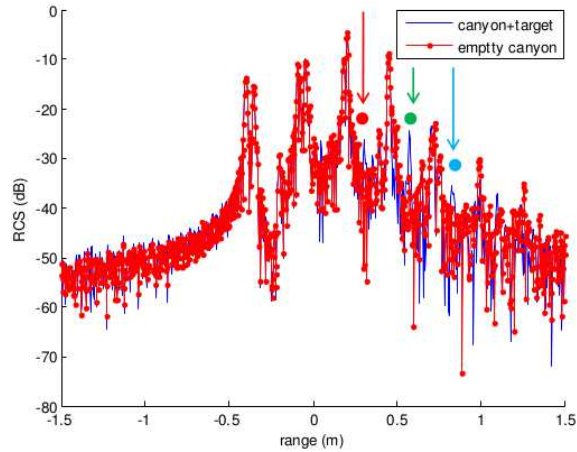


Figure 57: Measurement of the empty canyon range profile

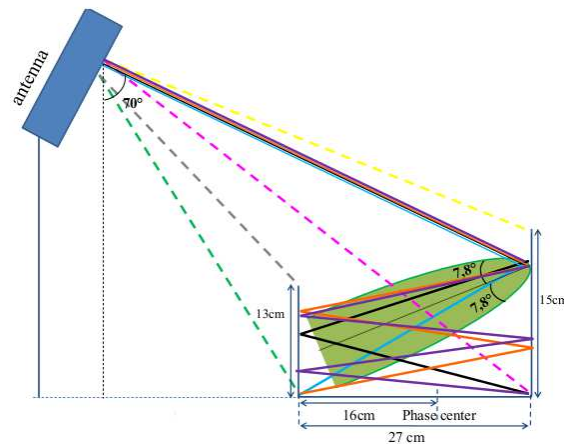


Figure 58: The various peaks present in a range profiles are explained by different paths involving different numbers of bounces

explains many peaks, but rather the widening of the main specular lobe of the return of a plate, when the dimensions of the latter are not large enough in comparison to the wavelength. This is represented in Fig. 58.

Thus, we find the same difficulties for validating a simulation tool in a real case, with the scale ratio, and the far-field condition.

The computation time of the exact codes becomes much too long when the frequency is increased. Therefore, during the PhD thesis of Azza Mokadem, this type of code was used to validate the experimental measurements scaled at a low frequency. As an example, in Fig. 59, two different simulation methods, the temporal one and the Methods of Moments, are able to reproduce the indoor measurement.

Then, the frequency was increased to observe the gradual decrease of the amplitudes of the secondary peaks, approaching a predicted range profile by a very simplified simulation tool.

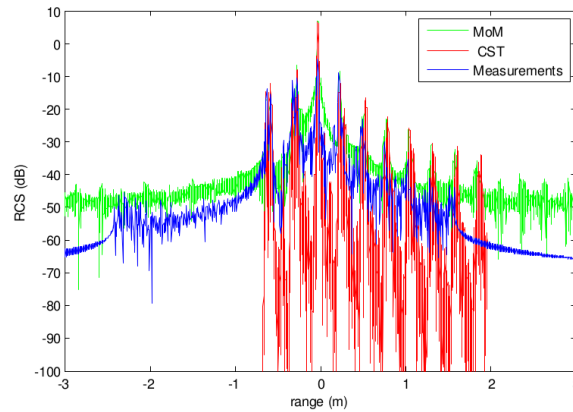


Figure 59: Comparison of different simulation tools and the indoor measurement

This simulation tool, called V3 Urban Canyon, was developed to simulate the range profiles of a canyon by taking into account specular reflections. It is also able to predict the area where a target can be detected by multipath. Meanwhile, it is now undergoing new developments, including:

- The calculation of exact amplitudes involving the areas of surfaces that are involved in multipath.
- The transition of the PEC case to the dielectric case.
- The determination of shadow range positions and the range positions of several key diffuse scattering zones: the ground seen in the Line of Sight of the radar, the roof in the Line of Sight of the radar and the scattering of the ground reflected by the vertical walls.

This last point is illustrated on a realistic example. We chose an existing neighborhood of San Francisco, Japantown, whose 3D modeling is given in Fig. 60 and we show in a given incidence plane how the different returns are synthesized along the range axis.

This representation along the range axis is given in Fig. 61. The point returns coming from specular multipath are given by the various peaks. Colored marks indicate the corresponding rays drawn in the same color. Above the range profile, the various scattering areas located along the range axis are indicated:

- the green areas correspond to direct backscattering of the ground, in direct line of sight of the radar.
- the blue areas correspond to the direct backscattering of the vertical walls.
- the red areas correspond to the direct backscattering of the roofs
- the magenta areas correspond to backscattering of the ground viewed after a reflection on the vertical wall.

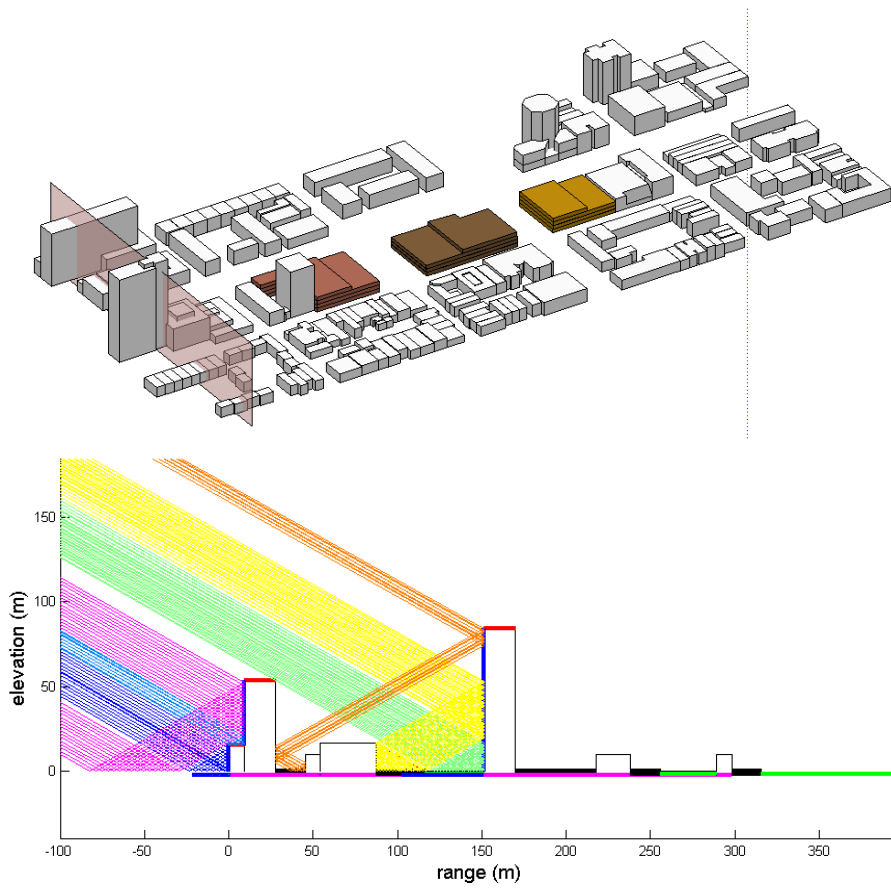


Figure 60: 3D model of Japantown in San Francisco and raytracing of specular scattering according to a section plane

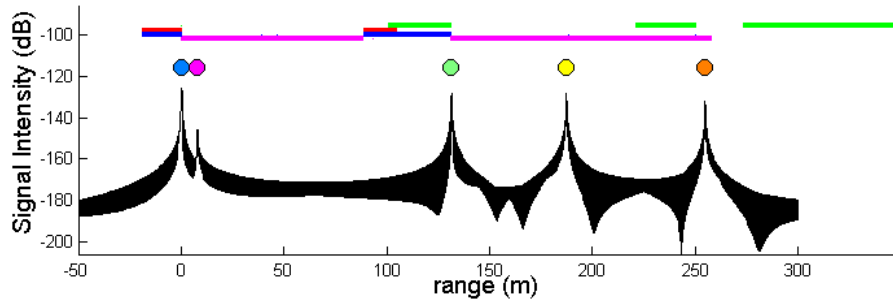


Figure 61: Range profile and diffusion area range positions predicted by URBAN-canyon

Such simulations are able to predict the superposition of different mechanisms within the same resolution, whose statistical return in terms of powers and interferometric coherence have already been discussed in Part 2. In this example, we see that up to three mechanisms can be mixed. Moreover, this simulation tool illustrates the importance of geometric effects in the interpretation of the image. Our feeling is that an algorithm dedicated to urban areas could be proposed. This algorithm would not make the assumption of a set of isotropic and white bright scatters, but rather a superposition of point responses associated with multipath and some diffuse returns whose positioning would result from a specific simplified 3D geometry.

Along with such a development of a tool based on the geometry, other urban area simulators have been evaluated. The Wireless Insite code was rejected because it failed to account for waveforms of large bandwidths as used by radar systems. Furthermore, its interface was not flexible enough to work on the definition of these waveforms ourselves. Finally, both MOCEM and Fermat codes continue to be investigated today at two different scales: MOCEM is used to report statistical detection performance and to be validated for urban areas; Fermat is used to account for the physical mechanisms on a real scale, such as the importance of diffraction effects.

These research perspectives within this context are therefore many as unprecedented in the open literature. Moreover, the detection problem in urban areas remains connected, as we have seen above in regard to entropy, to the understanding of electromagnetic phenomena and of the signal obtained.

## SUMMARY

This last part deals with processing tools for advanced applications.

The first section proposes the use of simulation tools, based on a long-standing collaboration with Laetitia Thirion-Lefevre (SONDRA). A general discussion on the use of simulation models has been proposed, as well as the presentation of our common research approach. This includes

- the development of simulation codes
- their validation, and a joint greater understanding of the scattering mechanisms present in a scene.

The second section outlines the achievements in the field of forestry. They include:

- Understanding the interconnection between canopy height, the phase center interferometric height, and attenuation.
- Understanding of the physical origin of the depolarization, in connection with the bistatic geometry, namely through the thesis of Etienne Everaere.
- Predictions of the most advantageous configurations for detection under forest cover.

The last section outlines the progress made in the field of urban areas, including

- Detection of built-up areas, developed in collaboration with Nicolas Trouvé at Onera.
- A better understanding of entropy in urban scenes. This work will remain ongoing throughout the PhD thesis of Flora Weissgerber.
- Estimation of building heights, through inversion of PolInSAR coherence shape.
- Detection of targets in urban environments. The latter work, more ambitious since we can find no precedent in the literature, is also a larger scale collaborative work, involving simulation and advanced processing.



## CONCLUSION

---

My areas of research on polarimetric imaging radar have been at the interface between physics and mathematical tools. They are now shifting towards image processing algorithms.

The combination of three aspects confers originality to my research:

- The first aspect is a recognized expertise in PolInSAR coherence shape modeling.
- The second aspect is the joint use of optical and radar theories for the development of a polarimetric theory. It includes the use of an optical device to anticipate radar measurements.
- The last aspect is the combination of electromagnetic modeling and signal processing, to meet specific applications.

My contributions in polarimetric imaging performed at Onera are:

- A bistatic polarimetric method that gave rise to a filed patent.
- The recommendation of a bistatic polarimetric coordinate system, suitable for target analysis, and the way to calculate it from the acquisition basis.
- An alternative to conventional bistatic polarimetry theory development, both
  - in terms of the ways of measurement, with the use of an optical device for cheap and quick measurement, and for a wide variety of scenes.
  - in terms of polarimetric decompositions, through the transfer of optics decompositions to the radar community.
- Alternatives to entropy and alpha polarimetric parameters, with reduced computation costs and with physical meaning. These alternatives are implemented in the PolSARpro software, a Polarimetric SAR Data Processing and Educational Tool from ESA.
- A hierarchical segmentation method for polarimetric images, coupled to an elevation estimation algorithm. It constitutes a proprietary software tool developed under the name of PAPIRUS (Polarimetry and Polarimetric Interferometry Rendering over Urban Scenes).
- Innovative mathematical techniques to study the geometrical properties of PolInSAR coherence shapes. They have also demonstrated in this context the inherent limitations of the two-mechanism coherence.

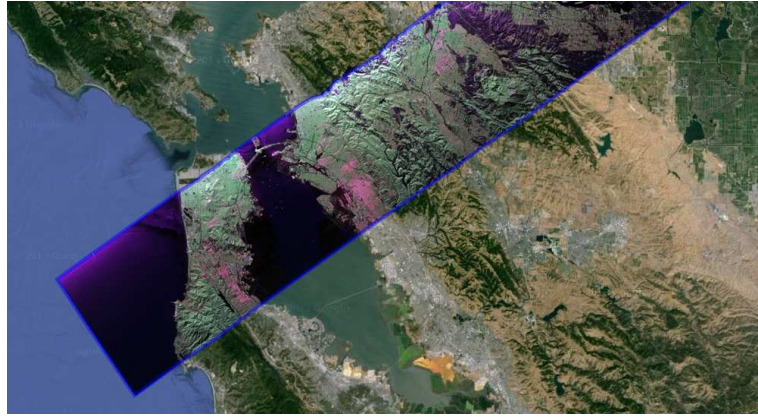


Figure 62: New polarimetric data: UAVSAR. The SAR polarimetric image appears in the blue rectangle

- An algorithm for building height estimation, adapted to the presence of layover, and based on the geometric properties of the coherence shape.
- A deep understanding of the cylinder bistatic polarimetric scattering, and a greater understanding of the forest bistatic polarimetric scattering.
- The prediction of the optimal configurations for target detection through the forest canopy.
- The prediction and understanding of urban canyon range profiles, under far-field or near-field conditions, at different scales.
- The demonstration of the causal link between urban canyon orientations and entropy.
- The demonstration of the causal link between improved resolutions, and the increase in polarimetric entropy in urban areas.
- A methodology for the performance assessment of a detection algorithm for built-up areas in a radar image, by comparison with a topographical database.

Radar polarimetry continues to grow and to raise issues, particularly relating to the diversification of sensors. Access to the data, which was scarce and expensive a few years ago, is increasingly easy. The Sentinel mission and the related approach of ESA in terms of distribution and data access testify to this. Another example are the UAVSAR polarimetric images distributed freely by NASA.

Images are huge, like the one given in Fig. 62: more than 200 000 x 10000 pixels. The revisit times are becoming shorter and the resolutions are improving. In short, we have increasingly more data from different sensors obtained in various configurations and with different characteristics. Due to this changing context, we have to adapt and anticipate future challenges.

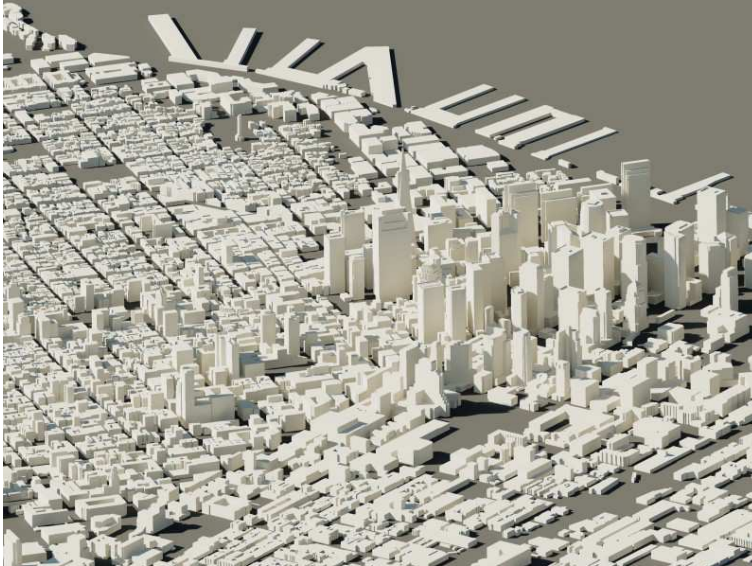


Figure 63: Example of a 3D data base that exists and could be enriched by a radar acquisition

Another point that seems important is the major role that the radar images can play in modern problems, particularly in the urban context. Indeed, radar has two major advantages:

- its responsiveness in a crisis situation, in case of poor visibility condition due to smoke or bad weather, and at night.
- its very good change detection performance, making it suitable for maintaining an up-to-date information.

While in comparison to optical tools (stereo, LIDAR), the maturity of radar processing methods is to date insufficient to consider SAR images for 3D reconstruction in dense urban areas, radar is nevertheless appropriate to promote two lines of research:

- updating data from an existing 3D database.
- quantifying human activity.

In Fig. 63, a 3D data base available on internet sites is an example of information that could be used and updated from remote sensing images, or used for vehicle detection by change detection. Another example of such a 3D modeling with more details, created at Onera, and used for change detection studies, is given in Fig. 64.

Other perspectives offered by the multi-temporal data explosion are:

- subsidence, i.e., measuring the rates of land displacements and the deformation of structures.
- tomography, i.e., the reconstruction of volumetric responses.

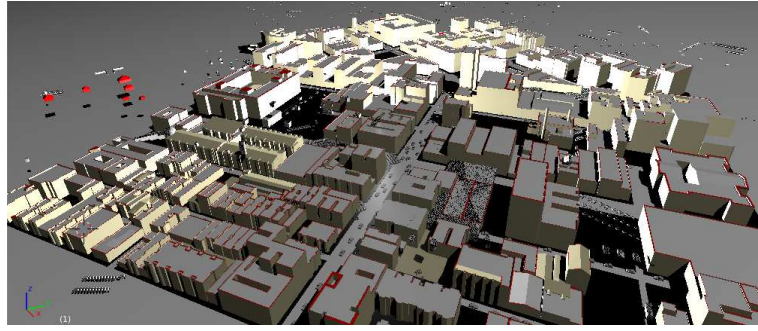


Figure 64: 3D model of San Francisco, created at Onera and used for the prediction of change detection performance by simulators

The contribution of polarimetry to subsidence has been recently evaluated in the ESA study PolSARAp. Up to now, benefit of polarimetry is mainly confined to an improved selection of permanent scatterers, on which the motion is estimated. However, I think that the contribution of polarimetry is not confined to this. Other contributions of polarimetry, such as the characterization of movements by the analysis of mechanisms, could be investigated.

Finally, I would like to express a final thought on future prospects about image processing of multi-temporal remote sensing images. The idea for this is to draw inspiration from the techniques developed in the area of video processing. Video processing also takes advantage of the temporal correlation between images. This temporal correlation offers the capacity to easily capture motion information or gradual changes in time. The processing of remotely sensed images could take advantage of the ideas already developed within the context of video processing, whether for compression, quality improvement, detection or tracking.

Similarly, the joint use of optics and radar polarimetry has been successful to better understand forest measurements. I believe that we should continue on this path, sharing the best algorithms in the fields of remote sensing images and biomedical images. This would include gains in terms of detection, learning and segmentation, supported by a study of the statistical behavior of the images encountered in polarimetric biomedical imaging applications.

## BIBLIOGRAPHY

---

- L. Bombrun, S.N. Anfinen, O. Harant, et al. A complete coverage of log-cumulant space in terms of distributions for Polarimetric SAR data. *ESA special publication SP-695*, pages 1–8, 2011.
- H. Cantalloube and **E. Colin**. POLINSAR for FOPEN using flashlight mode images along circular trajectories. In *IGARSS*, 2007.
- H. Cantalloube and **E. Colin-Koeniguer**. Assessment of physical limitations of high resolution on targets at X-band from circular SAR experiments. In *Synthetic Aperture Radar (EUSAR), 2008 7th European Conference on*, pages 1–4. VDE, 2008.
- H. Cantalloube, **E. Colin**, and H. Oriot. High resolution SAR imaging along circular trajectories. In *IGARSS*, 2007.
- H. Cantalloube, H. Oriot, and **E. Colin-Koeniguer**. Physic and experimental issues on high resolution SAR imaging of urban area. In *Geoscience and Remote Sensing Symposium, 2008. IGARSS 2008. IEEE International*, volume 1, pages I–70–I–73. IEEE, 2008.
- F. Cellier and **E. Colin**. Building height estimation using fine analysis of altimetric mixtures in layover areas on polarimetric interferometric X-band SAR images. In *IGARSS*, 2006.
- F Champagnat, A Plyer, G Le Besnerais, B Leclaire, S Davoust, and Y Le Sant. Fast and accurate PIV computation using highly parallel iterative correlation maximization. *Experiments in fluids*, 50(4):1169–1182, 2011.
- R.A. Chipman. Depolarization index and the average degree of polarization. *Appl. Opt.*, 44(13):2490–2495, May 2005.
- S.R. Cloude and K.P. Papathanassiou. Polarimetric optimisation in radar interferometry. *Electronics Letters*, 33(13):1176–1178, 1997.
- S.R. Cloude and K.P. Papathanassiou. Polarimetric SAR interferometry. *Geoscience and Remote Sensing, IEEE Transactions on*, 36(5):1551–1565, 1998.
- Y. Cui, Y. Yamaguchi, H. Yamada, and S. Park. PolInSAR Coherence Region Modeling and Inversion: The Best Normal Matrix Approximation Solution. *Geoscience and Remote Sensing, IEEE Transactions on*, 53(2), Feb 2015. ISSN 0196-2892.
- E. Everaere, **E. Colin-Koeniguer**, L. Thirion Lefevre, and A. De Martino. Influence of bistatic angle and forest structure description on classical polarimetric parameters. In *Geoscience and Remote Sensing Symposium (IGARSS), 2012 IEEE International*, pages 6531–6534. IEEE, 2012.

- T. Flynn, M. Tabb, and R. Carande. Coherence region shape extraction for vegetation parameter estimation in polarimetric SAR interferometry. In *Geoscience and Remote Sensing Symposium, 2002. IGARSS'02. 2002 IEEE International*, volume 5, pages 2596–2598. IEEE, 2002.
- P. Formont, N. Trouvé, J-P Ovarlez, F. Pascal, G. Vasile, and E. **Colin-Koeniguer**. PolSAR classification based on the SIRV model with a region growing initialization. In *POLINSAR*, 2011.
- A. Freeman. On ambiguities in SAR design. In *EUSAR*, 2006.
- A. Freeman. On the design of spaceborne polarimetric SARs. In *Radar Conference, 2009 IEEE*, pages 1–4, May 2009.
- H-L. Gau and PY. Wu. Numerical range and Poncelet property. *Taiwanese journal of mathematics*, 7(2):pp–173, 2003.
- A-L. Germond. *Théorie de la polarimétrie radar bistatique*. PhD thesis, Université de Nantes, 1999.
- J.J. Gil. Characteristic properties of mueller matrices. *J. Opt. Soc. Am. A*, 17(2): 328–334, Feb 2000.
- P. Goy. *Détection d'obstacles et de cibles de collision par un radar FMCW aéroporté*. PhD thesis, University of Toulouse, 2012.
- J-R. Huynen. *Phenomenological theory of radar targets*. PhD thesis, University of Technology, Delft, The Netherlands, 1970.
- T. Kempf and H. Anglberger. Image fusion of different spaceborne SAR sensors for change detection. In *Radar Conference (RADAR), 2013 IEEE*, pages 1–6. IEEE, 2013.
- J-S. Lee, K.W. Hoppel, S.A. Mango, and A.R. Miller. Intensity and phase statistics of multilook polarimetric and interferometric SAR imagery. *Geoscience and Remote Sensing, IEEE Transactions on*, 32(5):1017–1028, 1994a.
- J-S. Lee, A.R. Miller, and K.W. Hoppel. Statistics of phase difference and product magnitude of multi-look processed Gaussian signals. *Waves in random media*, 4(3):307–320, 1994b.
- C-K. Li, P.P. Mehta, and L. Rodman. A generalized numerical range: the range of a constrained sesquilinear form. *Linear and Multilinear Algebra*, 37(1-3): 25–49, 1994.
- Z. Li and J. Bethel. Image coregistration in SAR interferometry. *Proc. Int. Arch. Photogramm., Remote Sens. Spatial Inf. Sci*, pages 433–438, 2008.
- KV. Mardia. Directional statistics and shape analysis. *Journal of applied Statistics*, 26(8):949–957, 1999.
- SW. McCandless and Christopher R. Jackson. Principles of Synthetic Aperture Radar. *SAR Marine User's Manual*, pages 1–23, 2004.

- M. Neumann, L. Ferro-Famil, and A. Reigber. Multibaseline polarimetric SAR interferometry coherence optimization. *Geoscience and Remote Sensing Letters, IEEE*, 5(1):93–97, 2008.
- C. Pascual, E. Gimeno, and JM Lopez-Sanchez. The equivalence between the polarization subspace method (PSM) and the coherence optimisation in polarimetric radar interferometry. In *Proc. of the 4th European Conference on Synthetic Aperture Radar (EUSAR)*, pages 589–592, 2002.
- A. Plyer, G. Le Besnerais, and F. Champagnat. Massively parallel Lucas Kanade optical flow for real-time video processing applications. *Journal of Real-Time Image Processing*, pages 1–18, 2014.
- J. Praks and M. Hallikainen. A novel approach in polarimetric covariance matrix eigendecomposition. In *Geoscience and Remote Sensing Symposium, 2000. Proceedings. IGARSS 2000. IEEE 2000 International*, volume 3, pages 1119–1121 vol.3, 2000a.
- J. Praks and M. Hallikainen. A novel approach in polarimetric covariance matrix eigendecomposition. In *Geoscience and Remote Sensing Symposium, 2000. Proceedings. IGARSS 2000. IEEE 2000 International*, volume 3, pages 1119–1121, 2000b.
- J. Praks, **E. Colin-Koeniguer**, and M. Hallikainen. Alternatives to Target Entropy and Alpha angle in SAR Polarimetry. *IEEE Trans. Geosc. Remote Sensing*, 47(7):2262–2274, July 2009.
- J. Praks, M. Hallikainen, and **E. Colin-Koeniguer**. Polarimetric SAR image visualization and interpretation with covariance matrix invariants. In *Geoscience and Remote Sensing Symposium (IGARSS), 2010 IEEE International*, pages 2035–2038. IEEE, 2010.
- M. Qong. Coherence optimization using the polarization state conformation in polinsar. *Geoscience and Remote Sensing Letters, IEEE*, 2(3):301–305, 2005.
- J-C. Souyris and C. Tison. Polarimetric analysis of bistatic SAR images from polar decomposition: A quaternion approach. *Geoscience and Remote Sensing, IEEE Transactions on*, 45(9):2701–2714, 2007.
- C-T. Tai. Complementary reciprocity theorems in electromagnetic theory. *IEEE Transactions on Antennas and Propagation*, 40(6):675–681, 1992.
- E. Colin**. A mathematical study about the coherence set in polarimetric interferometry. In *EUSAR*, 2006.
- E. Colin**. Polarimetric optical tools and decompositions applied to SAR images. In *IGARSS*, 2007.
- E. Colin**, C. Titin-Schnaider, and W. Tabbara. A new parameter for IFPOL coherence optimization methods. In *IGARSS*, 2003.

- E. Colin, L. Thirion, C. Titin-Schnaider, and W. Tabbara. Comparison between simulations and interferometric polarimetric SAR P-band data on a pine-trees forest. In *IGARSS*, 2004a.
- E. Colin, M. Tria, C. Titin-Schnaider, W. Tabbara, and M. Benidir. SAR imaging using multidimensional continuous wavelet transform and applications to polarimetry and interferometry. *Int.J. of Imaging Systems*, 14(5):181–221, 2004b.
- E. Colin, C. Titin-Schnaider, and W. Tabbara. Polarimetric interferometry and time-frequency analysis applied to an Urban area at X-band. In *IGARSS*, 2005a. presented by A. Reigber.
- E. Colin, C. Titin-Schnaider, and W. Tabbara. Coherence optimization methods for scattering centers separation in polarimetric interferometry. *JEMWA*, 19(9):1237–1250, 2005b.
- E. Colin, C. Titin-Schnaider, and W. Tabbara. FOPEN with polarimetric interferometry: validations with experimental data at P-band. In *POLINSAR*, 2005c.
- E. Colin, H. Cantalloube, and X. Dupuis. FOPEN and change detection using POLINSAR data at P-band. In *EUSAR*, 2006a.
- E. Colin, C. Titin-Schnaider, and W. Tabbara. An Interferometric Coherence Optimization Method in Radar Polarimetry for High-Resolution Imagery. *IEEE Trans. Geosc. Remote Sensing*, 44(1), January 2006b.
- E. Colin-Koeniguer and L. Thirion-Lefevre. Bistatic scattering from forest components. Part 2: First validation of a bistatic polarimetric forest model at VHF-UHF band [225-475 MHz] using indoor measurements. *Waves in Random and Complex Media*, 20(1):62–85, February 2010.
- E. Colin-Koeniguer and N. Trouvé. Coherence Optimization for Estimation of Building Heights on a Segmented High Resolution PolInSAR Urban Area. In *POLINSAR*, 2011.
- E. Colin-Koeniguer and N. Trouvé. A review about alternatives to classical polarimetric SAR parameters. In *SONDRA workshop*, 2013.
- E. Colin-Koeniguer and N. Trouvé. Performance of buildings height estimation using High Resolution PolInSAR images. *IEEE Trans. Geosc. Remote Sensing*, 52(9):5870–5879, 2014.
- E. Colin-Koeniguer, N. Trouvé, and J. Praks. A review about alternatives to classical Polarimetric SAR parameters. In *Synthetic Aperture Radar (EUSAR), 2010 8th European Conference on*, pages 1–4. VDE, 2010.
- E. Colin-Koeniguer, N. Trouvé, E. Everaere, and A. DeMartino. Bistatic polarimetric decompositions applied to depolarizing targets. In *IGARSS*, 2012.

- L. Thirion and E. **Colin**. On the use of a coherent scattering model to determine the origin of artificial signatures of a target hidden in a forest. In *POLINSAR*, volume 586, page 33, 2005.
- L. Thirion, E. **Colin**, and C. Dahon. Capabilities of a forest coherent scattering model applied to radiometry, interferometry, and polarimetry at P- and L-band. *IEEE Trans. Geosc. Remote Sensing*, 44(4):849–862, April 2006.
- L. Thirion-Lefevre and E. **Colin-Koeniguer**. Investigating attenuation, scattering phase center, and total height using simulated interferometric SAR images of forested areas. *Geoscience and Remote Sensing, IEEE Transactions on*, 45(10):3172–3179, 2007.
- L. Thirion-Lefevre and E. **Colin-Koeniguer**. First polarimetric validation and results on the bistatic scattering by a set of cylinders using a forest scattering model. *Synthetic Aperture Radar (EUSAR), 2008 7th European Conference on*, pages 1–4, June 2008.
- L. Thirion-Lefevre, E. **Colin-Koeniguer**, and C. Dahon. Bistatic scattering from forest components. Part 1: Coherent polarimetric modelling and analysis of simulated results. *Waves in Random and Complex media*, 20(1):36–61, February 2010.
- J. Thomas, K. W. Bowyer, and A. Kareem. Color balancing for change detection in multitemporal images. In *Applications of Computer Vision (WACV), 2012 IEEE Workshop on*, pages 385–390. IEEE, 2012.
- C. Titin-Schnaider. Polarimetric characterization of bistatic coherent mechanisms. *IEEE transactions on geoscience and remote sensing*, 46(5):1535–1546, 2008.
- C. Titin-Schnaider. Physical meaning of bistatic polarimetric parameters. *IEEE transactions on geoscience and remote sensing*, 48(5):2349–2356, 2010.
- K. Tomiyasu. Tutorial review of synthetic-aperture radar (sar) with applications to imaging of the ocean surface. *Proceedings of the IEEE*, 66(5):563–583, May 1978.
- N. Trouvé and E. **Colin-Koeniguer**. Polarimetric study of an anisotropic cloud of cylinders in a bistatic configuration. In *POLINSAR*, 2009.
- N. Trouvé and E. **Colin-Koeniguer**. SIRV based distance for polarimetric SAR images hierarchical segmentation. In *EUSAR*, 2010.
- N. Trouvé and E. **Colin-Koeniguer**. Shape Constraint Region Growing process and application to 3D Rendering of High Resolution Urban Images. In *POLINSAR*, 2011.
- N. Trouvé and E. **Colin-Koeniguer**. Hybrid PolInSAR: High resolution and Polarimetry Applied to Urban. In *POLINSAR*. ESA, 2013. URL <https://earth.esa.int/web/guest/polinsar-2013/workshop-programme>.

- N. Trouvé, **E. Colin-Koeniguer**, P. Fargette, and A. De Martino. Influence of geometrical configurations and polarization basis definitions on the analysis of bistatic polarimetric measurements. *IEEE Trans. Geosc. Remote Sensing*, 49(6):2238–2250, June 2011.
- N. Trouvé, M. Sangnier, and **E. Colin-Koeniguer**. Statistics on High Resolution urban polarimetric images: Application to segmentation and classification. In *Synthetic Aperture Radar, 2012. EUSAR. 9th European Conference on*, pages 26–29. VDE, 2012.
- L. Tsang and Q. Li. Microwave remote sensing theory. *Wiley Encyclopedia of Electrical and Electronics Engineering*, 1985.
- F. Weissgerber, **E. Colin-Koeniguer**, and F. Janez. Urban change detection by comparing SAR images at different resolutions and polarimetric modes. In *10th European Conference on Synthetic Aperture Radar (EUSAR 2014)*, Berlin, Germany, June 2014.
- R.G. White. Change detection in SAR imagery. *International Journal of remote sensing*, 12(2):339–360, 1991.
- Y. Yamaguchi, Y. Yajima, and H. Yamada. A four-component decomposition of POLSAR images based on the coherency matrix. *Geoscience and Remote Sensing Letters, IEEE*, 3(3):292–296, 2006.

Troisième partie

## Sélection de publications

# Performance of Building Height Estimation Using High-Resolution PolInSAR Images

Elise Colin-Koeniguer and Nicolas Trouvé

**Abstract**—This paper investigates the use of polarimetry to improve the estimation of the height of buildings in high-resolution synthetic aperture radar (SAR) images. Polarimetric coherence optimization techniques solve the problem of layover effects in urban scenes by allowing a phase separation of the scatterers sharing the same resolution cell. Bare soil elevation estimation is also improved by the polarimetric phase diversity. First, we present an analysis of the statistical modeling of the generalized coherence set. A building height estimation method is then derived from this analysis. Finally, the method is tested and quantitatively validated over an X-band polarimetric interferometric SAR (PolInSAR) airborne image acquired in a single-pass mode, containing a set of 140 different buildings with ground truth.

**Index Terms**—Coherence optimization, interferometry, polarimetry, synthetic aperture radar (SAR), three-dimensional rendering, urban.

## I. INTRODUCTION

IN THE context of rapid global urbanization, urban environments represent one of the most dynamic regions on Earth. In 2008, according to the latest United Nations statistics, more than half of the world's population lives in urban areas. The world's urban population multiplied tenfold during the 20th century, and most of this growth was in low- and middle-income nations. Moreover, it is urban areas in these nations that will accommodate most of the world's growth in population between now and 2020. The current increase in population has resulted in widespread spatial changes, particularly rapid development of built-up areas, in the city and its suburbs. Due to these rapid changes, up-to-date spatial information is requisite for the effective management and mitigation of the effects of built-up dynamics [1], [2]. Various studies have shown the potential of high-resolution optical satellite data for the detection and classification of urban area. Nevertheless, optical satellite imagery is characterized by high dependence in weather conditions and daytime. Thus, particularly in the case of regional and national surveys within a short time, disaster management, or when data have to be acquired at specific dates, radar systems are more valuable. Moreover, radar images also open the possibility

to enrich the data with advanced SAR imaging and analyzing techniques, such as SAR polarimetry and interferometry.

Interferometry is an efficient approach used to reconstruct the topography of a given region. Polarimetry is another advanced SAR technique, known to improve or complement the results of interferometry. Indeed, the estimated heights obtained by interferometry differ, depending on the polarizations used [3].

In this paper, we are interested in the 3-D rendering of urban scenes. This application is a logical extension to the classification of buildings to enrich the data necessary to monitor the growth of the urban extension. However, it can be also considered part of the diagnostic of urban areas after natural disasters such as tsunamis or earthquakes. Previous studies have already illustrated the contribution of polarimetry in the estimation of building heights by interferometry [4]. However, most of the time, these works are theoretical, and validations from ground truth have been conducted on a very small set of buildings. Then, to demonstrate the interest of the polarimetric interferometric SAR (PolInSAR) techniques in this application framework, it is necessary to show its applicability and to estimate its accuracy in a large-scale scenario. This paper attempts to address this topic: the use of a PolInSAR algorithm for the estimation of building heights, and quantitative analysis of its effectiveness on a large number of buildings. Studies on this point are few. The main difficulty in this context is the presence of layovers, i.e., a mixture of several phase centers within the same resolution cell. Then, the estimated interferometric height is an intermediate height of the phase center located somewhere between the different heights involved. In this context, polarimetry can be used to better separate or better analyze these contributions. Among existing methods to estimate the heights of buildings from PolInSAR data, most methods are based on modeling the backscattered field as superposition of several scatterers at different heights and on using a phase separation method (ESPRIT) based on different polarimetric sources. Other methods are interested in the exploitation of multibaseline data, which is outside the scope of this paper. Here, the approach is original and is to rely on the geometrical properties of the coherence shapes. In addition, another originality is to include statistical considerations on these properties, which enables to have some perspective on the limits of the methods and the estimation of its accuracy. So far, studies on the coherence shapes have ignored the detailed modeling of statistical fluctuations. Moreover, few studies have focused on geometric properties of these forms in order to reverse the descriptive parameters of the target. The only studies that make an *a priori* modeling of the target are those for models involving

Manuscript received April 10, 2013; revised October 6, 2013; accepted November 26, 2013.

E. Colin-Koeniguer is with the Modeling and Information Processing Department, French Aerospace Laboratory (ONERA), 91123 Palaiseau, France.

N. Trouvé is with the Electromagnetism and Radar Department, ONERA, 91123 Palaiseau, France.

Color versions of one or more of the figures in this paper are available online at <http://ieeexplore.ieee.org>.

Digital Object Identifier 10.1109/TGRS.2013.2293605

a random volume, and we put ourselves in a different context here that concerns the deterministic targets.

This paper is organized as follows. Section II is dedicated to the theoretical modeling of the generalized coherence set in the case of urban targets. Section III concerns the empirical analysis of this coherence set in the case of the ground and on a building. Then, Section IV focuses on a proposed algorithm deduced from the analysis of this modeling for the estimation of a building height. Section V presents the quantitative analysis of the precision thus obtained over a large X-band image of Toulouse city (France), before concluding.

## II. MODELING OF THE COHERENCE SET FOR DETERMINISTIC TARGETS

### A. Definition of the PolInSAR Data Modeling

The model we present here has been already used to apply the ESPRIT algorithm [5], [6], or for coherence optimization studies [7]. From this matrix modeling of the scattering vectors, the ESPRIT algorithm is able to estimate the interferometric phases of dominant scattering mechanisms involved in the model. However, note that it does not give any information about the nature of the scattering mechanisms itself and does not exploit the geometric properties of the coherence shapes.

This modeling considers that a resolution cell contains several point scatterers without accounting for the interactions between scatterers or volume scattering effects. The signal  $k_1$  acquired by the first antenna in polarization  $xy$  consists of a sum of  $N$  different elementary scattering contributions, i.e.,

$$k_1^{xy} = c_A s_A^{xy} e^{-j4\pi \frac{\rho_{1A}}{\lambda}} + \dots + c_N s_N^{xy} e^{-j4\pi \frac{\rho_{1N}}{\lambda}} \quad (1)$$

and so does the electric field  $k_2$  for the second antenna, i.e.,

$$k_2^{xy} = c_A s_A^{xy} e^{-j4\pi \frac{\rho_{2A}}{\lambda}} + \dots + c_N s_N^{xy} e^{-j4\pi \frac{\rho_{2N}}{\lambda}}. \quad (2)$$

$c_A$  is the total amplitude of the field scattered by the point A,  $\rho_{1A}$  is the distance between point A and the first antenna, and  $s_A^{xy}$  is the complex reflectivity coefficient for polarization  $xy$ . For simplicity, we can assume that the complex diffusion vector  $s_A = (s_A^{hh}, s_A^{hv}, s_A^{vv})$  can be normalized. The points A, B, ..., N are in the same resolution cell defined by the first antenna, so that one may assume  $\rho_{1A} = \rho_{1B} = \dots = \rho_{1N} = \rho$ . Moreover, let us write

$$\rho_{2A} = \rho + \Delta\rho_A, \rho_{2B} = \rho + \Delta\rho_B, \dots, \rho_{2N} = \rho + \Delta\rho_N. \quad (3)$$

These expressions can be rewritten in a matrix form as

$$\mathbf{k}_1 = \mathbf{S}\mathbf{c} \quad \mathbf{k}_2 = \mathbf{SD}\mathbf{c}. \quad (4)$$

$\mathbf{S}$  is a complex  $3 \times N$  matrix whose columns contain the normalized polarimetric diffusion vectors for each point,  $\mathbf{c}$  is the real column vector of length  $N$  containing the total

amplitude scattered by each point, and  $\mathbf{D}$  is the  $N$ -diagonal matrix containing the interferometric phases, i.e.,

$$\mathbf{D} = \begin{pmatrix} e^{-j\Phi_A} & & & \\ & e^{-j\Phi_B} & & \\ & & \ddots & \\ & & & e^{-j\Phi_M} \end{pmatrix} \quad (5)$$

where the  $\Phi_M = 4\pi(\Delta\rho_M/\lambda)$  are the interferometric phases.

### B. Definition of the Generalized Coherence Set

When computing the coherency matrices, which is defined by

$$\begin{aligned} \mathbf{T}_{12} &= \langle \mathbf{k}_1 \mathbf{k}_2^\dagger \rangle \\ \mathbf{T}_{11} &= \langle \mathbf{k}_1 \mathbf{k}_1^\dagger \rangle \\ \mathbf{T}_{22} &= \langle \mathbf{k}_2 \mathbf{k}_2^\dagger \rangle \end{aligned} \quad (6)$$

where  $\dagger$  indicates the matrix conjugate transposition, and  $\langle \cdot \rangle$  is the statistical averaging, it gives

$$\mathbf{T}_{12} = \langle \mathbf{S}\mathbf{c}\mathbf{c}^\dagger \mathbf{D}^* \mathbf{S}^\dagger \rangle \quad \mathbf{T}_{11} = \langle \mathbf{S}\mathbf{c}\mathbf{c}^\dagger \mathbf{S}^\dagger \rangle \quad (7)$$

$$\mathbf{T}_{22} = \langle \mathbf{SD}\mathbf{c}\mathbf{c}^\dagger \mathbf{D}^* \mathbf{S}^\dagger \rangle. \quad (8)$$

If the same projection vector is chosen for both images, the generalized coherence can be written as follows:

$$\gamma = \frac{\boldsymbol{\omega}^\dagger \mathbf{T}_{12} \boldsymbol{\omega}}{\sqrt{\boldsymbol{\omega}^\dagger \mathbf{T}_{11} \boldsymbol{\omega}} \sqrt{\boldsymbol{\omega}^\dagger \mathbf{T}_{22} \boldsymbol{\omega}}}. \quad (9)$$

This generalized coherence is defined using the same polarimetric projection vector for the first antenna and the second antenna. This definition of the coherence set constrained to a unique mechanism is well adapted in case of an interferometric configuration without temporal decorrelation [7].

In practice, matrices  $\mathbf{T}_{11}$  and  $\mathbf{T}_{22}$  are very similar because they are both coherency matrices of the target seen under very close incidence angles. Provided that this assumption is valid, the mean average on the denominator is very close to the geometric average. It is then possible to replace the definition of  $\gamma$  by the following:

$$\tilde{\gamma} = \frac{\boldsymbol{\omega}^\dagger \mathbf{T}_{12} \boldsymbol{\omega}}{\boldsymbol{\omega}^\dagger \mathbf{T} \boldsymbol{\omega}} \quad (10)$$

where matrix  $\mathbf{T}$  is defined as  $\mathbf{T} = (\mathbf{T}_{11} + \mathbf{T}_{22})/2$  [8]. Since  $2\sqrt{\boldsymbol{\omega}^\dagger \mathbf{T}_{11} \boldsymbol{\omega}} \sqrt{\boldsymbol{\omega}^\dagger \mathbf{T}_{22} \boldsymbol{\omega}} \leq \boldsymbol{\omega}^\dagger \mathbf{T}_{11} \boldsymbol{\omega} + \boldsymbol{\omega}^\dagger \mathbf{T}_{22} \boldsymbol{\omega}$ , the modified coherence  $|\tilde{\gamma}|$  is lower than the generalized coherence  $|\gamma|$ , and then always lies between 0 and 1. Moreover, the argument is not modified by this definition change

$$\arg \gamma = \arg \tilde{\gamma}. \quad (11)$$

The set of all complex coherence values can be plotted in the complex plane. It will be called the ‘‘coherence set’’ and written as  $\Gamma(\mathbf{T}_{12}, \mathbf{T})$ .

It is mathematically proven in [8] that

$$\Gamma(\mathbf{T}_{12}, \mathbf{T}) = \Omega\left(\mathbf{T}^{-\frac{1}{2}}\mathbf{T}_{12}\mathbf{T}^{-\frac{1}{2}}\right). \quad (12)$$

The set  $\Omega(\mathbf{A})$  is called the “field of values of matrix  $\mathbf{A}$ ,” or “numerical range” of matrix  $\mathbf{A}$ , and it is defined by

$$\Omega(\mathbf{A}) = \{\mathbf{x}^\dagger \mathbf{A} \mathbf{x} : \mathbf{x} \in \mathbb{C}^n, \|\mathbf{x}\| = 1\}. \quad (13)$$

This definition of generalized coherence constrained to one single mechanism from a field value is not new [8]–[10]. However, most often, the studies of geometric properties of coherence shape are relevant for random media where interactions are taken into account.

Thus, the most commonly used random volume over ground (RVoG) model for the forest considers a description of a large number of scatterers. In this model, mean interaction effects are taken into account, by involving the attenuation effects. The corresponding coherence shape associated is a segment. There is no noise modeling. To do the average, the only assumption concerns the angular orientation and position distribution of scatterers and thus the description of the target itself and not the statistical fluctuations related to measurement. This model enables to derive inversion methods [11], [12]. More elaborated models, which are inspired by the RVoG one and its combination with physical model-based polarimetric decompositions, can also allow to develop techniques for the inversion of larger numbers of parameters [13]. However, in this paper, for the urban area, the process model differs slightly. The statistical fluctuations considered, which enable to compute the coherency matrix, concern measurement and are not intrinsic to the target, which is considered deterministic. The model on which we rely considers the target a superposition of a small number of completely independent scatterers with potentially different polarimetric characteristics and different heights, without any interaction.

This is investigated in the following.

### III. STATISTICAL ANALYSIS

To be able to predict the coherence shape, we must first choose which statistical fluctuations will be taken into account in the previous model and for what variables. Here, we conduct an empirical analysis, taking into account several fluctuation models and analyzing their impact on the corresponding coherence shape.

#### A. Statistical Variation of $\mathbf{c}$ Only

We first begin with a simplistic modeling to demonstrate how a coherence optimization allows separating and estimating various scattering centers mixed in the resolution cell.

The first hypothesis is that we take into account only the fluctuations on the power described by  $\mathbf{c}$ . This assumption presupposes first that we can separate the statistical fluctuations on the polarimetric behavior and the one on the span, which is not necessarily trivial. It also presupposes that the interferometric phase variations are negligible compared with power fluctuations. Although this hypothesis is not the most physically

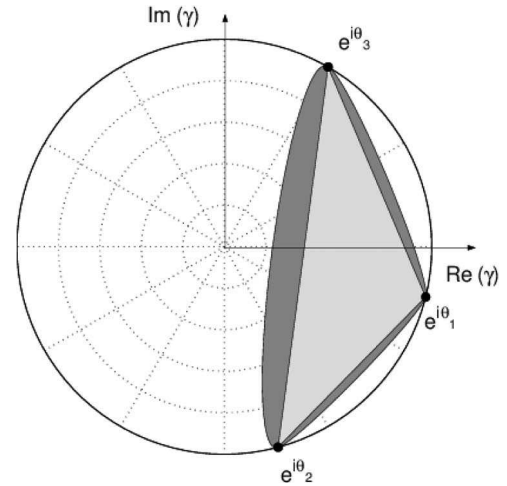


Fig. 1. Coherence set of a three-mechanism resolution cell modeled with a power statistical distribution.

relevant, it is presented here because it allows a simple matrix model of the coherency matrix, and particularly to demonstrate that in this case, the coherence optimization proposed in [7] leads to the estimation of interferometric phases of the different scatterers.

When only statistical fluctuations on  $\mathbf{c}$  are considered, and if  $\mathbf{C} = \langle \mathbf{c}\mathbf{c}^\dagger \rangle$  is the coherence matrix of the  $\mathbf{c}$  vector, then

$$\mathbf{T}_{12} = \mathbf{S}\mathbf{C}\mathbf{D}^*\mathbf{S}^\dagger \quad (14)$$

$$\mathbf{T}_{11} = \mathbf{S}\mathbf{C}\mathbf{S}^\dagger \quad \mathbf{T}_{22} = \mathbf{S}\mathbf{D}\mathbf{C}\mathbf{D}^*\mathbf{S}^\dagger. \quad (15)$$

As  $\mathbf{S}$  is a complex  $3 \times N$  matrix, its maximum possible rank is the smaller value of 3 and  $N$ , i.e., the number of independent scatterers. Then, the coherence matrices are rank 3 only if the number of independent polarimetric scatterers are equal or higher than 3. In the case of exactly three scatterers, the three local optima of the coherence set corresponds to three different scattering phase centers with different corresponding polarimetric mechanisms, as represented in Fig. 1. This has been the model deeply presented in [7] and [10].

However, this kind of modeling is not adapted to the case of a resolution cell containing one or two different polarimetric mechanisms only. Moreover, we find in practice that the coherence maxima are never found equal to 1. For these two reasons, we must therefore account for other sources of statistical fluctuations. In the following, we restrict ourselves to the case of interest here: the modeling of a set of one or two mechanisms.

#### B. Modeling of a PolInSAR Resolution Cell Containing Only One Single Mechanism

The hypothesis made in this section is that the statistical population observed concerns only one physical type of targets, which is denoted by  $\mathbf{A}$ . This is the case for bare soil. When only one type of bright point exists in the resolution cell, then the polarimetric scattering vector samples are simply written as follows:

$$\mathbf{k}_1^i = c_A^i \mathbf{s}_A^i = \mathbf{x}_A^i \quad \mathbf{k}_2^j = e^{-j\Phi_A^j} c_A^j \mathbf{s}_A^j = e^{-j\Phi_A^j} \mathbf{x}_A^j \quad (16)$$

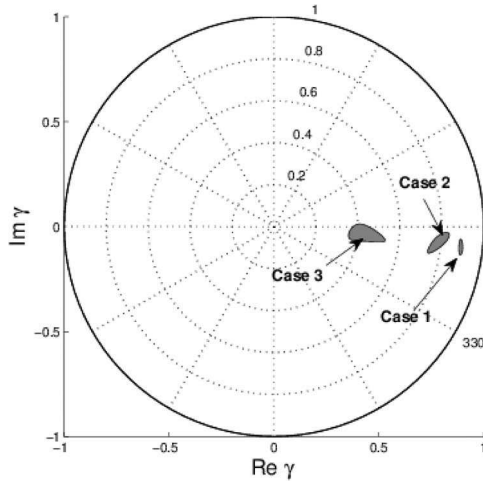


Fig. 2. Three coherence sets generated due to different  $\langle \mathbf{x}\mathbf{x}^\dagger \rangle$  distributions.

where  $\mathbf{k}_1^i$  is one sample of the scattering vector of the first image population, and  $\mathbf{k}_2^{bj}$  is the corresponding sample of the scattering vector of the same population in the second image. To account for statistical fluctuation, we can simply assume the following.

- Vectors  $\mathbf{x}_A^i = c_A^i \mathbf{s}_A^i$  and  $\mathbf{x}_A^j = c_A^j \mathbf{s}_A^j$  are two samples of the same population of vector  $\mathbf{x}_A$ , which is classically described by the probability density function of a circular Gaussian vector with a zero mean [14], [15].
- The statistical distribution of the interferometric angle follows a normal distribution. In reality, the theoretical distribution for the interferometric phase deduced from a Gaussian speckle pattern is more complicated, but it has already been shown that the Gaussian distribution is a good approximation [16].

Once these variables have been generated, we are able to reconstruct sets of polarimetric scattering vectors  $\mathbf{k}_1$  and  $\mathbf{k}_2$  and create associated coherence matrices. As an example, three different coherence sets are represented in Fig. 2. They have been generated using different coherence Wishart matrices  $\mathbf{M}_A = \langle \mathbf{x}_A \mathbf{x}_A^\dagger \rangle$ .

This shows that this simple model allows us to describe coherence sets representing various cases that we encounter in practice on an image. This allows us now to consider the modeling of a resolution cell containing two mechanisms with confidence.

### C. Modeling of a PolInSAR Resolution Cell Containing Two Mechanisms

Because of the presence of overlays, we can find several cells on urban images that can contain two different types of bright scatterers, with different polarimetric behaviors and different elevations. The most frequent cases are summarized in Fig. 3: They are superposition of ground and diffraction by the roof, the ground and the scattering by the roof, or the strong double-bounce echo and the scattering by the roof.

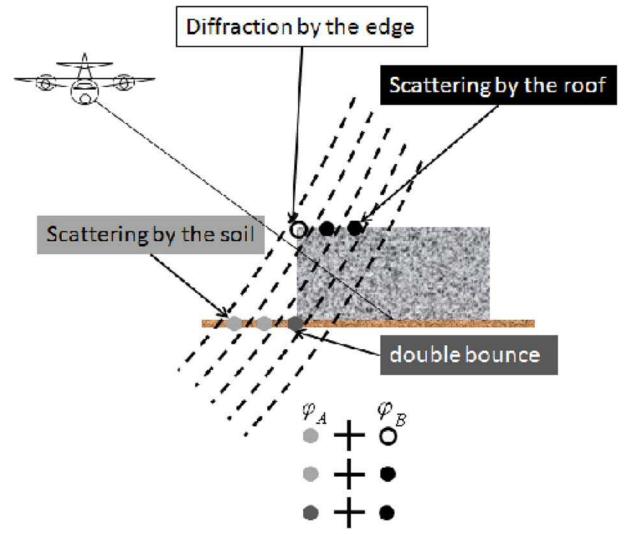


Fig. 3. Example of cases of resolution cells containing two mechanisms at two different elevations.

Now, the mathematical modeling of the statistical population becomes

$$\mathbf{k}_1^i = [\mathbf{s}_A^i \quad \mathbf{s}_B^i] \cdot \begin{bmatrix} c_A^i \\ c_B^i \end{bmatrix} \quad (17)$$

$$\mathbf{k}_2^j = [\mathbf{s}_A^j \quad \mathbf{s}_B^j] \cdot \begin{bmatrix} e^{-j\phi_A^j} & 0 \\ 0 & e^{-j\phi_B^j} \end{bmatrix} \cdot \begin{bmatrix} c_A^j \\ c_B^j \end{bmatrix}. \quad (18)$$

As it seems difficult to envisage the polarimetric statistical fluctuation independently from the total power fluctuation, we can consider here that  $c_A$  and  $c_B$  are just deterministic parameters quantifying the mixture of two types of scatterers A and B. Then, they can be viewed as proportion rather than amplitude, and replaced by  $p$  and  $1 - p$ , where  $0 < p < 1$ , and the model becomes

$$\mathbf{k}_1^i = p\mathbf{s}_A^i + (1 - p)\mathbf{s}_B^i \quad (19)$$

$$\mathbf{k}_2^j = p\mathbf{s}_A^j e^{-j\phi_A^j} + (1 - p)\mathbf{s}_B^j e^{-j\phi_B^j}. \quad (20)$$

We can still also assume here the same distribution for the interferometric phase than in the previous section. Now, we just need to define two statistical laws for the distribution of  $\mathbf{s}_A$  and  $\mathbf{s}_B$  vectors, using two covariance matrices, i.e.,

$$\mathbf{M}_A = \langle \mathbf{s}_A \mathbf{s}_A^\dagger \rangle \quad \mathbf{M}_B = \langle \mathbf{s}_B \mathbf{s}_B^\dagger \rangle. \quad (21)$$

Once this modeling is assumed, it is possible to see that the corresponding coherence shape looks similar to an ellipse, as given in Fig. 4, and as already shown in [17], [10], [4].

Different cases of similarity between  $\mathbf{M}_A$  and  $\mathbf{M}_B$  can be considered. It is possible to see that the more  $\mathbf{M}_A$  is similar to  $\mathbf{M}_B$ , the less we describe the angular diversity.

To conclude this section, we have shown empirically the following.

- A good way to model coherence shapes is to model separately the statistical laws of the different matrices or vectors used to parameterize our model: interferometric

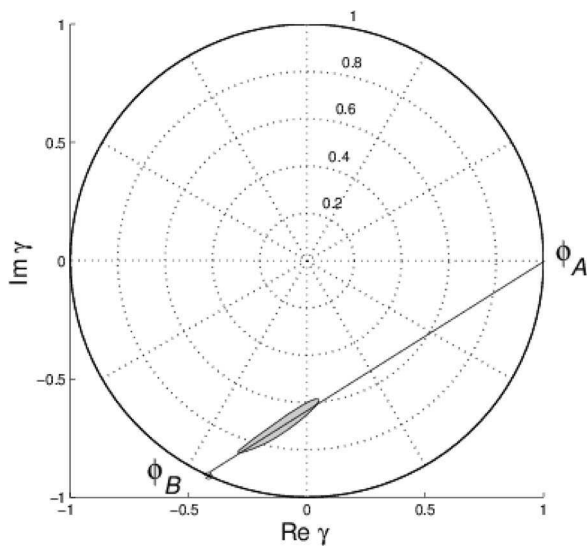


Fig. 4. Simulated coherence set of a resolution cell containing two different polarimetric mechanisms at two different interferometric phases  $\phi_A$  and  $\phi_B$ .

phase, polarimetric coherence matrices, and deterministic relative power.

- Statistical fluctuations on the power only allows to understand the interest of maximizing coherence but cannot account for the actual shapes nor model the cell resolution containing one or two mechanisms only.
- The coherence shape corresponding to a two-mechanism resolution cell looks like an ellipse whose major axis is parallel to the segment joining the two interferometric phases of the mixture. In the case where fluctuations in the phase are not too large, the major axis of the ellipse intersects the unit circle on the two interferometric phases involved in the mixture.

To confirm these findings, we used X-band SAR data, which we now describe and that we will use to propose an algorithm for estimating heights of buildings from the PolInSAR coherence shape.

#### IV. PRESENTATION AND ANALYSIS OF THE DATA SET

##### A. Case of the X-Band

To enable the 3-D rendering of buildings, we need to work on data of sufficient resolution and on wavelengths that do not penetrate the walls to get rid of any consideration of the phenomena of penetration, which would make analysis difficult. As such, the X-band frequency seems to be interesting, both in terms of achievable resolution and penetration. However, this frequency band, corresponding to a wavelength of 3 cm, will be very sensitive to the temporal decorrelation. Joint studies have shown also that, after 11 days, the decorrelation of the ground is too high to use its interferometric phase to estimate altitude. As our goal is to estimate both ground and building elevation from our PolInSAR data, we use an X-band single-pass data set. Only airborne systems today are able to provide such data. We use here PolInSAR data registered by the airborne system RAMSES from the French Aerospace Laboratory (ONERA).

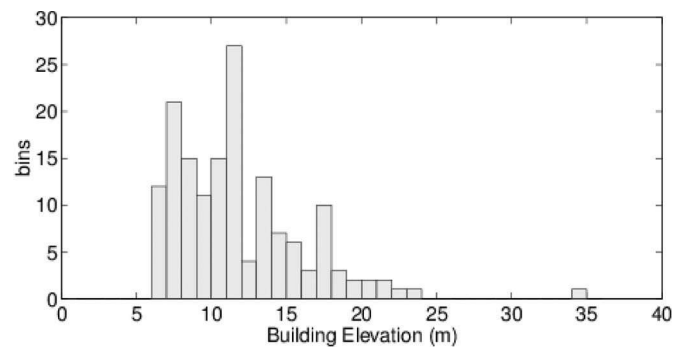


Fig. 5. Distribution of the building height used in our ground truth.

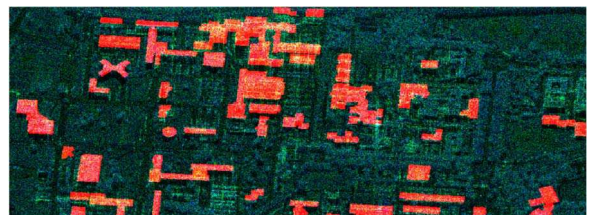


Fig. 6. Registration of the building footprints given by ground truth and the SAR image.

##### B. Site

We chose an image over Toulouse in France, for which a ground truth is adequate and available. Toulouse is a French city containing low residential districts and some industrial places. The Toulouse metropolitan area is the fifth largest in France, which one of the bases of the European aerospace industry. A file describing building footprints and their elevation is used as ground truth for this application. It is a shapefile with shp extension, which is organized as a structure containing a list of polygonal element. These polygons define the footprint of each building on the ground, and for each element, the minimum and maximum elevation data are given. We select the buildings of our ground truth over Toulouse that are in our PolInSAR image, and that are high ( $> 6$  m) and big ( $> 10$  m<sup>2</sup>) enough. That gives us 140 buildings whose elevation is given with a precision of 1 m. Distribution of the building heights that are used for our validation are given in Fig. 5.

The ambiguity height lies between 90 m for minimal ranges to 120 m for far range. In order to automatically select the pixels belonging to the building or on the ground nearby, we have registered the footprints of each building on our SAR image. An excerpt of this coregistration is given in Fig. 6.

We meet all of the cases provided by analyzing the coherence shapes corresponding to different buildings and associated ground areas. These different cases are represented in Fig. 7. The dark shapes correspond to the coherence shapes of the ground, and the black point is located at their optimal coherence. The light gray shape corresponds to buildings. The first one corresponds to a mixture of two mechanisms and can be approximated by an ellipse whose major axis appears as a black segment. In the second one, the coherence shape looks like the one of the resolution cells containing only one mechanism corresponding to the roof.

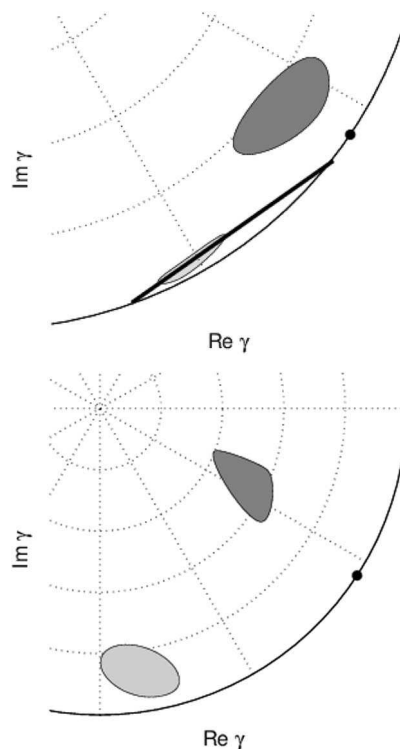


Fig. 7. Real SAR data examples of different resolution cells containing two different cases of coherence shape estimation.

## V. PROPOSITION OF AN ALGORITHM TO ESTIMATE BUILDING HEIGHTS

To recover the respective heights of the roof and ground from their coherence shapes, several solutions are possible. In particular, it is possible to choose to rely only on the coherence shape associated with the pixels of buildings, hoping that it contains both the interferometric phase information related to the ground and to the roof. Indeed, we have shown in Section IV that, in layover areas, the coherence set corresponding to the top of the roof mixed with the ground is a narrow ellipse. If the noise of the interferometric phase is low, then the major axis of this ellipse will intersect the unitary circle into the interferometric phase of the roof and the interferometric phase of the ground. However, most of time, the ground alone is not necessarily visible, or its interferometric phase can be noisy. Then, the extension of the major axis of the ellipse is not always sufficient to ensure a robust regression, as in Fig. 7. Another issue is that it is not uncommon, even in layover areas, that the polarization diversity in the pixels of the roof is insufficient to estimate relevant information on the ground. Moreover, we are also interested in solutions that remains robust even if pixels selected are not located in the layover area. That is why it seems more appropriate to use both coherence-shape information: the one associated with the pixels of bare ground, and those associated with the pixels of the roof. Then, if we want to use the information of both coherence shapes, the first and easiest idea is to think about selecting for the two respective coherence shapes, i.e., the interferometric phases obtained for the polarimetric linear combination that optimizes the coherence. Several coherence optimizations exist. The first technique has been proposed in [18]. This method is considered the most general since

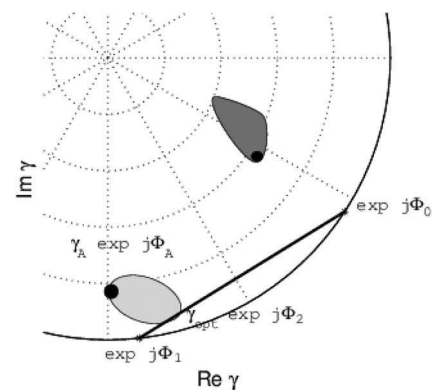


Fig. 8. Different parameters extracted from the observation of coherence set of the ground (dark gray) and coherence set of the roof (light gray).

it allows different polarization states for each interferometric antenna. The work in [7] outlines a general optimization routine with a constraint of equal polarization states, and recently, various other PolInSAR coherence optimization algorithms to optimize the coherence in a subspace and to give suboptimal solutions have been developed. In the following, we will use the method proposed in [7] since it relies on the same definition of the generalized coherence with equal interferometric combination for both antennas. To estimate the interferometric phase of the ground, the solution of the optimized coherence seems relevant as it has already been demonstrated that it is a good way to estimate the elevation of one resolution cell containing only one type of scatterer by reducing the noise level. This optimization enables us to find the point  $\exp(j\phi_0)$ , where  $\phi_0$  corresponds to the interferometric phase of the ground. This point is represented in Fig. 8. Once the interferometric phase of the ground has been estimated using a coherence optimization method, different algorithms can be investigated to estimate the interferometric phase of the roof. If the roof contains a superposition of several mechanisms associated with different heights in the layover case, its coherence shape looks like an ellipse, and the phase of the optimum coherence does not correspond necessary to the interferometric phase of the roof. Precisely because of this, we can say that it would be beneficial to use the angular extremities of the coherence shape that we can literally expressed in terms of eigenvalues of the coherence matrices, as explained in [8] and [10]. The extremity that is the farthest from the ground interferometric phase is represented in Fig. 8. However, many practical cases show low efficiency of an inversion based on this parameter, particularly when the coherence shape has low ellipticity, which is often the case in the presence of significant decorrelation. These practical findings led us to favor an intermediate method. The optimal coherence linked to the ground alone can be used to make a more robust linear regression of the ellipse, particularly in the case where the angular range observed is rather limited. Furthermore, using this optimal coherence rather than the angular ends of the ellipse can minimize errors, in cases of coherence shapes that are very different from those predicted by our model, i.e., with low ellipticity. Practically, we superimpose the two representations: the first coherence set related to the ground and the second one related to the roof of the building. Then,

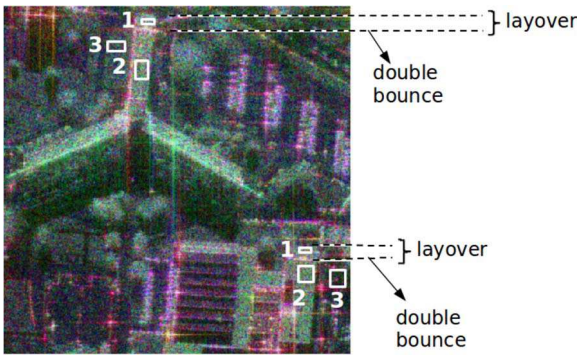


Fig. 9. Example of different selections of pixels on two buildings: layover area (1), roof area (2), ground area (3).

a line is drawn between two points. The first point is on the unit circle, and its phase is the phase of the optimal coherence of the ground. The second point is the optimal coherence of the roof. The intersection of the line joining these points and the unitary circle corresponds to  $\exp(j\phi_1)$ . The total height is deduced from  $\phi_1 - \phi_0$ . This solution is effective in many cases encountered.

- When the pixels selected on the building roof contain no or very little layover or when a mechanism is more coherent than the other mechanisms, then the optimal coherence of the building is very high and very close to the unit circle; in this case, the result of our method is close to the phase difference between two optimal coherence values.
- In the case that the roof contains a superposition of the two mechanisms, the previous modeling has shown that the coherence set is a thin ellipse and the extension of its major axis must pass from one side through the point of the unit circle whose phase is the interferometric phase of the ground, and the other one by a point very near of the optimal coherence.

One of the main issues of the PolInSAR algorithms is the choice of neighboring pixels of similar scattering characteristics to obtain the estimation of the coherence matrices through a statistical average. Here, pixels were selected for each of the buildings within the footprint given by ground truth, and in contiguous and homogeneous areas of ground. According to the selection of the pixels that are selected either in a layover area or not, coherence shapes obtained for a roof will therefore obviously be different. We illustrate this point by focusing on two specific buildings, which are shown in Fig. 9. This image is color coded using power classically expressed in the Pauli basis: green for cross-polarization HV, red for HH – VV channel signing double-bounce returns, and blue for the HH + VV channel signing the surface mechanism. In this figure, ground and roofs sign alternately blue or green, depending on the materials and the mechanisms involved. On both considered roofs, we can distinguish the layover area, which is located closest to the axis of the antenna trajectory (which is on the top of the image and horizontally), and before the red line that can be perceived in red. A more detailed analysis enables to see that the layover area has a color slightly different from the roof area itself.

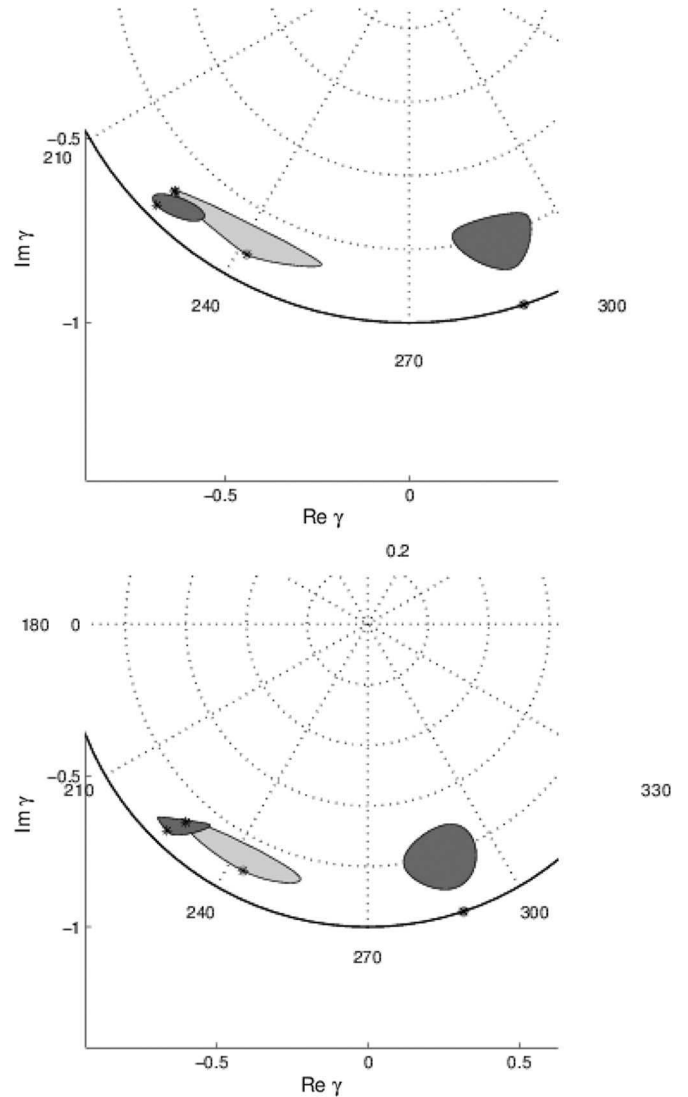


Fig. 10. Two examples of coherence sets associated with three groups of pixels, i.e., among ground, layover area, and roof, on the first building.

To illustrate each type coherence shape, we selected for each building, an area of layover, an area on the roof only, and then an area on the ground. Coherence shapes computed for the first building and for different groups of pixels are represented on Fig. 10. Coherence shapes associated to the second building are represented in Fig. 11.

These examples illustrate the findings presented earlier. The roof alone and the ground areas have coherence shapes with little angular diversity. Ground areas have relatively low coherence. Layover areas have a greater angular range and approximate ellipses whose major axis is oriented along an axis joining the interferometric phases of the roof and of the ground.

### VI. RESULTS

The different heights so found are evaluated in terms of mean error in the measurement compared with heights given by ground truth and root mean square error (see Fig. 12). The ambiguity height on this image is about 100 m. The proposed method is also compared with the estimation computed in the

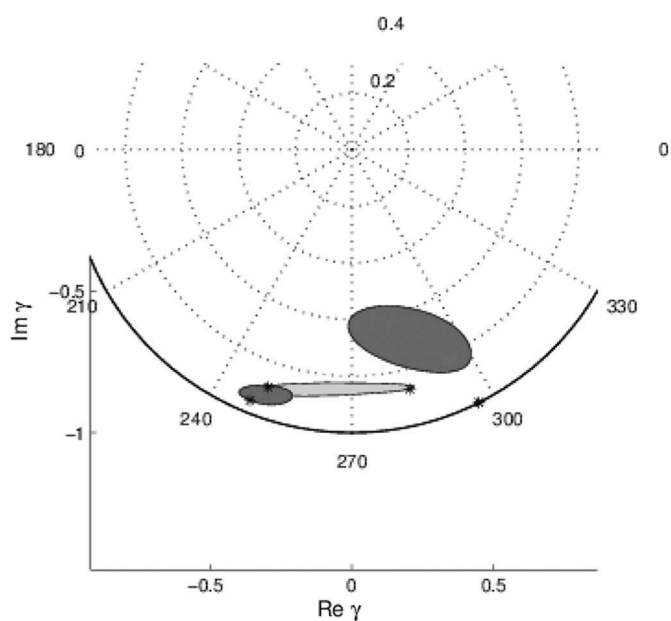


Fig. 11. Example of coherence sets associated with three groups of pixels, i.e., among ground, layover area, and roof, on the second building.

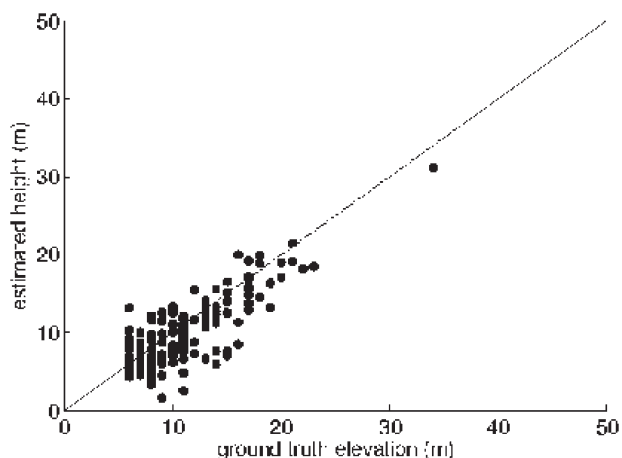


Fig. 12. Results of estimated height versus ground truth.

TABLE I  
ESTIMATED HEIGHT COMPARED WITH GROUND TRUTH

Polarization Use	Ground truth height - estimated height (m)	RMSE (m)
HH+VV	2.57	3.89
HH-VV	2.76	4.60
HV	2.23	3.79
Proposed method	1.20	2.87

single polarimetric channels of the Pauli basis. Results are presented in Table I. Note that the best single polarimetric channel for the estimation of interferometric heights is the HV. This corresponds to a previous observation that the roofs present here are often sufficiently rough to backscatter a signal higher than the ground, certainly because most of the roofs in this area consist of gravel. Consequently, the HV return is often high for these buildings.

In summary, polarimetry saves a factor of two in the estimation errors, for an average error of about 1 m, and a mean square error of 2.8 m. These results are encouraging given

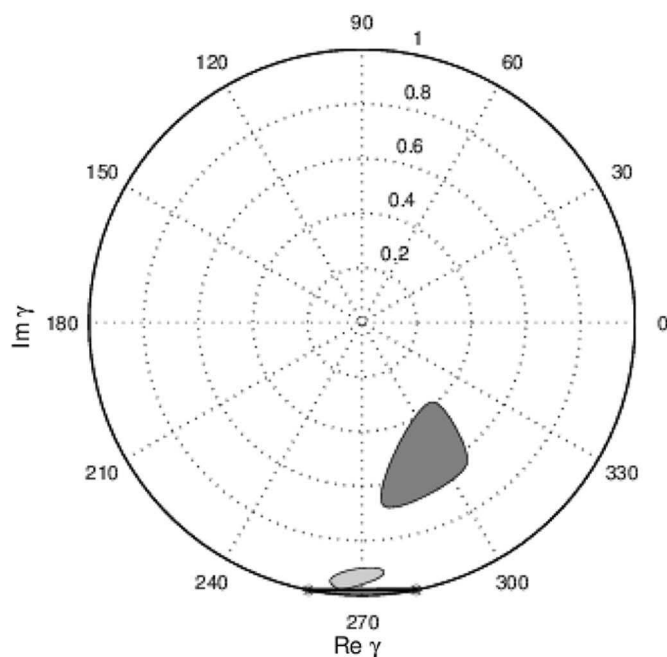
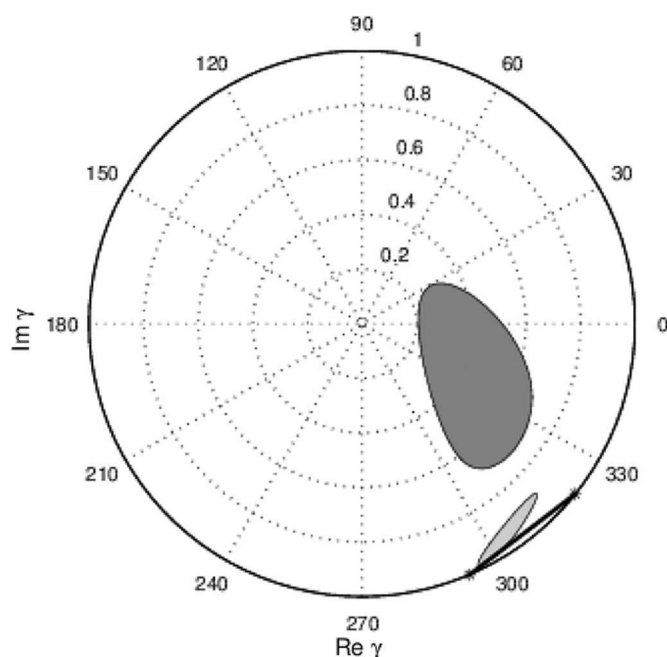


Fig. 13. Example of coherence sets of ground with low coherence that lead to a bad estimation of the building height.

that the ambiguity height is relatively high (100 m). They are very similar to results presented in [5], where the building elevations have been estimated using ESPRIT algorithm on seven buildings, but here, we make in addition to the robustness of the method, having deployed it on 140 buildings, with much lower heights. Moreover, generally speaking, we must keep in mind that we have to estimate the ground elevation in our process, and that the ground truth is provided here with an accuracy of 1 m.

The main difficulty in this type of algorithm is the selection of pixels for the estimate. Indeed, we have already demonstrated in [4] that a mixture of two different populations resulting from segmentation errors and boxcar filtering on a

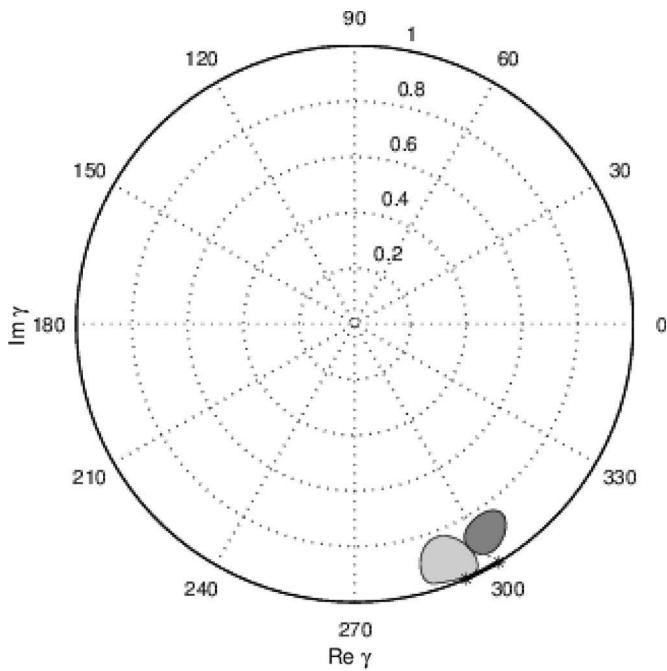


Fig. 14. Example of coherence sets of ground and building that lead to a bad estimation of the building height.

transition area has drastically consequences on the coherence shape conclusions as this mixture acts as a “mean” coherence shape, without preserving the angular diversity.

Sources of failure of the algorithm can be as follows.

- The correlation of the ground is very low; therefore, the coherence optimization not necessarily leads to a better estimate of its interferometric phase. These are the cases shown in Fig. 13.
- When the height of the building is very small, then the estimate of our building is unreliable, given the variability of the interferometric phase. This is for example the case shown in Fig. 14.

In general, we see in Fig. 12 that differences between our estimated heights and heights given by ground truth are even more important for low heights. Moreover, it is clear that lower heights of ambiguity allow for better results.

Another alternative is to apply automated segmentation of the image and then determine which segments belong to a building. This preliminary stage would also improve the visual product, by predetermining what buildings would give them straight contours before 3-D rendering. The results of this paper allow us to be confident about the possibility of rendering large-scale 3-D images as obtained in Fig. 15, with the corresponding ground truth in Fig. 16. These previous results were obtained on an extract of the whole PolInSAR image after a prior segmentation and a local estimation of height of the buildings.

### VII. CONCLUSION

This paper is the first large-scale demonstration of the potential of PolInSAR for the study of the urban environment. In the first parts, we have conducted an analysis of the statistical behavior of the generalized coherence shape. It allows us to

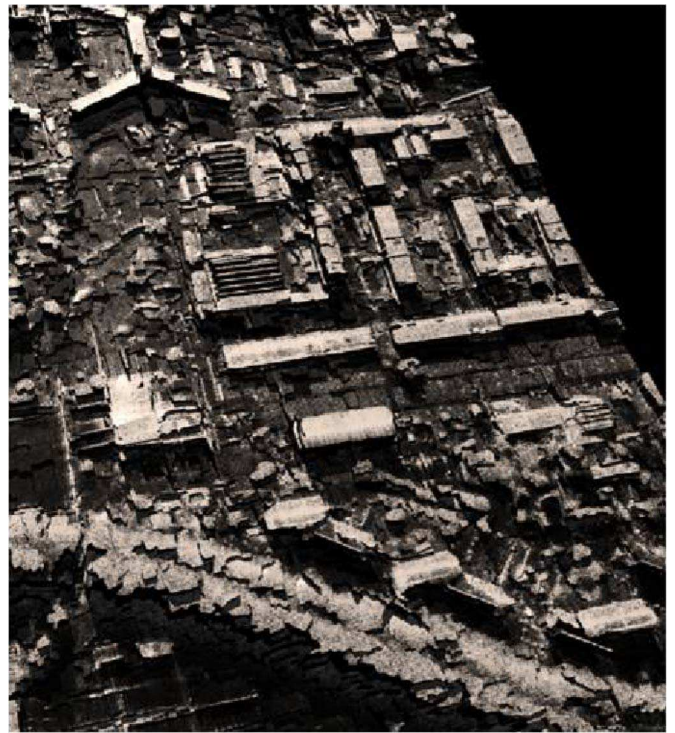


Fig. 15. Three-dimensional rendering of the part of the PolInSAR image of Toulouse after preprocessing and building height estimation.

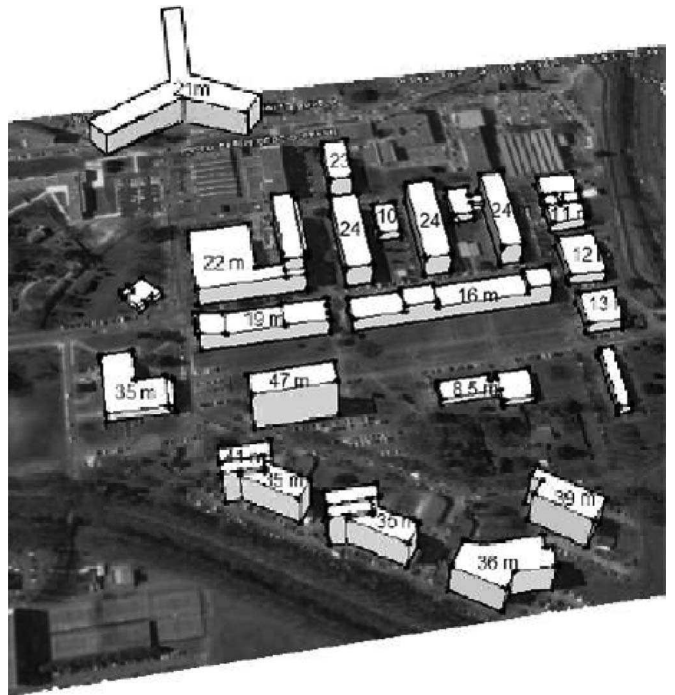


Fig. 16. Part of ground truth over Toulouse.

better understand the different statistical contributions to the final shape, and to better adapt the inversion algorithms based on these shapes.

We have shown that polarimetric correlations are the most critical to the resulting shapes and are more influent. Based on these findings, we have proposed a method to estimate the interferometric phase of the ground and the roof of a building,

in order to evaluate the elevation of the latter. The effectiveness of this method was tested on estimating heights of more than 140 buildings. Results have been compared with the evaluation based on pure polarimetric data. In these estimates, the gain brought by polarimetry is to improve the precision obtained on the estimates of a factor of two, and the mean square error has been reduced also.

Errors and estimation difficulties are mainly as follows:

- bad choice of the population of pixels belonging to the roof;
- sources of polarimetric decorrelation of interferometric noise.

Future prospects for this paper are mainly based on the following:

- inclusion of cases with more complex interactions between buildings;
- 3-D reconstruction taking into account the ground projection and layover phenomenon;
- understanding of polarimetric decorrelation based on electromagnetic considerations.

#### ACKNOWLEDGMENT

The authors would like to thank H. Cantalloube for the processing of PolInSAR images and B. Pannetier for his help about the ground truth data, and the anonymous reviewers for their very careful reading of the manuscript. The authors would also like to thank Direction Gnrale de l'Armement and Centre National d'Etudes Spatiales for their support to the acquisition campaign with the Onera RAMSES airborne system.

#### REFERENCES

- [1] Y. Dong, B. Forster, and C. Ticehurst, "Radar backscatter analysis for urban environments," *Int. J. Remote Sens.*, vol. 18, no. 6, pp. 1351–1364, 1997.
- [2] C. Ticehurst, "Development of models for monitoring the urban environment using radar remote sensing," Ph.D. dissertation, School Geomatic Eng., Univ. New South Wales, Sydney, NSW, Australia, 1998.
- [3] S. Cloude and K. Papathanassiou, "Polarimetric SAR interferometry," *IEEE Trans. Geosci. Remote Sens.*, vol. 36, no. 5, pp. 1551–1565, Sep. 1998.
- [4] E. C. Koeniguer and N. Trouve, "Coherence optimization for estimation of building heights on a segmented high resolution PolInSAR image," presented at the POLInSAR Workshop, 2011. [Online]. Available: [http://earth.eo.esa.int/pub/polsarpro\\_ftp/POLInSAR2011/Monday24/Applications\\_Urban/2\\_Coherence\\_shape\\_Colin\\_Koenguiier.pdf](http://earth.eo.esa.int/pub/polsarpro_ftp/POLInSAR2011/Monday24/Applications_Urban/2_Coherence_shape_Colin_Koenguiier.pdf)
- [5] S. Guillaso, L. Ferro-Famil, A. Reigber, and E. Pottier, "Urban area analysis based on ESPRIT/MUSIC methods using polarimetric interferometric SAR," in *Proc. IEEE 2nd GRSS/ISPRS Joint Workshop Remote Sens. Data Fusion over Urban Areas*, 2003, pp. 77–81.
- [6] S. Guillaso, L. Ferro-Famil, A. Reigber, and E. Pottier, "Building characterization using L-band polarimetric interferometric SAR data," *Geosci. Remote Sens. Lett.*, vol. 2, no. 3, pp. 347–351, 2005.
- [7] E. Colin, C. Titin-Schnaider, and W. Tabbara, "An interferometric coherence optimization method in radar polarimetry for high-resolution imagery," *IEEE Trans. Geosci. Remote Sens.*, vol. 44, no. 1, pp. 167–175, Jan. 2006.
- [8] T. Flynn, M. Tabb, and R. Carande, "Coherence region shape extraction for vegetation parameter estimation in polarimetric SAR interferometry," in *Proc. IEEE IGARSS*, 2002, vol. 5, pp. 2596–2598.

- [9] R. T. Fomena and S. R. Cloude, "On the role of coherence optimization in polarimetric SAR interferometry," *In Practice*, vol. 22, no. 11, p. 9, 2005.
- [10] E. Colin, "A mathematical study about the 'Coherence Set' in polarimetric interferometry," presented at the EUSAR Symp., Dresden, Germany, 2006.
- [11] S. Cloude and K. Papathanassiou, "Three-stage inversion process for polarimetric SAR interferometry," *IEE Proc.—Radar, Sonar Navigat.*, vol. 150, no. 3, pp. 125–134, Jun. 2003.
- [12] R. N. Treuhaft and P. R. Siqueira, "The calculated performance of forest structure and biomass estimates from interferometric radar," *Waves Random Media*, vol. 14, no. 2, pp. S345–S358, 2004.
- [13] M. Neumann, L. Ferro-Famil, and A. Reigber, "Estimation of forest structure, ground, and canopy layer characteristics from multibaseline polarimetric interferometric SAR data," *IEEE Trans. Geosci. Remote Sens.*, vol. 48, no. 3, pp. 1086–1104, Mar. 2010.
- [14] J.-S. Lee, K. W. Hoppel, S. A. Mango, and A. R. Miller, "Intensity and phase statistics of multilook polarimetric and interferometric SAR imagery," *IEEE Trans. Geosci. Remote Sens.*, vol. 32, no. 5, pp. 1017–1028, Sep. 1994.
- [15] J.-S. Lee, M. R. Grunes, and R. Kwok, "Classification of multi-look polarimetric SAR imagery based on complex Wishart distribution," *Int. J. Remote Sens.*, vol. 15, no. 11, pp. 2299–2311, 1994.
- [16] E. Rodriguez and J. Martin, "Theory and design of interferometric synthetic aperture radars," *IEE Proc. F Radar Signal Process.*, vol. 139, no. 2, pp. 147–159, Apr. 1992.
- [17] F. Cellier and E. Colin, "Building height estimation using fine analysis of altimetric mixtures in layover areas on polarimetric interferometric X-band SAR images," in *Proc. IEEE IGARSS*, 2006, pp. 4004–4007.
- [18] S. R. Cloude and E. Pottier, "A review of target decomposition theorems in radar polarimetry," *IEEE Trans. Geosci. Remote Sens.*, vol. 34, no. 2, pp. 498–518, Mar. 1996.



**Elise Colin-Koeniguer** was born in France on November 15, 1979. She received jointly the Dipl. Ing. degree in electrical engineering from École Supérieure d'Électricité (Supélec), Gif-Sur-Yvette, France, and the M.Sc. degree in theoretical physics from the University of Orsay (Paris XI), Orsay, France, in 2002, and the Ph.D. degree from the University of Paris VI, Paris, France, in 2005.

Then, she joined the Electromagnetism and Radar Department, French Aerospace Laboratory (ONERA), Palaiseau, France. Since 2013, she has been with the Modeling and Information Processing Department, ONERA, where her activities include image processing, radar, and optical polarimetry, and investigation of video processing. She is also the Principal Investigator in ONERA, taking part in the European Space Agency project "POL SARap" for defining the key applications of polarimetry in urban areas. She has been working on polarimetric interferometry with airborne systems. Her research interests cover various subjects in image processing (SAR and inverse SAR), theory of polarimetry, and the comparison between radar polarimetry and optical polarimetry.



**Nicolas Trouvé** was born in France on February 8, 1985. He received the Master's and Dipl. Ing. degrees in optical engineering from the Institut d'Optique Graduate School-ParisTech, Paris, France, in 2008 and the Ph.D. degree from the Ecole Polytechnique Graduate School, Palaiseau, France, in 2011.

Since then, he has been with the Electromagnetism and Radar Department, French Aerospace Laboratory (ONERA), Palaiseau. His research interests include polarimetric image processing, detection, and simulation tools for radar.

# Influence of Geometrical Configurations and Polarization Basis Definitions on the Analysis of Bistatic Polarimetric Measurements

Nicolas Trouvé, Elise Colin Koeniguer, Philippe Fargette, and Antonello De Martino

**Abstract**—Within the frame of bistatic polarimetry, this paper discusses the entangled effects of bistatic geometry and target features on polarimetric measurements. Three different geometrical effects are distinguished: antenna rotations, target orientation, and bistatic angle. Antenna rotations are addressed through the use of polarimetric bases taking the scattering plane as the reference plane. Target orientation effects are not considered since only spheres are studied. This paper focuses on the bistatic angle effect through a bistatic polarimetric analysis on classical parameters. Targets consisting of single or multiple spheres in the resonance region are investigated. Finally, the results of indoor polarimetric measurements on such targets are presented and discussed.

**Index Terms**—Bistatic polarimetry, optical polarimetry, Synthetic Aperture Radar (SAR) polarimetry.

## I. INTRODUCTION

SYNTHETIC aperture radar (SAR) operating at microwave frequencies has become a widely used remote sensing instrument. Bistatic SAR brings multiple benefits, from additional information to operational advantages. While raising many technical challenges such as transmitter and receiver synchronization, antenna orientation and motion compensation, bistatic configurations also engender many difficulties in the extraction of polarimetric parameters. Even in monostatic configurations, the geometry of the system has a major impact on the polarimetric information due to its heavy dependence on the polarimetric basis used in the definition and measurement of the signals. In the bistatic case, the geometry is much more difficult to handle. Actually, in a bistatic settings, we can differentiate three different geometrical effects:

- 1) Target orientations around the lines of sight in emission and reception.
- 2) Emitting and Receiving antenna polarimetric orientations (or linear polarimetric basis).
- 3) Emitting and Receiving antenna relative positions.

In a monostatic setting, antenna polarimetric basis and target orientation effects (Points 1 and 2) are usually removed in one

step because a rotation of a target about the propagation axis is equivalent to an antenna rotation. The basis invariance of one target decomposition makes parameters roll invariant, i.e., the parameters are independent of rotation of the target about the radar line of sight. It also means that the parameters can be computed independently of the polarization basis. Then, polarimetric basis issues are solved either by roll-invariant parameters or appropriate rotations, as in [1]–[4].

In a bistatic setting, the first point and the second one are no longer equivalent:

- Physical target rotations around the line of sight (in the incident or scattered direction) are not only related to rotations on the scattering matrix. A change of the target orientation in the incident wave plane can change the mechanism seen by the reception antenna, and not only the tilt angles.
- The words “disoriented target” means that the scattering matrix does not contain any more information about its tilt angles, as presented in [1], and more recently in [5]. When the tilt angles are estimated and removed or roll-invariant parameters are used, a rotation of the target in the incident wave plane or in the scattered wave plane (Point 1) still can impact the remaining parameters.

We illustrate this by a very simple example in Fig. 1. Conventions used to express the scattering matrices will be defined in the next section.

- In the upper panel (a) of the figure, the target is a thin cylinder located in the incident wave plane  $Oyz$ , with a  $45^\circ$  tilt angle. It is considered here as a polarizer. The reference plane used to define the polarimetric basis is the horizontal plane. Singular values of the canonical matrix are equal to 0 and 1.
- In the panel (b), we consider the same target in the same geometrical configuration. We just want here to express it scattering matrix with another convention to define the polarimetric bases. Now the Emitter-Target-Receiver plane is chosen as reference plane (ETR). A rotation of the system has been applied about the  $x$ -axis in order to make the ETR plane horizontal in the panel (b). This transformation just acts as a rotation on the emission antenna reference axis. This concerns point 2. The Sinclair matrix has changed but it keeps the same singular values.
- In the panel (c), we apply to the target a  $45^\circ$  rotation relatively to the panel (b) in its incident wave plane. This

Manuscript received November 23, 2009; revised April 12, 2010, June 22, 2010, and October 15, 2010; accepted October 31, 2010. Date of publication January 16, 2011; date of current version May 20, 2011.

N. Trouvé, E. Colin Koeniguer, and P. Fargette are with the ONERA, the French Aerospace Lab, 91761 Palaiseau, France.

A. De Martino is with the LPCIM, the Laboratory of Physics of Interfaces and Thin films, Ecole Polytechnique, 91128 Palaiseau, France.

Color versions of one or more of the figures in this paper are available online at <http://ieeexplore.ieee.org>.

Digital Object Identifier 10.1109/TGRS.2010.2093533

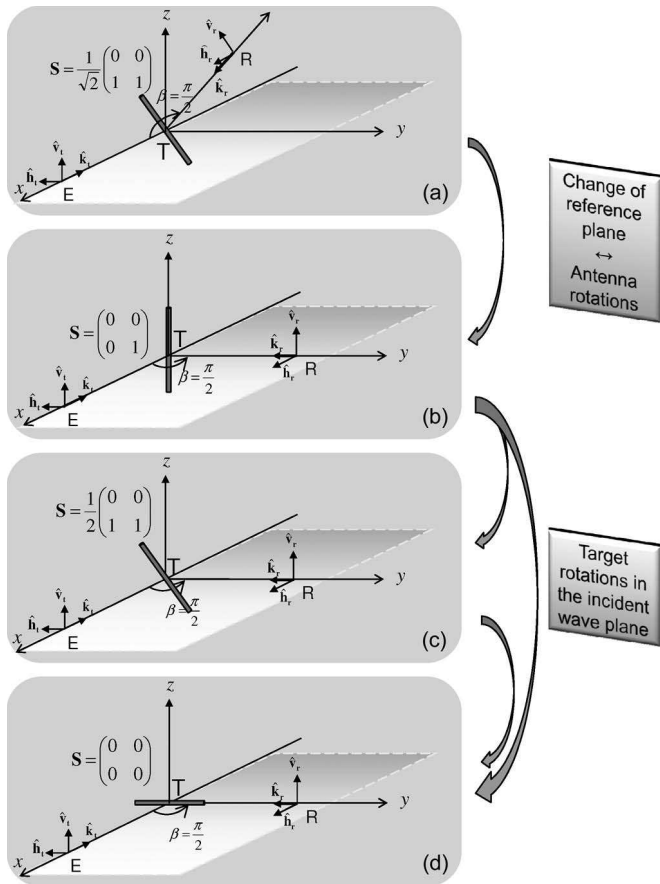


Fig. 1. Example of geometrical transformations: Point 1 and Point 2.

transformation concerns point 1, and does impact both the singular values and the tilt angles of the scattering matrix, because the rotation impacts the projection of the target in the scattered wave plane. Now singular values are equal to 0 and  $1/\sqrt{2}$ . The total received power has been reduced.

- In the panel (d), we apply again to the target a  $45^\circ$  rotation relatively to the previous panel in its incident wave plane. We obtain now a very particular case in which both singular values are null: the mechanism viewed by the receiver is changed. In the last two cases (c) and (d), the scattering matrix cannot be deduced from the previous one by a simple geometrical relation.

Roll invariant parameters extracted from disoriented Sinclair matrices  $\mathbf{S}_d$  (obtained when the tilt angles  $\theta_e$  and  $\theta_r$  are estimated and removed) are still meaningful in a bistatic setting. But we must keep in mind that they still depend on the target orientation in the incident and scattered wave planes (Point 1). If the tilt angles are estimated on a measured scattering matrix, they also still depend on the target orientation in the wave planes, as well on emitting and receiving antenna orientations (Point 1 and 2 indiscriminately).

In order to perform a classical polarimetric study (eventually involving the usual tilt angles estimation), first, we have to carefully define our convention that allows us then no longer consider point 2. In this way the knowledge of the remaining tilt angles can improve the understanding of the remaining parameters.

In this paper, we focus on the influence of Emitting and Receiving Antenna relative positions (Point 3), that we want to describe using a single angle  $\beta$ . For this objective, we choose a convention linked to the scattering plane (emitter-target-receiver) plane to define the polarimetric bases. The transition from the classical convention imposed by measurement to the convention chosen here is equivalent to two rotations. They effectively remove the influence of Point 2 and reduce the problem to a single variable: the bistatic angle.

Then, we conduct a polarimetric analysis on Point 3. With the scattering plane convention, a sphere, obviously unaffected by Point 1, will have a diagonal scattering matrix. That is why tilt angle estimation and removal will not be required for our targets. Hence, this paper will focus on isotropic targets, starting with a single metallic sphere, then gradually increasing the complexity by increasing the number of spheres and finally considering a cloud of sphere. The scattering from spherical particles is well known since Mie derived the exact solution in 1908 [6]. Bistatic measurements in anechoic chamber BABI in ONERA (Palaiseau) were made to corroborate our theoretical analysis.

This paper is organized as follows: first, the advantages of the scattering plane as well as the transformation matrices are presented. In Section II, we provide a theoretical analysis of one sphere at low frequency in a bistatic setting. In Section III, the low scattering case is compared to scattering in the resonance region for one, two, and four spheres. Section IV is devoted to the study of a cloud of Mie spheres in order to study the impact of bistatic angle on the multiple scattering. Finally, in Section V, we summarize the main issues raised by bistatic polarimetry analysis and the proposed solutions.

## II. DEFINITIONS OF POLARIZATION VECTORS: SPHERICAL COORDINATE SYSTEM OR HORIZONTAL REFERENCE PLANE SYSTEM

### A. Conventions

In this section, the definition of the propagation vectors is provided, using either the Forward Scatter Alignment (FSA) for  $\hat{\mathbf{k}}_i$ ,  $\hat{\mathbf{k}}_s$  or BSA (Back Scatter Alignment) convention for  $\hat{\mathbf{k}}_t$ ,  $\hat{\mathbf{k}}_r$ . When describing the propagation of a plane EM wave, the direction of the propagation vectors depends on the convention: from the transmitter to the scatterer or from the scatterer to the transmitter.

- In the FSA convention, these propagation unit vectors are denoted  $\hat{\mathbf{k}}_i$  and  $\hat{\mathbf{k}}_s$ , where the subscripts  $i$  and  $s$  refer to the incident and scattering wave. They are positive when pointing in the same direction as propagation of the wave.
- In the BSA convention these vectors are denoted  $\hat{\mathbf{k}}_t$  and  $\hat{\mathbf{k}}_r$ , where the subscripts  $t$  and  $r$  refer to the transmitting and receiving antenna.  $\hat{\mathbf{k}}_t$  and  $\hat{\mathbf{k}}_r$  are positive when pointing toward the target both before and after scattering.

It follows that  $\hat{\mathbf{k}}_t = \hat{\mathbf{k}}_i$  and  $\hat{\mathbf{k}}_r = -\hat{\mathbf{k}}_s$ . As the BSA convention is used in backscattering situations, it was chosen in this paper in order to keep the polarimetric interpretation commonly made in the monostatic case.

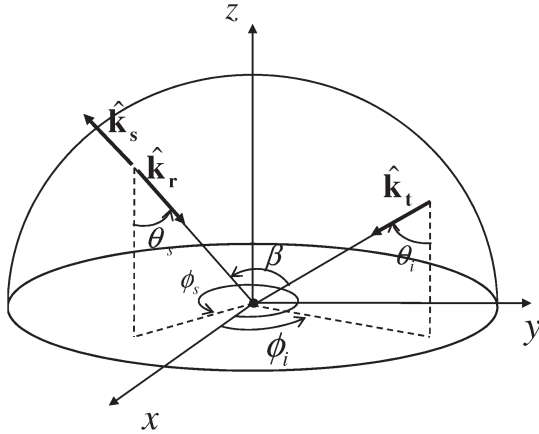


Fig. 2. Definition of the angles  $(\theta_i, \phi_i)$  and  $(\theta_s, \phi_s)$  using the target as the center of the reference frame.

For remote sensing applications, the polarization vectors of incident and scattered waves are usually represented in terms of spherical coordinates. The angles  $(\theta_i, \phi_i)$  and  $(\theta_s, \phi_s)$  are chosen using the target as the center of the reference frame as shown in Fig. 2. Using these conventions, the propagation unit vectors  $\hat{\mathbf{k}}_i = \hat{\mathbf{k}}_t$ ,  $\hat{\mathbf{k}}_s$ , and  $\hat{\mathbf{k}}_r$  are

$$\hat{\mathbf{k}}_i = \hat{\mathbf{k}}_t = \begin{pmatrix} \sin \theta_i \cos \phi_i \\ \sin \theta_i \sin \phi_i \\ -\cos \theta_i \end{pmatrix},$$

$$\hat{\mathbf{k}}_s = \begin{pmatrix} \sin \theta_s \cos \phi_s \\ \sin \theta_s \sin \phi_s \\ \cos \theta_s \end{pmatrix}, \quad \hat{\mathbf{k}}_r = \begin{pmatrix} -\sin \theta_s \cos \phi_s \\ -\sin \theta_s \sin \phi_s \\ -\cos \theta_s \end{pmatrix}. \quad (1)$$

The backscattering configuration ( $\hat{\mathbf{k}}_i = \hat{\mathbf{k}}_t = \hat{\mathbf{k}}_r = -\hat{\mathbf{k}}_s$ ) is obtained for  $(\theta_s = \theta_i, \phi_s = \phi_i + 180^\circ)$ . The forward scattering configuration ( $\hat{\mathbf{k}}_i = \hat{\mathbf{k}}_t = \hat{\mathbf{k}}_s = -\hat{\mathbf{k}}_r$ ) is obtained for  $(\theta_s = 180^\circ - \theta_i, \phi_s = \phi_i)$ . It is also convenient to introduce  $\beta$ , the bistatic angle, defined by:

$$\cos \beta = \hat{\mathbf{k}}_t \cdot \hat{\mathbf{k}}_r, \quad \sin \beta = |\hat{\mathbf{k}}_t \times \hat{\mathbf{k}}_r|. \quad (2)$$

With this definition, the range of the bistatic angle is supposed to be  $0 < \beta < \pi$ .

Two other orthogonal unit vectors are now required to describe the polarization. They are commonly called horizontal and vertical vectors. However, there are an infinite number of directions in the plane of polarization and we will define two as reference directions. In the next sections, we present two different ways of defining these directions.

### B. Definition of Polarimetric Vectors Imposed by Radar Measurement

The coordinate system commonly used in radar is imposed by the SAR or ISAR measurement conditions. In this coordinate system, the ‘‘horizontal’’ plane is defined as the plane tangent to the Earth’s surface. The unit vector normal to this plane will be denoted  $\hat{\mathbf{z}}$ . The bases used to define the polarizations of the incident and scattered waves are denoted  $(\hat{\mathbf{h}}_t, \hat{\mathbf{v}}_t)$  and

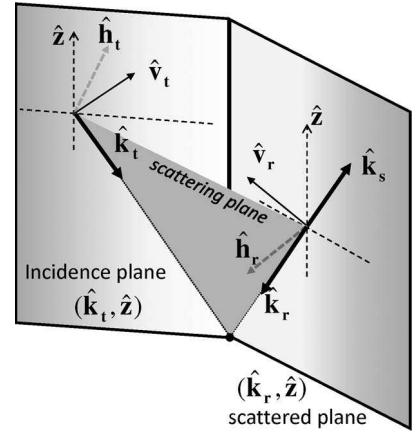


Fig. 3. Definition of the polarization vectors using the incidence and scattered planes.

$(\hat{\mathbf{h}}_r, \hat{\mathbf{v}}_r)$ . These coordinate systems are defined by imposing the following:

- $(\hat{\mathbf{k}}_t, \hat{\mathbf{h}}_t, \hat{\mathbf{v}}_t)$  and  $(\hat{\mathbf{k}}_r, \hat{\mathbf{h}}_r, \hat{\mathbf{v}}_r)$  are right-handed orthonormal bases.
- senses of both  $\hat{\mathbf{v}}$  vectors are the same than the sense of  $\hat{\mathbf{z}}$ .
- both  $\hat{\mathbf{h}}$  vectors are parallel to the horizontal plane.

That gives the following:

$$\hat{\mathbf{h}}_t = \frac{\hat{\mathbf{z}} \times \hat{\mathbf{k}}_t}{|\hat{\mathbf{z}} \times \hat{\mathbf{k}}_t|}, \quad \hat{\mathbf{v}}_t = \hat{\mathbf{k}}_t \times \hat{\mathbf{h}}_t, \quad (3)$$

$$\hat{\mathbf{h}}_r = \frac{\hat{\mathbf{z}} \times \hat{\mathbf{k}}_r}{|\hat{\mathbf{z}} \times \hat{\mathbf{k}}_r|}, \quad \hat{\mathbf{v}}_r = \hat{\mathbf{k}}_r \times \hat{\mathbf{h}}_r, \quad (4)$$

$$\hat{\mathbf{h}}_t = \begin{pmatrix} -\sin \phi_i \\ \cos \phi_i \\ 0 \end{pmatrix}, \quad \hat{\mathbf{v}}_t = \begin{pmatrix} \cos \theta_i \cos \phi_i \\ \cos \theta_i \sin \phi_i \\ \sin \theta_i \end{pmatrix}, \quad (5)$$

$$\hat{\mathbf{h}}_r = \begin{pmatrix} \sin \phi_s \\ -\cos \phi_s \\ 0 \end{pmatrix}, \quad \hat{\mathbf{v}}_r = \begin{pmatrix} -\cos \theta_s \cos \phi_s \\ -\cos \theta_s \sin \phi_s \\ \sin \theta_s \end{pmatrix}. \quad (6)$$

Note that all these equations are derived from [7], except that the right-handed trihedral is different in this paper.

In the backscattering configuration  $(\theta_s = \theta_i, \phi_s = \phi_i + 180^\circ)$ , the BSA convention leads to  $\hat{\mathbf{h}}_t = \hat{\mathbf{h}}_r$  and  $\hat{\mathbf{v}}_t = \hat{\mathbf{v}}_r$ .

These vectors are depicted on Fig. 3.

Note that in this case, we obtain the same results as if we set our coordinate systems using the components parallel and perpendicular to a ‘‘reference’’ plane: the incidence plane  $\hat{\mathbf{z}}, \hat{\mathbf{k}}_t$  for the incident wave, and the scattered plane  $\hat{\mathbf{z}}, \hat{\mathbf{k}}_s$  for the scattered wave.  $\hat{\mathbf{h}}_t$  and  $\hat{\mathbf{h}}_r$  play the role of the orthogonal components to these reference planes, and  $\hat{\mathbf{v}}_t$  and  $\hat{\mathbf{v}}_r$  play the role of the parallel components.

The choice of these bases suits perfectly the monostatic case, since the incidence plane matches the emitted and scattered wave. But for bistatic configuration, that choice may be not as suitable and can lead to interpretation issues.

In this paper, we are not interested in the estimation of  $\theta_E$  and  $\theta_R$  as defined in [8], which are related to two orientation angles relatively to the incident and scattered wave plane. We propose to remove only the influence of antenna orientations, through

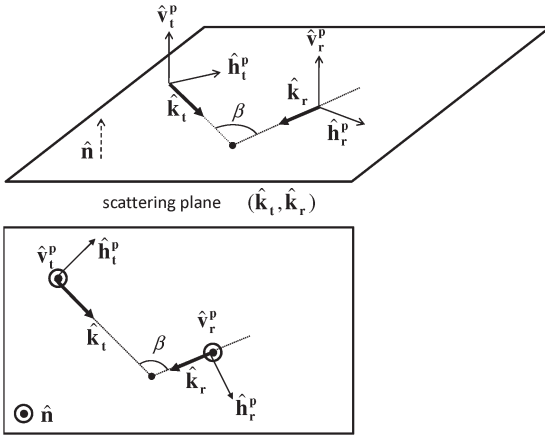


Fig. 4. Definition of the polarization vectors using the scattering plane.

the use of appropriate rotations based on the experiment setup independently of any target properties or orientation.

### C. Polarimetric Vectors Defined Using the Scattering Plane

This is the convention proposed for the example in [9]. The scattering plane  $\hat{\mathbf{k}}_t, \hat{\mathbf{k}}_r$  is defined by the incident and scattered propagation vectors as shown in Fig. 4. Let us denote  $\hat{\mathbf{n}}$  the unit vector normal to the scattering plane:

$$\hat{\mathbf{n}} = \frac{\hat{\mathbf{k}}_t \times \hat{\mathbf{k}}_r}{|\hat{\mathbf{k}}_t \times \hat{\mathbf{k}}_r|}. \quad (7)$$

In this convention, the normal to the scattering plane  $\hat{\mathbf{n}}$  replaces the vertical  $\hat{\mathbf{z}}$ . The polarization vectors will be denoted with a  $p$  exponent. Analogously to the previous section, the polarization bases  $(\hat{\mathbf{k}}_t, \hat{\mathbf{h}}_t^p, \hat{\mathbf{v}}_t^p)$  and  $(\hat{\mathbf{k}}_r, \hat{\mathbf{h}}_r^p, \hat{\mathbf{v}}_r^p)$  are defined so that they are right handed orthonormal bases, and  $\hat{\mathbf{v}}_t^p = \hat{\mathbf{v}}_r^p = \hat{\mathbf{n}}$ . The horizontal vectors can be written:

$$\hat{\mathbf{h}}_t^p = \frac{\hat{\mathbf{n}} \times \hat{\mathbf{k}}_t}{|\hat{\mathbf{n}} \times \hat{\mathbf{k}}_t|}, \quad (8)$$

$$\hat{\mathbf{h}}_r^p = \frac{\hat{\mathbf{n}} \times \hat{\mathbf{k}}_r}{|\hat{\mathbf{n}} \times \hat{\mathbf{k}}_r|}. \quad (9)$$

Now  $\hat{\mathbf{h}}_t^p$  and  $\hat{\mathbf{h}}_r^p$  play the role of the parallel component to the reference plane, and  $\hat{\mathbf{v}}_t^p$  and  $\hat{\mathbf{v}}_r^p$  play the role of the perpendicular component. These vectors are represented on Fig. 4.

### D. Relation Between Both Conventions

$\mathbf{S}$  will refer to the Sinclair matrix expressed with the classical radar convention.  $\mathbf{S}^p$  will refer to the matrix expressed using the scattering plane as reference plane. Both matrices are related by:

$$\mathbf{S} = \mathbf{R}_{\alpha_r}^t \mathbf{S}^p \mathbf{R}_{\alpha_t}. \quad (10)$$

$\mathbf{R}_{\alpha_t}$  and  $\mathbf{R}_{\alpha_r}$  are the rotations to apply in the incident and scattered wave planes, respectively

$$\mathbf{R}_{\alpha_{t,r}} = \begin{pmatrix} \cos \alpha_{t,r} & \sin \alpha_{t,r} \\ -\sin \alpha_{t,r} & \cos \alpha_{t,r} \end{pmatrix}. \quad (11)$$

$R_{\alpha_t}$  is a rotation that maps  $\hat{\mathbf{h}}_t^p$  onto  $\hat{\mathbf{h}}_t$  and  $\hat{\mathbf{v}}_t^p$  onto  $\hat{\mathbf{v}}_t$ . In the same way,  $R_{\alpha_r}$  is a rotation that maps  $\hat{\mathbf{h}}_r^p$  onto  $\hat{\mathbf{h}}_r$  and  $\hat{\mathbf{v}}_r^p$  onto  $\hat{\mathbf{v}}_r$ . Then  $\alpha_r$  and  $\alpha_t$  can be expressed using:

$$\cos \alpha_t = \hat{\mathbf{h}}_t^p \cdot \hat{\mathbf{h}}_t, \quad \sin \alpha_t = \hat{\mathbf{h}}_t^p \cdot \hat{\mathbf{v}}_t, \quad (12)$$

$$\cos \alpha_r = \hat{\mathbf{h}}_r^p \cdot \hat{\mathbf{h}}_r, \quad \sin \alpha_r = \hat{\mathbf{h}}_r^p \cdot \hat{\mathbf{v}}_r. \quad (13)$$

It is also possible to express  $\alpha_r$  and  $\alpha_t$  in terms of  $\beta$ ,  $\theta_{i,s}$  and  $\phi_{i,s}$ . To this end, we shall replace  $\hat{\mathbf{n}}$  in (8) and (9) by its expression given in (7). We are led to:

$$\hat{\mathbf{h}}_t^p = \frac{1}{\sin \beta} (\hat{\mathbf{k}}_r - \cos \beta \hat{\mathbf{k}}_t) \quad (14)$$

$$\hat{\mathbf{h}}_r^p = \frac{1}{\sin \beta} (\cos \beta \hat{\mathbf{k}}_r - \hat{\mathbf{k}}_t) \quad (15)$$

and then the cosines can be written:

$$\cos \alpha_t = \frac{1}{\sin \beta} \sin \theta_s \sin(\phi_i - \phi_s), \quad (16)$$

$$\cos \alpha_r = \frac{1}{\sin \beta} \sin \theta_i \sin(\phi_i - \phi_s). \quad (17)$$

The sines expressions are handled in the same way:

$$\sin \alpha_t = \frac{1}{\sin \beta} (\sin \theta_s \cos \theta_i \cos(\phi_s - \phi_i) + \sin \theta_i \cos \theta_s), \quad (18)$$

$$\sin \alpha_r = -\frac{1}{\sin \beta} (\sin \theta_i \cos \theta_s \cos(\phi_s - \phi_i) + \cos \theta_i \sin \theta_s). \quad (19)$$

## III. THEORETICAL ANALYSIS WITH A SINGLE SPHERE AT LOW FREQUENCY

To illustrate the impact of the chosen convention, we provide the theoretical study of a sphere at low frequency in a general bistatic setting using either the classical radar convention and the one which uses the scattering plane as reference plane. First, the convention linked to the scattering plane is presented since the theoretical model perfectly fits that convention. Then we use the classical convention imposed by measurement and raise some issues induced by the convention.

### A. Definitions of Studied Polarimetric Parameters

The objective of this paper is to see how the bistatic angle can influence polarimetric parameters of different types. For this paper, we will consider the parameters obtained by different polarimetric decompositions. Polarimetric decompositions are typically additive or multiplicative. Standard radar polarimetric decompositions are additive, they are performed as a sort of sum of more elementary quantities. This is the case of the Cloude–Pottier decomposition [10] or the Touzi decomposition [3]. It is also possible to consider a multiplicative decomposition. In the coherent class, such a decomposition could be the polar decomposition of the scattering matrix, as in the quaternion approach proposed by [11] in radar and by [12] in optics.

The additive decompositions consider the target as a sum of different canonical elements randomly distributed, whereas multiplicative decompositions are well adapted to describe a target viewed as a cascade of different elements [13]. Multiplicative decompositions are interesting alternatives when used with multilayer models. They can also differentiate the elements crossed by the ingoing and outgoing waves [14].

Both types of decomposition have different and also interesting physical contents. We choose parameters deduced from the most commonly used decomposition in these both categories: the eigenvalue decomposition with Cloude–Pottier parameters and the Lu–Chipman decomposition. When dealing with one isolated target, we will only consider the parameters which are meaningful for deterministic targets.

It must be noted that other types of parameters could be also used (Huynen parameters, Touzi parameters, etc.) and would have strong connections between them [15]. Here, we are not exhaustive and would not restrict ourselves to representative parameter sets belonging to each type of decompositions: additive and multiplicative.

We use the following notations:  $\mathbf{S}$  is the Sinclair matrix of a target. The four elements of this scattering matrix are  $S_{hH}$ ,  $S_{hV}$ ,  $S_{vH}$  and  $S_{vV}$ , where the first subscript in lower case represents the polarization of the scattered wave and the second in upper case, the polarization of the incident wave

$$\mathbf{S} = \begin{pmatrix} S_{hH} & S_{hV} \\ S_{vH} & S_{vV} \end{pmatrix}. \quad (20)$$

$\mathbf{J}$  is the Jones matrix, defined in FSA conventions and linked to  $\mathbf{S}$  by  $\mathbf{S} = \text{diag}([\mathbf{1} - \mathbf{1}])\mathbf{J}$ . The polarimetric scattering vector  $\hat{\mathbf{k}}$  expressed in the Pauli basis is written as:  $\hat{\mathbf{k}} = \mathbf{1}/\sqrt{2}[\mathbf{2}(S_{hH} + S_{vV}), S_{hH} - S_{vV}, S_{hV} + S_{vH}, \mathbf{j}(S_{hV} - S_{vH})]^t$ . These parameters are:

- The  $\alpha$  angle, given by the inverse cosine of the first component of the polarimetric scattering vector  $\hat{\mathbf{k}}$ .
- The diattenuation defined as a contrast between the intensities obtained for the two eigenpolarizations.
- The Retardance  $R$ , defined as the phase the eigenpolarizations phase difference, traditionally expressed in the Forward Scattering Alignment convention. In this convention,  $R = 180^\circ$  for a mirror in the backscattering case, and  $R = 0^\circ$  for the vacuum in the forward scattering case.

Let us introduce briefly the definition of these parameters in the case of a deterministic target. As mentioned in [12], polarization elements and Jones matrices are divided into two classes: homogeneous, with orthogonal eigenpolarizations and inhomogeneous, with nonorthogonal eigenpolarizations. Mathematically, it corresponds to Jones normal matrices. The basic polarization properties, diattenuation and retardance, of homogeneous polarization elements are characterized by their eigenvalues and eigenpolarizations, and are defined as follows:  $D = (\sigma_{\max}^2 - \sigma_{\min}^2 / \sigma_{\max}^2 + \sigma_{\min}^2)$  where  $\sigma_{\max}$  and  $\sigma_{\min}$  are the singular values of  $\mathbf{J}$ . Note that singular values of  $\mathbf{J}$  are the more similar than the singular values of  $\mathbf{S}$  because they are equal to eigenvalues of  $\mathbf{S}^\dagger\mathbf{S} = \mathbf{J}^\dagger\mathbf{J}$  where  $^\dagger$  denoted the hermitian operator.  $\sigma_{\max}^2$  and  $\sigma_{\min}^2$  represents the transmission (in intensity) of the eigenpolarization.

- In the particular case of an homogenous element (whose Jones matrix is hermitian), then  $\sigma_{\max}^2 = |\lambda_{\max}|^2$  and  $\sigma_{\min}^2 = |\lambda_{\min}|^2$  where  $\lambda_{\max}$  and  $\lambda_{\min}$  are the eigenvalues of  $\mathbf{J}$ , and then diattenuation is

$$D = \frac{|\lambda_{\max}|^2 - |\lambda_{\min}|^2}{|\lambda_{\max}|^2 + |\lambda_{\min}|^2} \quad (21)$$

and retardance is

$$R = |\arg \lambda_{\max} - \arg \lambda_{\min}|. \quad (22)$$

Note that it is possible to use the eigenvalues of Sinclair matrix  $\mathbf{S}$  instead of those of  $\mathbf{J}$  to compute the diattenuation, but not to compute the retardance.

- The diattenuation and the retardance of an inhomogeneous element are more complex, since it has nonorthogonal eigenpolarization. Although the eigenvalues are also well defined for inhomogeneous elements, they do not yield correct retardances and diattenuation. Instead we define the diattenuation and the retardance by applying a polar decomposition of the Jones matrix. This polar decomposition and relative definitions of retardance and diattenuation are given in [12].

The case of  $\alpha$  is more simple. It is given by the inverse cosine of the first component of the polarimetric scattering vector  $\hat{\mathbf{k}}$ . It can also be expressed as

$$\alpha = \arccos \sqrt{\frac{|S_{hH} + S_{vV}|^2}{2(|S_{hH}|^2 + |S_{vV}|^2 + |S_{vH}|^2 + |S_{hV}|^2)}}. \quad (23)$$

One of the great interest of  $\alpha$  is its roll-invariance in the monostatic case, which means it is robust under a change of wave polarization basis. However, we should keep in mind that  $\alpha$  is not necessarily roll-invariant in a bistatic case.

### B. Dielectric Sphere at Low Frequency in the Scattering Plane

The Rayleigh scattering model is applicable when the radius  $r$  of the scattering sphere is much smaller than the wavelength  $\lambda$  of the incident electromagnetic wave.

An isotropic dielectric particle, which matches this hypothesis, has the following Sinclair matrix in the scattering plane [16]:

$$\mathbf{SP} = \begin{pmatrix} \cos \beta & 0 \\ 0 & 1 \end{pmatrix}. \quad (24)$$

The expression of this matrix can be viewed as a geometrical transformation which affects the polarizations axes between the incidence plane and the scattered plane. All occurs as if the scattering on the sphere has only a geometrical effect and no electromagnetic effect. Therefore, the incident electric field  $\mathbf{E}_i$  is projected on the scattered wave plane giving  $E_v$  unchanged and  $\cos \beta E_h$ .  $\mathbf{E}_s$ , the projection of  $\mathbf{E}_i$  on the scattered wave is represented in Fig. 5.

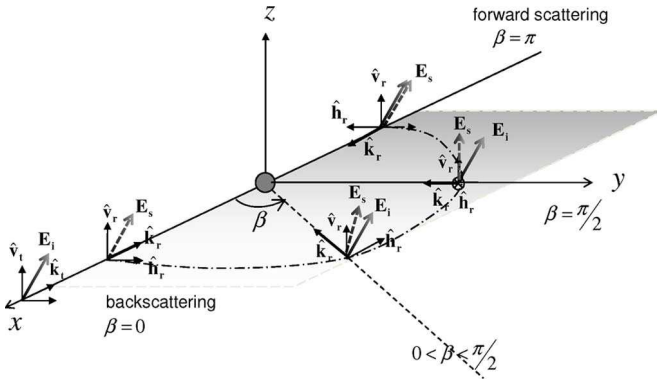


Fig. 5. Transformation of the polarization vectors in the scattered wave plane.

The polarimetric scattering vector  $\hat{\mathbf{k}}$  after normalization is written as:

$$\hat{\mathbf{k}} = \frac{1}{\sqrt{2(1 + \cos^2 \beta)}} \begin{pmatrix} \cos \beta + 1 \\ \cos \beta - 1 \\ 0 \\ 0 \end{pmatrix}. \quad (25)$$

From the canonical expression, we can express some classical polarimetric parameters:

- Diattenuation:

$$D = \frac{1 - \cos^2 \beta}{1 + \cos^2 \beta}, \quad (26)$$

- $\alpha$  angle:

$$\alpha = \arccos \frac{1 + \cos \beta}{\sqrt{2(1 + \cos^2 \beta)}}, \quad (27)$$

- The retardance of the dielectric sphere will be equal to  $180^\circ$  for  $\beta \in [0, 90^\circ]$  and equal to  $0$  for  $\beta \in [90^\circ, 180^\circ]$ .

In the expression of the polarimetric parameters, we can distinguish between the target's property and the geometrical effects due to the configuration. The example of the diattenuation in the case of the sphere at low frequency perfectly illustrates this effect. Diattenuation can be viewed as the anisotropy of the target, as it means a change in amplitudes of the fields. For the sphere at low frequency, it is null near the backscattering and forward scattering cases and maximum near  $\beta = \pi/2$ , as the scattering matrix becomes similar to a polarizer on the vertical polarization.

#### C. Dielectric Sphere at Low Frequency With Real Measurement Convention

With the classical radar measurement convention, the Sinclair matrix can be expressed using (10) and it leads to the following Pauli scattering vector  $\hat{\mathbf{k}}$ :

$$\hat{\mathbf{k}} = \frac{1}{\sqrt{2(1 + \cos^2 \beta)}} \begin{pmatrix} (\cos \beta + 1) \cos(\alpha_i + \alpha_s) \\ (\cos \beta - 1) \cos(\alpha_i - \alpha_s) \\ (\cos \beta - 1) \sin(\alpha_i - \alpha_s) \\ j(\cos \beta + 1) \sin(\alpha_i + \alpha_s) \end{pmatrix} \quad (28)$$

leading to the  $\alpha$  angle:

$$\alpha = \arccos \frac{|(1 + \cos \beta) \cos(\alpha_i + \alpha_s)|}{\sqrt{2(1 + \cos^2 \beta)}}. \quad (29)$$

We can note that in this case, any desired value for  $\alpha$  can be obtained for a given bistatic angle, if  $\theta_i, \phi_i, \theta_s, \phi_s$  are chosen accordingly. That means that geometry allows to exhibit some very particular cases, where  $\mathbf{S}$  is, for example, strongly non-symmetric even for a symmetric target.

#### D. Metallic Sphere at Low Frequency

The solution corresponding to a metallic sphere is different from the solution for a dielectric sphere [16]. A metallic particle considered at low frequency has the following Sinclair matrix in the scattering plane:

$$\mathbf{S}^P = \begin{pmatrix} \frac{1}{2} + \cos \beta & 0 \\ 0 & \frac{1}{2} \cos \beta + 1 \end{pmatrix}. \quad (30)$$

It is then possible to deduce about our polarimetric parameters that:

- Diattenuation is

$$D = \frac{\frac{3}{4}(1 - \cos^2 \beta)}{\frac{5}{4}(\cos^2 \beta + 1) + 2 \cos \beta}. \quad (31)$$

It is zero for  $\beta = 0^\circ$  and  $\beta = 180^\circ$ , and maximum for  $\beta = 120^\circ$

- $\alpha$  is

$$\alpha = \arccos \frac{3|1 + \cos \beta|}{\sqrt{10 \cos^2 \beta + 10 + 16 \cos \beta}}. \quad (32)$$

It is null for  $\beta = 0^\circ$ , is maximum and equal to  $90^\circ$  for  $\beta = 180^\circ$ , and we have  $\alpha = 45^\circ$  for  $\beta = 120^\circ$ .

- The retardance of the metallic sphere will be equal to  $180^\circ$  for  $\beta \in [0^\circ, 120^\circ]$  and equal to  $0^\circ$  for  $\beta \in [120^\circ, 180^\circ]$ .

The simple analytical expressions  $\alpha$ , retardance, and diattenuation computed on the theoretical sphere at low frequency are presented in Fig. 6. These expressions correspond to the scattering plane convention. Analytical expression for the metallic case with the measurement reference plane can be also found but they are too complex to be easily commented.

## IV. ANALYSIS OF THE MEASUREMENT OF ONE TO FOUR MIE SPHERES

In this section, we will present and analyze polarimetric bistatic measurements performed on one to four Mie spheres and compare them to simulation results.

#### A. Description of the Setup

Emission and reception antennas are carried on trolleys. They are pulled by engines that ensure a reproducibility of location of antennas better than  $10^{-2}^\circ$ . They can move either on a circular rail of radius 5.5 m that is lifted 2.5 m above the ground, or on a line segment rail located on the top of the anechoic chamber. This experiment is illustrated in Fig. 7 and pictured in Fig. 8.

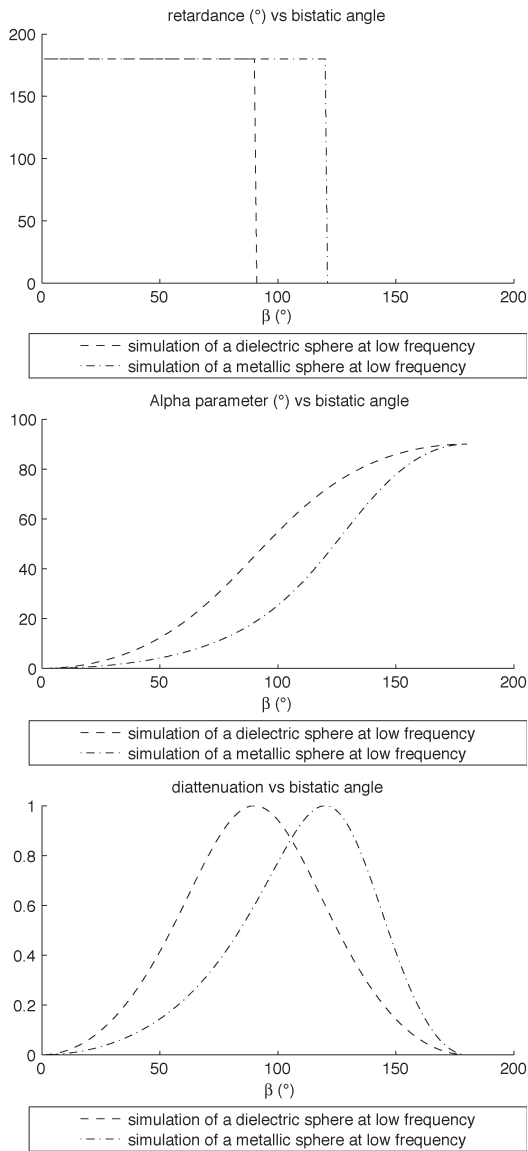


Fig. 6. Polarimetric parameters for a theoretical sphere at low frequency: retardance,  $\alpha$  and diattenuation.

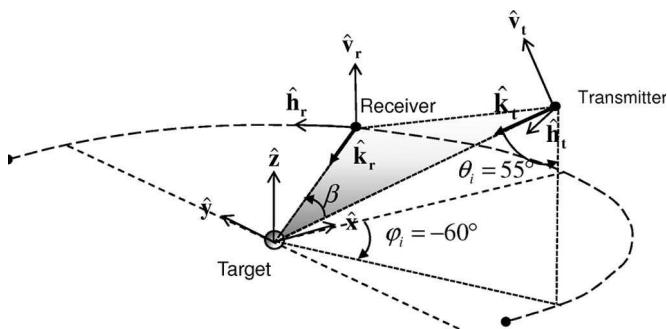


Fig. 7. Configuration and antennas location.

The targets, one, two and four 38-mm radius metallic spheres stand on the top of a polyfoam column rotatable around the  $z$ -axis. The height of this platform can be adjusted to obtain elevation angles between  $70^\circ$  and  $90^\circ$ .

To achieve a configuration representing both an elevation bistatic angle and an azimuth bistatic angle, the emitter is set

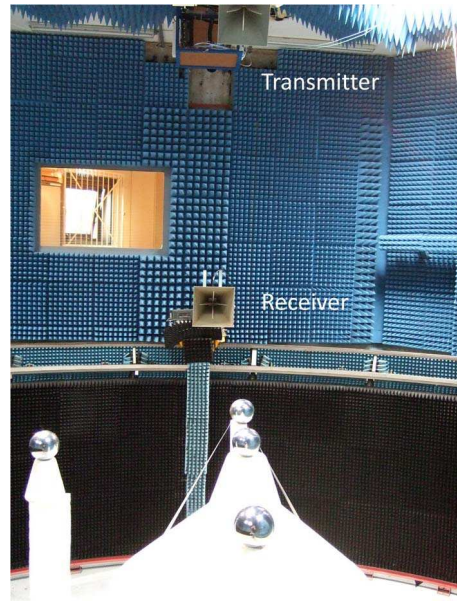


Fig. 8. Picture of the experiment.

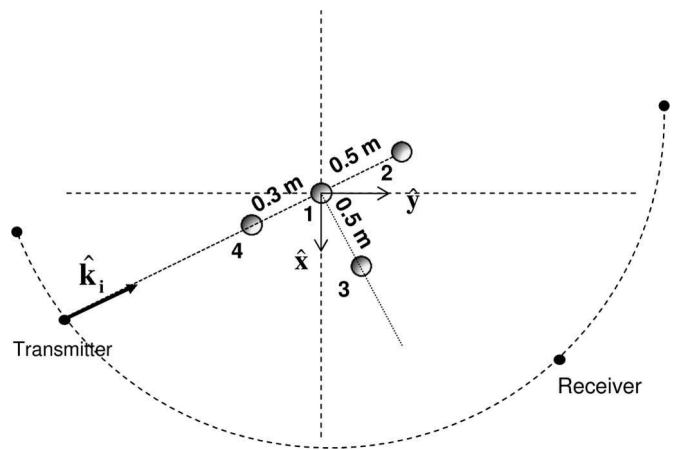


Fig. 9. Positions of spheres.

on the linear rail at a fixed position defined by  $\theta_i = 55^\circ$  and  $\phi_i = -60^\circ$ , whereas the receiver is moving on the circular rail, as shown in Fig. 7. The position of the receiver is defined by  $\theta_s = 90^\circ$  and  $\phi_s \in [-85^\circ, 100^\circ]$ . The frequency ranges from 1.47 GHz to 1.68 GHz with 801 frequency points.

The spheres positions are represented in Fig. 9 which is a top view of the chamber. In the case of one sphere, only sphere 1 is present on the center of the chamber. In the case of two spheres, spheres 1 and 2 are present. They are both located in the incidence plane. In the case of four spheres, there is no particular symmetry.

The calibration implies the measurements of different calibration targets (several spheres and oriented dihedral corners), each with a theoretically exactly known RCS matrix in the monostatic configuration. Then, the correction factors are applied to the bistatic configuration. A final measurement is performed on another canonical target in order to determine the accuracy. In this experiment, the accuracy has been found to be about less than  $1.2 \text{ dB.m}^2$  for the maximum gap in the frequency range.

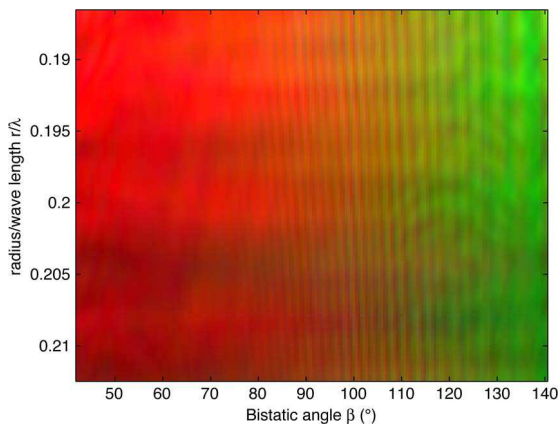


Fig. 10. Polarimetric representation of the fields scattered by one sphere according to frequency and bistatic angle—Red:  $|hH + vV|^2$ , Green:  $|hH - vV|^2$ , Blue:  $|hV + vH|^2$ .

### B. Theoretical

Due to the radius of the spheres and the frequency used, the Rayleigh scattering model cannot be applied. In contrast to Rayleigh scattering, the Mie scattering solution [6] is valid for all possible ratios of diameter to wavelength, although the technique results in numerical summation of infinite sums [16].

### C. Results

1) *Polarimetric Color Composite Representation*: We choose a color composite representation of our polarimetric signal. Three polarimetric parameters can be used in the composite and can be assigned to a different color (Red, Green, Blue) output to create a color image. In a monostatic radar configuration, the Pauli basis is often chosen to create such color composite image. In this paper, we generalize this representation to a bistatic mode. The red value corresponds to the measured energy level of that pixel in  $|hH + vV|$  polarization, the green value to the measured energy level of that pixel in  $|hH - vV|$  polarization, and the blue value to  $|hV + vH|$  polarization. In a monostatic configuration, if we consider a reciprocal target, then the reciprocity theorem yields  $S_{hV} = S_{vH}$  in the BSA convention, and three colors are sufficient to represent the three independent channels. In the general bistatic case, this representation does not allow to show the four independent polarimetric channels. However, it can still be used in this section with the scattering plane as the reference plane, because cross-polarizations returns of a symmetric target are null [17].

2) *One Mie Sphere*: An example of this type of representation is given in Fig. 10 for one Mie sphere. Some ripples are present on the figure, especially for large bistatic angles. After some investigations, we found that they are due to an interference with another bright point located far away from the target. However, we are not able to filter it because frequency bandwidth is not large enough. But these ripples do not contain any physical useful information here.

Like the sphere at low frequency, there is a continuous change according to  $\beta$  from a signal where  $S_{hH}$  and  $S_{vV}$  have the same sign (Retardance,  $R = 180^\circ$ , and angle  $\alpha = 0^\circ$ ) to

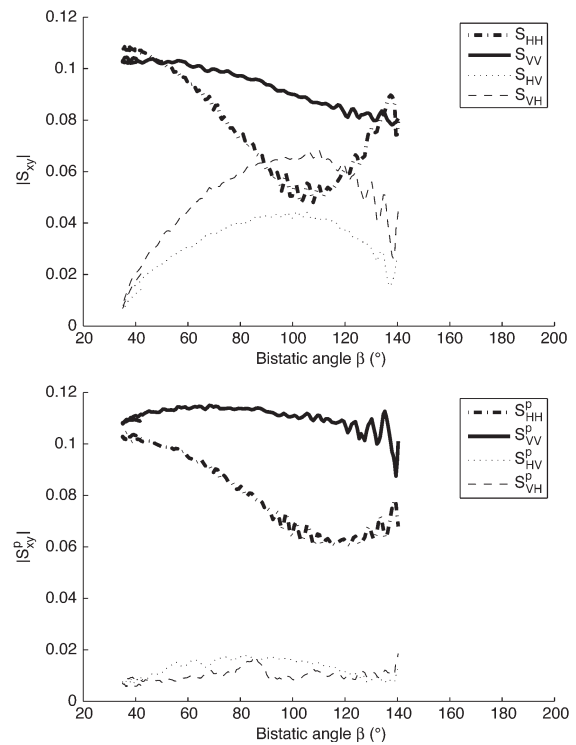


Fig. 11. Polarimetric amplitudes of the fields scattered by one sphere: comparison of the two conventions (incidence plane and scattering plane) for  $r/\lambda = 0.2$ .

a signal where they have opposite signs. We see in Fig. 10 that this transition from a polarimetric signature to another one is not symmetric with respect to  $\beta = 90^\circ$ ; the transition area between the two polarimetric colors lied around  $\beta = 110^\circ$  with the second convention. This transition is mathematically obtained for  $\alpha = R = 90^\circ$ . This seems to be close from the minimum of  $S_{hH}$  which can be seen on Fig. 11.

Moreover, Fig. 11 also enables us to confirm that with the incident plane as the reference plane, cross-polarizations returns of a symmetric target are neither null nor equal. When choosing the other convention based on the scattering plane, the cross-polarization returns are null, which is a well-known result [18]. All classical symmetry relations are discussed in the second convention, as in [17].

Now, let us see what is the behavior of our previous polarimetric parameter in the case of one Mie sphere.  $\alpha$ , retardance and diattenuation computed on the measured and simulated Mie sphere are presented in Fig. 12. They are compared with the simple analytical expressions presented in Section III for single spheres at low frequency.

From this figure, we can deduce that:

- When dealing with a sphere in resonance region rather than a sphere at low frequency, retardance is no longer discontinuous.
- The transition  $R = 90^\circ$  is obtained for  $\beta \simeq 110^\circ$ .
- The transition  $\alpha = 45^\circ$  is obtained for the same value of the bistatic angle, ie.  $\beta \simeq 110^\circ$ .
- Effects on diattenuation are of two types: the maximum of the function lies now around 0.5 instead of 1. This maximum is reached for  $\beta \simeq 110^\circ$  too.

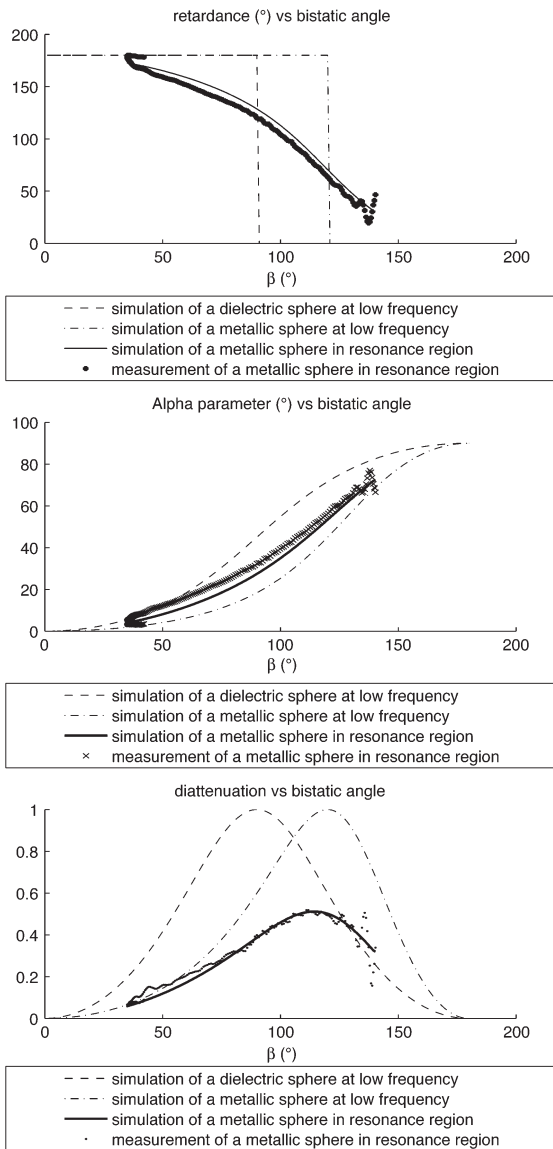


Fig. 12. Polarimetric parameters compared for one measured sphere in the resonance region and theoretical results: retardance,  $\alpha$  and diattenuation.

3) *Two and Four Mie Spheres:* When the number of spheres increases, destructive and constructive interference appear and cross-polarizations remain almost null when using the scattering plane. The behavior seems to indicate that only the usual interferences effects due to the path length difference affect the span of the signals. Signals are presented in Fig. 13 in the case of two spheres and in Fig. 14 in the case of four spheres.

V. MEASUREMENT OF A CLOUD OF MIE SPHERES

A. Polarimetric Interest

We have shown that even with four Mie spheres, multiple scattering effects could not be observed. In an attempt to examine a target that would behave like a natural medium and, if possible, produce depolarization effects, we drastically increased the number of spheres. Hence, in this section, the same polarimetric analysis is conducted for a cloud of a thousand spheres, and we discuss the possible presence of multiple scattering.

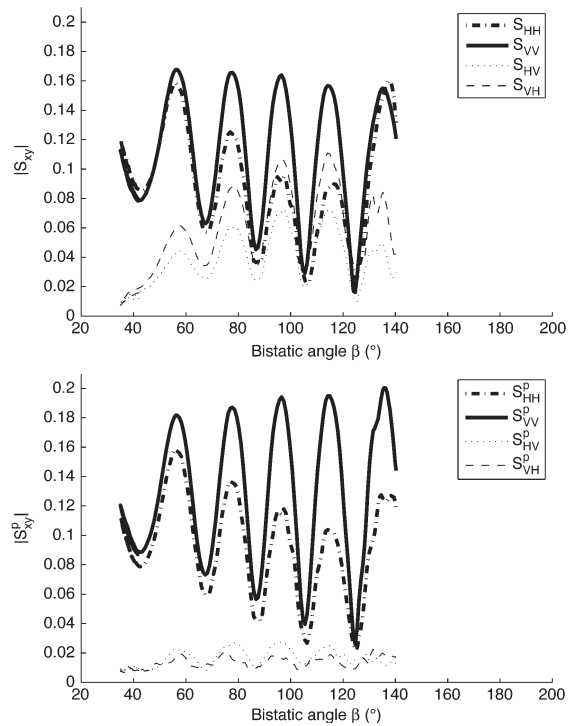


Fig. 13. Polarimetric amplitudes of the fields scattered by two spheres: comparison of both convention (classical radar convention and scattering plane) for  $r/\lambda = 0.2$ .

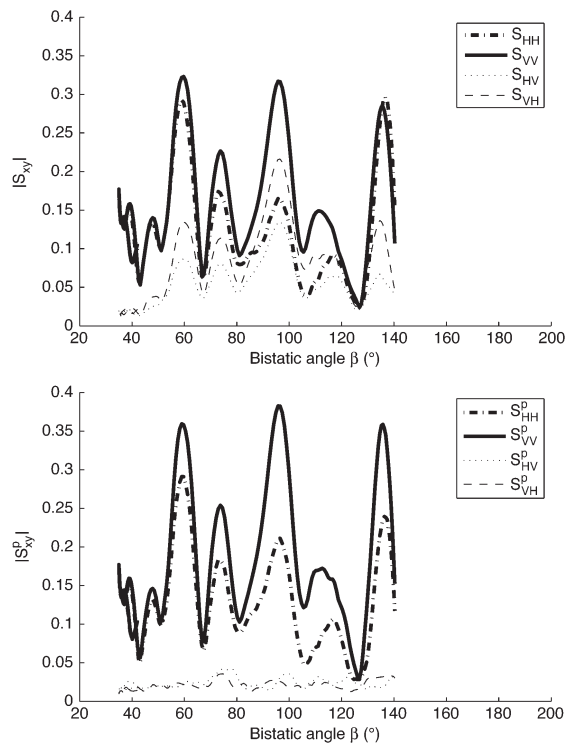


Fig. 14. Polarimetric amplitudes of the fields scattered by four spheres: comparison of both convention (classical radar convention and scattering plane) for  $r/\lambda = 0.2$ .

As depolarization effects and random mechanisms are also investigated, two new polarimetric parameters are considered:

- depolarization, obtained by the Lu and Chipman decomposition [19] of the Mueller matrix  $M$ . This decomposition

can be regarded as a generalized polar decomposition for depolarizing Mueller matrices into three factors. Lu and Chipman has shown in [19] that the Mueller matrix can be decomposed as  $M = M_{\Delta} M_R M_D$  where the elementary matrices  $M_{\Delta}$ ,  $M_R$ ,  $M_D$  represent a depolarizer, a retarder and a diattenuator. This decomposition makes possible to extend the definition of diattenuation and retardance to non-deterministic targets. Depolarization is defined from the depolarizer element

$$M_{\Delta} = \begin{pmatrix} 1 & \mathbf{0}^t \\ \mathbf{0} & \mathbf{m}_{\Delta} \end{pmatrix} \quad (33)$$

where

$$\Delta = 1 - \frac{\text{trace}(\mathbf{m}_{\Delta})}{3}. \quad (34)$$

- entropy, introduced by Cloude and Pottier [10]. This parameter is introduced in the eigenvector decomposition of the coherency matrix. This coherency matrix, defined by  $\mathbf{T} = \langle \mathbf{k}\mathbf{k}^{\dagger} \rangle$  can be decomposed by means of eigendecomposition as

$$\mathbf{T} = \lambda_1 \mathbf{k}_1 \mathbf{k}_1^{\dagger} + \lambda_2 \mathbf{k}_2 \mathbf{k}_2^{\dagger} + \lambda_3 \mathbf{k}_3 \mathbf{k}_3^{\dagger} \quad (35)$$

and is interpreted as an incoherent sum of three fully deterministic scattering mechanisms, described by eigenvectors  $\mathbf{k}_i$  and weighted by eigenvalues  $\lambda_i$ . Entropy  $H$  represents the randomness of the scattering mechanisms present in the averaged pixels, when interpreting  $p_i$  as the probability of a certain scattering mechanism  $\mathbf{k}_i$ :  $H = -\sum_{i=1}^3 p_i \log_3 p_i$ , where  $p_i = \lambda_i / \sum_{i=1}^3 \lambda_i$ .

Moreover,  $\bar{\alpha}$  is now an average defined in the sense of Bernoulli [20], weighted with the relative size of eigenvalues as  $\bar{\alpha} = \sum_{i=1}^3 p_i \alpha_i$  where each  $\alpha_i$  describes a unit eigenvector  $\mathbf{k}_i$ .

An incoherent averaging of several values is required to obtain these parameters because they are determined in terms of second order statistics of scattering matrix elements. The most widely used and implemented method in SAR imaging consists in performing this statistical average on several neighboring pixels. In our experiment, we chose to average over the frequency since the bandwidth is small enough to expect no meaningful variations of the deterministic parameters (diattenuation, retardance and  $\alpha$  angle). In both cases, we should keep in mind that this type of averaging is not physically correct.

### B. Setup

In order to produce a cloud of thousand randomly distributed spheres, we chose to include them in a medium made of polystyrene. The target is a stack of 26 circular polystyrene sections with a thickness ranging 3–10 mm and a diameter equal to 19.5 cm. The total height of the cylinder thus obtained is 13 cm. Each of these slices contains  $30 \pm 2$  4.5 mm diameter metal balls randomly distributed in the disc. All in all, 780 spheres were distributed in the volume, which gives them an average spacing of 2.7 cm. The thickness of the layers is also random to prevent array effects between the different layers. The target thus obtained is pictured in Fig. 15. Polystyrene is



Fig. 15. Targets of a cloud of spheres.

almost transparent at our wavelengths. To validate this assumption, a measurement was made of a single polystyrene cylinder of the same size in the same configuration. The resulting cross section was at least 20 dB below the one of the full target for bistatic angles lower than  $140^\circ$ . Moreover, in this experiment, the accuracy has been found to be about less than  $0.3 \text{ dB.m}^2$  for the maximum gap in the frequency range.

We draw our reasoning according to the scattering plane. Thus, both receiver and emitter are located on the circular rail ( $\theta_i = \theta_s = 90^\circ$ ). The emitter is fixed at  $\phi_i = 0$ , the receiver is moving from  $\phi_s = 4^\circ$  to  $\phi_s = 190^\circ$  with a  $0.5^\circ$  step. The frequency range is [29 GHz, 31 GHz] with a 15 MHz step. Actually, pure backscattering and forward direction configurations are not practically available. Because of the isolation required between transmission and reception antennas, the pure monostatic case could not be achieved and consequently no measurement has been collected for bistatic angles lower than  $4^\circ$ . In addition, for the pure forward scattering case, the measurements are noised by the strong response of the transmitter, as it is aligned with the receiver and the target. Isolation between both antennas has been proven to be sufficient (up to 20 dB) only for  $\beta < 140^\circ$ . That is why results presented for  $\beta > 140^\circ$  should be considered carefully.

### C. Analysis of the Results

This experimental data shown in Fig. 16 indicate that:

- The number of fringes is directly related to the dimension of the volume containing the spheres.
- Amplitudes of the crosspolarization signals (that are visible in blue color) seem to be significant in comparison with the copolarizations ones. As the color composite representation does not allow to see the behavior of the four polarimetric channels, we have plotted in Fig. 17 the different signals averaged in the frequency bandwidth. This figure confirms that crosspolarization signals are significant.

We try now to explain these observations using a very simple approach. If we neglect multiple scattering effects, then the scattering by the whole cloud of spheres results in the coherent sum of the fields scattered by each of its components. Each contribution is weighted by a phase shift induced by the relative

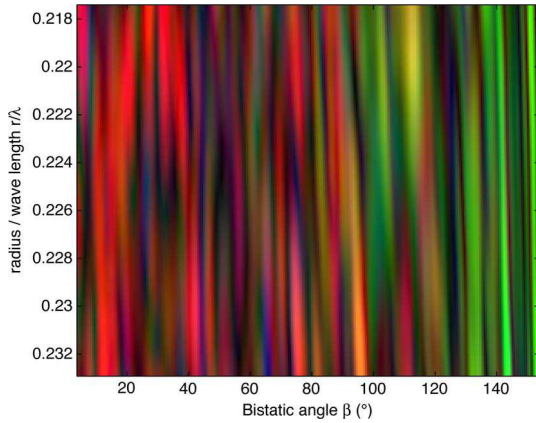


Fig. 16. Polarimetric representation of the fields scattered by a cloud of spheres according to bistatic angle and to radius/wavelength: results of measurement—Red:  $|hH + vV|^2$ , Green:  $|hH - vV|^2$ , Blue:  $|hV + vH|^2$ .

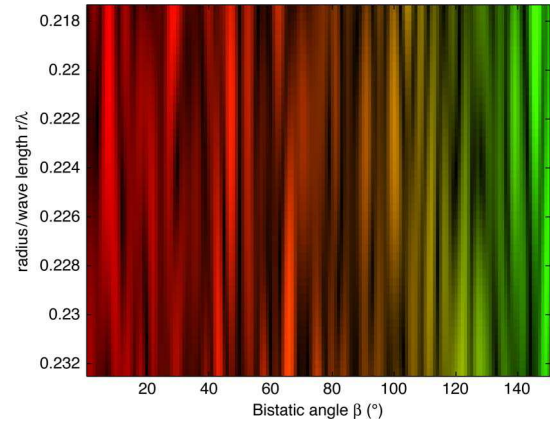


Fig. 18. Polarimetric representation of the fields scattered by a cloud of spheres according to bistatic angle and to radius/wavelength: results of simulation neglecting multiple scattering—Red:  $|hH + vV|^2$ , Green:  $|hH - vV|^2$ , Blue:  $|hV + vH|^2$ .

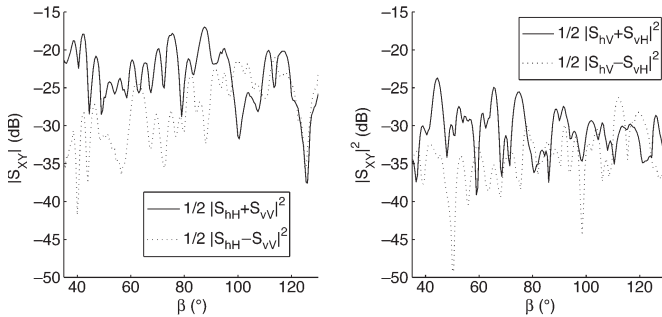


Fig. 17. Polarimetric amplitudes of the fields scattered by the cloud of spheres computed in the Pauli basis.

position of the scatterers. Using the plane wave hypothesis, the Sinclair matrix  $S$  is given by

$$S(f, \beta) = S_{\text{one sphere}}(f, \beta) \times \sum_i \exp\left(j2\pi \frac{f}{c}(x_i \cos \beta + y_i \sin \beta)\right) \quad (36)$$

where  $x_i$  and  $y_i$  are the coordinates of the spheres, and  $S_{\text{one sphere}}$  is their Sinclair matrix.

Thus resulting fields computed lead to the representation in Fig. 18. This figure confirms the presence of fringes. The simulation thus explains their presence by the variation of the total path length according to the bistatic angle between extreme spheres situated on the borders of the volume. These fringes can be viewed as a speckle phenomenon. The “size” of the speckles is a function of the wavelength and the size of the target which forms the speckle pattern. This is the case because when the angle of scattering changes, such that the relative path difference between wave scattered from the center of the target and wave scattered from the edge of the illuminated area changes by  $\lambda$ , the intensity becomes uncorrelated. Then, the parameter  $\lambda/D$ , where  $D$  is the diameter of the target, gives a rough order of magnitude of the angular size of the fringes. Here, we have  $\lambda/D = 2.9^\circ$ , which is a fairly representative of the size of fringes observed in terms of  $\beta$ .

Besides, simulation and measurements agree on radiometric and polarimetric behaviors in the first order. This means that

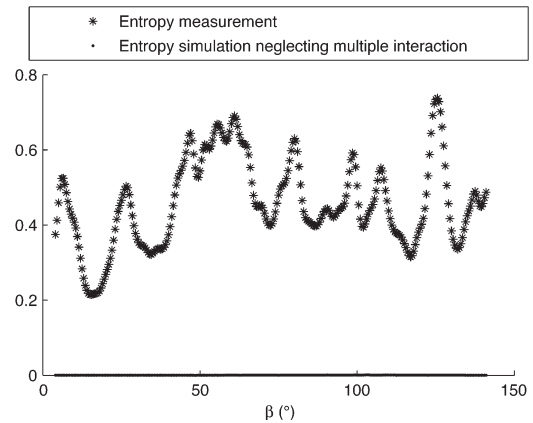


Fig. 19. Entropy parameter according to bistatic angle for a cloud of spheres in resonance region: results of simulation and measurement.

multiple scattering can be indeed neglected for radiometric calculations and determinist polarimetric parameters calculation (first moments). However, there is one limitation of this type of simulation: cross-polarization contributions are null, although they are visible in Fig. 18 in blue color, even though this is a weak effect.

Regarding second moments, polarimetric parameters dedicated to non-deterministic targets must be considered. As expected for those parameters, a simulation ignoring multiple scattering does not match with the measurements. Fig. 19 shows the entropy  $H$  from simulation and measurement. The model leads to a insignificant amount of randomness and then a entropy null, while measurements show a level of entropy oscillating around 0.5. Due to the strong speckle noise, we cannot deduce any trends from the measurements regarding the evolution of entropy with the bistatic angle  $\beta$ . The same type of comparisons can be made on the parameter of depolarization in Fig. 20. As expected, depolarization is present in the measurements while being null in the simulation. Again, we cannot conclude on the dependency of depolarization with the bistatic angle due to a too strong noise on the measurements. We can also note that the shape of depolarization curve is very similar to the shape of entropy curve.

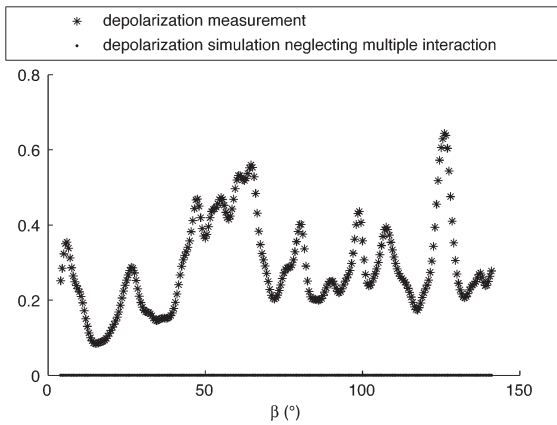


Fig. 20. Depolarization parameter according to bistatic angle for a cloud of spheres in resonance region: results of simulation and measurement.

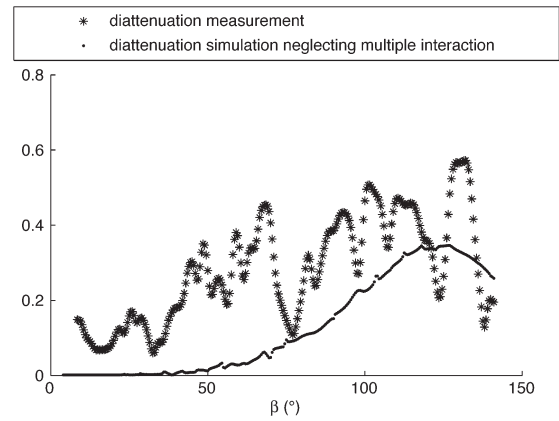


Fig. 23. Diattenuation parameter according to bistatic angle for a cloud of Mie spheres: results of simulation and measurement.

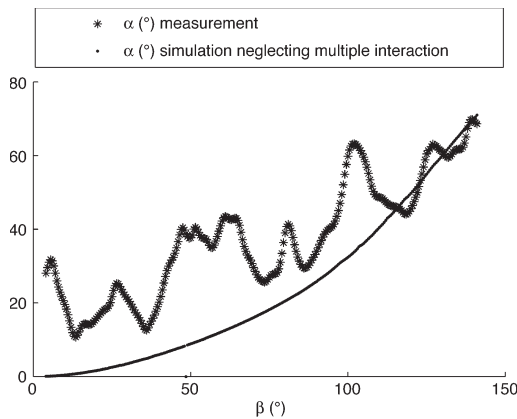


Fig. 21.  $\bar{\alpha}$  angle according to bistatic angle for a cloud of Mie spheres: results of simulation and measurement.

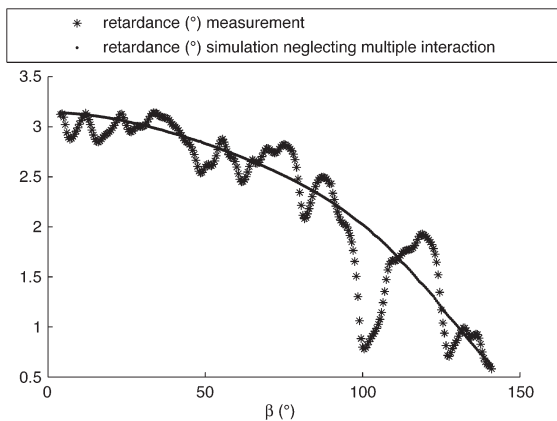


Fig. 22. Retardance parameter according to bistatic angle for a cloud of Mie spheres: results of simulation and measurement.

The same type of comparisons can be made on the parameters of  $\bar{\alpha}$  angle, retardance and diattenuation on Figs. 21–23. The global behavior of  $\bar{\alpha}$  angle is well simulated despite measurement noise. Modelling without multiple scattering also matches for the retardance and diattenuation parameters.

We can conclude that multiple scattering can be effectively neglected here for all the considerations concerning polarimetric parameters, which can be defined in a deterministic case (including  $\bar{\alpha}$  angle, retardance and diattenuation). On the other hand, as multiple scattering plays an important role

in the parameters connected to the randomness of the target (depolarization and entropy), multiple scattering cannot be neglected for a random medium. Note that the statistical averaging has been performed using different frequencies, and that this averaging makes it possible to obtain significant entropy and depolarization. So far, we cannot really discuss the impact of bistatic settings on entropy and depolarization, as they tend to be very sensitive to measurements noise and interferences fringes. Overall, it seems that they are not varying with the bistatic angle  $\beta$ , but more measurements and finer modeling would be required to conclude on that point.

## VI. CONCLUSION

This paper has drawn several points. First, two antenna rotations are not necessarily equivalent to a single rotation of the target in a bistatic setting. Hence, antenna rotation angles can be estimated from the measurements setup and applied in order to choose a convenient reference plane. According to the author, the scattering plane is the most fitting in a general bistatic setting because it allows more intuitive polarimetric analysis of isotropic scatterers and reduces the geometric parameters of antennas to a single angle  $\beta$ .

Second, concerning the influence of antennas relative position on polarimetric information, it was shown, both from simulation and measurements, that it can be very significant for large bistatic angles. From the targets under study, we note mostly:

- strong amplitude changes or diattenuation effects according to the bistatic angle  $\beta$ . These effects are null for backscattering and forward scattering configurations but reach a maximum near the orthogonal position ( $90^\circ$  for dielectric spheres and  $120^\circ$  for metallic sphere at low frequency, around  $110^\circ$  for a metallic sphere in the resonance region. ). The maximum value reached for diattenuation is very high ( $D = 0.6$  for the metallic sphere and  $D = 1$  for the dielectric sphere which corresponds to a pure diattenuator).
- Both retardance and alpha angle evolve continuously from ( $180^\circ$  to  $0^\circ$  and from  $0^\circ$  and to  $90^\circ$ , respectively). The bistatic angle  $\beta_{lim}$  for which there is a transition ( $\alpha = 45^\circ$  or  $R = 90^\circ$ ) can lie between  $\beta_{lim} = 90^\circ$  and  $\beta_{lim} = 120^\circ$ ; it corresponds to the maximum of diattenuation.

This paper may then be considered as a preliminary step in a work which would try to isolate target features from the bistatic angle  $\beta$ . We can anticipate that this task will be difficult in the most general case, for the following reasons:

- In the case of a single target having a symmetry axis, we can think that the geometrical effect described by  $\beta$  will remain simple so that it can be modeled and might be eventually corrected. But there could be a neighborhood of  $\beta = 110^\circ$  where the signal/ noise ratio might be an issue.
- For distributed target, regardless of the frequency, the geometrical effects are much more difficult to model and will be probably very difficult to invert even when the volume has a symmetry axis.

#### ACKNOWLEDGMENT

The authors would like to thank Mr. A. Cheraly who carried out the practical measurements and for the fruitful discussions on the ONERA measurement facility. The authors would also like to thank the anonymous reviewers whose remarks have greatly contributed to the improvement of the quality of this paper.

#### REFERENCES

- [1] J. Huynen, "Phenomenological theory of radar targets," Ph.D. dissertation, Tech. Univ., Delft, The Netherlands, 1987.
- [2] E. Pottier and S. R. Cloude, "Application of the  $h/a/\alpha$  polarimetric decomposition theorem for land classification," *Proc. SPIE*, vol. 3120, pp. 132–143, Jul. 1997.
- [3] R. Touzi, "Target scattering decomposition in terms of roll-invariant target parameters," *IEEE Trans. Geosci. Remote Sens.*, vol. 45, no. 1, pp. 73–84, Jan. 2007.
- [4] J. Praks, E. C. Koeniguer, and M. T. Hallikainen, "Alternatives to target entropy and alpha angle in SAR polarimetry," *IEEE Trans. Geosci. Remote Sens.*, vol. 47, no. 7, pp. 2262–2274, Jul. 2009.
- [5] C. Titin-Schnaider, "Physical meaning of bistatic polarimetric parameters," *IEEE Trans. Geosci. Remote Sens.*, vol. 48, no. 5, pp. 2349–2356, May 2010.
- [6] G. Mie, "Beiträge zur optik trüber medien, speziell kolloidaler metallösungen," *Ann. Phys.*, vol. 25, pp. 377–445, 1908.
- [7] F. T. Ulaby and C. Elachi, *Radar Polarimetry for Geoscience Applications*, Y. Bar-Shalom, Ed. Norwood, MA: Artech House, 1990.
- [8] C. Titin-Schnaider, "Polarimetric characterization of bistatic coherent mechanisms," *IEEE Trans. Geosci. Remote Sens.*, vol. 46, no. 5, pp. 1535–1546, May 2008.
- [9] A. Ishimaru, *Wave Propagation and Scattering in Random Media*. Los Alamitos, CA: IEEE Comput. Soc. Press, 1978.
- [10] S. R. Cloude and E. Pottier, "A review of target decomposition theorems in radar polarimetry," *IEEE Trans. Geosci. Remote Sens.*, vol. 34, no. 2, pp. 498–518, Mar. 1996.
- [11] J. Souyris and C. Tison, "Polarimetric analysis of bistatic SAR images from polar decomposition: A quaternion approach," *IEEE Trans. Geosci. Remote Sens.*, vol. 45, no. 9, pp. 2701–2714, Sep. 2007.
- [12] S.-Y. Lu and R. A. Chipman, "Homogeneous and inhomogeneous Jones matrices," *J. Opt. Soc. Amer. A, Opt. Image Sci.*, vol. 11, no. 2, pp. 766–773, Feb. 1994. [Online]. Available: <http://josaa.osa.org/abstract.cfm?URI=josaa-11-2-766>
- [13] S. Cloude, "On the status of bistatic polarimetry theory," in *Proc. IEEE IGARSS*, Jul. 25–29, 2005, vol. 3, pp. 2003–2006.
- [14] R. Ossikovski, "Analysis of depolarizing Mueller matrices through a symmetric decomposition," *J. Opt. Soc. Amer. A, Opt. Image Sci.*, vol. 26, no. 5, pp. 1109–1118, May 2009.
- [15] E. Colin-Koeniguer, N. Trouvé, and J. Praks, "A review about alternatives to classical Polarimetric SAR parameters," in *Proc. EUSAR*, 2010, pp. 414–417.
- [16] G. T. Ruck, *Radar Cross Section Handbook*, G. T. Ruck, Ed. New York: Plenum, 1970.
- [17] H. V. D. Hulst, *Light Scattering by Small Particles*. New York: Dover, 1981.
- [18] G. E. Heath, "Bistatic scattering reflection asymmetry, polarization reversal asymmetry, and polarization reversal reflection symmetry," *IEEE Trans. Antennas Propag.*, vol. AP-29, no. 3, pp. 429–434, May 1981.
- [19] S.-Y. Lu and R. A. Chipman, "Interpretation of mueller matrices based on polar decomposition," *J. Opt. Soc. Amer. A, Opt. Image Sci.*, vol. 13, no. 5, pp. 1106–1113, May 1996. [Online]. Available: <http://josaa.osa.org/abstract.cfm?URI=josaa-13-5-1106>
- [20] S. R. Cloude and E. Pottier, "An entropy based classification scheme for land applications of polarimetric SAR," *IEEE Trans. Geosci. Remote Sens.*, vol. 35, no. 1, pp. 68–78, Jan. 1997.



**Nicolas Trouvé** born February 8, in 1985, in France, received his master degree and Dipl. Ing. in optical engineering from Institut d'Optique Graduate School-ParisTech, Palaiseau, France, in 2008. He is currently working in ONERA, Palaiseau, France, as a Ph.D. student from Ecole Polytechnique Doctoral School.

His research interest focuses on radar and optical polarimetry and bistatic polarimetry. His studies also currently cover polarimetric and interferometric SAR image processing and polarimetric target detection

in urban settings.



**Elise Colin Koeniguer** born November 15, 1979, in France, received jointly the Dipl. Ing. in electrical engineering from Supélec and the M.Sc. degree in theoretical physics, from the University of Orsay (Paris XI), Paris, France, in 2002. In 2005, she received the Ph.D. degree from the University of Paris VI, Paris, France and joined the Electromagnetic and Radar Division of ONERA, Palaiseau, France.

During her Ph.D., she has been working on polarimetric interferometry with airborne systems. Her research interests cover various subjects in electromagnetism and radar, as well as the comparison between radar polarimetry and optical polarimetry, and bistatic images.



**Philippe Fargette** born July, 7 1965, in France, received the Dipl. Ing in engineering mechanics from ENSMM and the Master degree in acoustics from Besancon University, in 1989.

In 1990, he was with the Structural Dynamics Department of ONERA, Palaiseau, France and worked on identification techniques and flutter calculation. He joined the Electromagnetic and Radar Department of ONERA in 2003. His studies cover passive radar and radar simulation framework.



**Antonello De Martino** received the Ph.D. degree at Orsay University, Paris, France, in 1979 and is currently a CNRS senior researcher.

From 1980 to 1999, he worked at the Quantum Optics laboratory, at Ecole Polytechnique, Palaiseau, France on several topics involving nonlinear optics and molecular physics, such as far IR generation by stimulated Raman scattering, multiphoton spectroscopy, dynamics of cluster-surface interactions, etc. He joined LPICM (Thin Film Physics Lab), also in at Ecole polytechnique, in 2000, where he leads the development of optical polarimetric instrumentation, fundamental polarimetry and related applications, such as optical cancer detection and staging and nanometrology for process control in microelectronics.

## Bistatic scattering from forest components. Part II: first validation of a bistatic polarimetric forest model in the VHF-UHF band [225–475 MHz] using indoor measurements

Elise Colin-Koeniguer<sup>a\*</sup> and Laetitia Thirion-Lefevre<sup>b</sup>

<sup>a</sup>ONERA, DEMR-TSI, Chemin de la Hunière, 91761 Palaiseau, France;

<sup>b</sup>Supélec, SONDRRA, Plateau de Moulon, 3 rue Joliot Curie,  
91192 Gif-sur-Yvette Cedex, France

(Received 3 March 2009; final version received 13 September 2009)

This paper introduces the validation of the extension of a scattering model of forests to the bistatic configuration (COBISMO). The measurement in an anechoic chamber is first described. The various stages of the validation process are presented. One dielectric cylinder on a metallic plate is chosen as the canonical element to be tested. Indoor measurements are confronted with the results predicted by the model, first in the horizontal/azimuthal plane, then in the vertical/elevation plane. Then mutual coupling is also investigated using a group of three cylinders. The agreement between simulation and measurement is surprisingly good in light of the precision of such indoor measurements. Several other aspects are discussed: the influence of the frequency, of the shape of the section of the cylinder, and polarimetric effects.

### 1. Introduction

COSMO is a coherent scattering model dedicated to the electromagnetic study of backscattering by forested areas. It has been shown in [1] to satisfactorily simulate the backscattered fields of a forested area from the P- to the L-band. The extension of this modelling tool to the bistatic configuration is described in a companion paper [2]. This extension was originally aimed at predicting an optimal geometric configuration in the framework of a foliage penetration (FOPEN) application; however, the usefulness of such a tool is wider.

Having a reliable polarimetric bistatic modelling tool makes it possible to better understand the phenomenology (typically the polarimetric interpretation of the dihedral mechanism) and to validate new theories, as developed in [3].

The quantitative benefits of the bistatic measurement can be deduced from predictions obtained using modelling tools [4,5]. However, the predictions obtained through the application of these tools have to be confronted with experimental data.

---

\*Corresponding author. Email: elise.koeniguer@onera.fr

Very few bistatic models of vegetation adapted to the UHF or VHF bands are available in the open literature [6–8]. Among them, COBISMO has been widely tested and validated in its monostatic version [1], but not yet in its bistatic version. To our knowledge, this paper is the first that tries to assess the adequacy of a model by comparing its predictions with observations in the bistatic mode.

Three strategies for validating a model can be envisaged:

- Comparison of simulated results to real SAR data. Unfortunately, the use of scattering models is crucial to make progress in bistatic studies, clearly due to the small amount of available bistatic data; the cost and complexity of a bistatic SAR campaign is a great difficulty in this context.
- Comparison between several models. For simple targets, like dielectric cylinders, very accurate models based on nearly analytical solutions can be found and used for validation. But as matters stand, due to computational cost, few models have been developed that can handle a whole forest in a coherent, bistatic and polarimetric mode. In this new situation, descriptive models could be considered, as they do not rely on any a priori knowledge of either the quantities to be derived (as for analytical models) or on past observations (as for empirical models). However, we should keep in mind that similar approximations made in different descriptive models can lead to the same errors.
- By comparing scaled-model measurements and results of numerical simulations.

This last approach has been chosen and is at the heart of this paper in order to validate COBISMO. Of course, the results of this comparison with measurements should also be viewed with some degree of reservation since this comparison is not testimony to the adequacy of the tested dielectric cylinder representation for a trunk. However, the measurements will be shown to be consistent with the hypothesis made in the simulations. The principal aim of this work is to constitute the first step in the whole validation process; here we deal only with the main scatterer of the simulation tool which is a homogeneous dielectric circular cylinder. It is also the opportunity to confirm some observations made in a companion paper [2], where we have been able to draw a certain number of observations, which either concern the radar cross-section levels, or the polarimetric results. We observed that the coupling between trunks and ground dominate in the back- and specular scattering regions, whereas direct scattering of branches is the most important contribution between the two. We also pointed out the inversion of the polarimetric signature of scattering mechanisms when the bistatic angle varies using a classical monostatic polarimetric interpretation of the mechanisms. However, analysing and characterizing the polarimetric response of branches and trunks in between remains a thorny problem.

In this paper, the tests on a single cylinder will concern both the ability to simulate signal amplitudes in each polarization independently, and polarimetric results, which require us to validate the phase of the simulated signals. Section 2 contains a short description of the indoor measurement capabilities used at ONERA (the French Aerospace Lab) for this purpose. In Section 3, we limit ourselves to the validation of the response of one dielectric cylinder, which is the fundamental

scatterer used in the description of the forest at these frequencies for trunks and branches. The extension to the prediction and validation of a group of cylinders is proposed in Section 4. Finally, the conclusion is devoted to a discussion of some possibilities offered by the use of COBISMO.

## 2. Indoor measurement description

In this part, we present the indoor measurement capabilities at ONERA. Then we describe the geometrical testing configurations and we summarize the conventions used for this purpose. Next, we describe the targets used for the experiment.

### 2.1. Observables and parameters

BABI is an indoor coherent bistatic RCS measurement facility in ONERA. The frequency range of operation extends from 600 MHz to 40 GHz. It allows us to acquire the complex response (amplitude and phase) for targets whose dimensions are of the order of one metre.

Full polarimetric bistatic acquisitions have been made on models on 30:1 scale, from 6.75 GHz to 14.25 GHz with a constant step of 25 MHz to obtain levels of signature equivalent to that of a full-sized target from 225 MHz to 475 MHz.

The radar cross-section of a target is its effective area highlighted by the incident radar wave and then re-radiated isotropically. The radar cross-section is expressed as:

$$\sigma_{qp} = \lim_{r \rightarrow \infty} 10 \log_{10} \left( 4\pi r^2 \frac{|\hat{\mathbf{q}} \cdot \mathbf{E}_s|^2}{|\hat{\mathbf{p}} \cdot \mathbf{E}_i|^2} \right) \quad (1)$$

where  $\mathbf{E}_i$  and  $\mathbf{E}_s$  are the far field incident and scattered electric field vectors, respectively, and  $\hat{\mathbf{p}}$  and  $\hat{\mathbf{q}}$  are the received and transmitted polarization vectors. The subscripts  $qp$  can be hH, hV, vH or vV where h denotes the horizontal polarization, and v denotes the vertical polarization; lower case is used for the received polarization, whereas upper case is used for the transmit polarization vector. To compare this coefficient to the simulation of COBISMO, we should keep in mind in this definition that the incident field  $\mathbf{E}_i$  is assumed to be a plane wave whereas  $\mathbf{E}_s$  is mathematically defined as a spherical wave containing a term of propagation of the form  $\frac{1}{r}$ . Besides, the Sinclair matrix elements  $S_{qp}$  simulated by COBISMO for a target located at the centre of the scene are defined by:

$$\hat{\mathbf{q}} \cdot \mathbf{E}_s = \frac{e^{-jk_r r}}{r} S_{qp} \hat{\mathbf{p}} \mathbf{E}_i. \quad (2)$$

Using Equation (2), Equation (1) can be written:

$$\sigma_{qp} = 10 \log_{10} (4\pi |S_{qp}|^2). \quad (3)$$

The procedure of radiometric calibration allows us to collect radar cross-sections (Equation (1)), whereas the simulated radar cross-sections will be easily deduced from the Sinclair matrix simulated by COBISMO (Equation (3)).

## 2.2. Geometrical configuration capabilities

The experimental set-up is as follows.

Transmission and reception antennas are carried on trolleys. These trolleys are pulled by engines which ensure a reproducibility of location of antennas better than  $10^{-2}$  degree. They can move either on a circular rail of radius 5.5 m placed 2.5 m above the ground, or on a line segment rail located on the top of the anechoic chamber. We illustrate this in Figure 1. Targets are mounted on a turning polyfoam column that can typically support targets as large as several metres and up to 50 kilograms. The height of this platform can be adjusted to obtain elevation angles lying between  $70^\circ$  and  $90^\circ$ .

Due to the constraints on the positions of the antennas in the anechoic chamber, not all bistatic configurations can be tested. We have studied separately bistatic effects according to the azimuthal direction, and bistatic effects according to the incidence direction. In order to avoid a more fastidious calibration, we have only used the circular rail for all geometrical configurations. Thus, the emitter is located at a constant place and only the receiver is moving. To achieve a configuration representing an elevation bistatic angle, the target is set on a vertical plate, as pictured in Figure 3.

We summarize the basic conventions used in this paper, omitting details that can be found in Part 1. The incident and scattering unit vectors  $\hat{\mathbf{k}}_e$  and  $\hat{\mathbf{k}}_r$  are defined by

$$\hat{\mathbf{k}}_e = \sin \theta_i \cos \varphi_i \hat{\mathbf{x}} + \sin \theta_i \sin \varphi_i \hat{\mathbf{y}} - \cos \theta_i \hat{\mathbf{z}} \quad (4)$$

$$\hat{\mathbf{k}}_r = \sin \theta_s \cos \varphi_s \hat{\mathbf{x}} + \sin \theta_s \sin \varphi_s \hat{\mathbf{y}} + \cos \theta_s \hat{\mathbf{z}} \quad (5)$$

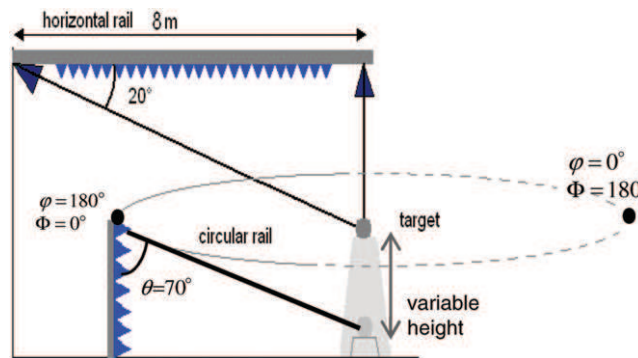


Figure 1. (Colour online) Indoor measurement capabilities. The target is mounted on a turning polystyrene column. We have only used the circular rail for our study.

where the angles  $(\theta_i, \varphi_i)$  and  $(\theta_s, \varphi_s)$  are defined in Figure 2, considering the centre of the scene. Thus,  $\theta$  refers to the elevation angle whereas  $\varphi$  refers to the azimuthal angle.

- For the elevation bistatic angle, we fix  $\theta_i=60^\circ$ ,  $\varphi_i=0^\circ$  and  $\varphi_s=180^\circ$ . The elevation angle  $\theta_s$  lies between  $20^\circ$  and  $85^\circ$  with a step of  $1^\circ$ . A pure monostatic configuration would be achieved for  $\theta_s=60^\circ$ , but this configuration is not practically available. Figure 3(a) shows this configuration.
- For the azimuthal bistatic configuration, we fix  $\theta_i=70^\circ$ ,  $\varphi_i=0^\circ$ ,  $\theta_s=\theta_i=70^\circ$ .  $\varphi_s$  lies between  $4^\circ+180^\circ$  and  $200^\circ+180^\circ$  with a step of  $1^\circ$ . The configuration is depicted in Figure 3(b).

For convenience, we use the variable  $\Phi_s = \varphi_s - \pi$  to deal with the measurement, so that the pure monostatic configuration would be achieved for  $\Phi_s=0^\circ$  and

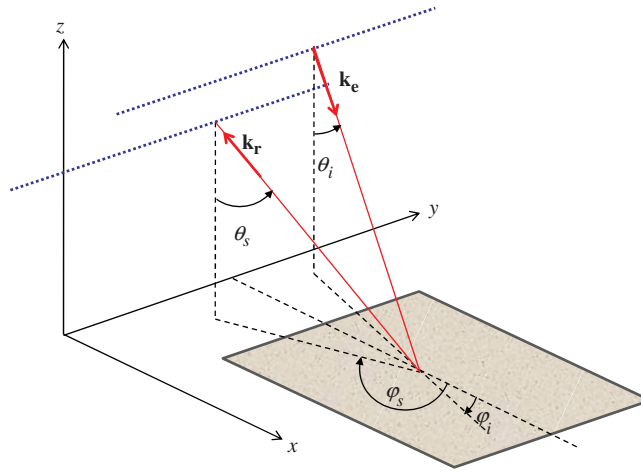


Figure 2. (Colour online) Indoor measurement capabilities.

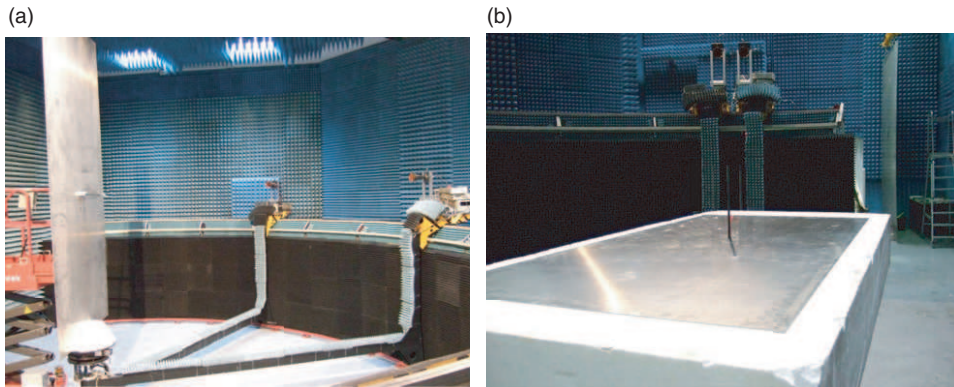


Figure 3. (Colour online) Indoor measurement capabilities for the elevation bistatic configuration (a) and the azimuthal bistatic configuration (b).

Table 1. Summary of conventions.

	Elevation bistatic configuration	Azimuthal bistatic configuration	Backscattering case	Specular case
Modelling convention	$\theta_i = 60^\circ$ $\varphi_i = 0^\circ$ $\varphi_s = 180^\circ$ $\theta_s \in [20^\circ, 85^\circ]$	$\theta_i = 70^\circ$ $\varphi_i = 0^\circ$ $\varphi_s \in [184^\circ, 380^\circ]$ $\theta_s = \theta_i = 70^\circ$	$\theta_i = \theta_s = 60^\circ   70^\circ$ $\varphi_i = 0^\circ$ $\varphi_s = 180^\circ$	$\theta_i = \theta_s = 60^\circ   70^\circ$ $\varphi_i = 0^\circ$ $\varphi_s = 0^\circ$
Measurement convention	$\theta_i = 60^\circ$ $\Phi_i = 180^\circ$ $\Phi_s = 0^\circ$ $\theta_s \in [20^\circ, 85^\circ]$	$\theta_i = 70^\circ$ $\Phi_i = 0^\circ$ $\Phi_s \in [4^\circ, 200^\circ]$ $\theta_s = \theta_i = 70^\circ$	$\theta_i = \theta_s = 60^\circ   70^\circ$ $\Phi_i = 180^\circ$ $\Phi_s = 0^\circ$	$\theta_i = \theta_s = 60^\circ   70^\circ$ $\Phi_i = 180^\circ$ $\Phi_s = 180^\circ$

specular configuration would be achieved for  $\Phi_s = 180^\circ$ . The conventions are summarized in Table 1.

Actually, pure backscattering and forward direction configurations are not practically available. Because of the isolation required between transmission and reception antennas, the pure monostatic case could not be achieved and consequently no measurement has been collected for bistatic angles lower than  $4^\circ$ . In addition, for the pure specular case, the measurements are noised by the strong response of the transmitter, as it is aligned with the receiver and the target.

### 2.3. Description of the targets

Testing has been conducted on models with a scale of 1 : 30 where the wavelength of the measuring radiation is scaled in direct proportion to the target size. The measurements were carried out over single cylinders or over ensembles of a few equal cylinders overlying a metallic plate. Therefore, attenuation effects are low or not significant at all, and soil scattering is not considered. Under these conditions the frequency scaling principle can be extended to a canopy with a reasonable approximation. The targets under study are dielectric cylinders with a height of 30 cm and a diameter of 1 cm. These scaled sizes have been chosen to be representative of vegetation elements: the corresponding height of this kind of target measured at [225–475 MHz] is 9 m and its diameter is 30 cm. Square cylinders are also available with a section of  $90 \times 90$  mm. We can then consider that the square cylinder and the circular cylinder have very close section areas:  $0.79 \text{ cm}^2$  for the circular cylinder and  $0.81 \text{ cm}^2$  for the square cylinder. The scaled permittivity of these cylinders in the VHF-UHF band is provided by the manufacturer. The real part of the permittivity lies between 11 and 13, and the imaginary part lies between 2 and 4. These values are interesting in comparison with standard values of vegetation given by INRA, the French National Institute for Agricultural Research. INRA has provided ground truth of SAR data on forests and has worked on the characterization of the electromagnetic parameters of vegetation elements at these frequencies. Their measurement of complex dielectric permittivities of vegetation elements like branches and trunks performed in 2004 on pine trees has led to values close to 20 for

the real part of the relative permittivity, and lying between 5 and 11 for the imaginary part [1]. Another recent measurement at L-band has led to  $\epsilon_r = 17 - 3.3j$  for the trunks [12]. These results allow us to use our scaled dielectric cylinders as representatives of trunks at these frequencies.

In order to take into account the dihedral or double-bounce scattering, the cylinders stood on a metallic plate. This metallic plate was chosen big enough to be able to filter the effects of bordering edges which are not of interest in this measurement: the plate is  $2 \times 4$  metres large. It would be difficult to choose larger dimensions since the elevation bistatic configuration is achieved with a vertical presentation of the target. In this last case, the metallic plate is maintained using a forklift truck (see Figure 3).

During the calibration step, the forklift truck and the metallic plate remained at the same final position in the chamber. Then, the calibration process was made in such a way that the direct response of the plate and surroundings is subtracted from the total signal. Therefore, in this case, we have to consider the contribution of the scatterer and of its interactions with the plate, but not the direct contribution of the plate.

As the modelling tool uses the infinite circular cylinder approximation, the extremities of the cylinders are not taken into account in the computation of the scattered fields. To compare the results of the simulation with our measurements, radiation absorbent materials were put on the top of the cylinders.

In order to study coupling effects, we have reproduced the same measurement for a group of three circular cylinders. As the elevation bistatic configuration is more delicate to achieve due to the vertical presentation of the plate, the measurement for the group of three cylinders has been performed only in the case of the azimuthal bistatic configuration.

### 3. Validation on one dielectric cylinder

#### 3.1. *Reminder of the general bistatic behaviour of one vertical cylinder standing on a plate*

In this section, we first recall some well-known results on the scattering by a dielectric cylinder in free space and above a metallic plane. Then we simulate the scattering coefficients in these cases, and we check their polarimetric signature.

We use here the BSA convention which is commonly used in the monostatic radar case, because the coordinate systems are the same (i.e. are co-aligned) for the cases of the EM wave propagating from the antenna to the target and for the wave scattered from the target back towards the antenna. For this reason, the BSA convention is the natural one to use for describing backscattering situations. In order to identify the types of scattering mechanisms that prevail on the target, the scattering matrix can be decomposed into submatrices in such a way that the individual components have a physical meaning. The Pauli decomposition is sometimes used to make a colour composite image for the initial interpretation. In the monostatic case of deterministic targets and using the BSA convention,  $|hH - vV|$  represents an odd-bounce mechanism (or dihedral effect),  $|hH + vV|$  an

even-bounce mechanism, and  $|2hV|$  represents a rotated  $45^\circ$  dihedral effect. These mechanisms are particularly well adapted to the analysis of our target, even if we must keep in mind that these interpretations are known to be valid in the monostatic case only and have no reasons to extend to a general bistatic configuration.

We consider here a vertical cylinder illuminated by a stationary incident field. In order to study the cylinder-ground double-bounce scattering, we then consider the vertical cylinder standing on a metallic flat plate, without taking into account the direct contribution of the plate alone. The incident direction is fixed with  $\theta_i$  and  $\varphi_i = 0$ . In this case, of a single cylinder over a metallic plate, the scattering directions that lead to the strongest scattering coefficients describe the surface of the upper cone defined by  $\theta_s = \theta_i$ ,  $\forall \varphi_s \in [0, 2\pi]$ . The maximal response occurs for  $\Phi_s = \varphi_i + \pi = \pi$ , i.e. in the specular direction, in  $hH + vV$  polarization (this is representative of the specular effect on the ground in the BSA convention for the monostatic case). Then, there is a continuous change of polarimetric behaviour along the cone, and for  $\Phi_s = hH - vV$  polarization (dihedral scattering in the monostatic case). The results of the simulation of  $\sigma_{pq}$  for a cylinder in free space and then standing on a plate can be plotted on a sphere as represented in Figure 4. We have used the following colour convention to show the polarimetric behaviour:  $|hH - vV|$  in green,  $|hH + vV|$  in red, and  $|hV + vH|$  in blue.

The scattering directions that lead to the strongest scattering coefficients appear clearly in this figure. They describe the surface of the lower part of a cone defined by  $\theta_s = \theta_i$ . On this cone,  $|hH + vV|$  is predominant for the cylinder without the plate in the backscattering direction, and  $|hH - vV|$  is predominant in the forward direction. When the cylinder is put on the plate, a mirror reflection mechanism is added and consequently  $|hH - vV|$  prevails in the monostatic case, whereas  $|hH + vV|$  is preponderant in the specular direction. Between both these extreme cases, the polarization response moves continuously with  $\Phi_s$  from one polarimetric mechanism to another. This shows that even if a simple polarimetric interpretation of the main

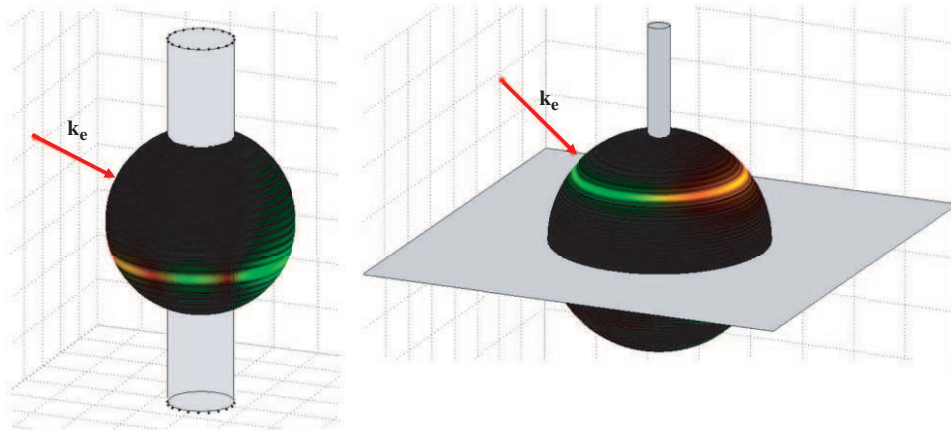


Figure 4. (Colour online) Polarimetric representation of  $\sigma_{qp}$  for one dielectric cylinder alone (left) or on a plate (right).  $|hH + vV|$ : red,  $|hH - vV|$ : green,  $|hV + vH|$ : blue.

mechanism is possible in the monostatic case and in the specular case, this interpretation is not possible for the geometric cases in between.

### 3.2. Testing configurations

As we are not able to measure the values of the intensity of the field scattered in all directions, we restrict the testing to two important configurations, which we call the ‘azimuthal bistatic’ and ‘elevation bistatic’ configurations. The azimuthal bistatic configuration makes it possible to analyse the radiometric and polarimetric evolution along the cone of maximal intensity, whereas the elevation bistatic configuration testifies to the directionality of the dihedral scattering according to the cylinder height.

The elevation bistatic case is represented in Figure 5. Here we represent only co-polarization channels, as cross-polarizations returns are null due to symmetry reasons: the incidence plane is a symmetry plane for both targets and the emitted and scattered directions. In this case, cross-polarization contributions from reciprocal targets are null.

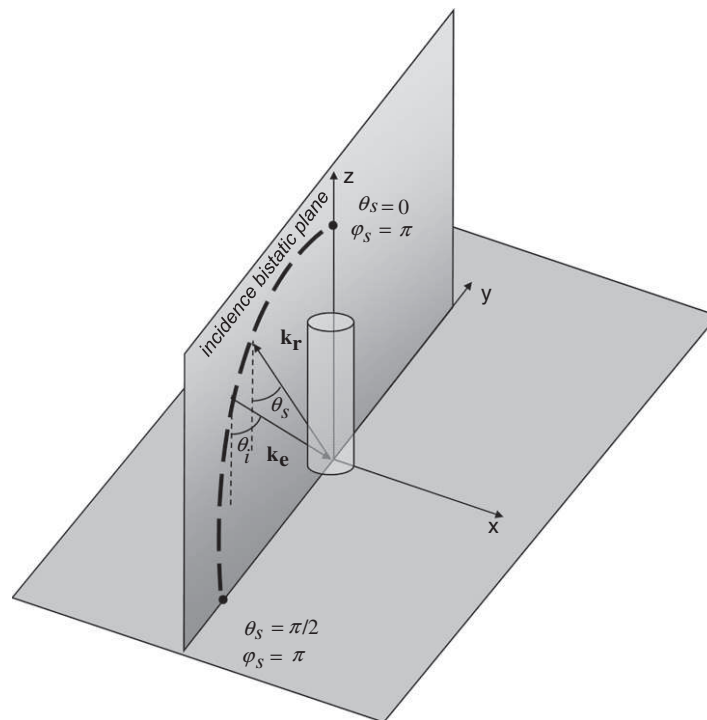


Figure 5. Configuration of measurement of one vertical dielectric cylinder standing on a plate in an elevation bistatic configuration. In this case the incidence and scattering planes are merged.

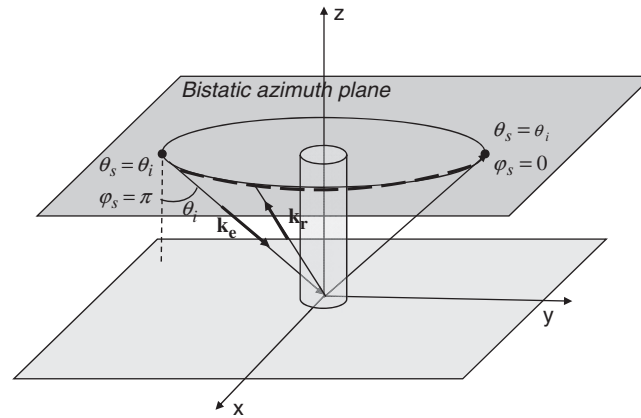


Figure 6. Configuration of measurement of one dielectric cylinder on a plate in an azimuthal bistatic configuration.

In the case of an azimuthal bistatic angle, represented in Figure 6, the cross-polarizations have to be equal; we are in the case where the bisector plane of the incidence plane and the scattered plane is a symmetry plane for the target. For more details about the relations between cross-polarizations due to symmetry reasons, we refer the reader to [11].

We have to specify that the aim of this paper is not to exhibit cases of geometry and targets for which the reciprocity assumption does not hold, but mostly to validate the simulation tool in the cases that best explain the behaviour of cylinders and to yield profound insight into it.

### 3.3. Validation of one cylinder on a plate for the azimuthal bistatic configuration

In this section, we try to validate COBISMO in the configuration called the azimuthal bistatic configuration. We first establish a qualitative representation of the polarimetric behaviour for all frequencies, and then consider numerical comparisons for specific frequencies.

In Figure 7, the variation of the scattering coefficient is plotted with respect to the frequency and the azimuthal angle  $\Phi_s$ . The Pauli basis is chosen:  $|hH-vV|$  in green,  $|hH+vV|$  in red and  $|hV+vH|$  in blue. Results are very encouraging. They confirm a result of a previous study, where we concluded that the polarimetric behaviour of a dielectric cylinder over the ground depends on the scattering azimuthal angle. Here we see that this polarimetric behaviour depends also on the frequency.

Now, we investigate the validation of the simulated scattering coefficients for a fixed frequency. Figure 8 represents the comparison between the simulated and measured scattering coefficients of a dielectric cylinder for all polarizations, in the case when only  $\Phi_s$  is varying. For simplicity, the frequency is fixed at  $f = 300$  MHz, which corresponds to  $\lambda = 1$  m and to cylinder dimensions such as  $r = 0.15\lambda$  and  $h = 9\lambda$ .

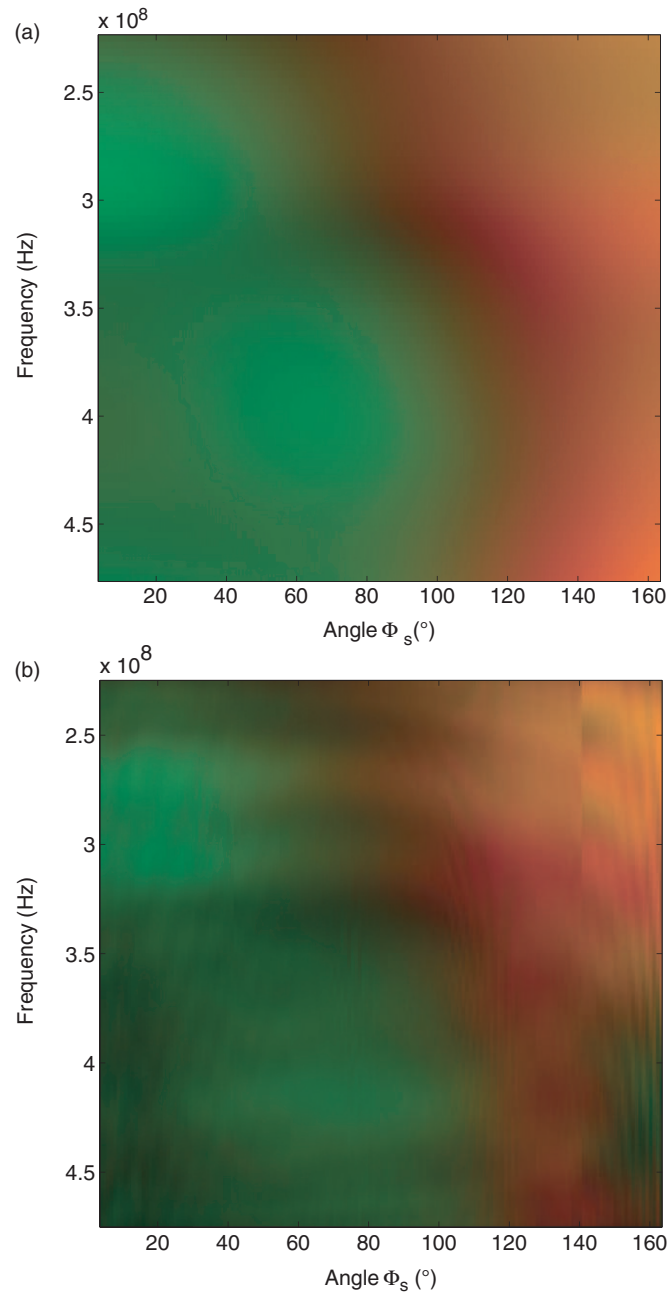


Figure 7. (Color online) Azimuthal bistatic configuration: comparison between polarimetric behaviour obtained by simulation (a) and measurement (b) for one dielectric cylinder standing on a flat plate.

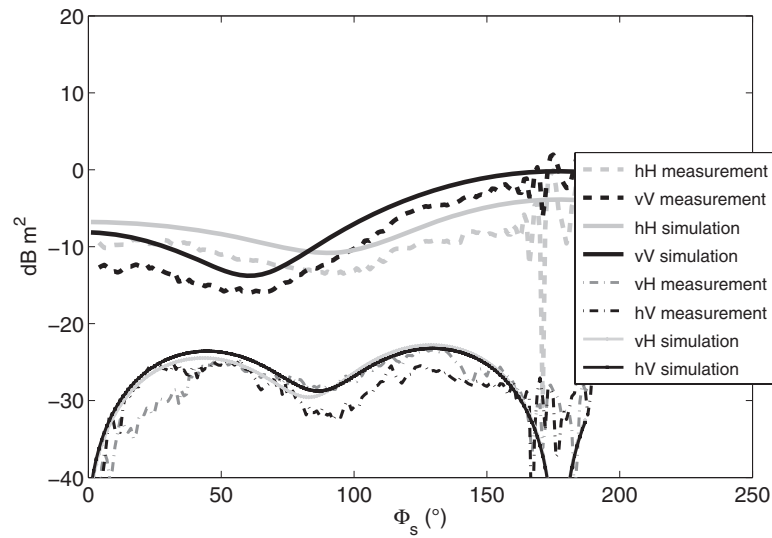


Figure 8. Azimuthal bistatic configuration: comparison between simulation and measurement of the scattering coefficients of a dielectric cylinder standing on a flat plate for all polarizations, at  $f=300$  MHz.

The error between the measurements and the simulation can reach 3 dB for co-polarizations and 5 dB for the cross-polarizations, but these results are very encouraging knowing the uncertainty on the measurement which can reach 2 dB at these frequencies and considering that the amplitude of the measurements is very small but well reproduced by the simulation.

Next we are interested in the phase evolution that should exist between the different hH and vV signals, to explain the evolution from a hH + vV polarization to the hH–vV polarization, from the backward case to the forward case. As can be seen either from measurement or simulations, the exact shape of the curve of the polarimetric change depends on the wavelength.

Figure 9 represents the differences between the phases of  $S_{hH}$  and  $S_{vV}$ , for three different frequencies: lower, middle and higher frequencies of the bandwidth. The behaviour of this phase is well reproduced for the three cases, and confirms that the exact angle  $\Phi_s$  where  $|\angle S_{hH} - \angle S_{vV}| = \pi/2$  strongly depends on the frequency. This result is very important, as it has a strong impact on the interpretation and consequently has to be taken into account in future bistatic polarimetric analysis. For example, the extent of the azimuthal angles for which dihedral scattering prevails is more important at higher frequency than at lower frequency. We can presume that this result depends also on other descriptive characteristics of the scatterer, such as its diameter or its permittivity.

Besides, these results cast some doubt upon the adequacy of the classical polarimetric interpretation in the case of a bistatic configuration. For example, the distinction between the double-bounce scattering mechanism and the single-bounce mechanism becomes irrelevant around an azimuthal bistatic angle equal to  $\pi/2$ .

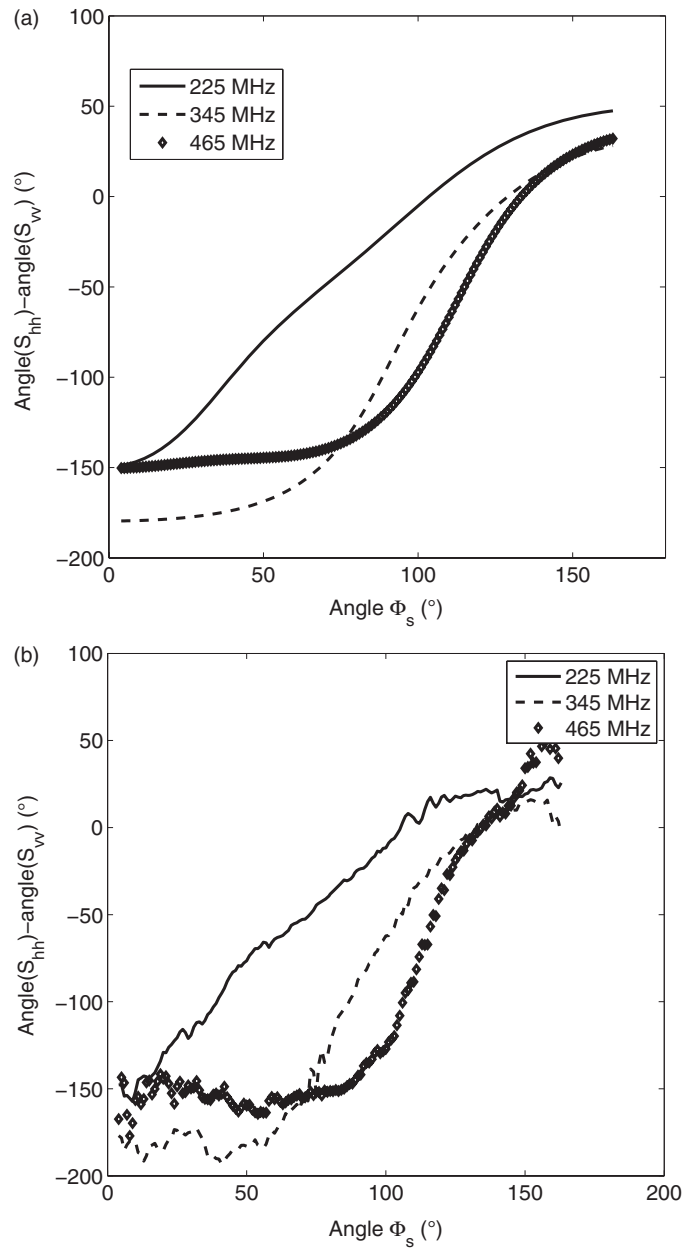


Figure 9. Phase difference between hH and vV scattered fields. (a) Simulation; (b) measurement.

### 3.4. Testing of one cylinder on a plate for the elevation bistatic configuration

In this section we are interested in the validation of COBISMO in the second configuration called the elevation bistatic configuration. The approach is the same as

in the previous section: we first establish a qualitative representation of the polarimetric behaviour for all frequencies, and then we consider numerical comparisons for a fixed frequency.

Figure 10 represents the same type of comparison as before but now in the case when  $f$  and  $\theta_s$  are varying. We recall that no data are available for bistatic angles lower than  $4^\circ$ , and there are no data for  $\theta_s \in [56^\circ, 64^\circ]$  around the monostatic case.

In this figure we see that there is no change of polarization because we are restricted to the case  $\theta_s \in [20^\circ, 80^\circ]$ . The same polarimetric evolution, as noted above, from  $|hH + vV|$  to  $|hH - vV|$ , should occur around the nadir point ( $\theta_s = 0$ ), which is not shown here. This evolution in the case of the elevation bistatic configuration has been reported and investigated more deeply in Part 1 [2]. However, we clearly see that the positions of the minima and maxima in the signal match well between simulation and measurement.

The plot in Figure 11 shows the behaviour of the scattering coefficients for the fixed frequency  $f = 300$  MHz ( $r = 0.15\lambda$  and  $h = 9\lambda$ ). We recall that in this geometric case and due to the symmetry of the target, cross-polarization returns are null and consequently are not represented here. In this figure, we obtain very good agreement for the first two maxima around the main one, corresponding to the monostatic case ( $\theta_s = \theta_i$ ,  $\varphi_s = \pi$ ).

Other maxima and minima are more difficult to compare. It is very likely that the measurement is affected by the interaction between the cylinder and the edge of the plate.

### 3.5. Comparison of cylinders with circular and square section

This section presents a brief study of the influence of the shape of a cylinder on its scattering. The aim is to validate the assumption made by several exact modelling tools (e.g. [8]), for which, for frequencies up to a few hundred megahertz, the shape of the cross-section of the trunk does not influence significantly the scattered field as long as the area of the cross-section remains the same [8]. This is important to check if we want to compare simulation tools between them. In addition, we have to state if this approximation can lead to a different polarimetric interpretation.

This assumption has been checked in the monostatic case [9], but not in the bistatic case to our knowledge. To this end we compare the scattering of a circular cylinder and a square cylinder with the same cross-sections.

In the case of an elevation bistatic angle, both polarimetric responses are shown on the left part of Figure 12. As compared to the circular cylinder, the amplitude of a square cylinder response is larger. The width of the signal is larger too.

In the case of an azimuthal bistatic angle, the differences are not so significant, as the dynamics in both scattering responses are low. Global patterns are similar for both cylinders. The resulting signals are plotted in Figure 12 on the right.

Another question naturally arises, that is to know whether the shape influences the polarimetric behaviour. Comparisons are made in Figures 13 and 14. In the azimuthal bistatic configuration, the conclusion is that the polarimetric behaviour of

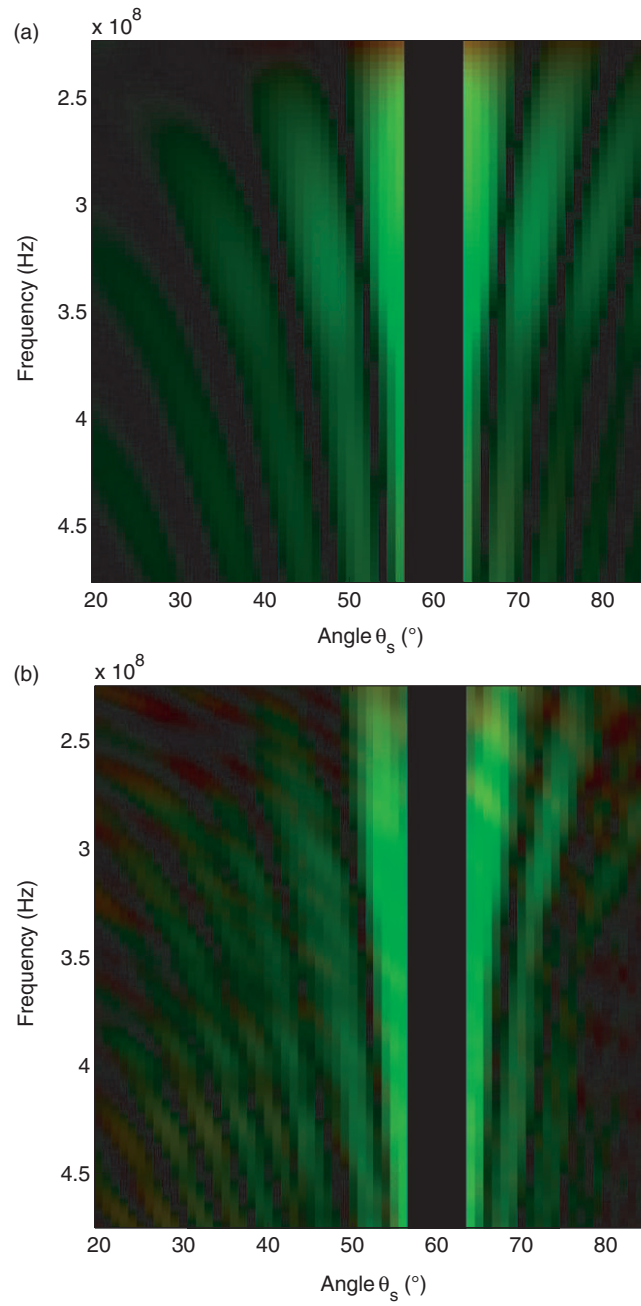


Figure 10. (Colour online) Elevation bistatic configuration: comparison between polarimetric behaviour obtained by simulation (a) and measurement (b) for one dielectric cylinder on a flat plate.

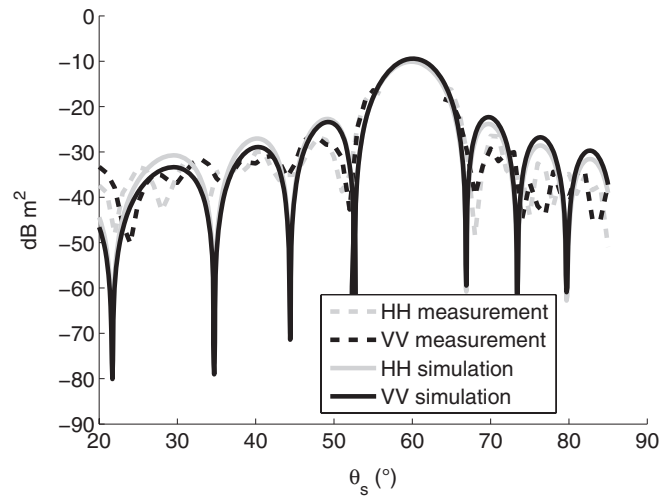


Figure 11. Elevation bistatic configuration: comparison between simulation and measurement of one dielectric cylinder on a flat plate for all polarizations at  $f=300$  MHz.

the signals between the square and circular cylinders is very similar. Concerning the elevation bistatic configuration, we can see that the intensities of the local maxima in the resulting signals are different but the shape of the main maxima look similar. Moreover, the hH + vV polarization prevails for the whole bandwidth and then the polarimetric analysis is not affected.

In summary, our view is that the shape of a vertical cylinder is not so important in the case of an azimuthal bistatic configuration; however, it could influence the radiometric results in the case of an elevation bistatic configuration.

This result may seem surprising: we would logically expect that the difference between square and circular cylinders is more pronounced in an azimuthal scan. We put forth the idea that in the elevation plane, the scattered wave can be sensible to the geometry of the cross-section of the cylinder. More precisely, the fringes seen in the signal becomes narrower when the height of the cylinder increases, whatever the cross-section of the cylinder is. But the exact dependency between the intensities of the local minima of the signal and the height depends also on the shape of the cylinder; and the shape of the cylinder could lead to different radiometric values for high bistatic angles. Of course we have to keep in mind that due to uncertainties in the measurement of the values far away from the monostatic case, this measurement can be considered only as a rough empirical check of this hypothesis.

Concerning the azimuthal scattering pattern, the variation of radiometric amplitudes is lower and so differences are less visible. Moreover, the polarimetric behaviour is explained more by the geometrical modification of the definition of the polarimetric vectors when the azimuthal angle varies. A continuous change of sign between the signals in hH and vV polarization is expected in this geometrical configuration for any target shape, as mentioned in [10].

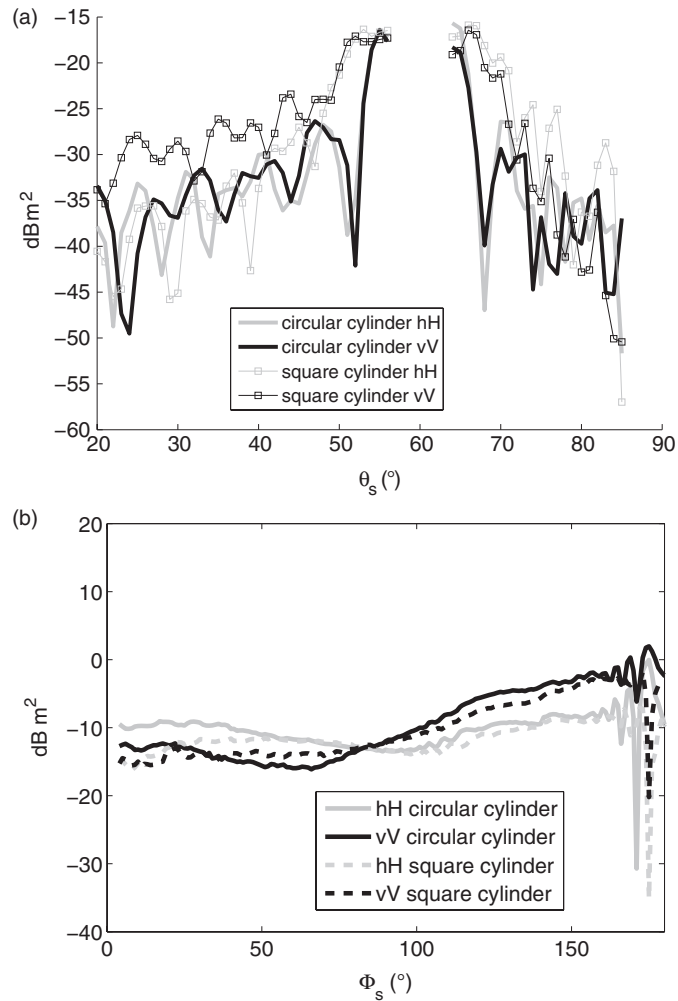


Figure 12. Comparison between the scattering coefficients of square and circular cylinders, at  $f=300$  MHz. (a) According to the elevation bistatic angle; (b) according to the azimuthal bistatic angle.

#### 4. Validation of the bistatic behaviour of a group of cylinders

In order to validate the behaviour of a group of cylinders, three dielectric cylinders were put on a plate and measured in the case of the azimuthal bistatic configuration.

They are located over a metallic surface. Their positions correspond to the edges of an equilateral triangle with a side of 3.5 cm, i.e. a scaled distance of 1.05 m in the VHF-UHF band. This distance is actually a very short one and is not really representative of the mean distance separating two trunks. The elevation bistatic configuration is not considered as it is fastidious to correctly set the target on the platform (see Section 2.3).

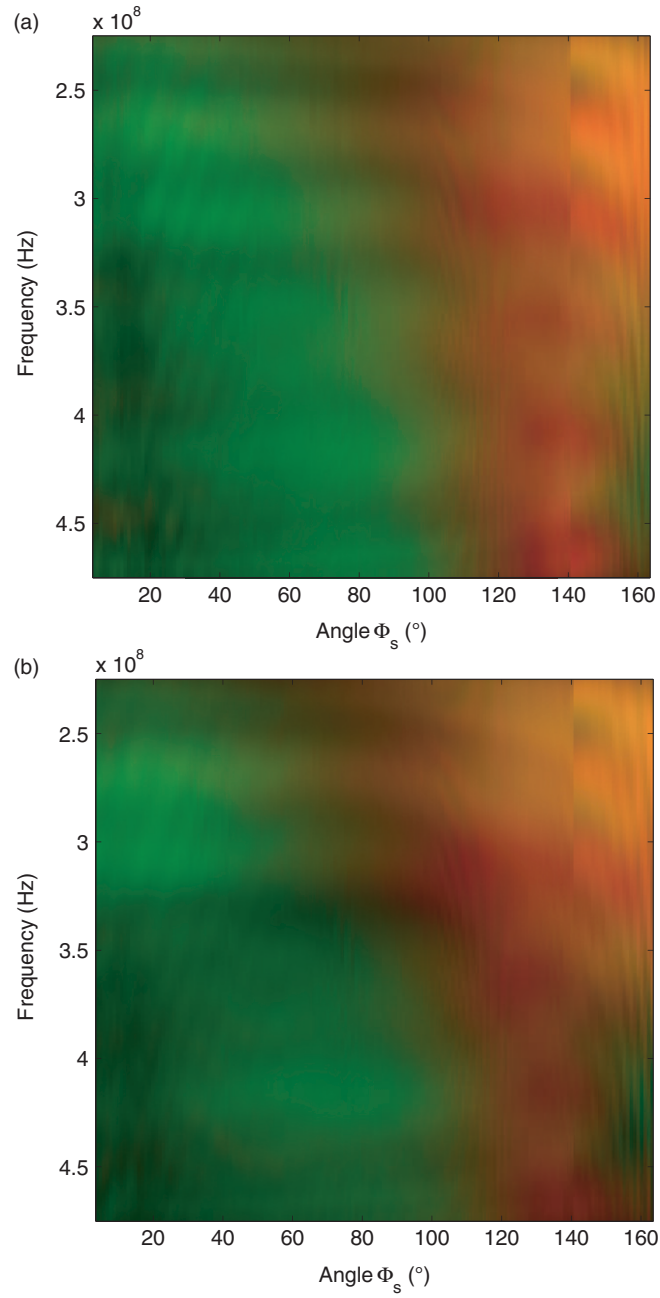


Figure 13. (Colour online) Azimuthal bistatic configuration: comparison between polarimetric behaviour obtained by measurement for one square cylinder (a) and a circular cylinder (b) on a flat plate.

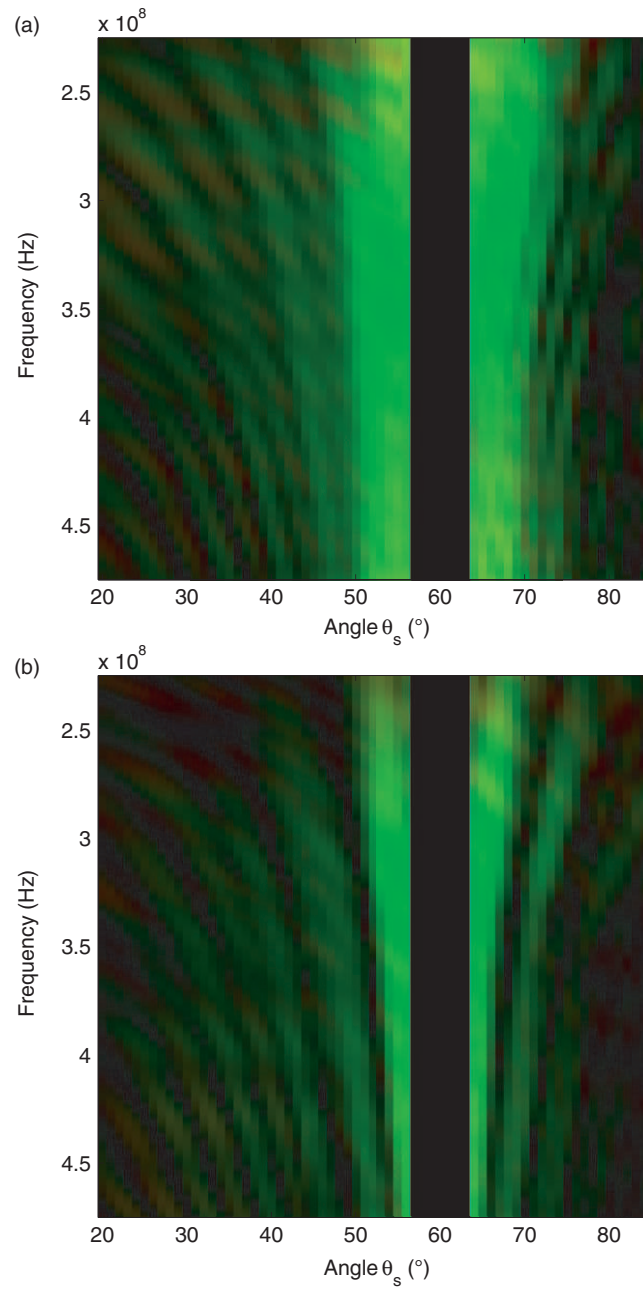


Figure 14. (Colour online) Elevation bistatic configuration: comparison between polarimetric behaviour obtained by measurement for one square cylinder (a) and a circular cylinder (b) on a flat plate.

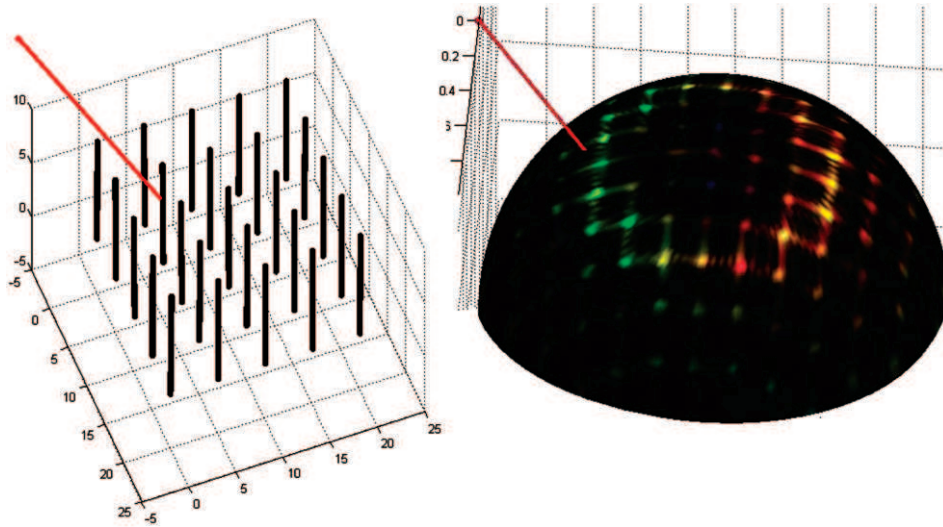


Figure 15. (Colour online) Representation on a sphere of the simulated scattering coefficients of a group of vertical cylinders periodically located over a metallic flat surface.  $f = 300$  MHz, red:  $|hH+vV|$ , green:  $|hH-vV|$ , blue:  $|hV-vH|$ .

In the following paragraphs, we first recall the behaviour of a group of cylinders standing on a plate using COBISMO, and then we describe the measurement we collected and we study the importance of the mutual coupling.

#### 4.1. Reminder of the general bistatic behaviour of a group of vertical cylinders standing on a plate

If we simulate a set of vertical cylinders periodically distributed over a dielectric ground plane (whose contribution is taken into account via the double-bounce scattering mechanism), the maximum occurs on the same cone defined previously for one single cylinder. In addition, the *Bragg effects* due to the regular positions of the cylinders are clearly visible on the sphere represented in Figure 15.

For a set of vertically oriented cylinders whose positions do not correspond to a perfect array, this Bragg effect disappears from the scattering pattern. This is shown in Figure 16. The same polarimetric conclusions as for one single cylinder can be drawn here.

If we now represent the scattering pattern of a set of cylinders which are randomly oriented and distributed (as in a uniform random volume), the directionality of the answer disappears. The signal prevails at polarization  $hH+vV$  for all scattering directions. Then the behaviour of a whole forest (simulated by vertical trunks and randomly oriented branches) differs very little from the behaviour of the trunks alone. The aim of the following sections is to validate the simulated signals of a group of several cylinders.

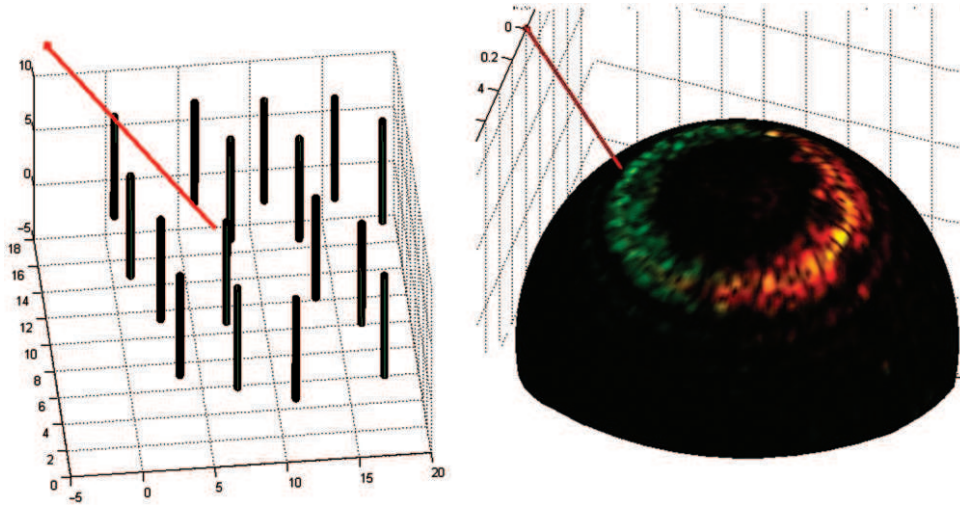


Figure 16. (Colour online) Representation on a sphere of the scattering coefficients of a group of vertical cylinders randomly located over a metallic flat surface.  $f=300$  MHz, red:  $|hH+vV|$ , green:  $|hH-vV|$ , blue:  $|hV-vH|$ .

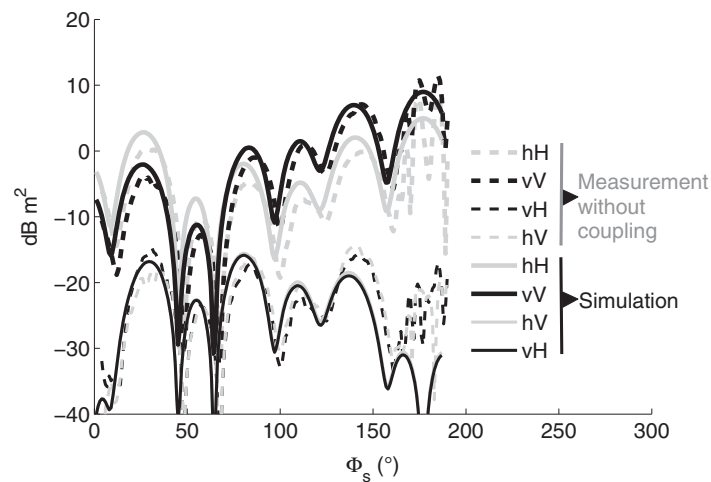


Figure 17. Comparison between the variations of the scattering coefficients for a group of three cylinders obtained by simulation and by measurement, at  $f=300$  MHz.

#### 4.2. Validation on a set of three cylinders on a flat plate

Comparisons between simulation and measurement are given in Figure 17. Note that mutual coupling between cylinders is not taken into account in COBISMO.

That is why we first compare COBISMO with the response of a single cylinder simply duplicated and whose phases are shifted accordingly to the location of each of the three cylinders.

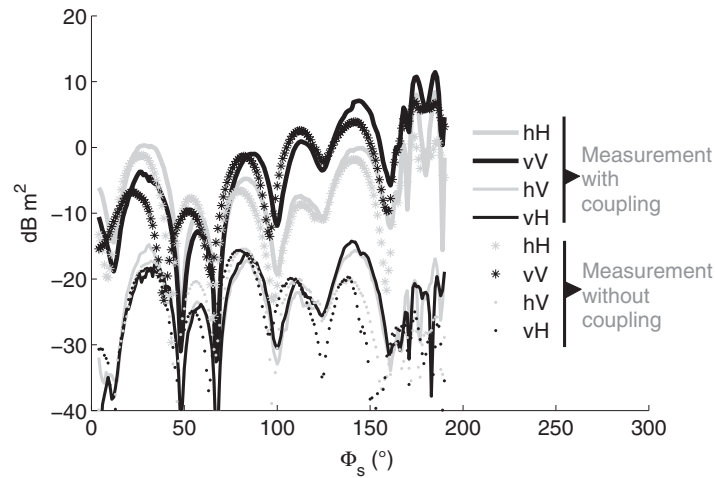


Figure 18. Comparison between two measurements of a group of three cylinders, with and without coupling, at  $f=300$  MHz.

Once again, the results are encouraging. We obtain good agreement between measurements and simulations both for co-polarizations and cross-polarizations.

It is interesting now to evaluate the impact of the mutual coupling. Nguyen et al. [8] concluded that when the distance between the trees is larger than  $2\lambda$ , the decoupling approximation is accurate. In the presented measurement, the space between trees lies between  $0.6\lambda$  and  $1.3\lambda$ . We are then in a more pessimistic configuration.

We compare the measurement of one trunk duplicated three times and shifted, to the direct measurement of the three cylinders. The result of our comparison is given in Figure 18.

The mean distance between the signal measured with coupling and the signal without coupling has been found to be around  $-1.6$  dB for hH polarization, and  $-0.8$  dB for vV polarization. These differences are under the threshold of measurement precision. Moreover, it has been noticed that these differences are almost constant in the frequency bandwidth, which means that the decoupling approximation is correct for all distances lying between  $0.6\lambda$  and  $1.3\lambda$ .

In realistic configurations, the distance between two adjacent trunks is generally larger than that considered for this study, and we can conclude that COBISMO simulates quite well the bistatic behaviour of a group of trunks in the VHF-UHF band, even neglecting mutual coupling.

## 5. Conclusion

The various comparisons between indoor measurements and scattered fields predicted by COBISMO yield results that make us confident in the use of this modelling tool in bistatic configurations. Measurement are also consistent with the

hypothesis of neglecting mutual interactions between trunks for azimuthal bistatic configurations.

Among other deductions, the validation of COBISMO sheds some light on the following aspects:

- Polarimetric evolution of the signal according to the azimuthal bistatic angle, from  $hH - vV$  polarization to  $hH + vV$  polarization, depends on the size of the object with respect to the wavelength.
- This polarimetric evolution is a priori very similar for a square cylinder and for a circular cylinder with the same area.
- On the other hand, the approximation of a circular cylinder by a square cylinder can fail to predict the radiometric levels when the elevation bistatic angle is high. In such configurations, care must be taken to ensure that the description of a circular cylinder by a square cylinder is still valid.
- Patterns that exist due to the presence of an orderly array of cylinders disappear very quickly as soon as the array of cylinders becomes irregular. It is improbable that these regular patterns could be observed practically even on well-planted artificial forests.

Obviously no model can be completely validated by experiment in all possible cases. Other results of investigation deduced from COBISMO should always be viewed with some degree of reservation. Future work will be dedicated to the validation of the model for more complex targets involving a group of cylinders. However, the good match of this model with an important number of experimental cases has let us use it for preparing future FOPEN campaigns. For this purpose, a target has been integrated in COBISMO in order to deduce the more relevant geometrical configurations.

Finally, this paper has been the opportunity to put forward this main idea: contrary to what might have been developed in the monostatic case, the polarization  $hH - vV$  is not necessarily representative of dihedral scattering in a bistatic configuration. A conjoint work introduced in [10] focuses on the extension of polarimetric parameters and decompositions in the azimuthal bistatic configuration.

### Acknowledgements

The practical measurements were carried out by Mr A. Cheraly, to whom we are deeply thankful. We thank Juan Carlos Castelli for fruitful discussions on the ONERA measurement facility.

### References

- [1] L. Thirion, E. Colin, and C. Dahon, *Capabilities of a forest coherent scattering model applied to radiometry, interferometry, and polarimetry at P- and L-band*, IEEE Geosci. Remote Sens. 44 (2006), pp. 849–862.

- [2] L. Thirion-Lefevre, E. Colin-Koeniguer, and C. Dahon, *Bistatic scattering from forest. Part I: coherent polarimetric modelling and analysis of simulated results*, Wave. Random Complex 20 (2010), pp. 36–61.
- [3] C. Titin-Schnaider, *Power optimization for polarimetric bistatic random mechanisms*, IEEE Geosci. Remote Sens. 45 (2007), pp. 3646–3660.
- [4] L. Thirion, C. Titin-Schnaider, C. Dahon, and E. Colin, *Modeling and study of the bistatic scattering of forested area at P-band*, European Conference on Synthetic Aperture Radar, Germany, 2006.
- [5] L. Thirion-Lefevre and C. Dahon, *Modeling and study of the polarimetric bistatic scattering of a forested area*, International Workshop on Science and Applications of SAR Polarimetry and Polarimetric Interferometry, Italy, 2007.
- [6] P. Ferrazzoli, L. Guerriero, C.I. Del Monaco, and D. Solimini, *A further insight into the potential of bistatic SAR in monitoring the Earth surface*, IEEE International Geoscience and Remote Sensing Symposium Proceedings, Vol. 2, 2003, pp. 776–777.
- [7] P. Liang, L. Pierce, and M. Moghaddam, *Radiative transfer model for microwave bistatic scattering from forest canopies*, IEEE Geosci. Remote Sens. 43 (2005), pp. 2470–2483.
- [8] H. Nguyen, H. Roussel, and W. Tabbara, *A coherent model of forest scattering and SAR imaging in the VHF and UHF band*, IEEE Geosci. Remote Sens. 44 (2006), pp. 838–848.
- [9] H. Israelsson, L.M. Ulander, T. Martin, and J.I.H. Askne, *A coherent scattering model to determine forest backscattering in the VHF-band*, IEEE Trans. Geosci. Remote Sensing 38 (2000), pp. 238–248.
- [10] N. Trouvé and E. Colin-Koeniguer, *Polarimetric study of an anisotropic cloud of cylinders in a bistatic configuration*, International Workshop on Science and Applications of SAR Polarimetry and Polarimetric Interferometry, Italy, 2009.
- [11] H.C. van de Hulst, *Light Scattering of Small Particles*, Courier Dover, New York, 1981.
- [12] A. Della Vecchia, P. Ferrazzoli, J.-P. Wigneron, and J.P. Grant, *Modeling forest emissivity at L-band and a comparison with multitemporal measurements*, IEEE Geosci. Remote Sens. 4 (2007), pp. 508–512.

# Alternatives to Target Entropy and Alpha Angle in SAR Polarimetry

Jaan Praks, *Member, IEEE*, Elise Colin Koeniguer, and Martti T. Hallikainen, *Fellow, IEEE*

**Abstract**—The purpose of this paper is to discuss two polarimetric parameters which are widely used in synthetic aperture radar (SAR) polarimetry, namely, target entropy and alpha angle. We propose alternative parameters based on our analysis on how they are connected to covariance matrix similarity invariants and how they can be physically interpreted in optical polarimetry. The proposed alternatives can be computed by a fairly simple algorithm and even by the use of software without complex mathematics abilities. As an example, a NASA/Jet Propulsion Laboratory Airborne SAR L-band image of the San Francisco Bay is used to compare the proposed parameter schemes with the original entropy and alpha. A coherent rationale for these alternative parameters is formulated in order to provide insight to polarimetric parameter interpretation.

**Index Terms**—Alpha, ellipsometry, entropy, optical polarimetry, synthetic aperture radar (SAR) polarimetry.

## I. INTRODUCTION

SYNTHETIC aperture radar (SAR) operating at microwave frequencies has become a widely used remote-sensing instrument. Many modern SAR systems, particularly airborne systems, have fully polarimetric capability, and a growing number of applications take advantage of fully polarimetric data. In these fully polarimetric systems, the four polarization combinations are used in orthogonal pairs in a coherent way. The four measured parameters constitute the scattering matrix, describing the transformation of the polarization of a wave, incident upon a scatterer to the polarization of the backscattered wave. In order to study distributed targets, the covariance matrix or related matrices are also used. The covariance matrix is related, in a simple manner, to the Stokes matrix, which is widely used in optical polarimetry.

With a view of understanding the scattering event better, several decompositions for the scattering matrix and covariance-type matrices have been suggested. One of the most popular schemes, noncoherent target decomposition, was proposed by Cloude [1] and was reviewed in [2]. The authors proposed an elegant interpretation of the decomposition as an incoherent sum of three orthogonal scattering mechanisms appearing with

a probability proportional to the covariance matrix eigenvalues. Interpretation of the eigenvalues as probabilities led also to the definition of entropy parameter, inspired by entropy from the information theory of Shannon [3], [4]. The alpha angle parameter has been proposed for the eigenvector description and is interpreted as the scattering mechanism index. The entropy  $H$  and alpha angle  $\bar{\alpha}$  have been widely used in SAR polarimetry [5]–[7].

Despite their great possibilities, certain drawbacks remain in the definition of these parameters. The alpha angle definition as a weighted average of eigenvector angles from a certain direction in complex spherical coordinates makes its physical meaning obscure, and the logarithm operator complicates the interpretation of the entropy parameter. The computation of  $H$  and alpha angle is also time consuming because it requires eigenvalue and eigenvector calculations for each pixel of a polarimetric image. This can be a limitation for high-resolution images, where the amount of pixels is vast. As it will be demonstrated subsequently, similar information can be extracted from the polarimetric SAR image without eigenvalue and eigenvector calculations. This indicates also that the potential of eigenvalue decomposition is underexploited when only the alpha angle and target entropy are used to describe the decomposition result.

The aim of this paper is to explore the background of these two popular parameters in order to deepen our understanding and to find alternative parameters that are faster to compute and could provide clearer physical interpretation. For this purpose, we investigate mathematical properties of covariance matrices and take a look at how physical interpretation is done in optical polarimetry. We believe that optical polarimetry provides an alternative and useful way to understand also the SAR polarimetry [8]. Optical polarimetry deals with the polarimetric measurement of light and uses its own formalism to describe the polarimetric properties of scattering. In spite of different formalisms, both the radar and optical polarimetries describe the same electromagnetic wave scattering phenomena, although for different wavelengths.

This paper is organized as follows. In the first section, we present the polarimetric entropy and the mathematical background which explains its form. The mathematical analysis of similarity invariants of Hermitian matrices leads to the definition of two parameters; the first alternative parameter is defined using the Frobenius norm of the normalized coherence matrix. The second one is defined using the determinant of the same matrix. In the second section, an alternative investigation is conducted to find a physical interpretation of the parameters. This consideration is inspired by optical polarimetry. It leads to

Manuscript received December 12, 2007; revised May 5, 2008, September 26, 2008, and December 19, 2008. First published April 24, 2009; current version published June 19, 2009.

J. Praks and M. T. Hallikainen are with the Department of Radio Science and Engineering, Helsinki University of Technology, 02015 Espoo, Finland (e-mail: jaan.praks@tkk.fi; martti.hallikainen@tkk.fi).

E. C. Koeniguer is with the Office National d'Etudes et de Recherches Aéropatiales, 91761 Palaiseau, France (e-mail: elise.colin@onera.fr).

Color versions of one or more of the figures in this paper are available online at <http://ieeexplore.ieee.org>.

Digital Object Identifier 10.1109/TGRS.2009.2013459

the definition of a third parameter. The statistical behavior of these alternative parameters is finally presented, including differences between them and the classical polarimetric entropy. As an example, NASA/Jet Propulsion Laboratory Airborne SAR (AIRSAR) L-band image of the San Francisco Bay is used to demonstrate the relation between the proposed schemes and the original entropy and alpha angles.

## II. TRADITIONAL ENTROPY AND $\bar{\alpha}$ DEFINITIONS

### A. Target Decomposition

Let us assume that we have, as a measured value, a complex scattering matrix in horizontal–vertical (HV) polarization basis in backscattering alignment (BSA) [9] convention

$$\mathbf{S} = \begin{bmatrix} S_{HH} & S_{HV} \\ S_{VH} & S_{VV} \end{bmatrix}. \quad (1)$$

Each pixel of the polarimetric image corresponds to a single scattering matrix. In order to calculate the average and second-order statistics of the scattering matrices, we need to express the properties of the received signal in the power domain by means of the covariance matrix.

The covariance matrix is defined as an expected value of the product of the scattering vector  $\vec{k}$  with its complex conjugate  $\vec{k}^\dagger$

$$\langle \mathbf{C} \rangle = \langle \vec{k} \vec{k}^\dagger \rangle. \quad (2)$$

The scattering vector  $\vec{k}$  is formed of measured values (scattering matrix elements or their linear combinations); the  $\langle \dots \rangle$  operator denotes statistical averaging (in SAR polarimetry, the averaging is usually done spatially), and  $^\dagger$  denotes a complex conjugate transpose. The covariance matrix is, by definition, always a Hermitian (or self-adjoint) matrix, i.e., a matrix which is equal to its conjugate transpose. Hermitian matrix diagonal elements are real, and it has real eigenvalues; the eigenvectors form a unitary basis. Covariance matrices in various bases have been often used to describe the polarimetric measurement. It is important to recall here that the averaged covariance matrix is sufficient to describe fully the measurement when measured variables follow a multivariate normal distribution—this means homogeneous distributed target in polarimetry.

Cloude and Pottier [2] have proposed to use the covariance matrix in the Pauli basis and named it the coherency matrix  $\mathbf{T}$ . Pauli matrices, together with the identity matrix, are chosen because they form an orthogonal basis in the sense of Hilbert–Schmidt, for the real Hilbert space of  $2 \times 2$  complex Hermitian matrices or the complex Hilbert space of all  $2 \times 2$  matrices. Moreover, each of them can be interpreted as a scattering matrix of a canonical target or mechanism (surface, double bounce, etc.), and they form a compact coordinate system in the monostatic reciprocal case.

The scattering matrix elements expressed in Pauli basis can be arranged into a measurement vector, which is called the scattering vector

$$\vec{k} = \frac{1}{\sqrt{2}} [S_{HH} + S_{VV}, S_{HH} - S_{VV}, S_{HV} + S_{VH}, S_{HV} - S_{VH}]^T. \quad (3)$$

The first component is pointing to a roll-invariant direction. If the radar is monostatic and the reciprocity assumption is valid, then  $S_{HV} = S_{VH}$ . In this case, the last component diminishes to zero, and the measurement vector can be written as

$$\vec{k} = \frac{1}{\sqrt{2}} [S_{HH} + S_{VV}, S_{HH} - S_{VV}, S_{HV} + S_{VH}]^T \quad (4)$$

with the three elements referred to as the Pauli components of the signal. In this case, the coherency matrix reduces to a  $3 \times 3$  matrix.

As proposed by Cloude and Pottier [2], the average coherency matrix

$$\langle \mathbf{T} \rangle = \langle \vec{k} \vec{k}^\dagger \rangle \quad (5)$$

can be decomposed by means of eigendecomposition as

$$\langle \mathbf{T} \rangle = \lambda_1 \vec{k}_1 \vec{k}_1^\dagger + \lambda_2 \vec{k}_2 \vec{k}_2^\dagger + \lambda_3 \vec{k}_3 \vec{k}_3^\dagger \quad (6)$$

and is interpreted as an incoherent sum of three fully deterministic scattering mechanisms, described by eigenvectors  $\vec{k}_i$  and weighted by eigenvalues  $\lambda_i$ .

When the eigenvectors are described in complex spherical coordinates  $\alpha_i, \beta_i, \sigma_i, \gamma_i$ , and  $\xi_i$ , an arbitrary unit eigenvector can be written as

$$\vec{k}_i = e^{j\xi_i} [\cos \alpha_i, \sin \alpha_i \cos \beta_i e^{j\sigma_i}, \sin \alpha_i \sin \beta_i e^{j\gamma_i}]^t. \quad (7)$$

The decomposition of a Hermitian matrix  $T$  into its eigenvalues  $\lambda_i$  and eigenvectors is then defined by

$$\mathbf{T} = \mathbf{U}_3 \begin{bmatrix} \lambda_1 & 0 & 0 \\ 0 & \lambda_2 & 0 \\ 0 & 0 & \lambda_3 \end{bmatrix} \mathbf{U}_3^\dagger \quad (8)$$

where

$$\mathbf{U}_3 = [\vec{k}_1 \quad \vec{k}_2 \quad \vec{k}_3] \quad (9)$$

is the unitary matrix, where the columns  $\vec{k}_i$  are the eigenvectors described in (7).

By using this eigendecomposition, Cloude and Pottier [2] define two parameters which are well known today. The averaged alpha angle is used to describe the scattering mechanism of the reflection. In spherical coordinates, the  $\bar{\alpha}$  angle measures how far the scattering mechanism is from a single bounce reflection, defined by an  $(S_{HH} + S_{VV})$  axis, which is also the roll-invariant direction in a monostatic case. The average is defined in the sense of Bernoulli [3], weighted with the relative size of eigenvalues as

$$\bar{\alpha} = \sum_{i=1}^3 p_i \alpha_i \quad (10)$$

where

$$p_i = \frac{\lambda_i}{\sum_{i=1}^3 \lambda_i}. \quad (11)$$

When interpreting  $p_i$  as the probability of a certain scattering mechanism  $\vec{k}_i$  occurring, Cloude and Pottier [5] define target

entropy  $H$  in a similar form as known in thermodynamics or the Shannon information theory

$$H = - \sum_{i=1}^3 p_i \log_3 p_i. \quad (12)$$

A target's total backscattered power is represented by

$$\text{span} = \lambda_1 + \lambda_2 + \lambda_3. \quad (13)$$

Span, entropy  $H$ , and  $\bar{\alpha}$  angle are considered as the main polarimetric features of a scatterer. However, entropy and  $\bar{\alpha}$  are not independent variables. If the target entropy is high, the alpha angle is restricted to a certain range of values, which diminishes to a single point when entropy is equal to one, the highest value. All these descriptors should be calculated for averaged coherency matrix in order to achieve any second-order statistical information. Sliding a box car window average is the simplest way to approach the calculation.

### B. Entropy in Thermodynamics and Information Theory

The concept of entropy was developed in the 1850s by Rudolf Clausius. Although entropy was originally a thermodynamic concept, it has been adapted in other fields of research, including by Shannon [3], [4] in the field of information theory. In thermodynamics, entropy is described as the transformation content; it measures the degree of uncertainty, which exists in a system. Von Neumann [10] entropy refers to the extension of classical entropy concepts to the field of quantum mechanics. In each of these fields of physics, the entropy parameter is characterized by a certain number of mathematical properties, which originate from certain physical boundary conditions, each of them having a physical interpretation in the field of application. In the following, we list these mathematical properties in order to see how they can be interpreted in the case of polarimetric entropy

- 1) Continuity: Entropy is a continuous measure. This means that a small change in the measurement gives a small change in entropy.
- 2) Symmetry: The parameter value is unchanged if the outcomes  $x_i$  are reordered.
- 3) Maximum: If all outcomes are equiprobable, then entropy should be maximal.
- 4) Additivity: The amount of entropy should be the same, independent of how the process is regarded as being divided into parts.

Any definition of a parameter  $A$  satisfying these four assumptions has the form  $A = -const \sum_{i=1}^n p_i \log p_i$ , where  $p_i = p(x_i)$  is the probability of the output  $x_i$ .

It is important to note that the necessity of the logarithm form is explained by the additivity property. Additivity property means that the entropy of a system composed of independent subsystems is the sum of the entropies of its subsystems. If subsystems are not independent, the entropy of a system can still be calculated from the entropy of its subsystems provided that we know how the subsystems interact with each other. In the context of radar polarimetry, a subsystem would correspond to a partially polarimetric system. In order to understand how

the additivity property of entropy can be used, let us take an educational example. A fully polarimetric monostatic system can be viewed as the superposition of two partially polarimetric systems, for example, the first one measuring  $S_{HH}$  and  $S_{VV}$  and the second one measuring  $S_{HV}$ . If azimuth symmetry is assumed, then these two subsystems are independent, as azimuth symmetry supposes  $\langle S_{HH} S_{HV}^* \rangle = \langle S_{VV} S_{HV}^* \rangle = 0$ . In this case, the entropy of the whole system is equal to the sum of the entropies of the two subsystems. We see here that this property has a limited physical importance, since polarimetry operates in a space with less than three or four dimensions, and moreover, dividing the measurement of a fully polarimetric radar into several partially polarimetric radars does not decrease the total number of measurements nor the computation complexity, since it is the Sinclair matrix which is measured before computing the coherence matrix.

In the next sections, we will propose alternative entropylike parameters to be used in polarimetry. They are similar to the entropy described earlier but they do not have the "additivity" property. However, all the other properties will be verified.

## III. HERMITIAN MATRIX SIMILARITY INVARIANTS

### A. Similarity Invariants

When two square matrices  $A$  and  $B$  are related by  $B = X^{-1}AX$ , where  $X$  is a square nonsingular matrix, the matrices  $A$  and  $B$  are said to be similar. In other words, similar matrices represent the same linear transformation after a change of basis. Matrix eigenvalues and their combinations are invariant under similarity transform; however, they are not the only invariants. Let us consider here the trace, the determinant, and the sum of squared elements of a  $3 \times 3$  Hermitian matrix. These invariants are easy to calculate for any matrix, and they are connected to eigenvalues as follows:

$$\text{trace}(\mathbf{C}) = \lambda_1 + \lambda_2 + \lambda_3 \quad (14)$$

$$\det(\mathbf{C}) = \lambda_1 \lambda_2 \lambda_3 \quad (15)$$

$$\|\mathbf{C}\|_F^2 = \lambda_1^2 + \lambda_2^2 + \lambda_3^2. \quad (16)$$

The last invariant  $\|\mathbf{C}\|_F^2$  in (16) is the square of Frobenius norm  $\|\mathbf{C}\|_F$  of matrix  $\mathbf{C}$ ; it is defined as the square root of the sum of the absolute squares of its elements, and it is also equal to the square root of the matrix trace of  $\mathbf{C}\mathbf{C}^\dagger$ , where  $\dagger$  denotes the conjugate transpose (older texts refer to it as the Hilbert–Schmidt or the Schur norm) [11]. For any square matrix  $\mathbf{C}$ , this important property is verified

$$\sum_{ij} |C_{ij}|^2 = \text{trace}(\mathbf{C}\mathbf{C}^\dagger) = \|\mathbf{C}\|_F^2. \quad (17)$$

It can be seen that the three eigenvalues are roots of a characteristic equation, expressed in terms of these invariants

$$\lambda^3 - \lambda^2 \text{trace}(\mathbf{C}) + \frac{\lambda}{2} (\text{trace}(\mathbf{C})^2 - \|\mathbf{C}\|_F^2) - \det(\mathbf{C}) = 0. \quad (18)$$

This shows that these three invariants form an equivalent parameter set to eigenvalues. This means that, regardless of the basis of the scattering vector, covariance matrices share the same invariants. In SAR polarimetry, this means that the

Stokes matrix, Mueller matrix, coherency matrix, covariance matrix, covariance matrix in circular basis, etc., have the same eigenvalues, determinant, trace, and Frobenius norm.

Clearly, the first invariant, trace of the covariance matrix, has a simple meaning in polarimetry; it is the total backscattered power, also called span. As it is seen from (12), the entropy does not depend on this invariant value as it is defined by using Bernoulli weighted eigenvalues. It is then possible to form a matrix, whose eigenvalues are directly weighted eigenvalues (11) of the covariance matrix [12]. We define a new coherency matrix as follows:

$$\mathbf{N} = \langle \vec{k}^\dagger \vec{k} \rangle^{-1} \langle \vec{k} \vec{k}^\dagger \rangle = \frac{\mathbf{T}}{\text{trace}(\mathbf{T})} \quad (19)$$

and call it the power-normalized coherency matrix. Note that, since the trace of the matrix is normalized to one, the third eigenvalue is redundant. The advantage of the matrix  $\mathbf{N}$  is that the Bernoulli weights (11) appear directly as eigenvalues of the matrix.

### B. Parameter Based on the Frobenius Norm

We see that the Frobenius norm (16) of the normalized coherence matrix shares common features with target entropy, defined in (12). In eigenvector space, the Frobenius norm is the magnitude of sum of the eigenvectors, whereas span is algebraic sum of eigenvalues. The Frobenius norm is also very closely related to root mean square of the eigenvalues, a classical measure of variability. As the matrix  $\mathbf{N}$  is normalized by span, the Frobenius norm of  $\mathbf{N}$  gives the ratio between the total received power (span) and the vector sum of three orthogonal scattering mechanisms. If there is only one polarized scattering mechanism, both are equal, and the ratio is equal to one; if there are more scattering mechanisms present, the ratio is always smaller than one. In an extreme case, the power is distributed equally between all three orthogonal scattering processes, and each of the parameters is equal to 1/3. The Frobenius norm of the normalized coherence matrix is a descriptor of the amount of power one scattering mechanism is representing from total power. We will call this parameter **specific scattering predominance**. The reciprocal of the Frobenius norm of  $\mathbf{N}$  gives an indicator of the number of scattering mechanisms presented.

- 1) The Frobenius norm of  $\mathbf{N}$  is a dimensionless ratio.
- 2) Its range is limited.
- 3) Extreme values of the function are obtained under the same conditions as the entropy—one eigenvalue equal to zero or three equal eigenvalues.

The function's extreme points are the following, when  $p_1 = 1$  and  $p_2 = p_3 = 0$ ,  $\|\mathbf{N}\|_F^2 = 1$ , whereas for  $p_1 = p_2 = p_3 = 1/3$ ,  $\|\mathbf{N}\|_F^2 = 1/3$ . To achieve the same extreme points as entropy, we can define the following parameter:

$$\hat{H} = \frac{3}{2} (1 - \|\mathbf{N}\|_F^2). \quad (20)$$

We call this parameter **scattering diversity**. As shown in Fig. 1, the two parameters  $H$  and  $\hat{H}$  are highly correlated. The extreme points and limit values can be easily calculated by using (12) and (16), with eigenvalues as parametric equations.

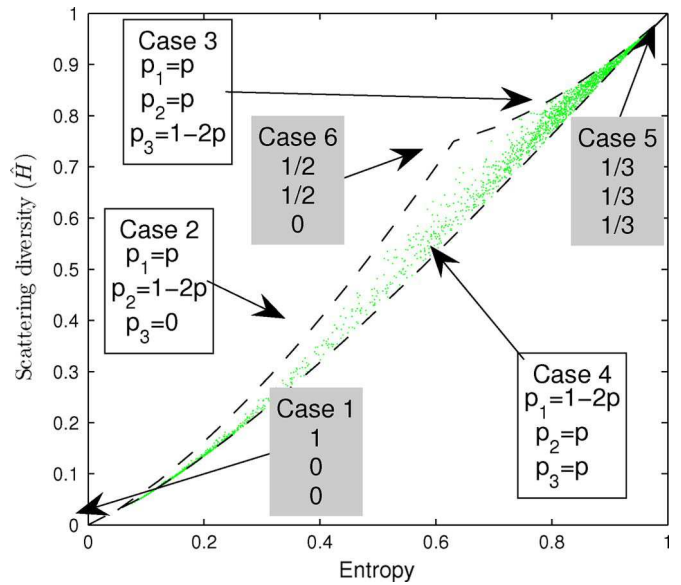


Fig. 1. Relation between the target entropy and the scattering diversity ( $\hat{H}$ ). Dots represent the scatterplot between parameter values calculated for the San Francisco image. The lines show extreme values of the parameters and conditions of these values in terms of eigenvalues.

Considering that  $p_1 + p_2 + p_3 = 1$ , one of the eigenvalues  $p_i$  of  $\mathbf{N}$  is redundant. In order to explain the resulting scatterplots, all precedent parameters can be easily expressed in terms of  $p_1$  and  $p_2$ , by using  $p_3 = 1 - p_1 - p_2$ . Several particular cases can be now envisaged

- Case 1) Two eigenvalues are zero,  $p_1 = 1, p_2 = p_3 = 0$ . This is the case of *deterministic targets*, where the entropy is equal to zero. In this case,  $\|\mathbf{N}\|_F = 1$ , and then,  $\hat{H} = 0$ .
- Case 2) Only one eigenvalue is zero.  $p_1 = p, p_2 = 1 - p$ , and  $p_3 = 0$ .
- Case 3) The two maximum eigenvalues are equal.  $p_1 = p_2 = p, p_3 = 1 - 2p$ , and  $1/3 \leq p \leq 1/2$ .
- Case 4) The two minimum eigenvalues are equal.  $p_1 = 1 - 2p, p_2 = p_3 = p$ , and  $0 \leq p \leq 1/3$ .
- Case 5) The three eigenvalues are equal.  $p_1 = p_2 = p_3 = 1/3$ . This corresponds to the case where  $H$  is maximum and equal to one.
- Case 6) When  $p_1 = p_2 = 1/2$  and  $p_3 = 0$ , show cases 2 and 3. The extreme points seen on the plot are, in this case,  $H = \log_3 2 \approx 0.63$ , whereas  $\hat{H} = 3/4$ .

Concerning  $\hat{H}$ , all these cases are shown in Fig. 1 as boundary lines for the scatterplot.

### C. Parameter Based on the Determinant

Several of the remarks for the Frobenius norm apply also to the determinant of  $\mathbf{N}$ . It is equal to zero for deterministic targets. However, it is zero also when only one eigenvalue is zero. It is maximum and equal to 1/9 when all eigenvalues are the same.

Thus, the determinant also shares common properties with the target entropy; however, the relation between entropy and the determinant of the normalized coherence matrix is clearly nonlinear, as shown in Fig. 2. The border lines are defined

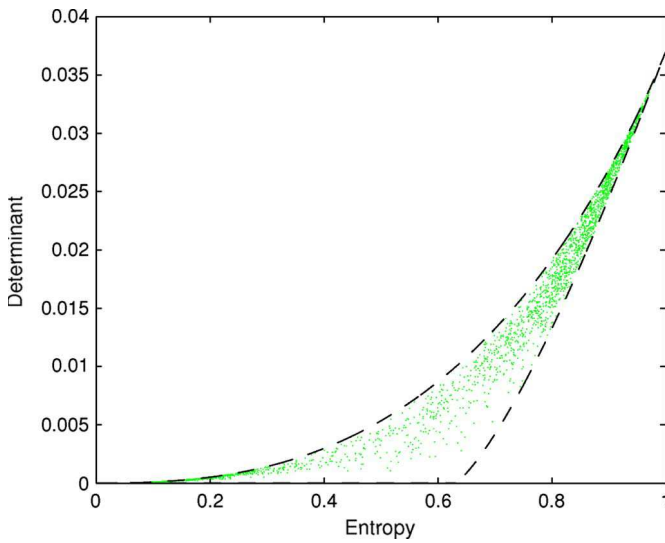


Fig. 2. Relation between the target entropy and the determinant of  $\mathbf{N}$ . Dots represent the scatterplot between parameters values calculated for the San Francisco image. The lines show extreme values of the parameters. Conditions for these values are the same as in Fig. 1.

by the same parametric equations mentioned in the previous section.

As proposed in [12], the determinant of  $\mathbf{N}$  can be used to approximate the target entropy. The matrix  $\mathbf{N}$  determinant in terms of eigenvalues is

$$\det(\mathbf{N}) = p_1 p_2 p_3. \tag{21}$$

By applying the spectral shift theorem [13], we can write

$$\det(\mathbf{N} + q\mathbf{I}) = (p_1 + q)(p_2 + q)(p_3 + q) \tag{22}$$

where  $\mathbf{I}$  is an identity matrix and  $q$  is a free parameter. We can arrange a nearly linear relationship between

$$\log_3(p_1^{p_1} p_2^{p_2} p_3^{p_3}) \propto \log_3((p_1 + q)(p_2 + q)(p_3 + q)) \tag{23}$$

when adjusting the free shift parameter to  $q = 0.16$ . Using (23), we can set up a new parameter nearly linearly related to the entropy (12)

$$H \approx H' = 0.78 \log_3(\det(\mathbf{N} + 0.16\mathbf{I})) + 2.52. \tag{24}$$

The relationship between the entropy and the approximated entropy is shown in Fig. 3. The relation does not deviate much from the linear one; however, the calculation of  $H'$  does not involve any eigenvalue calculation, as the determinant of a matrix can be calculated as simple linear combination of its elements.

#### IV. ENTROPY HIGHLIGHTED BY OPTICAL POLARIMETRY

Both radar and optical polarimetries are techniques that study the properties of the polarization of the scattered waves but traditionally refer to different wavelengths: optical wavelengths for optical polarimetry and high-frequency radio waves for radar polarimetry. These techniques have been developed in an independent way since the 1940s, and they follow different formalisms. The ‘‘Sinclair matrices’’ in radar polarimetry are

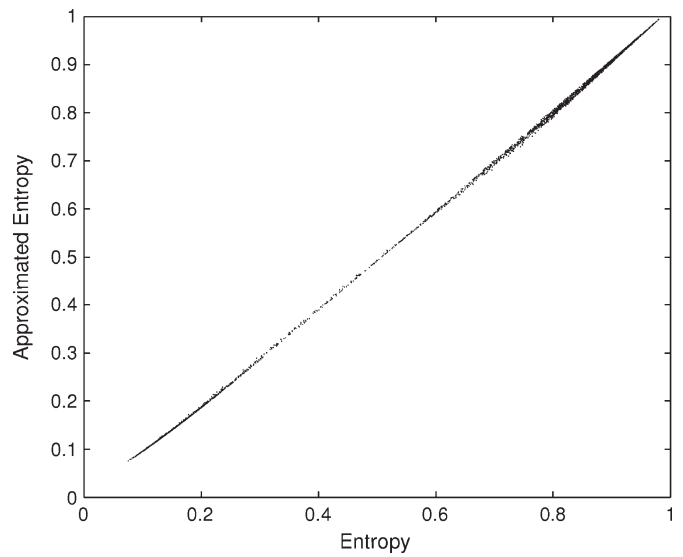


Fig. 3. Scatterplot between the target entropy (12) and the target entropy calculated by approximation (24).

adapted to the case of backscattering (known as the ‘‘monostatic’’ case), whereas the ‘‘Mueller’’  $4 \times 4$  matrices are adapted to the study of any geometrical configuration and to the measurements of the 16 power parameters obtained with a Mueller ellipsometer.

In the specific case of nondeterministic targets, we are able to deduce a set of radar polarimetric parameters, which is mathematically equivalent to the one obtained from the optical measurements by a Mueller ellipsometer; there is, then, a one-to-one linear mapping between the covariance and Mueller matrices, and the two approaches convey identically the same polarimetric information. To improve our understanding, it is worthwhile to investigate these concepts in order to understand how our entropy parameter is connected to the parameters used in optical polarimetry [8].

#### A. Connections Between Mueller and Coherence Matrices

We first discuss the link between the Kennaugh and the Mueller matrices. Both Mueller and Kennaugh matrices link the Stokes vectors of the emitted and received wave but are defined using different conventions. The Mueller matrix is expressed using the forward scattering alignment (FSA) convention, whereas the Kennaugh matrix is expressed using the back scattering alignment (BSA) convention [9]. The link between the ‘‘traditional’’ Mueller matrix  $\mathbf{M}$  and the Kennaugh matrix  $\mathbf{K}$  is

$$\mathbf{M} = [M_{kl}]_{k,l=0,\dots,3} = \begin{pmatrix} 1 & 0 & 0 & 0 \\ 0 & 1 & 0 & 0 \\ 0 & 0 & -1 & 0 \\ 0 & 0 & 0 & 1 \end{pmatrix} \mathbf{K}. \tag{25}$$

Note that we use for Mueller and Kennaugh matrix element an indexing from zero to three. This notation is used traditionally in optical polarimetry, where the first line and first column have a particular meaning from the squared submatrix indexed from one to three.  $K_{00} = M_{00}$  is the transmittance (transmission in intensity) for unpolarized light.

The  $\mathbf{T}$  and  $\mathbf{K}$  matrices are linked as follows. The Kennaugh matrix is defined by

$$\mathbf{K} = \mathbf{B}^\dagger \langle \mathbf{S} \otimes \mathbf{S}^* \rangle \mathbf{B} \quad (26)$$

where  $\mathbf{S}$  is the scattering matrix defined in (1), and  $\mathbf{B}$  is the following unitary matrix:

$$\mathbf{B} = \frac{1}{\sqrt{2}} \begin{pmatrix} 1 & 1 & 0 & 0 \\ 0 & 0 & 1 & -j \\ 0 & 0 & 1 & j \\ 1 & -1 & 0 & 0 \end{pmatrix}. \quad (27)$$

In order to study the proposed scattering diversity (20) in a Kennaugh matrix framework, we start by relating traces ( $\mathbf{T}$ ) and ( $\mathbf{T}^2$ ) to the  $\mathbf{K}$  matrix. The first relation is the following:

$$\text{trace}(\mathbf{K}^\dagger \mathbf{K}) = \text{trace}(\mathbf{T}^2) = \sum_{i,j} |T_{ij}|^2. \quad (28)$$

It can be demonstrated using the properties of Kronecker products, denoted by  $\otimes$ , and of Frobenius norm

$$\sqrt{\text{trace}(\mathbf{K}^\dagger \mathbf{K})} = \|\mathbf{K}\|_F = \|\langle \mathbf{S} \otimes \mathbf{S}^* \rangle\|_F \quad (29)$$

$$= \left\langle \sqrt{\text{trace}((\mathbf{S} \otimes \mathbf{S}^*)(\mathbf{S} \otimes \mathbf{S}^*)^\dagger)} \right\rangle \quad (30)$$

$$= \left\langle \sqrt{\text{trace}((\mathbf{S} \otimes \mathbf{S}^*)(\mathbf{S}^\dagger \otimes \mathbf{S}^t))} \right\rangle \quad (31)$$

$$= \left\langle \sqrt{\text{trace}((\mathbf{S}\mathbf{S}^\dagger)\text{trace}(\mathbf{S}^*\mathbf{S}^t))} \right\rangle \quad (32)$$

$$= \langle \text{trace}(\mathbf{S}\mathbf{S}^\dagger) \rangle = \text{trace}(\mathbf{T}^2). \quad (33)$$

The second property is related to the span defined in (13)

$$\text{trace}(\mathbf{T}) = 2K_{00} = 2M_{00}. \quad (34)$$

### B. Differences Between the Monostatic and the Bistatic Cases

As  $\mathbf{T}$  is a positive Hermitian matrix, the Cauchy–Schwartz inequality applied to the definition of the coherence matrix shows that

$$\text{trace}(\mathbf{T}^2) \leq \text{trace}(\mathbf{T})^2 \quad (35)$$

where the case of equality  $\text{trace}(\mathbf{T}^2) = \text{trace}(\mathbf{T})^2$  is obtained for deterministic targets. In order to find the minimum value of  $\text{trace}(\mathbf{T}^2)$ , two different cases have to be distinguished. The first one is the monostatic case and reciprocal target; the second one is the bistatic case or nonreciprocal target. The study of this last case is meaningful here, since most of ellipsometric measurements and theoretical studies are performed in a bistatic configuration without reciprocal assumption.

1) *When Reciprocity Assumption Holds:* In this case, the reciprocity assumption leads to a symmetric Sinclair matrix and then to the definition of  $3 \times 3$  coherency matrices. The corresponding coherency matrix of an “ideal depolarizer” is obtained for three equal eigenvalues

$$\mathbf{T}_{\text{ID monostatic}} = \text{trace}(\mathbf{T}) \begin{pmatrix} \frac{1}{3} & 0 & 0 \\ 0 & \frac{1}{3} & 0 \\ 0 & 0 & \frac{1}{3} \end{pmatrix}. \quad (36)$$

This matrix allows one to find the minimum value of  $\text{trace}(\mathbf{T}^2)$

$$\text{trace}(\mathbf{T}^2) \geq \frac{\text{trace}(\mathbf{T})^2}{3} \quad (37)$$

and combining the two inequalities (35) and (36) leads to

$$\frac{1}{3} \leq \text{trace}(\mathbf{N}^2) \leq 1. \quad (38)$$

2) *When Reciprocity Assumption Does Not Hold:* In the second case of bistatic geometry or nonreciprocal target, the Sinclair matrix is no longer symmetric; the coherency matrix is a  $4 \times 4$  matrix, and the case of maximal entropy is given by four equal eigenvalues. We now have

$$\frac{1}{4} \leq \text{trace}(\mathbf{N}^2) \leq 1. \quad (39)$$

If we want to extend our scattering diversity parameter to the bistatic case, achieving zero and one as extreme points, it leads to the definition

$$\hat{H}_{\text{bistatic}} = \frac{4}{3} (1 - \text{trace}(\mathbf{N}^2)) = \frac{8}{9} \hat{H}_{\text{monostatic}}. \quad (40)$$

### C. Degree of Purity and Connection to $\hat{H}$

To describe the characteristics of depolarization of a Mueller matrix, at least two parameters are used in optical polarimetry. The first one is called **degree of purity** [14] or **depolarization index** [15]. It is defined as the Euclidian distance of the normalized Mueller matrix  $\mathbf{M}/M_{00}$  to the ideal depolarizer of the nonreciprocal case

$$d(\mathbf{M}) = \left\| \frac{\mathbf{M}}{M_{00}} - \begin{pmatrix} 1 & 0 & 0 & 0 \\ 0 & 0 & 0 & 0 \\ 0 & 0 & 0 & 0 \\ 0 & 0 & 0 & 0 \end{pmatrix} \right\| = \frac{\sqrt{\sum_{i,j} M_{ij}^2 - M_{00}^2}}{M_{00}} \quad (41)$$

$d(\mathbf{M})$  is zero for an ideal depolarizer and  $\sqrt{3}$  for a nondepolarizing Mueller matrix.  $d(\mathbf{M})$  can be expressed in terms of elements of the coherency matrix using (13) and (28) as follows:

$$d(\mathbf{M}) = \frac{\sqrt{\sum_{i,j} T_{ij}^2 - \frac{(\text{trace} \mathbf{T})^2}{4}}}{\frac{\text{trace}(\mathbf{T})}{2}} \quad (42)$$

$$d(\mathbf{M}) = 2\sqrt{\|\mathbf{N}\|_F^2 - \frac{1}{4}} \quad (43)$$

which can be expressed here as twice the Euclidian distance of the normalized coherency matrix  $\mathbf{N}$  to the ideal depolarizer in the nonreciprocal case. The simple link between  $d(\mathbf{M})$  and  $\hat{H}_{\text{bistatic}}$  is

$$\hat{H}_{\text{bistatic}} = 1 - \frac{d(\mathbf{M})^2}{3} \quad (44)$$

$$d(\mathbf{M}) = \sqrt{3} \sqrt{1 - \hat{H}_{\text{bistatic}}}.$$

#### D. Depolarization and Connection to $\hat{H}$

Optical polarimetry uses another parameter called the depolarization of the matrix

$$\text{dep}(\mathbf{M}) = 1 - \frac{\sqrt{\sum_{i,j} M_{ij}^2 - M_{00}^2}}{\sqrt{3}M_{00}}. \quad (45)$$

This parameter indicates how far the matrix is from a set of Mueller matrices of nondepolarizing targets. It is connected to the average depolarization of the outgoing light. It is related to  $\hat{H}_{\text{bistatic}}$  by

$$\text{dep}(\mathbf{M}) = 1 - \sqrt{1 - \hat{H}_{\text{bistatic}}}. \quad (46)$$

#### E. Other Links

As in SAR polarimetry, optical polarimetry distinguishes between nondepolarizing Mueller or pure Mueller matrices, which correspond to deterministic targets in radar polarimetry, and depolarizing matrices, which correspond to nondeterministic or natural targets. A decomposition of the Mueller matrices into the product of several physically descriptive components has been proposed by Lu and Chipman [16]. Among the three components obtained by this decomposition, the retarder and the diattenuator correspond to pure elements, whereas depolarizers do not. Depolarizers are elements that convert completely polarized light into partially polarized light. They are the ones that “create” entropy. Once the depolarizer element is extracted from the general Mueller matrix by the Lu and Chipman decomposition, we are able to compute the **depolarization power**. This factor is defined as the average of the principal depolarization factors, and then, it indicates the averaged depolarization capability of this depolarizer. However, the calculation of this parameter requires application of the Lu and Chipman decomposition on the Mueller matrix. The distribution of the experimental errors induced by this decomposition was studied in [17]. It indeed showed, by a simulation, that, when the depolarization is significant, the computation errors in the depolarization and the retardance are often very high, considering that errors in the original matrix propagate through the decomposition. Then, the use of this parameter offers no advantage over the use of classical entropy.

To conclude this section, the alternative parameters to entropy proposed in this paper are strongly related with the physical interpretation of average depolarization of the outgoing light and with distance of the target to an ideal depolarizer. Note that the ideal depolarizer has different Kennaugh matrices in both the monostatic reciprocal and bistatic cases.

### V. ALTERNATIVES TO $\bar{\alpha}$ ANGLE

#### A. First Element of Normalized Coherence Matrix $\mathbf{N}$

Similarity invariants are independent of polarimetric basis and target orientation. However, in order to study the target orientation (relative to the measurement system) related polarimetry, we should also study the covariance matrix properties, which are connected to a certain basis. Thus, we should take a step back from invariants and go to basis definitions.

The coherency matrix was defined in (5) in such a way that one dimension is pointing to a roll-invariant direction. The  $\bar{\alpha}$  angle is a basis-invariant parameter, telling how far the scattering mechanism is from the roll-invariant single bounce scattering. Note that this last mechanism is defined in the monostatic case. By studying closely the definition of the coherency matrix eigenvalue problem described in (8), we can note that the first element of  $\mathbf{T}$ , which is  $T_{11}$ , is defined as

$$T_{11} = \sum_{i=1}^3 \lambda_i \cos^2 \alpha_i. \quad (47)$$

This relationship is not very far from the definition of the mean alpha angle given in (10), only the eigenvalues  $\lambda_i$  are not normalized to total power. Now, when looking at the same parameter of  $\mathbf{N}$ , we can write

$$N_{11} = \sum_{i=1}^3 p_i \cos^2 \alpha_i. \quad (48)$$

It is easy to show that both  $\bar{\alpha}$  and  $N_{11}$  depend on  $p_i$  and  $\alpha_i$  through positive monotonically increasing functions in the range  $0 \leq \alpha \leq \pi/2$ .

On the other hand, by the definition of  $\mathbf{N}$ ,  $N_{11}$  can be written as

$$N_{11} = \frac{\langle |S_{\text{hh}} + S_{\text{vv}}|^2 \rangle}{\text{span}}. \quad (49)$$

The parameter can therefore be interpreted as a fraction of surface scattering (strictly speaking, odd-bounce scattering) from total backscattered power. We will call it **surface scattering fraction**. When the parameter has a value of one, all backscattering comes from odd-bounce scattering; if the parameter has a value of zero, there is no odd-bounce scattering present. It can be also interpreted as a fraction of right-left polarized response from total backscattered power in a circular basis.

In relation to average alpha, we can distinguish three extreme cases.

- 1) When we have only one nonzero eigenvalue,  $N_{11} = \cos^2(\bar{\alpha})$ .
- 2) When one eigenvector corresponds to a pure single-bounce scatterer  $\alpha_i = 0$  (this determines the other two alphas to be  $\pi/2$ ), the relation becomes linear;  $N_{11} = 1 - 2\bar{\alpha}/\pi$ .
- 3) When one eigenvalue is zero and the noncorresponding alpha value is  $90^\circ$ , the linear envelope line of extreme values has the following form:  $N_{\text{env}} = R(\bar{\alpha} - \pi/2)$  for  $\bar{\alpha}$  range  $0 \leq \bar{\alpha} \leq \eta$ , where  $\eta = 1/2 \arcsin(2/\pi)$  and  $R = \cos(\eta)^2 / (\eta - \pi/2)$ .

These three lines are shown as dashed-dotted, dashed, and dotted lines, respectively, in Fig. 4. These lines form an envelope for all possible combinations of  $N_{11}$  and  $\bar{\alpha}$ . Green points in Fig. 4 are the data points from the well-known San Francisco image (Fig. 8). The points seldom reach some of the bounding lines because some combinations of eigenvectors and eigenvalues are not likely.

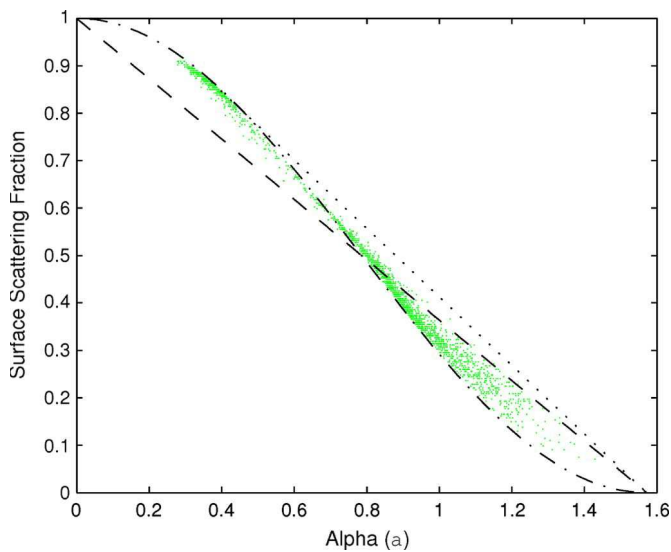


Fig. 4. Scatterplot between the mean alpha (10) angle and the surface scattering fraction (48).

### B. Retardance

Once again, it is possible to find an alternative interpretation of parameters used in SAR polarimetry when linking them to parameters used in optical polarimetry. Here, we show that the  $\bar{\alpha}$  angle is strongly related to the retardance.

The effect of a retarder upon polarization states is equivalent to a rotation on the Poincare sphere. Linear retardance can be interpreted as the degree of angular shift in the phase of eigenpolarizations.

Let us consider a pure linear retarder, whose axes are parallel to  $H$  and  $V$  polarizations. Its Sinclair matrix is given by

$$\mathbf{S}_R = \frac{1}{\sqrt{2}} \begin{pmatrix} e^{j\frac{\delta}{2}} & 0 \\ 0 & e^{-j\frac{\delta}{2}} \end{pmatrix}. \quad (50)$$

Based on the definitions given in [16], this is the matrix of a pure retarder with retardance  $\pi - \delta$ .  $\delta$  is the supplement of retardance defined in optical polarimetry, considering the different conventions FSA and BSA used by the radar and optics communities, respectively. Hence, in FSA convention, the diffusion matrix for vacuum is equal to identity; thus, the vacuum retardance is null, whereas, in BSA convention, the Sinclair matrix of a mirror is equal to identity, and the retardance is equal to  $\pi$ . Considering  $\pi - \delta$  in the monostatic case enables one to deal with a null parameter in the case of a simple mirror or sphere.

Computing the coherency matrix from this Sinclair matrix leads to the deduction that, in the case of a pure retarder with retardance,  $\pi - \delta$ ; then

$$N_{11} = \cos^2 \frac{\delta}{2}. \quad (51)$$

Total retardance  $R$  can be written as a combination of linear retardance  $\delta$  and optical rotation or circular retardance; however, in the monostatic case, circular retardance can only be due to external effects (as Faraday rotation) and not to the physical structure of the target. In other words, there is

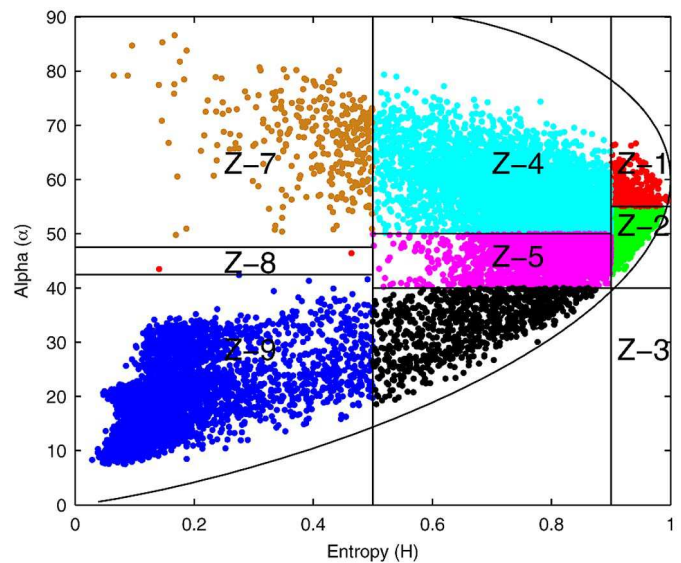


Fig. 5. Well-known entropy–alpha classification space with the San Francisco image classified according to the classification limits proposed by Cloude and Pottier [2].

no optical rotation in the reciprocal case, and then, in the monostatic limited case,  $\alpha = R/2$ .

## VI. DISCUSSION

### A. Benefits of Proposed Parameters in Interpretation

The proposed surface scattering fraction is intuitive, very straightforward to calculate, and the interpretation does not depend on whether we use a single- or multilook image. As shown, the information content in the parameter is very similar to the one in the alpha angle. The definition of the surface scattering fraction (48) shows also that only part of the span-independent polarimetric information is described by  $\bar{\alpha}$  or  $N_{11}$ .  $N_{22}$  or  $N_{33}$  should be also used in order to gather all the information contained in the three eigenvalues. The surface scattering fraction idea can be expanded to another parameter, for example, cross-polarized scattering fraction.

The concept of retardance from optical polarimetry or ellipsometry can give insight to the surface scattering fraction and alpha angle interpretation. In the monostatic case, the surface scattering fraction is linked to linear retardance in a simple manner. The linear retardance of a sample is indicative of the phase shift imparted to an incident beam according to two principal axes. This light-modifying behavior is representative of the anisotropy of the target's structure for nondeterministic targets.

The proposed scattering diversity is directly connected to the depolarization coefficient in optical polarimetry, which means that it quantifies the ability of the target to transform a perfectly polarized wave into a partially polarized one.

### B. Alternative Parameters in Classification

Scattering diversity  $\hat{H}$  combined with the surface scattering fraction can be used to form a classification space very similar to the well-known entropy–alpha classification space.

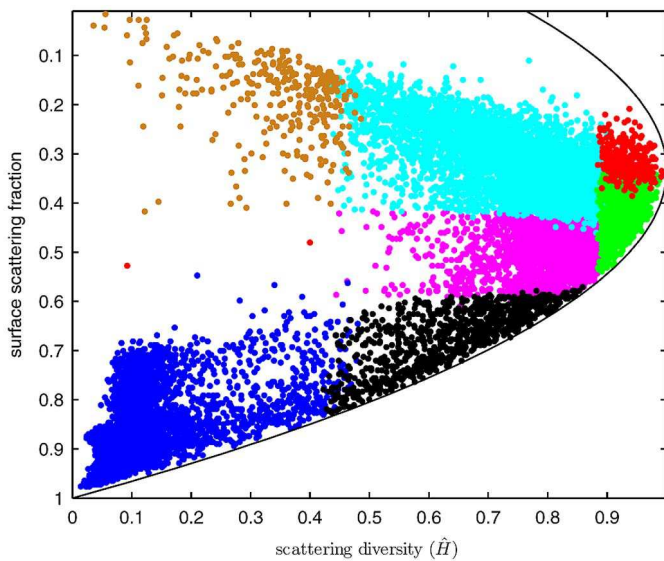


Fig. 6. Scattering diversity ( $\hat{H}$ ) and surface scattering fraction classification space, where dots are colored according to entropy-alpha classification results shown in Fig. 5.

In Figs. 5 and 6, we show comparisons of the original entropy-alpha classification with the alternative parameter classification abilities. Different classes are colored according to the original entropy-alpha classification result, and the same points are transferred to the space of surface scattering fraction and scattering diversity  $\hat{H}$ . As shown, the alternative parameter pair leads to very similar results, where original classes separate well but are slightly mixed near class borders. This is caused by the fact that the corresponding parameters do not have an unambiguous relationship with each other, considering that the used classification parameters depend on more than one variable and use different functions for computation.

By using the concept of maximal possible entropy (or zero anisotropy) for a certain  $\bar{\alpha}$  value, it is possible to derive the boundary lines of feasible regions for proposed parameter spaces. Maximal possible entropy is obtained, when two eigenvalues are equal and the third is the surface scattering fraction. This corresponds to cases 3 and 4 in Fig. 1. In this case, the three normalized eigenvalues are  $N_{11}$ ,  $1/2 - N_{11}/2$ , and  $1/2 - N_{11}/2$ , and

$$\hat{H}_{\max} = \frac{3}{4} - \frac{9}{4}N_{11}^2 + \frac{3}{2}N_{11}. \quad (52)$$

Once again, we can deduce the coordinate of the plot for  $N_{11} = 0$ , which is  $3/4$ , instead of  $\log_3(2)$  in the case of classical entropy.

When we interpret the eigenvalue space geometrically, we see that the presented classification space is a projection of the surface, where all possible normalized eigenvalue combinations are located. When the vector sum of eigenvalues is equally far from all three axes, the entropy is maximal. As we showed, the entropy-alpha classification space is essentially the same, except that the space is differently curved due to the logarithm function used in entropy definition. It seems that the classifica-

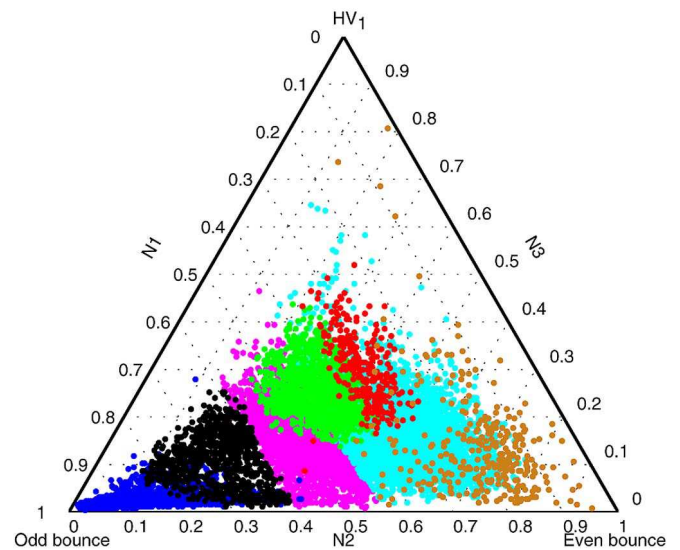


Fig. 7. Polarimetric ternary diagram. Classification-space-based N matrix main-diagonal elements. A point in the diagram shows the relative strength of three basic scattering mechanisms described by Pauli matrices. The diagram shows all  $N_{11}$ ,  $N_{22}$ , and  $N_{33}$  combinations without overlap. Scattering diversity or entropy is lowest on the edges and highest in the center of the triangle, where all scattering mechanisms have equal strength. Dots are colored according to entropy-alpha classification results shown in Fig. 5.

tion results provided by entropy and alpha can be achieved in a simpler manner. It should be mentioned that an entropy-alpha type of classification has problems. The classification space is highly nonlinear, and the class definitions are somewhat arbitrary and do not have a strict physical background. Using scattering diversity and surface scattering fraction for classification does not overcome these shortages; however, it improves the calculation efficiency.

For illustrative purposes, we can also use the values of  $N_{11}$ ,  $N_{22}$ , and  $N_{33}$  directly for classification. Considering that we have three variables, whose sum is constrained to one, we can use the classical ternary diagram to construct an easily interpretative classification space (equal to the situation when  $N_{11}$ ,  $N_{22}$ , and  $N_{33}$  are used in 3-D classification space where all points lie on the surface determined by a constant sum constraint). This polarimetric ternary diagram is shown in Fig. 7. In this diagram, the relative strength of three basic scattering mechanisms described by Pauli matrices can be represented unambiguously. The representation also includes information about the entropy parameter in an intuitive way. The high entropy class is in the middle of the triangle, and low entropy lies on the edges. As the odd-bounce direction is roll invariant, the corresponding class is clearly defined and is similar to the one in the entropy-alpha plot. Differences arise when we have double-bounce scattering, which can appear in different places depending on the orientation of the reflector. Normally, eigenvectors are not far from the original axis, i.e., odd bounce, even bounce, and cross polarizer. This means that coherency matrix off-diagonal elements are often insignificant. Therefore, classification by using just diagonal elements of the normalized coherency matrix gives results similar to those from the eigenvalue-based classification. The significance of

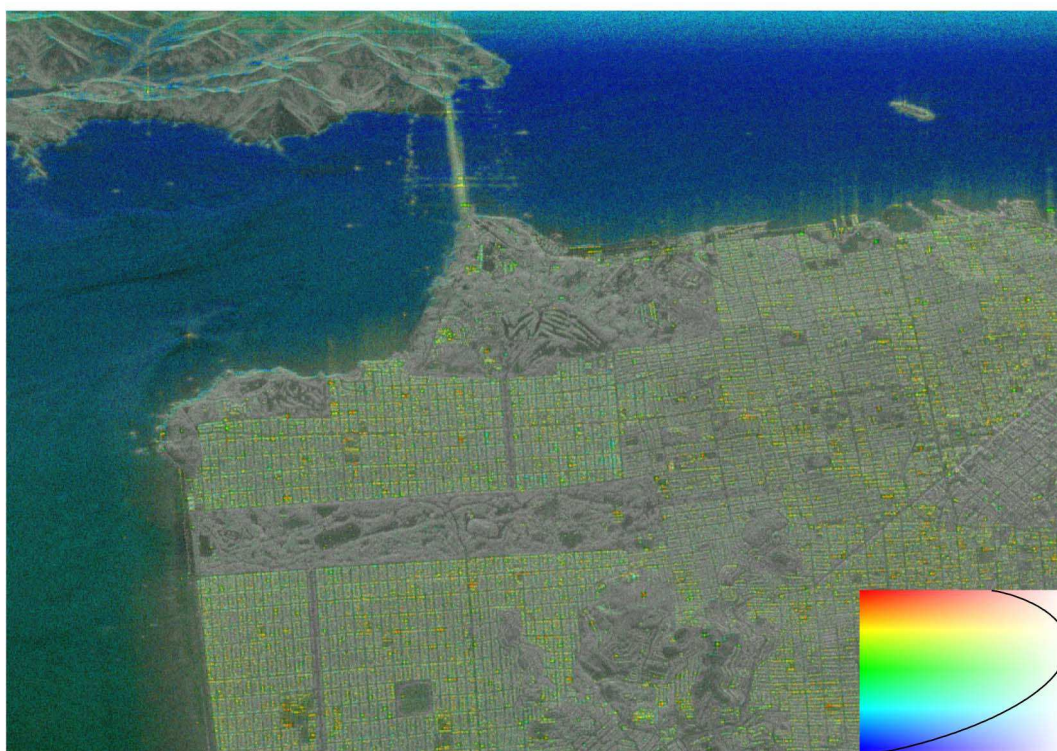


Fig. 8. Fully polarimetric SAR (AIRSAR) image of San Francisco Bay in multiresolution-synoptic visualization, where the hue is described by  $\bar{\alpha}$ , the saturation by entropy ( $H$ ), and the intensity by  $\log(\text{span})$ . Span and  $\bar{\alpha}$  are averaged over a  $4 \times 4$  window, and the entropy is calculated for a  $20 \times 20$  window. Gray denotes areas, where polarimetric information is random (parks and forest). (Blue) Single-bounce scattering. (Red) Double-bounce scattering.

off-diagonal elements of the coherence matrix can be easily tested by a parameter where the sum of squared elements of the coherency matrix off-diagonal elements is divided by the sum of squared elements of the main-diagonal elements.

### C. Polarimetric SAR Image Visualization

Another example of the usage of the new parameters is image visualization. As the parameters are easy to calculate, the visualization scheme can be used also in simple software packages. We use the visualization scheme for polarimetric SAR images first proposed by Imbo *et al.* [18]. The method utilizes hue-saturation-intensity color space to represent the SAR image scattering mechanism ( $\bar{\alpha}$  angle), entropy, and intensity. The main benefit of the scheme is the image-independent color space and constant scaling of parameters, as opposed to the red-green-blue (RGB) representation, where the colors of the image depend on the image intensity distribution. In [19], the method was further developed by the proposal that the intensity and hue layers of the image can be presented with higher resolution than the entropy layer. The proposed parameters are particularly well suited for this application. They are fast to calculate even for big images, and their interpretation is straightforward.

Fig. 8 shows the well-known SAR image of the San Francisco Bay. The hue of the image is controlled by entropy (averaged over a  $20 \times 20$  window); the saturation is determined by the  $\bar{\alpha}$  angle (averaged over a  $4 \times 4$  window), and the intensity is  $\log(\text{span})$  (averaged over a  $4 \times 4$  window).

Fig. 9 shows the same image but, instead of entropy and alpha, scattering diversity and surface scattering fraction are used for the saturation and hue, respectively. The images are very similar, although slightly different in color shades. The second image is faster to calculate. A combination of the ternary diagram and RGB image also gives an interesting possibility to visualize a polarimetric image. Fig. 10 shows the same SAR image of the San Francisco Bay in ternary-*RGB* color scheme. In this representation, colors have the same meaning independent of the image, and the white color denotes equal eigenvalues or high scattering diversity.

### D. Practical Calculation

The scattering diversity  $\hat{H}$  and surface scattering fraction  $N_{11}$  are faster to calculate than the target entropy  $H$  and average alpha  $\bar{\alpha}$ . The main advantage is gained by avoiding the eigendecomposition of the covariance matrix.

In Matlab environment, the evaluation of scattering diversity  $\hat{H}$  is approximately five times faster than the evaluation of  $H$  when eigenvectors and eigenvalues are found using an analytical formula available for  $3 \times 3$  coherency matrices. It is 28 times faster than using a Matlab built-in eigenvalue function.

Moreover, the square of the Frobenius norm of the covariance matrix can be easily calculated without advanced mathematical software. As shown, the calculation involves summing, squaring, and averaging of complex variables. All these arithmetical operations are additive and can be done for the imaginary and real parts separately and independently. This means that all

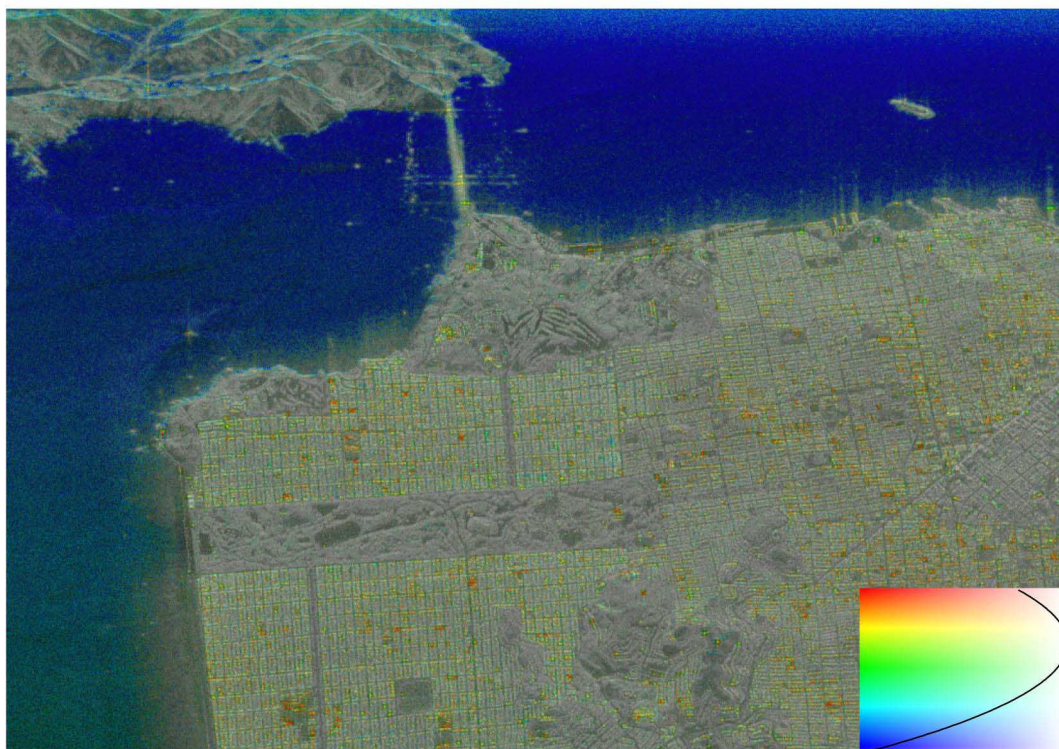


Fig. 9. Visualization of the same image as is in Fig. 8 shown in an equivalent manner. Instead of  $\bar{\alpha}$  and entropy, the surface scattering fraction and scattering diversity  $\hat{H}$  are visualized. The images are very similar in nature and can be interpreted in a similar way.

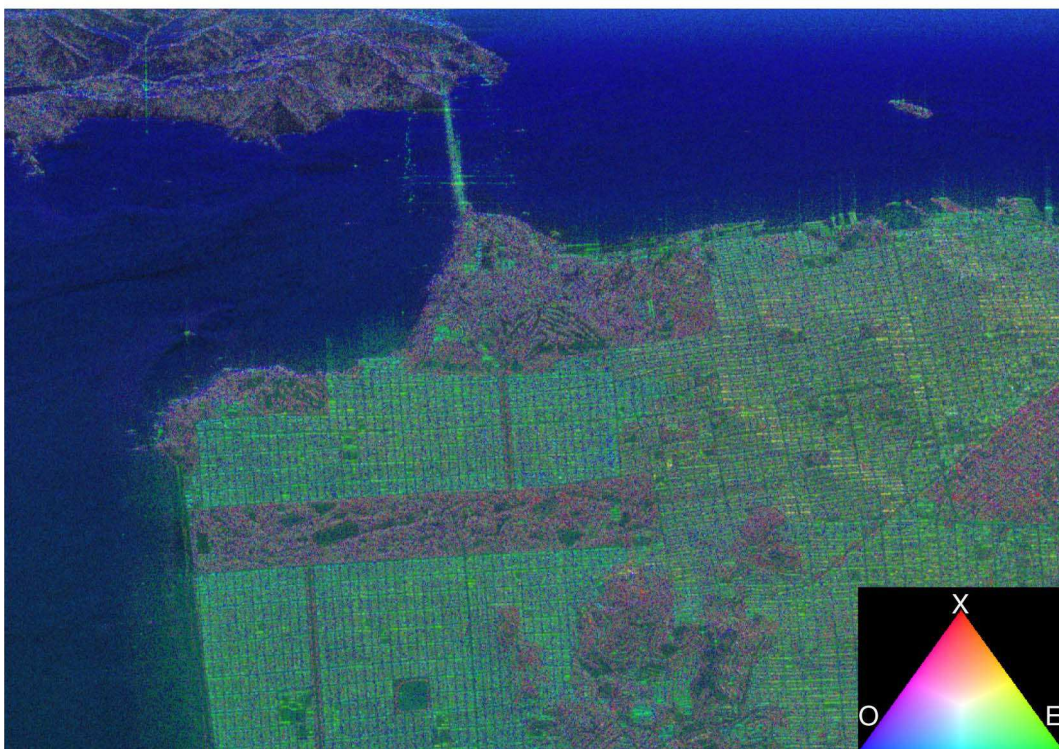


Fig. 10. Visualization of the same image as is in Fig. 8 shown in ternary- $\text{RGB}$  color scale. The color of a pixel is determined by the relative strength of basic scatterers represented by Pauli matrices  $(N_{11}, N_{22}, N_{33})$ , as shown in the ternary diagram in the lower right. The letters denote three pure scattering mechanisms. (O) Odd bounce. (E) Even bounce. (X) Cross polarizer. The intensity of a pixel is determined by the logarithm of total backscattered power (span).

the complex image layers can be interpreted as real variables and calculation is easy to carry out using remote-sensing software that supports multiband data. When classical parameters

are needed, the entropy approximation  $H'$  and  $\arccos \sqrt{N_{11}}$  can be used (although  $H'$  is not useful for theoretical studies).

### E. About Eigenvalue Analysis

Eigenvalue analysis of the coherency matrix is a powerful tool; however, when we are using only the entropy and alpha angles, we do not exploit, very efficiently, the possibilities of the approach. The power of eigenvalues lies in individual eigenvalues rather than in averaged parameters. The average information is possible to retrieve without eigendecomposition.

One of the great advantages of entropy and alpha parameters is the roll-invariance property; these parameters do not depend on the orientation of the target around the line of sight. Fortunately, scattering diversity and surface scattering fraction are also roll invariant.

There are also some limitations, which should be taken into account when interpreting the results of classical and alternative parameters. These limitations arise particularly when spatial average is used to calculate the covariance matrix estimate or any other second-order statistical descriptor for SAR images.

The eigendecomposition is made on the basis of received energy in three orthogonal measurement channels. Unfortunately, these channels are not equally powerful due to the monostatic imaging geometry. Most powerful are the single and, sometimes, double reflections back to the receiver direction. Because of this, the two strongest eigenvectors point mostly to the odd- and double-bounce directions, thus determining also the third eigenvector, which is always perpendicular to the previous ones. As a consequence, cross-polarizing target features are weakly presented in eigendecomposition parameters. This is shown in Fig. 5, where data are distributed mainly along the curve low alpha–high entropy–high alpha. Even more clearly, we can see the feature shown in Fig. 7, where most of the data are distributed between the odd and the even bounces, combined sometimes with high scattering diversity. The upper triangle, where the cross-polarizing features lie, contain only a few points. Another problem is that the eigendecomposition (or, rather, the averaged covariance matrix) preserves polarimetric features only in the case of a strictly homogeneous distributed target when the data distribution is multivariate Gaussian. Information about different underlying distribution functions is lost in averaging. In the case of inhomogeneity, averaging emphasizes polarimetric features of the strong scatterer. Moreover, the averaged and eigenvalue-weighted parameters, such as alpha and entropy, emphasize the polarimetric properties of strong scatterers. This can be avoided by using elaborated filtering and by assuring that averages are taken only over homogeneous parts. Unfortunately, sometimes, images are provided, which are readily geocoded and prefiltered by simple filters. We believe that small eigenvalues and corresponding eigenvectors can contain useful polarimetric information and should not be neglected.

## VII. CONCLUSION

We have presented an analysis of target-entropy and alpha-angle ( $\bar{\alpha}$ ) parameters frequently used in SAR polarimetry target description. In order to provide alternative ways for interpretation, we have shown how these parameters are connected to the covariance matrix symmetry properties and to parameters

used to describe the polarization of the scattering in optical polarimetry. The target entropy can be related to depolarization index and alpha angle to retardance.

Our analysis reveals that the proposed parameters can be used instead of entropy and alpha to describe the same polarimetric properties of the target. Instead of entropy, **scattering diversity** or **specific scattering predominance** can be used. The alpha angle can be replaced by **surface scattering fraction**. The proposed parameters are suitable for image interpretation, classification, and visualization in a similar manner to entropy-alpha, but are easier to interpret and calculate as they do not require the calculation of eigenvalues or eigenvectors of the coherency matrix. The eigenvalue decomposition is a powerful tool in polarimetry, which provides a sound framework for understanding; however, alpha and entropy do not fully exploit its possibilities. In eigenvalue decomposition practical usage, more attention should be paid to individual eigenvectors and eigenvalues, in order to retrieve the polarimetric information not accessible by other means. We hope that our analysis has given also a fresh insight to the interpretation of eigenvalue-analysis-based parameters and motivates the SAR community to search connections between various approaches in polarimetry.

## REFERENCES

- [1] S. R. Cloude, "Uniqueness of target decomposition theorems in radar polarimetry," in *Direct and Inverse Methods in Radar Polarimetry, Part 1, NATO-ARW*, W. M. Boerner, L. A. Cram, W. A. Holm, D. E. Stein, W. Wiesbeck, W. Keydel, D. Giuli, D. T. Gjessing, F. A. Molinet, and H. Brand, Eds. Norwell, MA: Kluwer, 1992, pp. 267–296.
- [2] S. R. Cloude and E. Pottier, "A review of target decomposition theorems in radar polarimetry," *IEEE Trans. Geosci. Remote Sens.*, vol. 34, no. 2, pp. 498–517, Mar. 1996.
- [3] C. E. Shannon, "A mathematical theory of communication," *Bell Syst. Tech. J.*, vol. 27, pp. 379–423, Jul. 1948.
- [4] C. E. Shannon, "A mathematical theory of communication," *Bell Syst. Tech. J.*, vol. 27, pp. 623–656, Oct. 1948.
- [5] S. R. Cloude and E. Pottier, "An entropy based classification scheme for land applications of polarimetric SAR," *IEEE Trans. Geosci. Remote Sens.*, vol. 35, no. 1, pp. 68–78, Jan. 1997.
- [6] J. Lee, M. Grunes, T. Ainsworth, L. Du, D. Schuler, and S. Cloude, "Unsupervised classification using polarimetric decomposition and complex Wishart classifier," in *Proc. IEEE IGARSS*, Jul. 6–10, 1998, vol. 4, pp. 2178–2180.
- [7] C. Fang, H. Wen, and W. Yirong, "An improved Cloude–Pottier decomposition using  $h/\alpha/\text{span}$  and complex Wishart classifier for polarimetric SAR classification," in *Proc. CIE*, Oct. 2006, pp. 1–4.
- [8] E. Colin, "Polarimetric optical tools and decompositions applied to SAR images," in *Proc. IEEE IGARSS*, Jul. 23–27, 2007, pp. 4191–4194.
- [9] E. Luneburg, S. Cloude, and W.-M. Boerner, "On the proper polarimetric scattering matrix formulation of the forward propagation versus backscattering radar systems description," in *Proc. IEEE IGARSS*, Aug. 3–8, 1997, vol. 4, pp. 1591–1593.
- [10] J. Von Neumann, *Mathematische Grundlagen der Quantenmechanik (Mathematical Foundations of Quantum Mechanics)*. Berlin, Germany: Springer-Verlag, 1995.
- [11] G. Golub and C. Van Loan, *Matrix Computations*, 3rd ed. Baltimore, MD: Johns Hopkins Univ. Press, 1996.
- [12] J. Praks and M. Hallikainen, "A novel approach in polarimetric covariance matrix eigendecomposition," in *Proc. IEEE IGARSS*, Jul. 24–28, 2000, vol. 3, pp. 1119–1121.
- [13] E. Kreyszig, *Advanced Engineering Mathematics*, 7th ed. E. Kreyszig, Ed. New York: Wiley, 1993.
- [14] J. J. Gil, "Characteristic properties of Mueller matrices," *J. Opt. Soc. Amer. A, Opt. Image Sci.*, vol. 17, no. 2, pp. 328–334, Feb. 2000.
- [15] R. Chipman, "Depolarization index and the average degree of polarization," *Appl. Opt.*, vol. 44, no. 13, pp. 2490–2495, May 2005.

- [16] S.-Y. Lu and R. A. Chipman, "Interpretation of Mueller matrices based on polar decomposition," *J. Opt. Soc. Amer. A, Opt. Image Sci.*, vol. 13, no. 5, pp. 1106–1113, May 1996.
- [17] D. M. Hayes, "Error propagation in decomposition of Mueller matrices," in *Proc. SPIE Polarization: Meas., Anal., Remote Sensing—Presented at the Society of Photo-Optical Instrumentation Engineers (SPIE) Conference*, D. H. Goldstein and R. A. Chipman, Eds., Oct. 1997, vol. 3121, pp. 112–123.
- [18] P. Imbo, J. Souyris, A. Lopes, and P. Marthon, "Synoptic representation of the polarimetric information," in *Proc. CEOS SAR Workshop*, Toulouse, France, Oct. 26–29, 1999, p. 341.
- [19] J. Praks and M. Hallikainen, "Combining high resolution and low resolution information in synoptic representation of fully polarimetric SAR images," in *Proc. 2nd Int. Workshop Appl. Polarimetric Interferometry, POLinSAR*, Jan. 17–21, 2005. [Online]. Available: <http://earth.esa.int/cgi-bin/confpol.pl?abstract=143>



**Jaan Praks** (S'98–M'02) was born on November 16, 1971, in Estonia. He received the M.Sc. degree in physics from Tartu University, Tartu, Estonia, in 1996 and is currently working toward the Ph.D. degree in remote sensing of boreal environment in the Department of Radio Science and Engineering, Helsinki University of Technology, Espoo, Finland.

In 1995 and 1996, he was with the Vegetation Remote Sensing Group, Tartu Observatory. Since 1997, he has been with the Helsinki University of

Technology, first with the Laboratory of Space Technology and then as a Teaching Assistant of space technology with the Department of Radio Science and Engineering. During his career, he has participated in many international remote-sensing projects on optical and SAR remote sensing and managed several airborne measurement campaigns. His main research interests include SAR polarimetry and interferometry.



**Elise Colin Koeniguer** was born on November 15, 1979, in France. She jointly received the Dipl. Ing. degree in electrical engineering from L'École Supérieure d'Électricité, Gif-sur-Yvette, France, and the M.Sc. degree in theoretical physics from the University of Orsay (Paris XI), Orsay, France, in 2002 and the Ph.D. degree from the University of Paris VI, Paris, France, in 2005, working on polarimetric interferometry with airborne systems.

Since 2005, she has been with the Electromagnetic and Radar Division of ONERA, Office National d'Études et de Recherches Aérospatiales, Palaiseau, France. Her research interests cover various subjects in electromagnetism and radar. Her current interests include comparison between radar polarimetry and optical polarimetry, and bistatic images.



**Martti T. Hallikainen** (M'83–SM'85–F'93) received the D.Tech. degree from the Helsinki University of Technology, Espoo, Finland, in 1980.

He was a Postdoctoral Fellow with the Remote Sensing Laboratory, University of Kansas, Lawrence, in 1981–1983. Since 1987, he has been a Professor of space technology with the Helsinki University of Technology. He was a Visiting Scientist with the European Union's Joint Research Centre, Institute for Remote Sensing Applications, Ispra, Italy, in 1993–1994 and with the Jet Propulsion Lab-

oratory and NASA Goddard Space Flight Center/Goddard Earth Sciences and Technology Center, University of Maryland, Baltimore, MD, in 2007–2008. His research interests include the development of microwave sensors for airborne and spaceborne remote sensing, development of methods to retrieve the characteristics of geophysical targets from satellite and airborne measurements, and cryospheric applications of remote sensing.

Prof. Hallikainen has been an IEEE Geoscience and Remote Sensing Society (GRSS) Honorary Life Member since 2007. He was a member of the GRSS Administrative Committee in 1988–2006 and the General Chair of the International Geoscience and Remote Sensing Symposium '91 held in Espoo. He served as the President of the IEEE GRSS in 1996–1997, and he currently serves as the Cochair of the IEEE GRSS Awards Committee. He has been the Vice President of the International Union of Radio Science (URSI) since 2005, and he served as the Chair of URSI Commission F in 2002–2005. He has been the national official member of URSI Commission F since 1988, and he was the Chair of the URSI Finnish National Committee in 1997–2005. He has been the Vice Chair of the Finnish National Committee of the Committee on Space Research since 2000. He was a member of the European Space Agency's Earth Science Advisory Committee in 1998–2001. He was the Secretary General of the European Association of Remote Sensing Laboratories (EARSeL), in 1989–1993, and was the Chairman of the Organizing Committee for the EARSeL 1989 General Assembly and Symposium held in Espoo. He has been a member of the EARSeL Council since 1985. He is the recipient of three IEEE GRSS Awards: the 1999 Distinguished Achievement Award; the IGARSS'96 Interactive Paper Award; and the 1994 Outstanding Service Award. He was the recipient of the IEEE Third Millennium Medal in 2000 and the Microwave Prize for the best paper in the 1992 European Microwave Conference.

# An Interferometric Coherence Optimization Method in Radar Polarimetry for High-Resolution Imagery

Elise Colin, Cécile Titin-Schnaider, and Walid Tabbara, *Member, IEEE*

**Abstract**—This paper investigates to what extent a new interferometric coherence optimization in radar polarimetry allows the separation of point scatterers located in the same resolution cell according to their interferometric phases. An interferometric coherence definition called the single-mechanism coherence is introduced, and the corresponding optimization method is briefly discussed. This method was first validated theoretically when no volume decorrelation occurs. Then, it has been applied to simple target measurements acquired in an anechoic chamber, and to an X-band polarimetric and interferometric synthetic aperture radar image containing man-made targets. In both cases, the single-mechanism coherence optimization enables to resolve the interferometric phases of several scattering centers inside the same resolution cell.

**Index Terms**—Coherence optimization, interferometry, polarimetry.

## I. INTRODUCTION

INTERFEROMETRY is an efficient approach used to reconstruct the topography of a given region [1]. It is based on the measurement of the phase difference between two paired pixels of two complex synthetic aperture radar (SAR) images obtained from the data collected by two antennas. The elevation of the terrain is proportional to this phase difference, known as interferometric phase.

PolInSAR processing (combining polarimetric and interferometric data) has been first investigated in forest, which is a random media [2], [3]. One of the key ideas is that it is possible to obtain interferograms from all possible linear combinations of polarization states. One benefit that results from the use of these combinations is the possible improvement of the coherence level using the polarimetric information, and consequently an increase in the accuracy of the reconstructed elevation profiles for each scatterer.

In this context, the generalized coherence has been introduced in [3] as a stochastic variable which measures the resemblance between the response of an electromagnetic mechanism at the first antenna, and another electromagnetic mechanism at the second antenna. The optimization problem has been introduced and solved to obtain the optimum scattering mechanism which leads to the highest interferometric coherence, and therefore, to the best phase estimates. In this paper, it will be called the two-mechanism coherence (2MC) optimization. The efficiency of this method to obtain accurate estimation of interferometric

phases has been proven. For example in [4], the impact of this polarimetric coherence optimization technique on phase unwrapping is assessed. The results show that the polarimetric coherence optimization reduces the density of noise-induced residues and, as a consequence, alleviates the resulting bias in phase unwrapping.

However, there are other possible definitions of a generalized coherence for polarimetry, and therefore other possible methods to perform an optimization. For example, the so-called polarization subspace method (PSM) described in [5] is based on finding local maxima of the copolar or crosspolar coherence functions. Physically, the mechanisms must be represented as an elliptic polarization transformation. The approach of the polarization state conformation (PSC) algorithm in [6] is very similar: it is based on the knowledge of the polarimetric basis transformation along with the polarization signatures of both interferometric images.

Another aspect investigated in PolInSAR is the possibility of separating the relative positions of points located inside the same resolution cell. Thus, the ESPRIT algorithm has been used in order to separate and retrieve the interferometric phase centers of local dominant scatterers in a target [7]. In [8], the same approach is applied to estimate the height of buildings.

The aim of this paper is first to propose another coherence optimization, which performs the optimization of the coherence using the same complex unitary vector for both antennas. This coherence will be called the single-mechanism coherence (1MC). In the interferometric configuration, both antennas as well as the incidence angles are very close, and it is sensible to calculate a coherence for two equal mechanisms [9]. It is even more suitable in a single-pass acquisition since signals are not affected by temporal decorrelation effects.

Using this 1MC coherence observable, a study about the possibility of point scatterers discrimination inside a resolution cell using single-baseline PolInSAR data was made in [10], and first numerical results for a typical urban scenario were provided. The analysis showed that two scatterers can be separated from single baseline dual-polarization interferometric SAR data. On the other hand, three scatterers can be separated from fully polarimetric interferometric data provided to make assumptions about the scattering properties of two scatterers.

In this paper, we investigate the use of a coherence optimization algorithm to separate several individual scattering centers. The results of the optimization obtained with this 1MC definition are always mathematically suboptima of the 2MC optimization. However, the choice of the method (1MC coherence optimization or 2MC coherence optimization) depends on the circumstances of the problem. In the context of high-resolution and high-frequency imagery, ionospheric or orientation effects

Manuscript received April 13, 2005; revised June 13, 2005.

E. Colin and C. Titin-Schnaider are with the Electromagnetism and Radar Department (DEMR), French Aerospace Research Center (ONERA), Palaiseau 91761, France (e-mail: elise.colin@onera.fr).

W. Tabbara is with the University of Paris VI, 75005 Paris, France.  
Digital Object Identifier 10.1109/TGRS.2005.859357

need not be taken into account. The 1MC coherence optimization results can be considered as physically optima, since using different vectors introduces polarimetric decorrelation between the two scattering mechanisms. Moreover, the 1MC coherence is easier to interpret, due to the intrinsic assumption that both images are transformed in the same way.

Gomez-Danz and Quegan [11] have recently undertaken the study of layered targets in the context of polarimetric interferometry, and the use of coherence optimizations was examined for layer information retrieval. The 2MC optimization results were poor unless a large number of independent looks were combined. The 1MC optimization on the other hand was proved to be a more robust technique. Moreover, it was also able to retrieve interferometric heights of two individual layers in a layered model of a crop scattering application.

An important point is the physical interpretation of the optimum polarization states in terms of scatterer characteristics. Section II presents the general interpretation of such a scattering mechanism. Then, the 1MC coherence is introduced, and a numerically efficient optimization method is proposed in Section III. In Section IV it is mathematically proven that for a resolution cell containing few independent scattering centers, the optimum polarization states lead to the estimation of the interferometric phases of these point scatterers. Results and investigations obtained from the application of the optimization techniques to measures in an anechoic chamber and to a PolInSAR image are discussed in Section V. In the context of high-resolution imagery, this technique is able to separate up to three dominant point scatterers in a resolution cell, and the optimization can also be efficiently used in order to obtain better phase estimates on a SAR image of an urban area at X-band.

## II. HOW TO CHOOSE AN ELECTROMAGNETIC MECHANISM $\omega$ ?

### A. Data model

With *a priori* knowledge of the polarimetric behavior of the point scatterers located in the same resolution cell, we will discuss how to choose a mechanism  $\omega$  to select these points. We use the same data model as with the ESPRIT algorithm [7], [8] which can be applied for resolution cells containing several point scatterers without taking into account the interactions between scatterers or the volume effects. The signal  $\mathbf{E}_1$  acquired by the first antenna in polarization xy consists of a sum of  $N$  different elementary scattering contributions

$$\mathbf{E}_1^{xy} = \sigma_A s_A^{xy} e^{-j4\pi \frac{\rho_{1A}}{\lambda}} + \dots + \sigma_N s_N^{xy} e^{-j4\pi \frac{\rho_{1N}}{\lambda}} \quad (1)$$

and so does the electric field  $\mathbf{E}_2$  for the second antenna

$$\mathbf{E}_2^{xy} = \sigma_A s_A^{xy} e^{-j4\pi \frac{\rho_{2A}}{\lambda}} + \dots + \sigma_N s_N^{xy} e^{-j4\pi \frac{\rho_{2N}}{\lambda}}. \quad (2)$$

$\sigma_A$  is the total power (span) of the point  $A$ ,  $\rho_{1A}$  is the distance between point  $A$  and the first antenna, and  $s_A^{xy}$  is the complex reflectivity coefficient for polarization  $xy$ . For simplicity, we can assume that the complex diffusion vector  $s_A = (s_A^{hh}, s_A^{hv}, s_A^{vv})$  can be normalized. The points  $A, B, \dots, N$  are in the same resolution cell defined by the first antenna, so that one may assume  $\rho_{1A} = \rho_{1B} = \dots = \rho_{1N} = \rho$ . Moreover, let us write

$$\rho_{2A} = \rho + \Delta\rho_A \quad \rho_{2B} = \rho + \Delta\rho_B, \dots, \rho_{2N} = \rho + \Delta\rho_N. \quad (3)$$

These expressions can be rewritten in a matrix form as

$$\mathbf{E}_1 = S\sigma \quad \mathbf{E}_2 = SD\sigma. \quad (4)$$

$S$  is a complex  $3 \times N$  matrix whose columns contain the normalized polarimetric diffusion vectors for each point,  $\sigma$  is the real column vector of length  $N$  containing the total power (span) of each point, and  $D$  is the  $N$ -diagonal matrix containing the interferometric phases

$$D = \begin{pmatrix} e^{-j\Phi_A} & & & \\ & e^{-j\Phi_B} & & \\ & & \ddots & \\ & & & e^{-j\Phi_M} \end{pmatrix} \quad (5)$$

where the  $\Phi_M = 4\pi(\Delta\rho_M/\lambda)$  are the interferometric phases.

### B. Choosing $\omega$ Knowing the Polarization States $S$ of Each Points

The coherency matrices are expressed in terms of the matrices  $S, D$ , and  $\sigma$  without applying any averaging window

$$T_{12} = E_1 E_2^\dagger = S\sigma\sigma^\dagger D^* S^\dagger \quad (6)$$

where  $\dagger$  indicates the matrix conjugate transposition. Let  $M$  be a matrix such as  $M^\dagger S = I$ , where  $I$  is the  $N \times N$  identity matrix.  $M^\dagger$  is the inverse of  $S$  only in the particular case where  $S$  is a square matrix ( $N = 3$ ). We will discuss further the existence of the matrix  $M$ .

Let  $\omega_i$  be the  $i$ th column vector of  $M$ . Then

$$\omega_i = M\mathbf{e}_i \quad (7)$$

where  $\mathbf{e}_i$  is an  $N$  length basis vector. The interferometric coherence defined with one mechanism  $\omega$  is expressed in terms of the coherency matrices as

$$\gamma(\omega) = \frac{\omega^\dagger T_{12} \omega}{\sqrt{\omega^\dagger T_{11} \omega} \sqrt{\omega^\dagger T_{22} \omega}}. \quad (8)$$

Without considering any averaging to compute the coherency matrices, the absolute value of this cross correlation always equals 1. But in the context of statistical fluctuations, this coefficient becomes important since it can provide the measure of the loss of coherence and then of the phase noise of the interferogram. Let us now consider the phase of the coherence which is obtained with the mechanism  $\omega_i = M\mathbf{e}_i$

$$\omega_i^\dagger T_{12} \omega_i = \mathbf{e}_i^\dagger M^\dagger S\sigma\sigma^\dagger D^* S^\dagger M\mathbf{e}_i = \mathbf{e}_i^\dagger \sigma\sigma^\dagger D^* \mathbf{e}_i. \quad (9)$$

$D^* \mathbf{e}_i$  is the  $i$ th column vector of  $D^*$ , i.e.,  $e^{j\Phi_i} \mathbf{e}_i$ . Moreover,  $\mathbf{e}_i^\dagger \sigma\sigma^\dagger \mathbf{e}_i$  is the  $i$ th element of diagonal of  $\sigma\sigma^\dagger$ , i.e.,  $\sigma_i^2$ . We thus obtain

$$\omega_i^\dagger T_{12} \omega_i = \sigma_i^2 e^{j\Phi_i}. \quad (10)$$

The mechanism  $\omega_i$  enables the calculation of the interferometric phase of the point  $i$  because

$$\arg \gamma(\omega_i) = \arg (\omega_i^\dagger T_{12} \omega_i) = \Phi_i. \quad (11)$$

Let us now discuss the existence of matrix  $M$ .

- If  $N = 3$ ,  $S$  is a  $3 \times 3$  matrix, and  $M$  is the conjugate transpose of the  $S$  inverse.  $M$  exists if and only if the three columns of  $S$  are linearly independent, which means the three points have three different polarimetric responses. In the particular case where the polarimetric responses are orthogonal,  $S$  is a unitary matrix and then  $M = S$ .
- If  $N < 3$ , finding  $M^\dagger$  is an overdetermined problem.  $M$  exists except if two points have similar polarimetric responses. Besides this particular case, it is important to note that  $M$  is not unique. For example, if  $S$  is

$$S = \begin{pmatrix} 0 & 0 \\ 1 & \frac{1}{\sqrt{2}} \\ 0 & \frac{1}{\sqrt{2}} \end{pmatrix} \quad (12)$$

then

$$M^\dagger = \begin{pmatrix} * & 1 & -1 \\ * & 0 & \sqrt{2} \end{pmatrix} \quad (13)$$

where  $*$  can be replaced by any value. Therefore, the different interferometric phases can be estimated by the mechanisms

$$\omega_1 = \begin{pmatrix} * \\ 1 \\ -1 \end{pmatrix} \quad \omega_2 = \begin{pmatrix} * \\ 0 \\ \sqrt{2} \end{pmatrix}. \quad (14)$$

- If  $N > 3$ , finding  $M$  is an underestimated problem.  $M$  exists if and only if several points have the same polarimetric behavior. This is a well-known result: we cannot separate more than three points with only three independent polarization couples.

To conclude, points having polarimetric responses which are different but not orthogonally represented by a matrix  $S$  will be selected using mechanisms in the space orthogonal to the space spanned by  $S$ .

### C. Nonuniqueness of the Matrix $S$

Unfortunately,  $S$  cannot be obtained from the knowledge of the measurements  $E_1$  and  $E_2$  without any other assumptions. Even worse,  $S$  is not uniquely defined by  $E_1$  and  $E_2$  when no statistical average is performed. If  $E_1$  and  $E_2$  are known, the two matrix relations given in four are equivalent to six complex equations.  $\sigma$  is a real vector of  $N$  components,  $S$  is a  $3 \times N$  complex matrices ( $6N$  real unknowns).  $D$  contains  $N$  real unknowns: the  $N$  interferometric phases. We have then 12 real equations and  $8N$  unknowns.

The normalization of the column vectors of  $S$  gives three additional equations. But even in this case the problem is generally underdetermined for  $N \geq 2$ .

The conclusion here is that separation of point scatterers will be impossible using only the two measurements  $E_1$  and  $E_2$ . Therefore, any polarimetric and interferometric method will require a statistical analysis with the computation of second-order parameters, like the coherency matrices. Besides, this inability to separate coherent centers has already been treated in polarimetry [12] studying coherent decomposition of the scattering matrix.

## III. IMC COHERENCE OPTIMIZATION SCHEME

Since the measurements of  $E_1$  and  $E_2$  are not sufficient to determine the matrices  $S$  and  $D$ , we need to compute second-order statistical parameters. One of these possible parameters is the interferometric coherence.

### A. General Scheme

If the same projection vector is chosen for both images, the generalized coherence can be written as follows:

$$\gamma = \frac{\omega^\dagger T_{12} \omega}{\sqrt{\omega^\dagger T_{11} \omega} \sqrt{\omega^\dagger T_{22} \omega}}. \quad (15)$$

In practice, matrices  $T_{11}$  and  $T_{22}$  are very similar because they are both coherency matrices of the target seen under very close incidence angles. Provided this assumption is valid, the mean average on the denominator is very close to the geometric average. It is then possible to replace the definition of  $\gamma$  by the following:

$$\tilde{\gamma} = \frac{\omega^\dagger T_{12} \omega}{\omega^\dagger T \omega} \quad (16)$$

where matrix  $T$  is defined as  $T = (T_{11} + T_{22})/2$  [13]. Since  $2\sqrt{\omega^\dagger T_{11} \omega} \sqrt{\omega^\dagger T_{22} \omega} \leq \omega^\dagger T_{11} \omega + \omega^\dagger T_{22} \omega$ , the modified coherence  $|\tilde{\gamma}|$  is lower than the generalized coherence  $|\gamma|$ , and then always lies between 0 and 1. Moreover, the argument is not modified by this definition change

$$\arg \gamma = \arg \tilde{\gamma}. \quad (17)$$

$\tilde{\gamma}$  will be called the *IMC coherence*. The set of all complex coherences can be plotted in the complex plane. It will be called the coherence set and written  $\Gamma(T_{12}, T)$ .

It is mathematically proved in [13] that

$$\Gamma(T_{12}, T) = \Omega\left(T^{-\frac{1}{2}} T_{12} T^{-\frac{1}{2}}\right). \quad (18)$$

The set  $\Omega(A)$  is called field of values of matrix  $A$  or numerical range of matrix  $A$ , and it is defined by

$$\Omega(A) = \{\mathbf{x}^\dagger A \mathbf{x} : \mathbf{x} \in \mathbb{C}^n, \|\mathbf{x}\| = 1\}. \quad (19)$$

Mathematically, the optimization of  $\tilde{\gamma}$  is then equivalent to calculating the numerical radius of the matrix  $T^{-(1/2)} T_{12} T^{-(1/2)}$  [13]. By definition, the numerical radius of a matrix  $A$  is  $r(A) = \max\{|\mathbf{x}^\dagger A \mathbf{x}| : \mathbf{x} \in \mathbb{C}^n, \|\mathbf{x}\| = 1\}$ . There is no analytical method to find the numerical radius of a matrix  $A$ . However, a numerical algorithm exists which is described in [14]. A block diagram of which is shown in Fig. 1.

A local optimum is thus reached associated with a vector  $\mathbf{x}$ . The associated optimal vector  $\omega$  for the coherence is given by  $\omega = T^{-(1/2)} \mathbf{x}$  [13].

Although the definition of the IMC coherence is satisfactory, we have to keep in mind that this iteration approach leads to a local maximum and not to a global one.

### B. First Method: Three Independent Optimizations

This optimization results in a local maximum associated with only one mechanism  $\omega_1$ . However the workspace is of dimension 3. In order to obtain the other mechanisms  $\omega_2$  and  $\omega_3$ , one

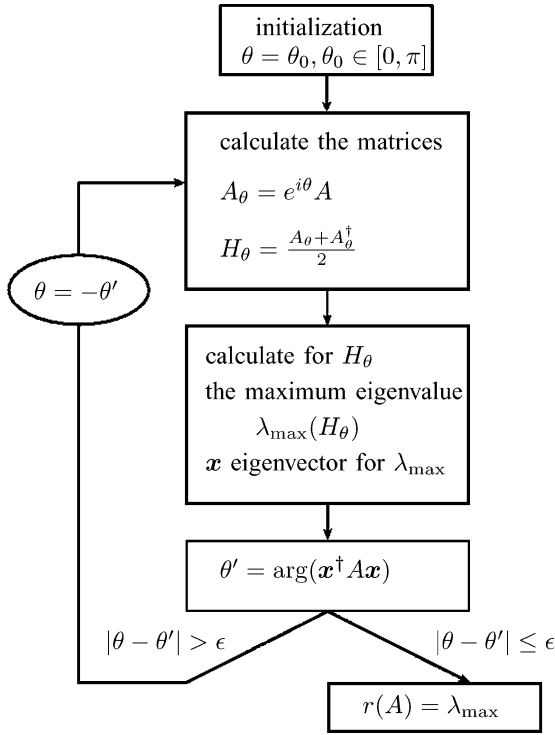


Fig. 1. Block diagram of an estimation method for the numerical radius of a matrix  $A$ .

can apply again the optimization procedure with another initial angle. The choice of this initial angle is delicate if one does not want to try too many optimizations. If the coherence set can be delimited by an angular sector, this angular sector is defined by its angles  $\theta_{\min}$  and  $\theta_{\max}$ , and we can compute these angles. After that, the algorithm will be started using  $\theta_{\min}$  for the initial angle, then  $\theta_{\max}$ , and finally the last initial angle will be chosen by  $(1/2)(\theta_{\min} + \theta_{\max})$ . Otherwise, we can test the optimization procedure with other initial angles depending on the configuration. The procedure is summarized as follows.

- Compute the matrices  $T_{11}, T_{22}, T_{12}, T = (1/2)(T_{11} + T_{22})$  and  $A = T^{-(1/2)} T_{12} T^{-(1/2)}$ .
- Represent the numerical range of  $A$  and choose three different initial angles  $\theta_1^0, \theta_2^0, \theta_3^0$ .
- Compute three times the algorithm of the numerical radius on matrix  $A$  using  $\theta_1^0, \theta_2^0, \theta_3^0$  as initial angles. You obtain three interferometric phases  $\theta_1, \theta_2, \theta_3$  and three vectors  $\mathbf{x}_1, \mathbf{x}_2, \mathbf{x}_3$ .
- Compute the three vectors  $\boldsymbol{\omega}_1 = T^{(1/2)} \mathbf{x}_1, \boldsymbol{\omega}_2 = T^{(1/2)} \mathbf{x}_2, \boldsymbol{\omega}_3 = T^{(1/2)} \mathbf{x}_3$ . Then form the matrix  $M = [\boldsymbol{\omega}_1, \boldsymbol{\omega}_2, \boldsymbol{\omega}_3]$  and compute  $S = M^{\dagger -1}$ . The next section shows that matrix  $S$  contains the diffusion vectors of each individual scatterer whose interferometric phases are  $\theta_1, \theta_2, \theta_3$ .

### C. Second Method: Optimization in an Orthogonal Basis

After having found a first optimal coherence and the associated vector  $\mathbf{x}_1$ , the second optimization can be achieved in the two-dimensional subspace orthogonal to  $\mathbf{x}_1$ . The procedure is summarized as follows.

- Compute the matrices  $T_{11}, T_{22}, T_{12}, T = (1/2)(T_{11} + T_{22})$  and  $A = T^{-(1/2)} T_{12} T^{-(1/2)}$ .

- Compute the algorithm of the numerical radius on matrix  $A$  using  $\theta_1^0 = 0$ . You will find a first interferometric phase  $\theta_1$  and the corresponding vector  $\mathbf{x}_1$ . This vector is found by an eigenvalue problem. It belongs to a basis change matrix. Let  $P$  be this matrix whose first column is  $\mathbf{x}_1$ .
- Then consider the restriction of  $A$  to the subspace orthogonal to  $\mathbf{x}_1$ : compute  $A' = P^{\dagger} A P$ . The restriction of  $A$  is defined by the submatrix of  $A'$  where the first line and the first column of  $A'$  are replaced by zeros. Let us call  $A''$  this new matrix.
- Compute the numerical radius on this matrix  $A''$ . You will find two interferometric angles  $\theta_2$  and  $\theta_3$ , associated with two vectors  $\mathbf{x}'_2$  and  $\mathbf{x}'_3$ .
- Compute  $\mathbf{x}_2 = P \mathbf{x}'_2$  and  $\mathbf{x}_3 = P \mathbf{x}'_3$ . Vectors  $\mathbf{x}_1, \mathbf{x}_2, \mathbf{x}_3$  are orthogonal. The corresponding mechanisms can be computed according to  $\boldsymbol{\omega}_1 = T^{(1/2)} \mathbf{x}_1, \boldsymbol{\omega}_2 = T^{(1/2)} \mathbf{x}_2, \boldsymbol{\omega}_3 = T^{(1/2)} \mathbf{x}_3$ .  $\mathbf{x}_1, \mathbf{x}_2, \mathbf{x}_3$  are orthogonal, but since  $T$  is not a unitary matrix, the mechanisms  $\boldsymbol{\omega}_1, \boldsymbol{\omega}_2, \boldsymbol{\omega}_3$  are not necessarily orthogonal.

## IV. SEPARATING UP TO THREE SCATTERING CENTERS IN A RESOLUTION CELL USING THE IMC COHERENCE OPTIMIZATION

This section describes when and why the previous optimization coherence methods can estimate correct interferometric phases of isolated point scatterers in a resolution cell.

### A. Theoretical Approach With a Resolution Cell Containing Exactly Three Point Scatterers

With the same conventions as above we will first study the case of three point scatterers. The coherency matrices are given by

$$T_{12} = S \sigma \sigma^{\dagger} D^* S^{\dagger} \quad T_{11} = S \sigma \sigma^{\dagger} S^{\dagger} \quad T_{22} = S D \sigma \sigma^{\dagger} D^* S^{\dagger} \quad (20)$$

If no statistical average is applied to compute the coherence, all these matrices have a determinant equal to zero because  $\sigma \sigma^{\dagger}$  is of rank 1. In the context of high-resolution imagery, our model is a set of point-like scatterers measured over large synthetic apertures. The scatterers are fixed in location, so spatial decorrelation is not as important as in the presence of volume decorrelation for lower frequencies and natural targets. We can then consider a decorrelation caused by additive noise of SAR system and introduce a statistical fluctuation on  $\sigma$ . Therefore, the coherency matrices become

$$T_{12} = S C D^* S^{\dagger} \quad T_{11} = S C S^{\dagger} \quad T_{22} = S D C D^* S^{\dagger} \quad (21)$$

with

$$C = \langle \sigma \sigma^{\dagger} \rangle. \quad (22)$$

$C$  is the correlation matrix of the vector  $\sigma$ ; it is a real positive symmetric matrix which can be considered of full rank 3. The IMC coherence is then written

$$\begin{aligned} \gamma(\boldsymbol{\omega}) &= \frac{\boldsymbol{\omega}^{\dagger} T_{12} \boldsymbol{\omega}}{\frac{1}{2}(\boldsymbol{\omega}^{\dagger} T_{11} \boldsymbol{\omega} + \boldsymbol{\omega}^{\dagger} T_{22} \boldsymbol{\omega})} \\ &= \frac{\boldsymbol{\omega}^{\dagger} S C D^* S^{\dagger} \boldsymbol{\omega}}{\frac{1}{2}(\boldsymbol{\omega}^{\dagger} S C S^{\dagger} \boldsymbol{\omega} + \boldsymbol{\omega}^{\dagger} S D C D^* S^{\dagger} \boldsymbol{\omega})}. \end{aligned} \quad (23)$$

Let  $\mathbf{v} = S^\dagger \boldsymbol{\omega}$  in this expression, and  $M = S^{\dagger-1}$  so that  $\boldsymbol{\omega} = M\mathbf{v}$

$$\gamma(\boldsymbol{\omega}) = \gamma(M\mathbf{v}) = \frac{\mathbf{v}^\dagger CD^*\mathbf{v}}{\frac{1}{2}(\mathbf{v}^\dagger C\mathbf{v} + \mathbf{v}^\dagger DCD^*\mathbf{v})}. \quad (24)$$

Changing  $\mathbf{v}$  by  $\lambda\mathbf{v}$ , where  $\lambda$  is a scalar, does not change the resulting coherence. We can then suppose that  $\mathbf{v}$  is normalized. Moreover, we can quickly check that  $|\gamma(\boldsymbol{\omega})| < 1$ . Let us indicate the scalar product of two vectors with

$$\begin{aligned} |\mathbf{v}^\dagger CD^*\mathbf{v}| &= \left| \left( C^{\frac{1}{2}}\mathbf{v} \right) \cdot \left( C^{\frac{1}{2}}D^*\mathbf{v} \right) \right| \\ &\leq \sqrt{\mathbf{v}^\dagger C\mathbf{v}} \sqrt{\mathbf{v}^\dagger DCD^*\mathbf{v}} \\ &\leq \frac{1}{2} \left( (\mathbf{v}^\dagger C\mathbf{v}) + (\mathbf{v}^\dagger DCD^*\mathbf{v}) \right). \end{aligned}$$

The first inequality is the Schwarz's inequality, whereas the second one means that the geometrical mean is always less than the arithmetic mean.

Let us consider the numerical range of  $D^*$ . Since  $D$  is a diagonal matrix, it is mathematically proved in [15] that its numerical range is the triangle whose vertices are the diagonal elements. We can check that this numerical range is included in the coherence set. Let  $\lambda_i$  be  $e^{j\Phi_i}$ .  $\lambda_i$  can be obtained thanks to  $D^*\mathbf{e}_i = \lambda_i\mathbf{e}_i$

$$\begin{aligned} \gamma(M\mathbf{e}_i) &= \frac{\mathbf{e}_i^\dagger CD^*\mathbf{e}_i}{\frac{1}{2}(\mathbf{e}_i^\dagger C\mathbf{e}_i + \mathbf{e}_i^\dagger DCD^*\mathbf{e}_i)} \\ &= \frac{\lambda_i \mathbf{e}_i^\dagger C\mathbf{e}_i}{\frac{1}{2}(\mathbf{e}_i^\dagger C\mathbf{e}_i + \lambda_i \lambda_i^* \mathbf{e}_i^\dagger C\mathbf{e}_i)} \\ &= \lambda_i. \end{aligned} \quad (25)$$

This proves that the three complex values  $\lambda_i$  belong to the coherence set. Moreover this set is convex, so it contains the convex hull whose vertices are  $\lambda_i$ ; in other words it contains the whole numerical range of  $D^*$ . A theoretical graphical example is given in Fig. 2. The numerical range of  $D^*$  is represented in light gray; an associated coherence set lies in dark gray. It contains the  $D^*$  numerical range, and it is bounded by the unitary circle.

We can immediately deduce from (25) that the coherence is maximum and is equal to 1 at three points, which are obtained with  $\mathbf{v}_i = \mathbf{e}_i$ , i.e.,  $\boldsymbol{\omega}_i = M\mathbf{e}_i$ .

Theoretically, the first method (the general optimization with three different initial angles) allows to find exactly the three mechanisms  $\boldsymbol{\omega}_i = M\mathbf{v}_i = M\mathbf{e}_i$  associated with coherences equal to 1. Because this optimization method does not provide a unique solutions and that the choice of initial parameters can be difficult, this method is intended for measurements of simple targets, for example in an anechoic chamber.

With the second method, the optimization in an orthogonal basis  $\boldsymbol{\omega}_2$  and  $\boldsymbol{\omega}_3$  will not give exactly the second and third interferometric phases but will find a good approximation of these angles in a faster way. Moreover, it can be a better estimate of these interferometric angles when one takes into account other stochastic components, as explained in the next section. The drawback is that it will be difficult to interpret physically  $\boldsymbol{\omega}_2$

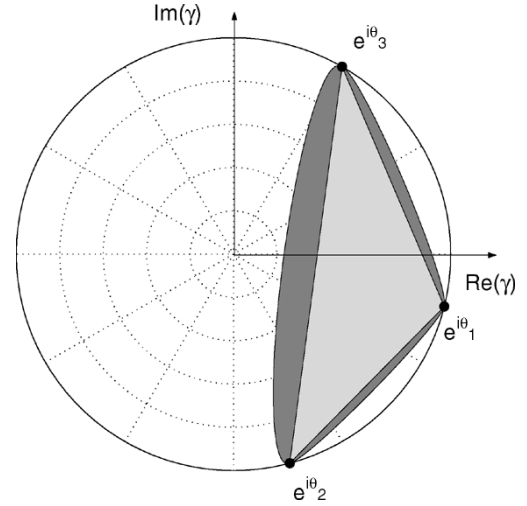


Fig. 2. IMC coherence optimization results on simulated data. (Dark gray) The coherence set. (Light gray) The numerical range of  $D^*$ . (Black dots) The coherences in the optimal basis.

and  $\boldsymbol{\omega}_3$ , but we should have this method in reserve in case an accurate estimation of phase is required rather than a physical interpretation of different polarimetric mechanisms.

#### B. When the Resolution Cell Contains Less Than Three Point Scatterers

When the resolution cell contains only one or two main independent scatterers, the optimization algorithm will still provide the estimation of their interferometric phase. The three interferometric phases found in the optimum basis will be equal.

#### C. When the Resolution Cell Contains More Than Three Point Scatterers

When the resolution cell contains more than three scattering centers, the conclusions about the coherence set are no more valid (see Fig. 3). However the following statements may be argued.

- All points with similar polarimetric responses will not be separated. They will be regarded as a single point located on a weighted-average phase center. No polarimetric method is able to separate local scatterers with the same scattering mechanisms.
- If a point has a polarimetric diffusion vector  $\mathbf{s}$  which is orthogonal to all the other ones, it can be estimated by the optimum scattering vector.
- In the other cases, points have polarimetric vectors which are not orthogonal but are linearly independent. Preliminary investigations show that the optimization procedure is not always able to separate them. However, the different results obtained in this configuration need further investigations using the properties of the numerical range described in [15].

#### D. Stochastic Contributions Other Than $\sigma$

The optimization capabilities have been assessed assuming that the stochastic components of the data model come from the amplitude vector  $\sigma$ . The study can be generalized assuming other sources of noise, as follows.

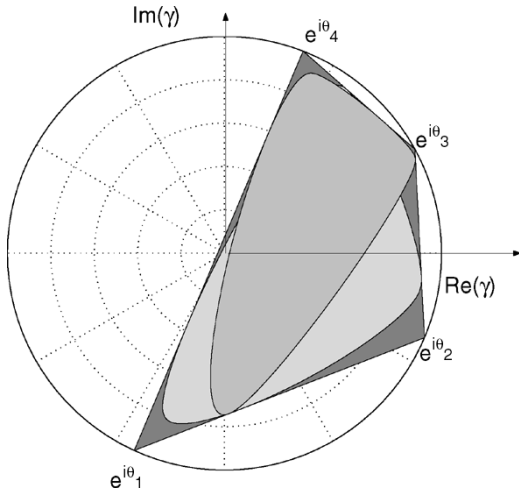


Fig. 3. (Gray) Two different simulated coherence sets obtained with four scattering centers. (Black dots) Theoretical interferometric phases of the point scatterers.

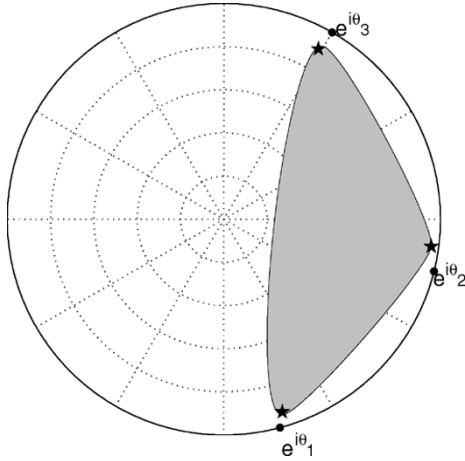


Fig. 4. (Gray) Simulated coherence set obtained with statistical variations of  $D$ . (Black stars) Interferometric phases obtained in the orthogonal optimal basis. (Black dots) Theoretical interferometric phases of the point scatterers.

- If the interferometric phase measurement contains a stochastic component, a numerical simulation of the effects of a variation of  $D$  on the optimization procedures is given in Fig. 4. On this simulation, the interferometric phases are supposed to be normally distributed:  $\Phi_i \sim \mathcal{N}(\Phi_{i0}, \sigma)$  where  $\sigma = 20^\circ$ , and the coherency matrices are computed using 25 samples.
- The optimization method of the IMC coherence in an orthogonal basis will extract a good approximation of the mean interferometric phases. We see that averaging on several matrices  $D$  leads to lower coherence observations. This trend involves some biases in the estimation of the interferometric phases which do not exceed  $5^\circ$  in all our simulations. The second optimization performed in an orthogonal basis leads to better estimates than the first optimization method (three independent optimizations).
- Let us suppose that  $S$  contains stochastic signal components. Many simulations have been conducted. Here we present a case where the stochastic components of the column vectors of  $S$  are Gaussian vectors with an additive

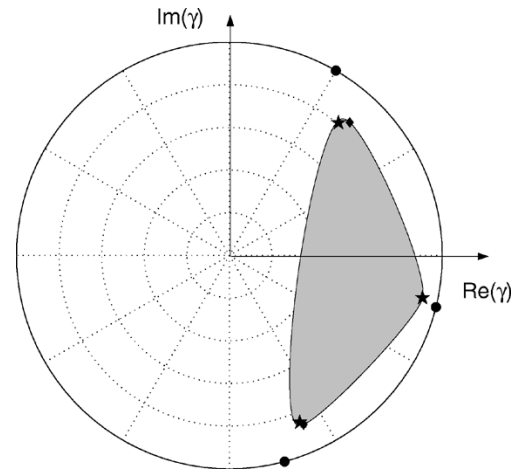


Fig. 5. (Light gray) Simulated coherence set obtained with statistical variations of  $S$ . (Black stars) Interferometric phases obtained in the orthogonal optimal basis. (Black diamonds) Interferometric phases obtained in the general independent basis. (Black dots) Theoretical interferometric phases of the point scatterers.

noise of relative standard deviation 0.15:  $S = S_0 + s$ ,  $s \sim \mathcal{N}(0, 0.15)$ . The matrices  $D$  and  $C$  are the same ones as previously, and the average on  $S$  has been made on 25 samples. A resulting coherence set is shown in Fig. 5. Once again, the optimization procedure corresponds to the extremities of this set, which are plotted in black. The numerical range of  $D$  is drawn in dark gray. Same conclusions as with statistical variations of  $D$  can be drawn: the optimization performed in an orthogonal basis leads to better estimates than the three independent optimizations, as shown in Fig. 5.

## V. EXPERIMENTAL RESULTS

The aim of the section is to verify the theoretical results of the previous section, i.e., the interferometric phases calculated with the optimal basis  $(\omega_a, \omega_b, \omega_c)$  give convincing results for the separation of interferometric phases of scattering centers. In the following, results are presented using the second optimization method (in an orthogonal basis).

### A. In an Anechoic Chamber

Previous results have been obtained using data acquired in the anechoic chamber CAMERA at the French Aerospace Research Center (ONERA). Full experiment description and results can be found in [16]. The optimization methods have been tested on a simple metallic target. This target is considered as a collection of a few scattering centers located inside a single resolution cell. In this context, both ESPRIT or the IMC coherence optimization methods are able to retrieve the theoretical interferometric phases of bright scatters. The model developed in the previous section is well adapted in this particular case because coherences are very high, and because there is no volume decorrelation. It is then possible to consider statistical fluctuation coming from measurement noise. This is confirmed by the fact that the coherence sets have been found to be identical to those predicted by this theoretical approach. Fig. 6 presents one of these coherence sets and the coherences found in the optimization basis.

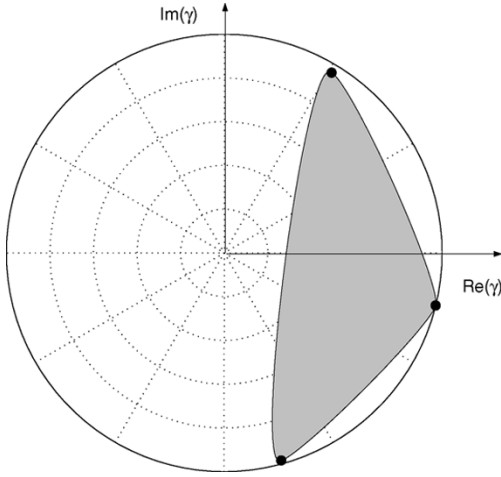


Fig. 6. IMC coherence optimization results on coherence set computed using REAL EXPERIMENTAL data. The black dots are the coherence found in the optimal polarization basis.

In this case, the coherence optimization makes it possible to separate the different phase centers, but also to obtain polarimetric information contained in the mechanism vector  $\omega$ . Using the first optimization method we are able to find the estimation of matrix  $S = M^{\dagger-1}$  and therefore to have the polarimetric answer of each selected bright point. Thus, the polarimetric response of the dihedral point expressed in the Pauli basis has been found to be close to  $(\epsilon, 1, \epsilon)^t$ , ( $\epsilon \ll 1$ ) which is the classical double-bounce response. The polarimetric answer of an edge of a metallic plate has been found to be close to  $(0.9, \alpha e^{j1.8}, \epsilon)^t$  where  $\alpha$  lies between 0 and 0.4, increasing with the incidence angle. The polarimetric answer of a cylinder roof has been found to be close to  $(0.9, 0.3, \epsilon)^t$ . All these diffusion vectors are similar to those obtained with an image of the target constructed using a bidimensional Fourier transform of the hologram. In this image the different bright points are located in different cells whose diffusion vectors can be extracted.

#### B. On Real SAR Data

In this section, the approach is validated on a PolInSAR image. We will see in this case how the IMC coherence optimization can give a better estimation of the interferometric phase of the target, which can be considered as one or two scattering points in a noisy environment.

#### C. How to Compute the Coherence

The calculation of the interferometric coherence requires averaging over many samples from the same distribution. Computationally, it is generally estimated using a boxcar filter where samples are in a  $N \times N$  window. The coherence estimation improves as  $N$  increases. The drawback of this is that samples used to compute the coherence can be finally chosen in heterogeneous areas and do not belong to the same statistical population.

In order to avoid this problem, another idea is to use as a statistical population of the pixel, the complex backscattering coefficients obtained using a subaperture and a subset of the frequency bandwidth of the emitted wave. These complex coefficients are computed thanks to a multidimensional wavelet transform of the backscattering signal registered for a pixel located at position  $\mathbf{r}_0$ . This coefficient computed for this pixel

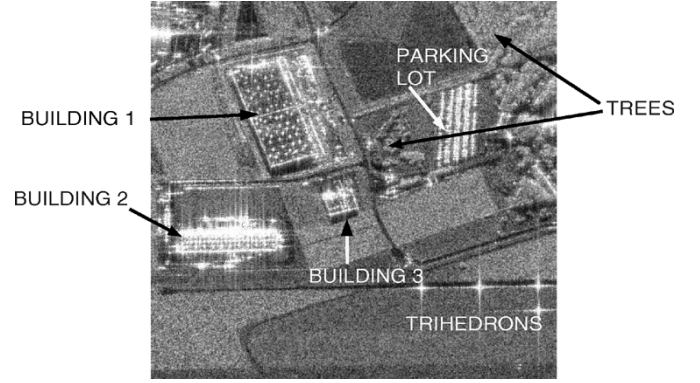


Fig. 7. Urban SAR image at X-band.

and centered around the frequency  $f_0$  and the aspect angle  $\phi_0$  is written  $C(f_0, \phi_0)$ . Detailed information about how to compute this coefficient can be found in [17]. The coherence is computed for each polarization using an average performed on all wavelet coefficients of the pixel, which belong to the same distribution. Then the IMC coherence optimization has been performed using this coherence value. After examination of coherence sets, it has been found that secondary maxima are often not significant. For this reason, we applied the second optimization method in an orthogonal basis which has been found to provide better estimates when working with important noise sources different from strictly amplitude fluctuations.

#### D. Results on a X-Band Urban SAR Image

A SAR image (see Fig. 7) of  $500 \times 500$  pixels has been selected in the airborne RAMSES X-band data on Bretigny. It contains industrial buildings, trees, a parking lot, and four canonical trihedrals used for calibration. Wavelet coefficients  $C(f, \phi)$  have been calculated for ten angles  $\phi_0$ , ten frequencies  $f_0$ . That means that 100 looks are available to compute the coherence. The parameters of the wavelets are chosen in order to obtain spread in frequency and aspect angle domains representing both 10% of the angular and frequency bandwidth.

The height  $h$  corresponding to an interferometric phase  $\Phi$  can be estimated by

$$h = \frac{h_a}{2\pi} \Phi \quad (26)$$

where  $h_a$  is called the ambiguity height and depends on the geometrical parameters of the radar

$$h_a = \frac{\lambda R}{b_{\perp}} \sin \theta. \quad (27)$$

$R$  is the distance between the radar and the target,  $b_{\perp}$  is the baseline component perpendicular to the incidence direction,  $\lambda$  is the wavelength, and  $\theta$  is the incidence angle.

The resulting digital elevation model obtained with the interferometric phase corresponding to the optimum scattering mechanism is shown in Fig. 8.

For most of the pixels of the image, the three optimum vectors lead to similar elevations. That means that the target can be considered as a single point in a noisy environment. The optimization procedure leads then to an accurate estimation of the interferometric phases of the target with a significant noise



Fig. 8. Digital elevation model after 1MC coherence optimization.

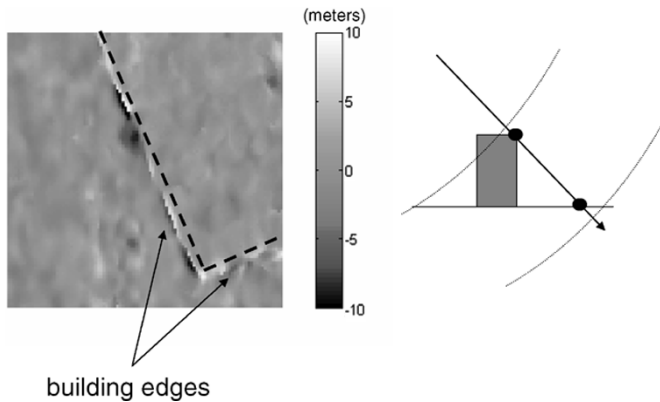


Fig. 9. Zoom on edge of building 1. Digital elevation model different between the first optimum mechanism and the second optimum mechanism.

amplitude. The standard deviations of the optimal elevation on homogeneous areas is improved in comparison with the ones which would be obtained with a single polarization.

A more detailed study allows us to highlight some points where the heights are not similar for the three optimal mechanisms: for example the points located at the edge of building 1. The average process leads to high-resolution degradation. Thus, there are pixels which contain the building roof and the building shadow together. These correspond to two different interferometric phases: the one of the roof and the one of the ground. We will see now that these two different heights can be separated in the optimal polarimetric basis.

The difference between the heights obtained using the optimum vector and the heights obtained using the second optimum vector are thus shown in Fig. 9. We can distinguish two sorts of points: some of them have a height computed using  $\omega_a$  higher than the height computed using  $\omega_b$ . These heights are selected and plotted in Fig. 10. The other ones have a height computed using  $\omega_a$  lower than the one computed using  $\omega_b$ . These heights are plotted in Fig. 11. We can guess that the optimization procedure has separated the heights of two different points located in the same resolution cell and having two different polarization mechanisms: one point belonging to the ground and one point belonging to the roof, whose height is then related to the top of the building, which has been evaluated

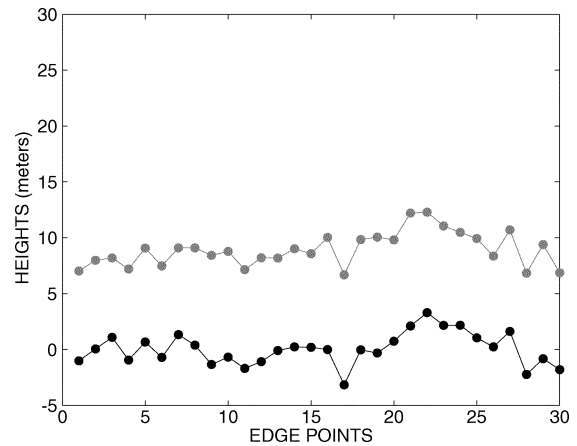


Fig. 10. Heights of points located on the edge of building 1. (Dark) Using  $\omega_1$ . (Gray) Using  $\omega_2$ .

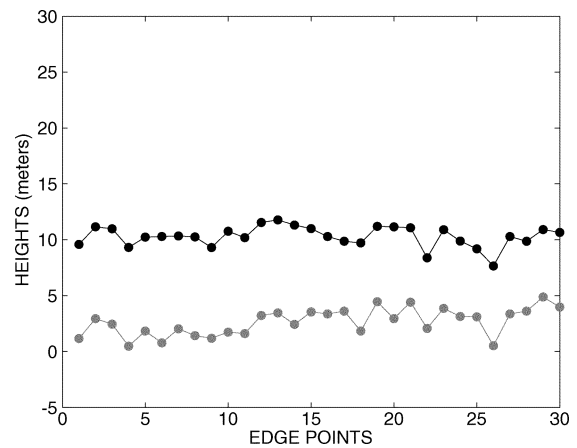


Fig. 11. Heights of points located on the edge of building 1. (Dark) Using  $\omega_1$ . (Gray) Using  $\omega_2$ .

according to ground truth to 10 m. However, the remaining poor accuracy of the measured heights is due to the geometrical configuration of the radar which lead to a very high ambiguity height  $h_a$  (around 200 m). With this configuration, an error of  $1^\circ$  on the interferometric phase corresponds to an error of 55 cm on the corresponding height.

## VI. CONCLUSION

The choice of a polarimetric coherence optimization controls the resulting interferometric phases. The 2MC coherence optimization produces the highest possible coherence level, but it does not necessarily generate more accurate interferometric phases. With a resolution cell consisting of several point scatterers, the 1MC coherence optimization gives convincing results: we have shown for the first time that this optimization makes it possible to determine the vertical position of different phase centers associated with different mechanisms.

However, it is not possible with this technique to separate the contributions of the same scattering mechanism distributed over different heights. In this case, the method measures the mean phase center of the respective mechanism. Moreover, interaction effects are not taken into account.

This approach can be applied to real SAR data in order to retrieve both accurate interferometric phases of dominant scattering mechanisms and the polarization state of the main scatterer. Applications to X-band SAR data show that results are more accurate using IMC coherence optimization, even when only one significant interferometric phase can be estimated.

Further studies should be devoted to a better statistical characterization of the noise effects on the coherence set as well as on the method. Moreover the method should be applied to other SAR images of man-made targets with better height accuracy.

#### ACKNOWLEDGMENT

The authors are thankful to the anonymous reviewers, who have greatly contributed by their remarks to improve the quality of this paper, and to J. Delille for her careful reading of the manuscript.

#### REFERENCES

- [1] L. C. Graham, "Synthetic interferometric radar for topographic mapping," *Proc. IEEE*, vol. 62, no. 6, pp. 763–768, Jun. 1974.
- [2] K. Papathanassiou, "Polarimetric SAR interferometry," Ph.D. thesis, Univ. Graz, Graz, Austria, Jan. 1999.
- [3] S. R. Cloude and K. P. Papathanassiou, "Polarimetric SAR interferometry," *IEEE Trans. Geosci. Remote Sens.*, vol. 36, no. 5, pp. 1551–1565, Sep. 1998.
- [4] G. Nico, J. M. Lopez-Sanchez, J. Fortuny, D. Tarchi, D. Leva, and A. J. Sieber, "Assessment of the impact of polarimetric coherence optimization on phase unwrapping," in *Proc. EUSAR 2000*, Mar. 2000, pp. 523–536.
- [5] C. Pascual, E. Gimeno, and J. M. N. Lopez-Sanchez, "The equivalence between the polarization subspace method (PSM) and the coherence optimization in polarimetric radar interferometry," presented at the *EUSAR 2002*, 2002.
- [6] M. Qong, "Coherence optimization using the polarization state conformation in PolInSAR," *IEEE Geosci. Remote Sens. Lett.*, vol. 2, pp. 301–305, Jul. 2005.
- [7] H. Yamada, Y. Yamaguchi, Y. Kim, E. Rodriguez, and W-M. Boerner, "Polarimetric SAR interferometry for forest analysis based on the ES-PRIT algorithm," *IEICE Trans. Electron.*, vol. E84C, pp. 1917–1924, Dec. 2001.
- [8] S. Guillaso, L. Ferro-Famil, A. Reigber, and E. Pottier, "Analysis of built-up areas from polarimetric interferometric SAR images," in *Proc. IGARSS*, vol. 3, Jul. 2003, pp. 1727–1729.
- [9] E. Colin, C. Titin-Schnaider, and W. Tabbara, "Investigation on different IFPOL coherence optimization methods," presented at the *POLINSAR*, Jan. 2003. [Online]. Available: <http://earth.esa.int/workshops/polinsar2003/participants/colin75/polinsar03.pdf>.
- [10] R. Z. Schneider, A. Liseno, K. P. Papathanassiou, and I. Hajnsek, "Polarimetric SAR interferometry over urban areas: Frst results," presented at the *EUSAR 2004*, 2004.
- [11] J. L. Gomez-Dans and S. Quegan, "Constraining coherence optimization in polarimetric interferometry of layered targets," presented at the *POLINSAR*, Jan. 2005. [Online]. Available: <http://earth.esa.int/workshops/polinsar2005/participants/264/>.
- [12] S. R. Cloude and E. Pottier, "A review of target decomposition theorems in radar polarimetry," *IEEE Trans. Geosci. Remote Sens.*, vol. 34, no. 2, pp. 498–518, Mar. 1996.
- [13] M. Tabb, J. Orrey, T. Flynn, and R. Carande, "Phase diversity: A decomposition for vegetation parameter estimation using polarimetric SAR interferometry," presented at the *EUSAR*, 2002.
- [14] G. Watson, "Computing the numerical radius," *Linear Alg. Its Appl.*, vol. 234, pp. 163–172, 1996.
- [15] D. S. Keeler, L. Rodman, and I. M. Spitkovsky, "The numerical range of  $3 \times 3$  matrices," *Linear Alg. Its Appl.*, vol. 252, pp. 115–139, 1997.
- [16] E. Colin, C. Titin-Schnaider, and W. Tabbara, "Coherence optimization methods for scattering centers separation in polarimetric interferometry," *J. Electromagn. Waves Appl.*, vol. 19, no. 9, pp. 1237–1250, 2005.
- [17] E. Colin, M. Tria, C. Titin-Schnaider, and J-P. Ovarlez, "Imaging using multidimensional continuous wavelet transform and applications to polarimetry and interferometry," *Int. J. Imaging Syst. Technol.*, vol. 14, no. 5, pp. 181–221, 2004.



**Elise Colin** was born on November 15, 1979. She received jointly the engineering degree from Supelec and the Diplôme d'Etudes Approfondies degree in theoretical physics (fields, particles, and matter) from the University of Orsay (Paris XI), Orsay, France, and the Ph.D. degree from the University of Paris VI, Paris, France, in 2002 and 2005, respectively.

She joined the Electromagnetic and Radar Division, French Aerospace Research Center (ONERA), Palaiseau, France, in 2005. She has been working on polarimetric interferometry with airborne systems.

Her other research interests are SAR signal processing, time-frequency analysis by means wavelets, and vegetation modeling.



**Cécile Titin-Schnaider** was born in Paris, France, in 1946. She received the Ph.D. degree in nuclear physics from the University of Orsay (Paris XI), Orsay, France, in 1974.

She joined SNECMA and worked on mathematical methods in thermics. Then, she joined the French Aerospace Research Center (ONERA), Palaiseau, France, in 1975. Her research interests cover various subjects in electromagnetism and radar. Her current interest is polarimetric radar calibration and polarimetric images analysis.



**Walid Tabbara** (M'83) was born in Beirut, Lebanon, in 1946. He received the Doctorat ès Sciences (Ph.D.) degree from the University of Paris VI, Paris, France, in 1976.

He is currently a Full Professor at the University of Paris VI, since 1981. His research is done at the Département de Recherche en Electromagnétisme (DRE), Supélec. From 1987 to 1996, he acted as a Deputy Director of the Laboratoire des Signaux et Systèmes (Supélec-CNRS). After working for a long period in the field of inverse scattering in elec-

tromagnetics and acoustics, his present fields of interest are Electromagnetic Compatibility (EM, remote sensing, indoor propagation and high-power microwaves (HPM)). His present and passed researches has led to the publication of 48 papers in international journals and to 158 presentations at international and national conferences. He is on the editorial boards of the *Journal of Electromagnetic Waves and Applications* and the *Journal of Computer Applications in Engineering Education*.

Dr. Tabbara has organized and/or chaired sessions at national and international conferences. He was the French delegate to Commission B of URSI from 1984 to 1990. He is a member of URSI and the Electromagnetics Academy.